Title

Impact Resistance in Biological Materials as a Source of Inspiration for Engineered Designs

Permalink

https://escholarship.org/uc/item/7w50s7k1

Author

Lazarus, Benjamin Seth

Publication Date

2022

Peer reviewed|Thesis/dissertation

UNIVERSITY OF CALIFORNIA SAN DIEGO

Impact Resistance in Biological Materials as a Source of Inspiration for Engineered Designs

A dissertation submitted in partial satisfaction of the requirements for the degree

Doctor of Philosophy

in

Materials Science and Engineering

by

Benjamin Seth Lazarus

Committee in charge:

      Professor Marc A. Meyers, Chair
      Professor Shengqiang Cai
      Professor Iwona Jasiuk
      Professor Falko Kuester
      Professor Vlado Lubarda

2022

The Dissertation of Benjamin Seth Lazarus is approved, and it is acceptable

in quality and form for publication on microfilm and electronically.

University of California San Diego

2022

TABLE OF CONTENTS

LIST OF FIGURES

LIST OF TABLES

ACKNOWLEDGEMENTS

Chapter 7, in part, is in preparation for submission authored by B. Lazarus, R. Luu, V. Leung, S. Ruiz-Perez, M. Wong, J. Barbosa, M. Meyers. The dissertation author is the primary investigator and co-first author of this work.

VITA

2019   Bachelor of Science, William & Mary

2020   Master of Science, University of California San Diego

2022   Doctor of Philosophy, University of California San Diego

PUBLICATIONS

Lazarus BS, Luu RK, Leung V, Ruiz-Perez S, Wong M, Barbosa JDV, Meyers MA, "Pé na jaca: composition, structure, and progressive collapsibility in the largest fruit on Earth (the jackfruit) for impact resistance", (in preparation).

Lazarus BS, Luu RK, Ruiz-Perez S, Wong M, Leung V, Jasiuk I, Meyers MA, "Fracture control, structural recovery, and compressive behavior of the horse hoof wall investigated with in-situ microCT", (in preparation).

Shiang A, Bonney C, **Lazarus BS,** Meyers MA, Jasiuk I, "Hierarchical Modeling of Elastic Moduli of Equine Hoof Wall", Journal of Materials Research and Technology (under review).

Bezerra WB, Costa UO, Rodrigues JGP, **Lazarus BS**, Tavares SS, Santos da Luz, Monteiro SN, "Influence of Arapaima gigas fish scales as reinforcement in DGEBA/TETA epoxy composites for flooring applications: mechanical and thermal behavior", Tecnologia em Minerais, Metais e Materiais (under review).

Lazarus BS, Luu RK, Ruiz-Perez S, Bezerra WB, Becerra-Santamaria K, Leung V, Durazo VHL, Jasiuk I, Barbosa JDV, Meyers MA, "Equine hoof wall: structure, properties, and bioinspired designs" Acta Biomaterialia, August 20, 2022.

Araujo D, Azevedo J, Cardoso P, **Lazarus BS**, Morreira M, Silva L, Barbosa J, "Polymeric Composite Reinforced with PET Fiber Waste for Application in Civil Construction as a Cladding Element", Polymers, March 23, 2022.

Cardoso PSM, Ueki MM, Barbosa JDV, Garcia Filho FC, **Lazarus BS**, Azevedo JB, "The Effect of Dialkyl Peroxide Crosslinking on the Properties of LLDPE and UHMWPE", Polymers, September 10, 2021.

Lima GPA, Barbosa JDV, Beal VE, Gonçalves MAMS, Machado BAS, Gerber JZ, **Lazarus BS**, "Exploratory analysis of fire statistical data and prospective study applied to security and protection systems", Internation Journal Disaster Risk Reduction, May 14, 2021.

Lazarus BS, Chadha C, Velasco-Hogan A, Barbosa J, Jasiuk I, Meyers MA: "Engineering with Keratin: A Functional Raw Material and Source of Bioinspiration" iScience, August 20, 2021.

Lazarus BS, Velasco-Hogan A, Gómez-del Río T, Jasiuk I, Meyers MA: "A Review of Impact Resistant Biological and Bioinspired Materials and Structures" Journal of Materials Research and Technology, October 20, 2020.

Lazarus BS: "Controlled Hierarchical Biomaterial Utilizing Diatom Nanostructure"; Honors thesis accepted April 23, 2019, College of William and Mary.

ABSTRACT OF THE DISSERTATION

Impact Resistance in Biological Materials as a Source of Inspiration for Engineered Designs

by

Benjamin Seth Lazarus

Doctor of Philosophy in Materials Science and Engineering

University of California San Diego, 2022

Professor Marc A. Meyers, Chair

Biological materials are often composed of relatively weak constituents yet have evolved complex, hierarchical structures that allow them to achieve remarkable mechanical properties. In biological systems that need to survive impact scenarios, convergent evolution has resulted in design motifs which appear repeatedly in organisms that come from vastly different areas of the natural world. In this work, the structure-property relationships of two systems, the horse hoof wall and the jackfruit, are examined as sources of inspiration for impact resistance.

The horse hoof wall, capable of withstanding large, repeated, dynamic loads, has been touted as a candidate for impact-resistant bioinspiration. However, the scientific community's understanding of this biological material and its translation into engineered designs is incomplete. A model of the hoof wall's viscoelastic response was developed and the role of hydration, strain-

rate, and impact energy on the material's response were elucidated. Post-impact fractography identified hierarchical failure mechanisms of the unique hoof structure. Multi-material 3D printed designs based on the hoof's meso/microstructure were fabricated and exhibited advantageous energy absorption and fracture control relative to control samples.

In-situ microCT suggest that the hollow tubules in the hoof wall may be a progressive failsafe mechanism meant to absorb energy from biaxial lateral compression. These results also highlight behavior variations that arise from different loading orientations, hydrations, and locations within the hoof wall. Toughening mechanisms such as tubule crack deflections, tubule bridging, tubule arresting, and fiber bridging are also visualized providing valuable context to previous studies.

The jackfruit is the largest fruit on Earth reaching 50 kgs and falls from heights of up to 50 m. To survive such large impact energies, the layered structure of the jackfruit includes a series of collapse mechanisms that absorb energy and mitigate damage. Quasi-static, viscoelastic, and dynamic tests are performed on the different layers of the fruit to establish an understanding of the fruit's mechanical behavior. The structures are then replicated using 3D printing to show that the architectures identified in the jackfruit can be utilized in engineered materials to improve their impact resistance.

Chapter 1: Introduction

In the mid-20th century, engineers and materials scientists started to take note of the fascinating mechanical accomplishments of the natural world around them and began drawing inspiration from biological materials in their own material designs. The term bioinspiration was coined to describe this new approach to solving engineering problems and an explosion in research papers characterizing natural systems ensued as researchers looked high (i.e., bird feathers, beaks, and bones) and low (i.e., dragonfish teeth, mantis shrimp dactyl clubs, and lobster shells) for natural muses to learn from. While this new way of thinking spanned from reusable adhesives (such as Velcro, which was inspired by burdock burrs attaching to dog fur) to fluid dynamics (where the unique pattern of whale tubercles is beneficial for controlling leading edge fluid flow), it has proven to be particularly captivating within the materials engineering research community.

Biological materials are often composed of relatively weak constituents due to their low energy synthesis conditions and limited access to building components. However, many biological materials have evolved admirable mechanical properties that are comparable to some of the most advanced engineered materials.[1,2] For example, some spider silk is stronger and tougher than steel or Kevlar .[3,4] These stellar traits are often achieved through the inherent hierarchical structure (structural geometries at multiple different length scales) found in natural materials and the complex structural designs that have been tuned by generations of evolution to withstand environmental demands.[5,6]

Amongst biological materials, systems capable of withstanding dynamic loading and impact have garnered significant attention for their potential in engineering applications. These systems include defensive (i.e. armors) and offensive (i.e. strikers) anatomies and span a vast array

of lifeforms. However, biological materials are also multifunctional filling different roles in different systems and often performing more that one task at a time. This senate proposal will discuss impact resistance in biological systems before exploring the many functionalities of one of the most impact resistant biopolymers found in nature, keratin. It will then discuss my own work with keratinous hoof walls as well as one of the impact resistance of one of the largest fruits in the world, the jackfruit. Chapter 1 will focus on some of the most prominent impact resistant biological materials that have already been studied, including numerous keratinous and fruit systems. Chapter 2 will build on this by exploring the key takeaways for bioinspired designs and the different ways that researchers have utilized these findings for engineered materials. Chapter 3 will discuss the tunability and multifunctionality of keratin, one of the most impact resistant materials found in nature. Chapters 4 and 5 will highlight the work I have done thus far on hooves and jackfruit, respectively. Chapter 6 will layout the proposed future work for the completion of my doctoral thesis. Section 7 will concisely summarize the proposal.

Chapter 2: Impact resistance in nature

Impact events are characterized by the collision of two bodies at high velocities. This can further be classified into different realms of impact, ranging from explosive (5-15 km/s) and ballistic (200-1200 m/s) impacts down to those seen in the natural world (1 m/s-30m/s). The key distinction between impact and quasi-static loading is that the process is not allowed to equilibrate as the force is applied. In impact systems, the load is transmitted through the material as a series of elastic and plastic waves, and these pulses engender the deformation at any given Lagrangian point. Despite these differences, most biological materials that experience impacts in nature have primarily been studied under quasi-static loading. This is likely because this type of testing is easier

to perform and analyze, but while these results are useful, they can lead to very different results and conclusions.

For example, the conch shell exhibits an intricate cross-lamellar structure with three orders of hierarchy. Under quasi-static three-point bending and compression loading, fractures develop along the interface of these crossed-lamellae which create tortuous crack paths, arrest cracks, and can lead to multiple cracks developing in a single first-order lamellae. All of this has been shown to absorb a significant amount of energy and improve the toughness of the conch shell.[7–9] However, studies of predation on juvenile conch shows a significant number of fatalities from crushing or chipping predators (such as sharks, rays, and hermit crabs).[10] This implies a degree of dynamic impact that the conch must protect itself from. When tested under impact conditions the conch responded entirely differently. Instead of cracks deflecting along each order of lamellae, the third-order lamellae were pulverized into nanorods that absorbed energy through rotation and separation from the shell. This failure mechanism delocalizes damage along the surface of the shell and helps protect the internal tissue of the conch.[11] A comparison between the fracture surfaces of conch shells under dynamic loading (left) and quasi-static loading (right) are shown in Figure 2.1A.

Similar phenomena have been observed in wood as well, where the strain-rate plays a vital role in the failure mechanism of the system. Often, denser woods are considered more mechanically robust under quasi-static loading, however Matsushita et al. [12] observed that this trend becomes less surefire at higher strain rates. Effects that arise from flaw density, interlocking grains, and fiber configuration begin to dominate over bulk properties in the impact realm. For example, wood species with bands of pores (which typically develop seasonally) performed worse than species with uniformly diffuse pores because the closely packed pores acted as crack initiators

3

which lead to failure at lower impact energies. Structural reinforcement in the form of lignified aggregate ray cells confine crack paths and stress concentrations and localize damage, causing fractures to travel through the material resulting in premature failure. Features like interlocking grains on the other hand, disperse impact energy and damage, recruiting more material to resist the impact. These are visualized in Figure 2.1 B.

These examples illustrate not only the importance of strain-rate when testing impact in nature but also the role that different structural features have on a materials' performance. This is typically referred to as the structure-property relationship of a material. In nature, this is immensely important as many of the functions performed by biological materials arise from their structure rather than from the inherent bulk properties of their constituent parts like traditional engineered materials. The quintessential example of this is nacre, the iridescent inner layer of mollusk shells. It is composed of 95% aragonite tablets, a brittle naturally occurring mineral composed of calcium carbonate. On a microscale, nacre is famous for it's "brick and mortar" structure where adjacent tablets are held together by a thin organic layer. [13–15] When loaded, cracks tend to preferentially travel along the weaker organic layer – mineral tablet interface rather than fracturing directly through. The result is tortuous crack paths that increase energy absorption and endow nacre with a fracture toughness up to nine times that of aragonite.[14] As the cracks travel through the organic layer, fiber bridging occurs behind the blunted crack-tip. This is an example of an extrinsic toughening method, a strategy that is commonly employed in nature, where structural elements behind the crack tip resist its propagation.

The structure property relationship of nacre's brick and mortar arrangement, depicted in Figure 2.1C has been reported since the early 1980s, however, subsequent research has revealed a plethora of smaller features that further enhance this relatively simple structure. Asperities on the

surface of the aragonite tablets create a surface waviness that interlocks them with the organic matrix and reduces delamination. Mineral bridges between vertically adjacent lamellae form as a byproduct of nacre's growth process and play a similar structural role, reducing delamination and regulating the shell's tensile strength.[16–24] These features are just a snippet of the hierarchical structure found in nacre, ranging from the fibrous arrangement of the organic matrix up to macroscale curvature of the abalone shell.
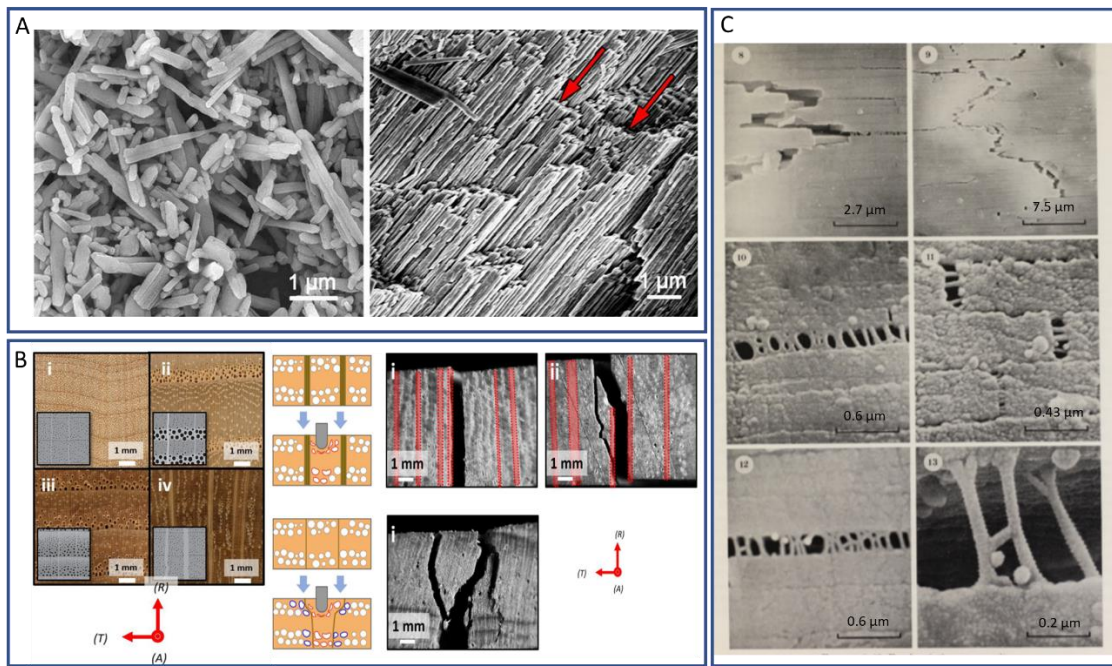
Figure 2.1 A.) Fracture surface of conch shell after dynamic (left) and quasi-static (right) loading. B.) While density is the primary determinant of wood's quasi-static properties, the structure of certain species becomes very important under dynamic loading. C.) Abalone is the quintessential example of a biological material toughened by its structure. The brick and mortar arrangement absorbs energy via crack deflection, fiber bridging and platelet rotation amongst other mechanisms.

In a recent publication entitled "A review of impact resistant biological and bioinspired materials and structures" a broad range of biological materials were studied to determine recurrent design motifs used in nature to resist impact. The results were classified into general architectures, being features that are omnipresent in natural materials but whose arrangements are vital for impact

resistance, and specific design elements, that is geometries that are found frequently in natural materials subject to impact loading and have been shown to improve their functionality. These are summarized in Figure 2.2 in the next section.

2.1 General Features of Biological Materials that Affect Impact Resistance

All biological materials, including impact resistant materials, have the following characteristics:

- **Hierarchical:** discrete structural elements identified across several length scales (nano, micro, meso, macro) that work synergistically to enhance the overall mechanical properties of the structure. All biological materials are hierarchical due to their self-assembly from the atomistic to macro-scale. Every other arrangement, whether a general feature or specific structure contributes to the hierarchical organization of biological materials.

- **Composite:** material made of two or more materials or phases, with distinct interfaces, having properties different from those of its constituents. Biological materials are composites typically made of a ceramic and a polymeric phase for mineralized systems or a crystalline and an amorphous phase for non-mineralized systems. The stiffer phase provides the necessary rigidity and strength while the soft phase imparts ductility. Often, biological composites outperform the simple composite nature of their constituent parts.

- **Porous:** gaps in solid material that are filled with air or fluid can exist across all length scales. All biological materials have some degree of porosity as various pore shapes and densities can be found throughout nature. Porous materials often

increase the energy absorbing capabilities, with an added benefit of decreasing the overall weight.

- **Interfaces:** shared boundaries between two phases with different properties. Interfaces can arrest cracks, enhance flexibility, and contribute to the viscous response of materials during deformation. All biological materials have interfaces due to their composite nature. There is a vast array of arrangements and materials that are used to define these interfaces.

These components are found across nature and play a significant role in a material's impact resistance. The arrangement and magnitude of these features are also significant factors in a material's response to dynamic loading. In parallel, all biological materials exhibit viscoelastic and/or viscoplastic behaviors. This is due to the inherent response of their polymeric constituents during loading.

- **Viscoelastic**: material property exhibiting both viscous and elastic responses with time-dependent stress and strain. The damping of the pulses is an important characteristic of impact-resisting materials.
- **Viscoplastic**: material properties that involve time-dependent permanent deformations, including sliding, delamination, and microcracking. These mechanisms dissipate energy.

The time dependence of a material's response to loading is important during impact. This inelastic behavior is a result of the polymeric constituents found in biological materials (collagen, keratin, cellulose, hemi-cellulose, lignin, and chitin) which ultimately determines deformation mechanisms and their capacity to absorb and dissipate energy under dynamic conditions. This material behavior can be expressed by the time constant in stress relaxation and by the ratio of loss to storage moduli

(tan(delta)) in the regime of interest. The features identified in this section are found across all biological materials.

2.1.1 Hierarchical structure

As alluded to previously, the overarching theme for mechanical biological materials is their hierarchical structures. This often involves a combination of different specific design elements at multiple length scales. A common example of this is the sutured structure on the surfaces of a layer arrangement. This works well because the layered arrangement is good at creating tortuous crack paths, providing flexible articulated armors, and recruiting large amounts of material to resist impact energy. However, delamination is often a primary failure mode for this type of structure and has been observed in horn sheaths [25,26], turtle shell scutes[27], and pangolin scales[28,29]. Much like nacre, each of these systems has developed a sutured surface arrangement to help interlock adjacent layers, increasing the energy required for pullout/delamination and increasing crack path tortuosity.

Unfortunately, manufacturing hierarchical structures is quite challenging.[30] For additive manufacturing there is an inherent tradeoff between minimum feature scale and overall part size. For example, 3D printing an airplane wing using a 0.5mm nozzle to obtain minute features would be nearly impossible, not to mention impractical. Similarly, despite great strides in nano/microfabrication techniques, it is difficult to create patterned nano and microstructures on a macroscale part. Subtractive manufacturing suffers a similar dilemma and can be even more time intensive. Nature overcomes these limitations by employing a bottom-up self-assembly approach where individual molecules are manipulated to form larger arrangements.[31,32] Many researchers have tried to overcome the limitations of traditional manufacturing methods by copying not only nature's designs but also biological fabrication techniques. These are based on

molecular interactions that can be tuned with external stimuli to modify the resulting architectures and functionality.[33]

Xu [34] reviews the many processes that have been developed for manufacturing hierarchical materials and categorizes them into three primary groups: porous materials, structural materials, and smart materials. Of these, research in porous materials have seen the most exciting growth with advancements in freeze casting, gas bubbling, and emulsion templating just to name a few. Xu asserts that, almost unexceptionally, these hierarchical porous materials have structure-enhanced performance [34]. In the world of impact resistance, hierarchical materials have been similarly successful. Estrada et al. [6] constructed hierarchical laminar organic fibrous composites with graded mineralization based on Arapaima scales and found significant improvements in energy absorption under impact. Jia et al. [35] show that using higher orders of self-similar hierarchies allowed for the improvement of stiffness, strength, and toughness simultaneously, while also confining damage to smaller length scales under dynamic loading. Using multiple structures on the same length scale gave the advantages of each, while also providing synergistic bonuses.

2.1.2 Porous, Composite, Interfacial

The other three features identified as vital general architectures in biological impact resistant materials are pores, interfaces, and composite arrangements. Each of these are found in all biological materials but are particularly important for impact resistance. Pores, for example, absorb strain energy when they compact and are often deployed to create a lightweight, deformable foam-like layer. The pericarp of pomelos effectively utilizes this strategy to mitigate damage to the fruit's internal structure when it falls to the forest floor. The pericarp has a closed-cell strut structure. The struts are filled with a shear-thickening fluid that dampens impact while the gaps

between the struts densify to allow the material to achieve up to 60% strain before densification begins.[36,37] This design has served as inspiration for fiber-reinforced metal cast foams, hierarchical honeycomb structures, and damping materials via shear-thickening fluids.[36–40] Other biological systems, such as human skulls[41–44], turtle shells[45–49], beetle elytra[50,51], and fruits/nuts [52–56] have porous designs for the sake of dissipating strain energy through densification.

As engineers have become increasingly aware over the past century, composite designs, (systems composed of two or more materials with varied properties) are capable of achieving stellar properties by exploiting the strengths of each constituent component. However, like many hard-learned engineering lessons, nature has been making the most of this principle for eons. Stomatopods (mantis shrimp) evolved ~ 175 million years ago and developed their characteristic hammers for hunting hard-shelled prey approximately 50 million year later.[57] Today, these strikers have taken their place as one of the most impact resistant biological materials in the world and have been rigorously studied by researchers to understand how these biocomposites survive impacts that can reach up to 23m/s.[58] On the surface, the mantis shrimp's dactyl club is composed of highly ordered hydroxyapatite (HAP) crystals. These provide remarkable stiffness for the transference of impact energy to prey and at the same time absorb energy through rotation, translation, and ablation over the course of the molt's lifetime. An interpenetrating organic phase composes about 17% by weight of this surface layer creating two bicontinous phases and toughening the highly mineralized exterior. The organic layer guides the grain formation of the HAP crystals so that they are closely aligned with low-angle grain-boundaries. This further toughens the impact surface.[59] Beneath this ~70 μm thick surface coating are herringbone shaped chitin fibers mineralized with HAP. This arrangement eventually transitions into a softer

"periodic zone" where amorphous mineralized fibers are arranged into a helicoidal Bouligand structure (often referred to as a twisted ply structure).[60] This fibrous arrangement is famous for providing isotropic macroscale in-plane mechanical behavior and for creating twisted crack interfaces that improve the toughness of the material.[61–67] Due to the higher polymer content in this inner layer, it is more viscoelastic and exhibits strain hardening behavior due to densification of microchannels that collapse and dissipate impact energy.[68] The result of this ingenious composite is a highly damage tolerant, tough, yet stiff impactor that can pack a punch while also withstanding thousands of high-velocity impacts.

Finally, the interfaces between different components in biological materials are of utmost importance. This can be clearly seen in the previous examples regarding nacre, conch shell, and stomatopod dactyl clubs, however arguably the best example of this can be found in scales. Pangolin scales, for instance, have an articulated arrangement that allows for remarkable flexibility without sacrificing protection.[28,69] In fact, the overlapping nature of the pangolin scales can be beneficial for protection since damage cannot travel easily between adjacent plates. Cracks are arrested at the interface between scales and any predator hoping to penetrate the pangolin's armor must cause multiple scales to fail independently. Similar designs are observed in arapaima scales [70–72], who's articulated dermal armor allows them to resist predation from the fearsome piranha. While many natural interfaces involve trapping cracks in sacrificial layers or preventing damage from jumping between adjacent features, interfaces can also be tuned to force a crack into a tough material. Liu et al. [73] studied suture structures and found that increasing structural hierarchy and the sharpness of suture tooth interfaces encourages cracks to penetrate into the skeletal layer rather than traveling along the interface. This can be beneficial for systems that are highly polymeric and inherently tough rather than mineralized and brittle. This example highlights

how interfaces can be utilized in many different ways to affect the mechanical properties of biological materials.

2.2 Specific Architectures Found in Impact Resistant Biological Materials

Additionally, many impact resistant biological systems have developed specific impact resistant structural elements typically found on the micro- and meso-scale which include:

- **Layered:** laminate layers consisting of fibrous structures with distinct interfaces which serve as crack dissipators. Fiber orientations change from layer to layer, either in plane (laminated structures) or out-of-plane (Bouligand structures)

- **Gradient:** a gradual change in a material property (e.g., modulus, density), architecture (e.g., porosity), and/or composition.

- **Tubular:** hollow channels typically aligned along a given axis.

- **Sandwich:** two stiff layers separated by a softer, porous layer allowing for a lightweight yet stiff, strong, and energy absorbent material.

- **Sutured:** an interlocking interface connecting two neighboring components.

These elements are found in a variety of biological systems that experience impact and are often used in conjunction with each other, leading to impressive properties under dynamic loading. While these structures act as the building blocks for hierarchical, impact resistant structures, tests using computer simulations, 3D printing, and composite prepregs have allowed researchers to probe the function of these architectures as independent designs. Many studies have found that even as the sole design components, these arrangements can improve the impact resistance of a material.
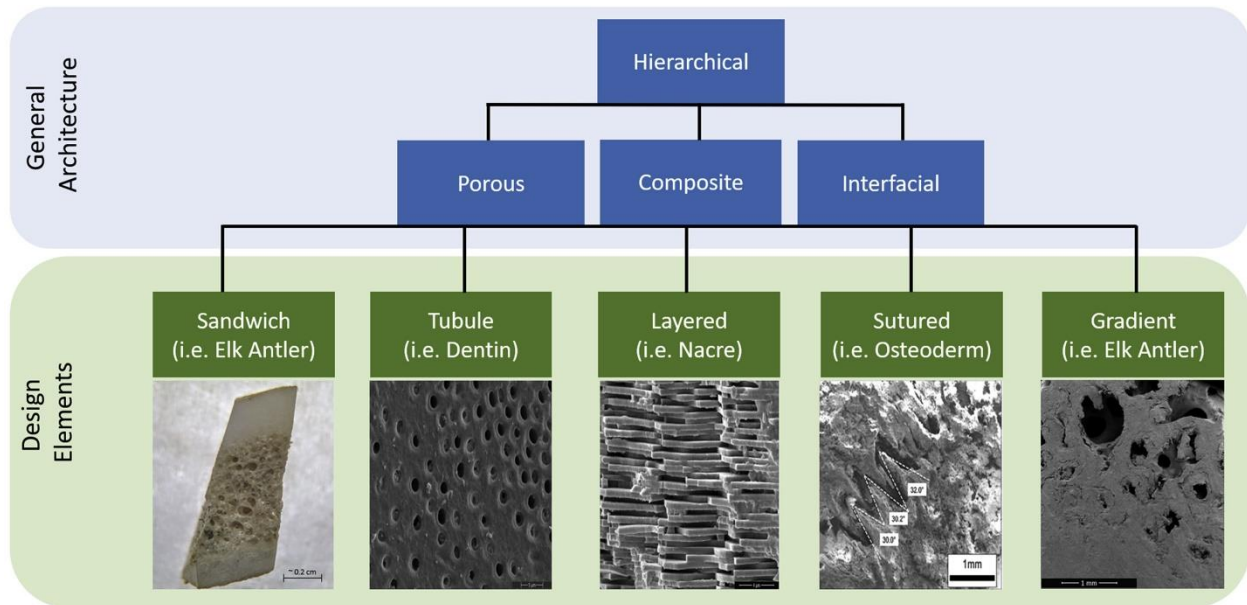
Figure 2.2 General architecture and specific design elements found in biological materials and, more particularly, impact resistant materials. (Top) Four general features found in all biological materials that are especially important for impact resistance. All biological materials are hierarchical. These hierarchies are composed of various arrangements of composite materials, pores, and interfaces. (Bottom) Five micro- and meso-structures that are commonly found in impact resistant biological materials and have been shown to improve performance under dynamic loading. These include sandwich, tubule, layered, sutured [74], and gradient structures. Image taken from [75].

2.3 Testing Methodology

To understand the impact resistance of biological materials researchers have utilized a number of different mechanical tests. These tests differ in their ability to consider different loading conditions, loading orientations, and strain rates. With materials that are highly anisotropic (i.e. dry big horn sheep horn [76]) or strain rate sensitive (i.e., bone [77]), it is important to test materials in a number of different orientations in a broad strain-rate range. Table 2.1 compiles different testing methods and strain rates used to examine the impact resistance of biological materials in the preceding sections. This table does not provide an exhaustive list of all testing done on these systems but provides an idea of what work has been done.

Table 2.1 Summary of dynamic testing techniques and strain rates on biological systems.

Biological System	Drop tower	Hopkinson bar	Compression test	Tensile test	Flexural test	Shear Punch test	Other
Pomelo	--	--	5 mm/min [53]	--	--	--	(free fall) 10.85 m/s [53]
Coconut	--	--	--	0.3 mm/min and 0.6 mm/min [55]	--	--	--
Wood	1.6 m/s [12]	--	12 mm/min [12]	--	--	--	--
Hooves	--	1000 s^{-1} [78]	$2.5 – 1.7 \times 10^{-5}$ m/s [79], $0.1 \text{s}^{-1}, 0.01 \text{s}^{-1}, 0.001 \text{s}^{-1}$ [78]	5mm/min [80], 8.3×10^{-5} m/s [81], 2 mm/min [82]	--	--	--
Horns	>3.8 m/s [83], 4.4 m/s [25]	4000 s^{-1} [76]	$0.5 \text{s}^{-1}, 0.1 \text{s}^{-1}, 10^{-3} \text{s}^{-1}$ [76], 3mm/min [25]	2 mm/min [26]	2 mm/min [26]	--	--
Pangolin Scales	--	--	10^{-3} s^{-1} [29]	$10^{-1} – 10^{-5} \text{ s}^{-1}$ [29]	--	--	--
Tendon	--	--	--	5, 0.5, 0.05% s^{-1} [84]	--	--	--
Ligament	1.5 m/s [85]	--	--	--	--	--	(Impactor Trolley) ~1 m/s [86]
Cartilage	1500-740 s^{-1} [87], 1, 0.75 m/s [88]	--	--	--	--	--	--
Bone	--	6.1 m/s [89]	$1,500 \text{ s}^{-1} – 0.001 \text{ s}^{-1}$ [77], 0.6 mm/min [89]	--	--	--	--
Turtle Carapace	--	--	$10^{0} – 10^{-4} \text{s}^{-1}$ [46], 10^{-3} s^{-1} [74], 2 mm/min [47]	--	0.5 mm/min [49]	--	--
Human Skull	8-7.1 m/s [43]	–	2.5mm/s [43]	--	--	0.1 and 0.001 s^{-1} [44]	--
Elk Antler	>3.8 m/s [83]	--	--	--	0.9 mm/min [90]	--	--
Conch Shell	--	1383 - 1686 s^{-1} [11]	$10^{-2} – 10^{-4} \text{s}^{-1}$ [11]	--	0.1 mm/min [7]	--	--

One of the most popular testing techniques is the drop tower, which is capable of reproducing impacts that occur in the natural regime (< 25 m/s). These experiments are useful for understanding the energy absorption and damage tolerance of a material and is good for comparing different materials tested under the same conditions. However, drop towers have a number of

important variables that can make it difficult to compare results between different studies. These include sample size, clamping mechanism, and indenter shape and size. For very high strain rate tests and insight into stress-wave interaction in a sample, Hopkinson bar tests have been utilized to examine biological materials. These tests give unique insight into a material's response to dynamic loading but can be expensive [76] and may necessitate modifications for low impedance materials, which is characteristic of biological materials. These modifications involve using bars with the proper impedance mismatch ratio relative to the sample such as woven glass epoxy composite, PMMA, or magnesium alloy bars [76,91]. Further, a pulse shaper is often used to ensure stress equilibrium and homogenous deformation in the sample [76,92]. The most popular testing methods for impact resistant materials are simple compression, tensile, and flexural tests, often using a universal testing machine. As has been examined in previous sections, these tests are restricted to strain rates below the ones in dynamic, impact regime ($\sim$1-2 s^{-1}) but can provide insight into deformation and fracture mechanics. The allure of compression, tensile, and flexural tests is their ease of use and simplicity. These tests can provide valuable material parameters such as elastic modulus, Poisson's ratio, fracture toughness, ultimate strength (even though these may vary with strain-rate). Different strain rates can also be accessed using these simple techniques and important strain-rate dependent trends can be observed. Free-fall experiments (where the sample is dropped onto a surface rather than a weight onto the sample as in drop tower experiments) and shear-punch tests are used much more sparingly than other testing methods and were only examined in this chapter for the pomelo and human skull, respectively. There are other techniques for quantifying impact resistance, such as Izod and Charpy testing, but these have not been as widely used to study biological materials mostly in part due to samples being too small.

For lower strain-rate tests ($<10^{0}\,s^{-1}$) the inertia of the sample can be ignored, but for higher

strain-rates experiments must take into account the force required to accelerate a material to high deformation speeds. Above 10^0 s^{-1}, the force is not simply dictated by the material's intrinsic strength. Inertial effects are also greater in larger samples [93]. Another consideration for high and low strain-rate testing is the use of plane stress approximations. In shock tests that involve strain rates $\geq 10^6$ s^{-1} this approximation breaks down and plane strain must be used. Figure 2.3 shows the achievable strain rates for a variety of mechanical tests, including each of the tests discussed in this section. The figure also indicates the strain-rate thresholds for plane stress approximations and disregarding inertial effects of the sample.

Strain Rate (s⁻¹)	Testing Methods		

Strain Rate (s^{-1})		Testing Methods	
10^8 10^6	Shock	- Light Gas-gun - Pulsed laser - Exploding foil - Including plate impact (pressure-shear)	Plane strain
10^4	Dynamic High	- Taylor anvil - Split-pressure Hopkinson bar - Expanding ring	Inertia relevant
10^2	Dynamic Low	- High-velocity hydraulic or pneumatic - Drop-weight tower - Charpy/Izod pendulum - Free-fall testing (gravity)	
10^0 10^{-2} 10^{-4}	Quasi-Static	- Conventional testing machine - Hydraulic - Servo-hydraulic - Screw-driven - Shear-punch	Plane stress
10^{-6} 10^{-8}	Creep and Stress Relaxation	- Conventional testing machine - Creep testers	Inertia negligible

Figure 2.3 Testing methods and their achievable strain rates.

This section will highlight nature's most successful impact resistant materials and will identify several trends that are observed in representative systems. We group these materials into the following categories: cellulose, hemi-cellulose, and lignin systems (fruits, nuts, and wood); keratinized systems (horns, hooves, pangolin scales), collagenous systems (tendons, ligaments, cartilage), and mineralized systems (bone, skulls, turtle carapace, and marine systems).

2.4 Cellulose, Hemi-Cellulose, and Lignin Systems

Many nuts and fruits need to be able to endure the natural process of falling to the ground and seed dispersal mechanisms which can involve significant impact forces. Tree trunks are exposed to dynamic loading during extreme natural events such as avalanches or hurricanes. These systems are also subjected to impacts from animals and even from other trees falling. This section focuses on the dynamic loading conditions and the energy absorbing mechanisms of cellulose, hemi-cellulose, and lignin based systems.

2.4.1 Nuts and Fruits

Pomelos have developed a protective exterior that has three distinct layers: a compact layer of external cells (exocarp), a thick spongy middle layer (mesocarp), and a dense layer adjacent to the fruit's pulp termed the endocarp. This layered system is conventionally referred to as a sandwich structure. The dense endocarp and exocarp are tough and prevent puncture while the highly porous mesocarp can collapse elastically absorbing strain energy. The mesocarp can reach a porosity of up to 80% and only begins to densify after 55% strain [53].

Similarly, coconuts have a three-layered sandwich structure, with a firm exterior and internal layer with a soft mesocarp in between [53]. The coconut shell is highly hierarchical, having hollow channels (~200 μm diameter) surrounded by hollow fibers (~15 μm diameter) whose walls

are composed of an intercellular ladder structure (with gaps on the scale of 1-10 μm) [55]. As the coconut ages, it becomes more porous and has higher strength and fracture toughness [55]. The microstructures of old and young coconuts are shown in Figure 2.4. The porous nature of the coconut mesocarp has also been shown to trap, blunt, and deflect cracks, forcing them to take circuitous paths [55]. In older coconuts, these effects are magnified as can be seen in Figure 2.5A, where cracks formed in old coconuts (i,ii) are jagged and tortuous compared to the relatively straight cracks (iii,iv) in young coconuts. This leads to improved strength as well as crack initiation and growth toughness in older coconuts (v-viii) [55]. Further, individual fibers and fiber bundles in the coconut mesocarp are capable of enduring strains up to 40% before experiencing benign failure [53]. The porosity and fiber ductility of the mesocarp allow the coconut to sustain significant deformation without failure.
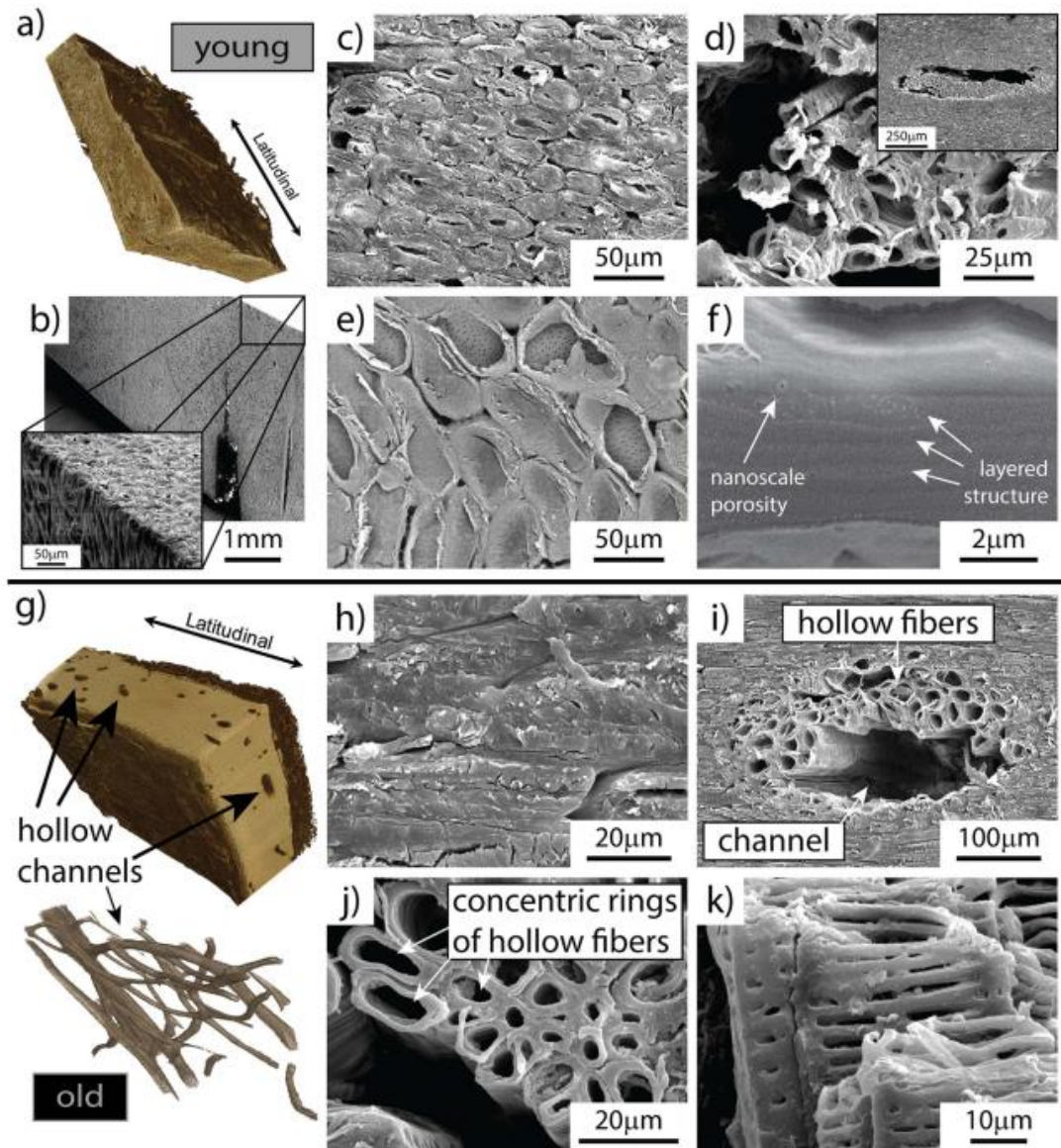
Figure 2.4 Structural comparison of young and old coconuts. Coconuts develop a porous hierarchy composed of hollow channels, surrounded by hollow fibers with ladder structured walls, and nanopores embedded in the lamellar arrangement of the coconut shell [55].

Figure 2.5B shows the typical stress-strain curve for the foam sandwich structures found in coconuts and pomelos. In the first region of the curve, the stress and strain rise to the necessary threshold to begin deforming the porous central layer of the material. Once this stress level has been achieved, it remains relatively constant while the foam layer begins to compact. This process of pore collapse absorbs significant amounts of energy, even at higher strain rates. Damage begins to occur in the rest of the material only after the pores have been compacted. This structure is not only impact resistant due to its high strain endurance, but also because it spreads the impact throughout the porous network as it collapses. This is important for pomelos and coconuts which can resist impact energies up to 1.5 kJ [53].

Figure 2.5 Impact results on cellulose, hemi-cellulose, and lignin based systems. A) (i-iv) Fracture patterns in old and young coconuts loaded in tension in the longitudinal and latitudinal directions. (v & vi) Stress strain curves obtain from tensile testing and (vii-ix) K_j (resistance) R-curves for coconut fracture tests performed under three-point bending conditions [55]. B) Typical stress strain curve for biological sandwich structures; There is an initial linear elastic response from the material, followed by the green region of the stress-strain curve where the foam's pores collapse, allowing for high strain endurance and energy absorption, until finally in the red region of the stress-strain curve the foam layer has densified and can no longer collapse anymore, resulting in plastic deformation and damage. C) Wood structure and deformation under impact. (i-iv) Different arrangements of pores and aggregate rays and (v-vii) the fracture patterns of representative wood samples under impact. (viii) Micro-computed tomography images of wood after impact at 0.4 mm, 0.3 mm, 0.2 mm, and 0.1 mm respectively from the impact center. (ix) Force displacement curves of three different types of wood, with images showing their deformation mechanism [12].
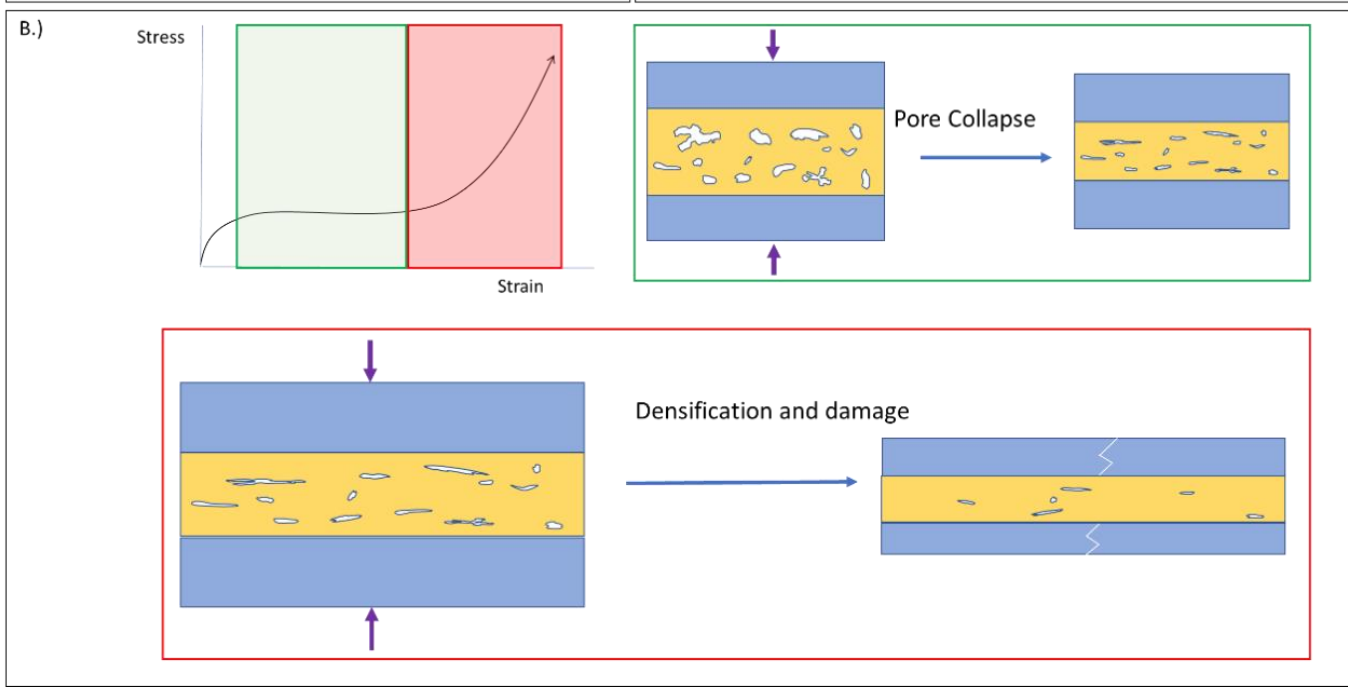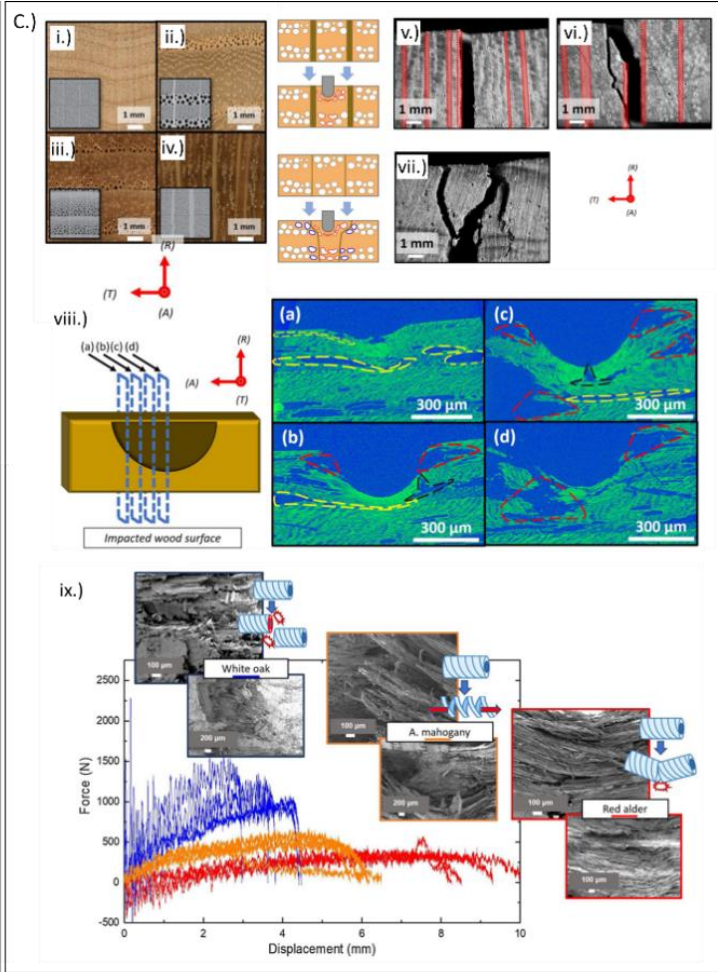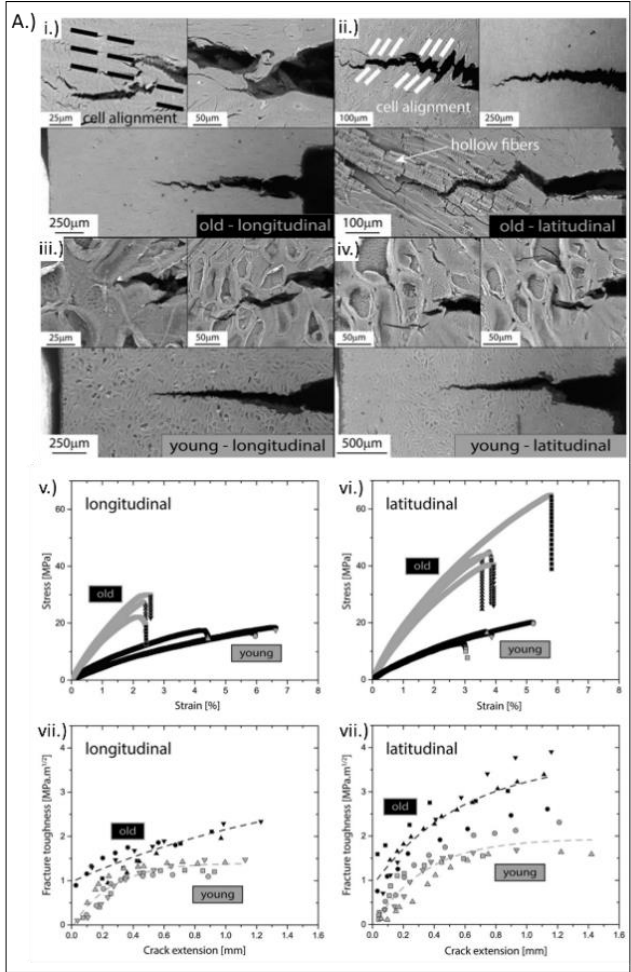
2.4.2 Trunks and Stems

Many woods can be conceptualized as closed cell foams with a rigid outer layer (bark) and a stiff compact core creating a porous sandwich structure. Different species have different porous arrangements which can be seen in Figure 2.5C (i-iv). Matsushita et al. [12] examined eight different wood species under impact conditions and concluded that the banded nature of the woods affected their impact strength. While pores sometimes act as crack arresters, they can also act as flaws that initiate cracks and delamination. Figure 2.5C (viii) shows microcomputed tomography images of white ash after impact. Near the impact center, delamination initiates at pores which are outlined in red, while farther from the impact zone compressed pores and cracks that are arrested at pore interfaces are outlined in yellow and black, respectively. When pores are packed close together in ring or semi-ring porous arrangements, this effect is magnified leading to rapid catastrophic failure at the porous bands. Several of the species that were tested also contained arrangements of aggregated ray cells. These cells are more rigid than the surrounding tissue and when grouped into large bundles divide the pores into enclosed sections. Matsushita et al. [12] determined that these bundles localize the damage zone of the material, so that only small areas of the porous structure are affected by the impact. Figure 2.5C (v,vi) shows how the rigid rays can confine cracks. In these instances, very little material contributes to the dissipation of impact energy. Further, these bundles compartmentalize crack deflection, resulting in straight smooth cracks unlike the rough cracks that meandered through the porous networks found in similar wood species without aggregated ray cell bundles (Figure 2.5C (vii)).

Of the eight types of wood tested, African mahogany exhibited the best impact resistance. It dissipated energy via fiber bending and pullout, a mechanism observed in a number of other biological systems [94] as well as in engineered composites [95]. After impact, entire tracheid

fibers would be bent, the ends of which showed evidence of cell wall delamination and helical unwinding. These processes significantly delocalize damage and absorb energy without causing catastrophic failure. Less impact resistant species, like white oak, did not disperse the load throughout the entire material and instead simply fractured across the fibers near the impact zone. Other species, such as the Red alder, dissipated energy through fiber bending before rupturing at low displacements. Figure 2.5C (ix) shows the force displacement curves of these three species alongside SEM images that illustrate these deformation mechanisms. The most impact resistant of the species, African mahogany, had an intermediate force displacement curve, enduring larger displacements than Red alder and larger peak forces than White oak. Matsushita et al. [12] contends that wood can be viewed as a fiber reinforced composite, where adhesion between the fibers in the wood and the surrounding matrix is key to understanding the impact resistance. Adhesion plays a particularly important role at higher strain rates, when the viscous response of the wood is minimized and shear stress between the fibers and the surrounding matrix builds rapidly.

2.5 Keratinized Systems

Keratin is a highly prevalent protein in nature, found in the integument of a variety of animals. Keratinous materials serve a wide range of functions such as insulation (i.e., hair and wool), filtration (i.e., whale baleen), and flight (i.e., feathers). Additionally, one of the most common uses of keratinous materials in nature is for impact-resistant applications. The hoof walls of many ungulates such as horses, bovines, and donkeys are composed almost entirely of keratin. The same is true for the horns of the bighorn sheep, yaks, and rhinoceros. These body parts experience repeated impacts over the course of an animal's life and since keratin is often embedded in dead cells that do not self-repair, these structures are prime candidates for biomimetic materials.

The outer-most layers of many defensive biological systems, such as turtle shells and armadillo armor, are composed of keratin scutes. However, the primary structural components of these systems are the subdermal bony layers, so they will be discussed in the next section. Pangolins, on the other hand, have a dermal armor composed solely of overlapping keratin scales that provide protection from predators like lions [29]. Important keratinous structures will be examined in this section.

2.5.1 Hooves and horns

The hooves of horses suffer repeated high impacts with a deceleration of ~43 g [96]. Horse hooves are composed of keratin and, like all keratinous materials, have mechanical properties that are highly dependent on hydration. The hoof has two hydration gradients, (1) distal to proximal and (2) interior to exterior. These hydration gradients originate at the living tissue adjacent to the hoof which supplies moisture to the dead keratin cells. The exposed surfaces of the hoof release moisture and dry out more quickly than the internal layers. These variations in hydration lead to a significant gradient in the mechanical properties of the hoof, since dry keratin is stiffer and less tough than hydrated keratin [97]. This stiffness gradient is further enhanced by a slow decrease in keratin intermediate filament density from the exterior of the hoof to the interior [82]. This gradient structure allows the load-bearing keratin of the hoof wall to dissipate energy to the skeletal structure while also cushioning sensitive tissue at the hoof interior [98]. The hard, exterior surfaces of the hoof are firm and puncture resistant. Since the hoof wall becomes tougher towards the interior, cracks that are traveling inward will often be blunted and can more easily be redirected [79]. Similar hydration gradients can be found in other keratin systems such as steer horn sheaths, where the hydrated base of the horn wall is more flexible, increasing bending toughness under impact [26].

Additionally, there exist gradients in tubule shape, size, and density found in the hoof wall. The hollow tubules in the hoof are approximately 40 µm in diameter and are surrounded by a rigid cortex of dense keratin as depicted in Figure 2.6A (i) [78]. Towards the edge of the hoof wall the volume fraction of tubules increases and the shape of the tubules becomes more elliptical and smaller as shown in Figure 2.6A (ii) [97,99]. These gradients in tubule shape, size, and density serve multiple functions. The denser tubules provide more reinforcement along the outside of the hoof, enhancing the stiffness gradient, and deflect cracks away from the living tissue at the interior of the hoof. The change in tubule shape is thought to increase the moment of inertia as a response to the significant bending stresses found at the edges of the hoof during impacts [97,98]. Hopkinson bar impact testing on hoof showed minimal cracking in the tubular region, suggesting that the tubules deflect cracks. Further, the reinforced tubules prevented the shear banding that is evident in similar tests on horns. Compression tests along the tubule axis showed that the tubules buckle and crack to dissipate energy but are able to completely recover their shape at strains up to 30%, indicative of the viscoelastic behavior of the keratin [78].
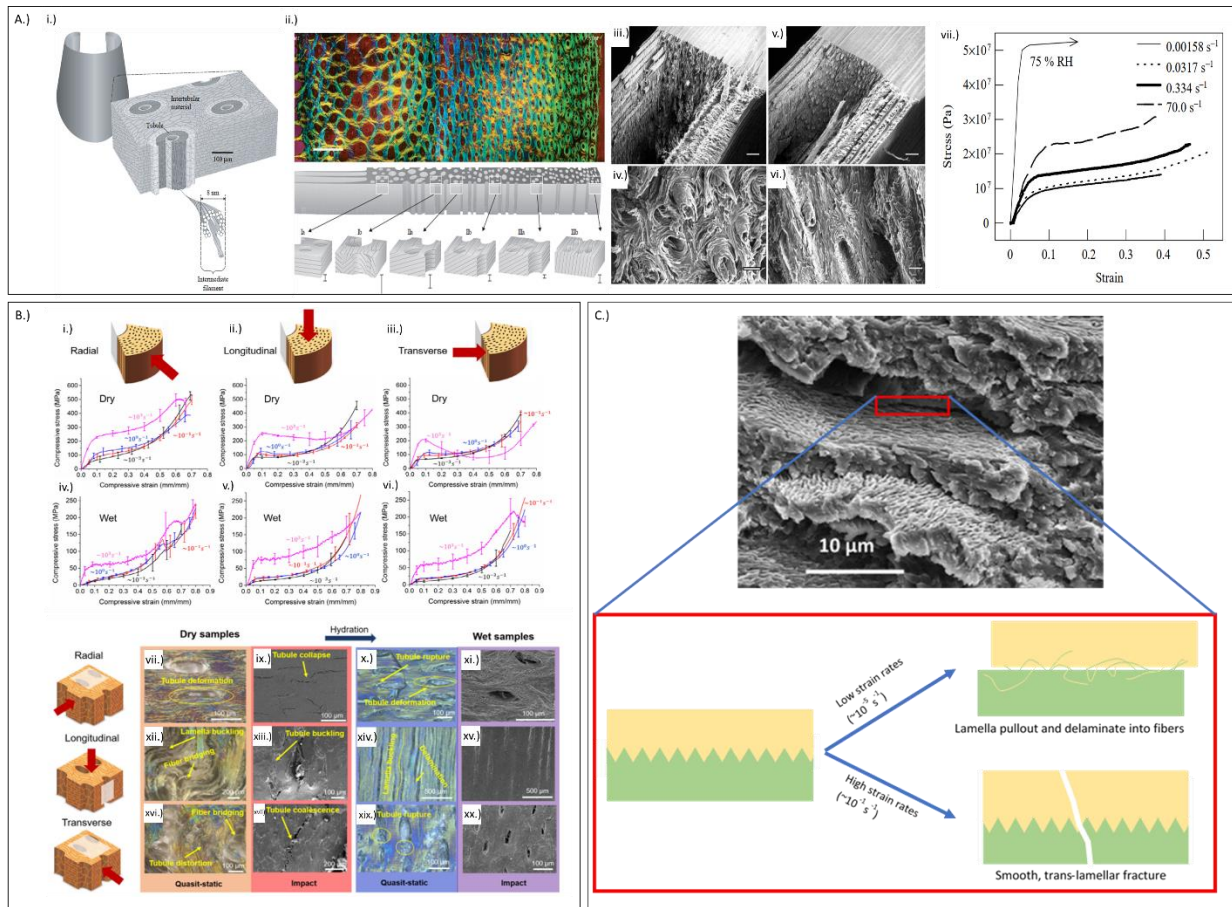
Figure 2.6 Keratinous systems such as hooves, horns, and pangolin scales exhibit common impact resistant structures. A) (i,ii) Horse hooves have a gradient of tubular structures that vary in shape, size and density through the thickness of the hoof wall. These structures are composed of dead cells that are embedded with keratin intermediate filaments. These cells form layers whose arrangement can be seen in the bottom of figure A (ii) [81]. (iii, iv) The fracture pattern of horse hooves under tension at low strain rates alongside (v,vi) the fracture pattern of horse hooves at high strain rates. (vii) The stress strain curve of the horse hoof at different strain rates [79]. B) (i-vi) Stress strain curves of bighorn sheep horn under compression in three different directions. Each orientation was compressed at three different strain rates under wet and dry conditions. (vii-xx) Optical and SEM images show the different deformation mechanisms of the horn under varying loading conditions, hydration levels, and orientations[76]. C) The sutured pangolin lamellae have different deformation mechanisms at high and low strain rates. At low strain rates, lamella pullout and delaminate while at high strain rates, there is smooth fracture across the interface. These mechanisms are shown in the schematic.[29]

While horse hoof walls have both a tubular and gradient character, they also have a tri-

laminar ply structure that varies in orientation through the hoof [79]. At the nanometer level, the

keratin in horse hooves is arranged into intermediate filaments (IFs) that are approximately 7 nm

28

in diameter. These filaments fill cells that interlock with wavy, suture like surfaces and then align themselves into layers with weak interfaces in between them [81,100]. This hierarchical structure is depicted in Figure 2.6A (i). As cracks propagate within the hoof wall, they get caught in these sacrificial layers which deflect them away from the living tissue at the hoof's interior. In fact, tensile testing revealed that it is nearly impossible to propagate a crack through the hoof in any direction other than between the aligned IFs, regardless of the orientation of the notch [80]. Figure 2.6A (ii) shows the orientation of the IFs, with filaments oriented radially in the hoof appearing yellow, axially oriented filaments appearing blue, and filaments perpendicular to the hoof section appearing purple.

High strain rate tensile tests confirmed that in the central portion of the hoof wall, cracks had a strong tendency to travel along the intercellular, laminar planes (pictured at the bottom of Figure 2.6A (ii)) similar to the quasi-static tensile tests, while in the inner and outer regions of the hoof, cracks traveled along tubule interfaces leading to delamination. The response of the hoof under impact is a prime example of how quasi-static tests can be useful for understanding a material under dynamic loading but do not always capture the full nature of a material's impact resistance. Figure 2.6A (iii, iv) shows fracture patterns of the hoof at low strain rates compared to the fracture pattern of the hoof at high strain rates (v,vi). Impacted samples had smoother fractures and less tubule pullout but experienced the same regional preferences for the cracking direction. The viscoelastic nature of the hoof keratin has also been shown to increase the toughness of the hoof with increasing strain-rate and lead to crack tip rounding. However, at higher strain rates smoother fracture patterns through cellular layers and less tubule pullout were observed suggesting brittle failure for higher velocity impacts [79]. This is akin to what is observed in toucan beak keratin [101]. At higher strain rates, the hoof absorbed more energy and had a higher ultimate

stress, as can be seen in Figure 2.6A (vii). All of the lower curves are on samples that were kept fully hydrated and then left in ambient conditions for 24 hours, the upper curve label 75% RH is a sample that was left in a 75% relative humidity environment until it equilibrated. The difference in the shape and maximum values of the stress-strain curves shows how hydration can drastically affect the properties of the hoof [79].

Lee et al. [83] performed drop tower tests on elk antler, steer horn, ram horn, armadillo carapace, and abalone and concluded that delamination was one of the dominant modes of energy dissipation in each material. They proposed that the large increase in surface area that occurs with delamination represents a highly effective mechanism of absorbing energy. The most impact resistant structure tested by Lee et al. [83] was the steer horn sheath in ambient hydration conditions, which exhibited a normalized failure impact strength of 99 kJ/m^2. This value was over eight times that of abalone and nearly twice the one for elk antler. Significant amounts of energy were dissipated by internal delamination within the horn samples during impact. Steer horn likely accomplishes this high impact strength with the wavy lamellar layers formed by keratinized cells in the sheath wall. These wavy layers resist the nucleation of new cracks and impede crack propagation. Further, the interfaces between the lamellae are characterized by labyrinth-like surfaces, which create large amounts of interlaminar friction during delamination [26].

Horns of other species, such as the yak and bighorn sheep, also possess impressive impact properties. The yak horn is a tapered, gradient structure that is narrow at the tip and gradually widens towards the base. It is composed of a keratin sheath around a bony core. The tip of the yak horn is older and denser and exhibits higher hardness, strength, and energy absorption under impact. Quasi-static compression tests revealed a multitude of failure mechanisms including densification under lateral tests and lamellar buckling, delamination, and fiber tearing in the keratin

sheath when the samples were compressed axially. However, impact testing of the yak horn revealed a lower energy absorption and brittle failure at higher strain rates. This is counterintuitive, considering that the horn's primary role in nature is under impact. The authors [25] suggested that this may have been a result of ambient moisture levels that were not representative of the fresh yak horn. This example underscores the importance of hydration and the difficulties of comparing results between studies on biological samples when ambient conditions are not the same.

Bighorn sheep horns have a similar composition to yak horn but are spiraled rather than straight. This macroscale geometry makes the horn act as a loaded torsion spring and vibrates after impact to dissipate energy. Further, the porous trabecular bone found in the core of the horn resists bending and absorbs a significant amount of strain energy during impact [102]. The keratin sheath of the horn has an intricate microstructure of tubules and cell lamellae which are oriented at a 30° angle to each other [76]. Similar to the hoof, there is a porosity gradient through the hoof with a porosity of ~10% at the exterior of the keratin and 0% at interior. However, the tubules are oriented perpendicular to the loading direction, unlike hooves where tubules are parallel to the impact [103].The lamellar cells are pancake shaped and filled with keratin fibers (intermediate filaments) that are in plan of the flat surface. Figure 2.6B (i-iv) shows the response of horn samples in the wet and dry states under various loading conditions (different strain-rates and orientations). Dry samples were able to withstand much larger stresses as water softens the keratin and makes it more compliant. However, dry samples were also much more anisotropic, performing noticeably better when compressed in the radial direction (the natural loading direction). This was true for impact and quasi-static tests. This anisotropy arises from the asymmetrical microstructure, although hydration can override these effects. Some of these microstructural effects can be visualized in Figure 2.6B (vii-xx). When dynamic loading is applied along the radial direction (Fig. 3B(i)), the

tubules oriented perpendicular to the impact direction collapse, absorbing significant amounts of energy. Impacts from other directions lead to shear banding, delamination, microcracking, buckling of the lamellae as well as tubule buckling but absorb less energy and recover less after impact [76]. Wet samples (xi, xv, xx) showed no obvious microstructural damage under impact, strengthening the claim that hydration can override microstructural effects. Similar to horse hooves, the bighorn sheep horn absorbed more energy and withstood larger stresses at higher strain rates. Much like yak horn, bighorn sheep horn properties are highly dependent on hydration, exhibiting brittle failure and anisotropy at low moisture levels. In the hydrated state, the horn is more isotropic, recovers its original length after dynamic loading at strains of up to 30%, and becomes much more ductile [76,104].

2.5.2 Pangolin scales

Fiber orientation has also been explored in pangolin scales where a crossed-fiber arrangement exists between crossed-lamellar structures which are interlocked with sutures. While each of these structures undoubtedly contributes to the mechanical properties of the scales, the crossed-fiber arrangement is unique compared to other keratinized systems. When torn, the pangolin scales fracture in a zig-zag manner unlike fingernails or feather rachis which have uniaxially oriented fibers and tear in smooth lines. In nature, systems like fingernails and feathers are typically subjected to predictable uniaxial stress, whereas the impact experienced by pangolin armor is unpredictable and can be multidirectional. With fibers crossed in multiple directions it is difficult for cracks to propagate through the lamellae. Failure of the scale at low strain rates typically requires fracturing or delaminating these crossed-fibers as the lamellae pullout. At high strain rates, these mechanisms begin to break down and the lamellae do not have time to delaminate and deform. Instead they experience brittle failure with smooth fracture surfaces through lamellae

[29]. These failure mechanisms and their strain-rate dependence are illustrated in Figure 2.6C.

2.6 Collagenous Structures

Collagen is the most abundant protein in mammals, serving as a building block of most tissues with mechanical functions. Collagen has a hierarchical structure and a characteristic axial 67 nm periodicity seen in electron microscopy images [105,106]. Many tissues are made of collagen, including bone, tendon, ligament, muscle, intervertebral disc, intestine, cornea, and others [105,106]. Collagen provides strength in tension for soft tissues and flexibility, keeps the form, and serves as a framework for mineralization in hard tissues. Experimental studies on collagen report initially linear stress-strain curves and time-dependent recovery (i.e., viscoelastic behavior) [107,108].

2.6.1 Tendons and Ligaments

The tendon has the highest content of collagen out of all collagenous tissues. Its function is to connect a muscle to the bone while ligament's purpose is to link bones together. Tendons and ligaments also facilitate motion and keep joint stability. They are subjected to uniaxial tensile loadings along their length. Thus, it is not surprising that their fibrous structures at different scales are all aligned in one direction. Their functions require that they are elastic and flexible but sufficiently stiff to transmit tensile forces and absorb large amounts of energy, such as in landing from a jump. This combination of properties is achieved by their hierarchical organization, which includes waviness at different scales and sliding of elements at different structural levels.

The hierarchical organization in tendon and ligament allows the distribution of stresses at each level of structure, minimizing stress concentrations, which could lead to failure and fracture. Such architecture is advantageous in handling dynamic and fatigue loadings. The stress-strain curve

exhibits initial non-linear behavior due to fiber uncoiling, which can be extended with very little force, followed by steeper, linear segment resulting from progressive straightening of the crimps. At normal physiological loads, the material response is at the initial non-linear toe region [106]. At very high strains, collagen fibers start to disassociate into subfibers, fibrils, and microfibrils, accompanied by yielding and irreversible damage. Tendons and ligaments have time- and history-dependent viscoelastic/viscoplastic properties, which are due to viscoelasticity of solid phase and water interaction with ground substance [106,109]. Tendons and ligaments are connected to bone, which is mineralized and thus has much higher stiffness. Those interfaces are again highly hierarchical, composite, and functionally graded to minimize stresses at the junctions [110].

2.6.2 Cartilage

Cartilage is a connective tissue that is present in three different forms (hyaline, fibrous, and elastic). Articular (also called hyaline) cartilage makes up the fetal skeleton, ribs, the wall of thorax, and the friction-reducing material at joints. Fibrous cartilage forms discs in spine which render it flexible, while elastic cartilage is found in nose, ears, and walls of thorax and larynx. Our interest is in articular cartilage, found at joints, which has impressive ability to absorb high loads [106,111].

Articular cartilage, when healthy, provides a smooth and low-friction surface for joints, excellent lubrication in combination with synovial fluid, cushioning, and it distributes applied forces to the underlying bone. Its excellent and multifunctional properties are due to its composite and hierarchical structure. Articular cartilage is a composite material consisting of 20-30 wt% of a solid phase (mainly collagen Type II and proteoglycans), with the rest being a fluid. The following structural scales can be identified in articular cartilage: (a) nanoscale – the dense extracellular matrix (ECM) consisting of water, collagen, proteoglycans and other organics. (b)

microscale – the ECM and small percentage of cells, (c) mesoscale – the four zones: the tangential, intermediate, radiate, and calcified zones, and (d) macroscale – the functionally graded fluid-filled cartilage tissue [106,111,112].

In the tangent zone collagen fibers are aligned tangentially to the surface to resist shear stresses exerted by bone; in the intermediate zone fibrils are randomly arrayed and less densely packed; in the radiate zone, fibrils are aligned normal to the underlying bone, while the calcified zone secures cartilage to bone. These four zones give rise to a functionally graded material, with collagen fibrils gradually changing their orientation, which is ideally designed to have on one side shear resistant surface providing smooth contact and be solidly attached to bone at the other side.

Articular cartilage forms a thin layer (0.5-5 mm) on ends of long bones in a synovial joint. In addition to providing a smooth, nearly frictionless surface for joints to slide on, it distributes the loads and transfers loads across bones. Dynamic loads amplify the impact forces acting on the joints. The fluid has a significant impact on the properties of cartilage. The pressurization of water gives the articular cartilage ability to withstand dynamic loads, often as high as several times one's body weight. The presence of a fluid, which can be considered as incompressible, plays an integral role in resisting and damping the loads. Thus, cartilage is a porous solid filled with fluid. Macroscopic properties of cartilage depend on the movement of fluid flowing in and out of pores during the deformation, resulting in a complex non-linear and time-dependent behavior [113]. Articular cartilage is a non-linear viscoelastic/viscoplastic, or more accurately poro-viscoelastic material. In poroelasticity theory, mechanical loading gives rise to pressure gradients in fluid-filled pores [106].

2.7 Mineralized Systems

The biological systems discussed so far are composed almost exclusively of protein or fibrous constituents. Mineralized systems incorporate a stiff ceramic phase in conjunction with these tough biopolymers, allowing for the creation of more complex composite arrangements with impressive properties. Many mineralized systems such as the shells of marine organisms, turtle carapace, and bone (especially the skull) are defensive armors that are used to protect internal tissue. Other mineralized systems are utilized for more specified offensive functions, like the hammering of wood by the woodpecker beak or smashing of shells by the mantis shrimp dactyl club. Both offensive and defensive systems have evolved an intriguing range of structures to improve impact resistance.

2.7.1 Bony systems

Bone is a connective tissue that, among its other functions, serves as structural support for soft tissues in the body and protection of organs. As a structural material, bone has excellent properties: high stiffness, strength, toughness, energy absorption, while being lightweight. These impressive properties are due to bone's composite, spatially heterogeneous, and hierarchical structure [106,114].

At the macroscale, bone consists of cortical (compact) low-porosity bone forming an outer shell and cancellous (trabecular) highly porous bone filling space between or at long bone's ends. Such structure is optimal as it allows the body to withstand high functional loads, minimizes weight, and porous network at ends distributes loads at joints. Bone is a composite material that at the nanoscale is made of soft and deformable organics (mainly collagen) and stiff but brittle apatite minerals, with about 1:1 ratio by volume, and fluid-filled pores. Collagen fibrils are mineralized with nanoscale crystals forming mineralized collagen fibrils, which align preferentially into a

single lamella. These lamellae arrange in layers at the microscale to form trabeculae in cancellous bone and osteons embedded in interstitial bone in cortical bone. Osteons are hollow cylinders made of concentric helically-wound lamellae. At mesoscale, a network of struts forms trabecular bone and osteons embedded in interstitial bone form cortical bone [114]. Osteons align in long bone's axis to carry loads and absorb impacts due to running and other dynamic activities. Lamellar structures deflect cracks at interfaces.

Stress-strain curves of cortical bone show a linear portion with non-linear portion following after yield stress is reached. Human cortical bone (with 5-30% porosity by volume) is transversely isotropic and has a longitudinal elastic modulus of 5-20 GPa in the long bone direction. Trabecular bone (with up to 90% porosity) exhibits a typical porous material response with an initial linear portion, followed by a plateau due to compaction of trabeculae, following with an increase after compaction [115,116]. Bone has been mostly studied as a linear elastic and elasto-plastic material [117,118]. However, it has time-dependent properties, so it is viscoelastic and viscoplastic [115,119]. Bone is fluid filled so it can also be considered as a poroelastic material.

The turtle shell is composed of fused bone covered in keratin scutes [120]. These keratin scutes easily delaminate and deflect cracks, toughening the shell before the load reaches the more brittle bone [49]. As the most likely region to experience high impacts from predators, the upper section of the shell, called the carapace, has been the focus of most structure-property research. The box turtle carapace is composed of two firm, exterior, cortex layers with a porosity of ~ 7% sandwiching an interior, closed-cell, cancellous layer with a porosity of ~65%. The Young's modulus of these layers is approximately 20 GPa and 1 GPa, respectively. Compression tests revealed familiar sandwich structure behavior (Figure 2.7A); a small linear elastic regime as the closed cells in the foam layer resist buckling, followed by a plateau where the pores collapse, after

which another linear elastic regime is evident as the foam densifies and damage occurs. Samples that contained all three layers of the turtle carapace performed better than samples that were composed of just a single exterior layer under compression; the latter exhibited near-linear stress-strain curves. The three-layered samples, pictured on the right side of Figure 2.7A, absorbed more energy compared to single-layer exterior plate samples and both absorbed more energy as strain rate increased. The specific energy absorbed for each type of sample at different strain rates can be seen in the center of Figure 2.7A. Comparison with the entire turtle carapace showed that it responds to flexure in a very similar way to the smaller specimens, with the same stress-strain and energy absorption trend [46].

Figure 2.7 A) (Left) Stress-strain curve of turtle shell samples with various strain rates and locations. The upper curve represents samples taken from just the exterior portion of the shell that has minimal porosity. The lower curve represents samples that include all three layers of the turtle shell's sandwich structure. (Middle) The three-layer samples have a higher energy absorption by volume than the single layer samples. This bar chart also shows how much energy was absorbed in each deformation regime. (Right) A cross section of the turtle shell where the three layers can be easily observed [46]. B) Interlocking sutures. (i) The interlocking sutures found between osteoderms in the turtle carapace allow the shell to flex without fracturing, but also provide an energy absorbing mechanism during failure. (ii) When the sutures are pulled apart the collagen network holding it together stretched before the fibers fracture. Fractured fibers are marked by the white arrows [74]. (iii-viii) Sutures in the red-eared slider turtle have a gradient in elastic modulus. (iii,iv) Nanoindentation tests were performed moving from the tip of the suture tooth to the bulk of the turtle shell. (vi-viii) Elastic modulus decreases towards the tip of the suture teeth in wet and dry conditions[49]. C) Skull section prior to and after of punch test. Conical damage zone after impact indicates that the porous structure recruits nearby material to resist the load. After image also shows densification mechanism that is common in sandwich structures [44]. D.) SEM image of Bouligand structure in Mantis shrimp dactyl claw (left) and 3D representation of the Bouligand structure (right) [61].
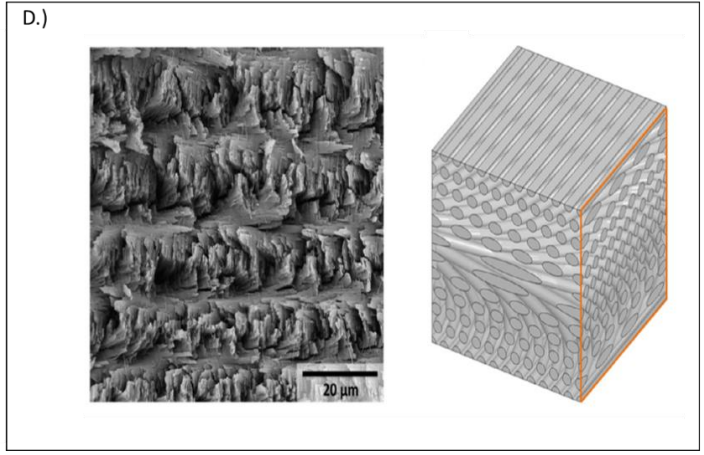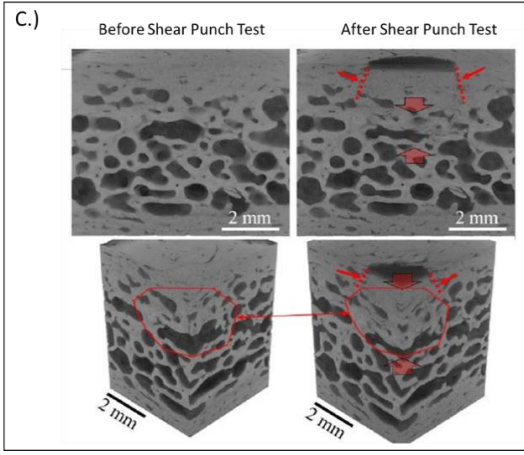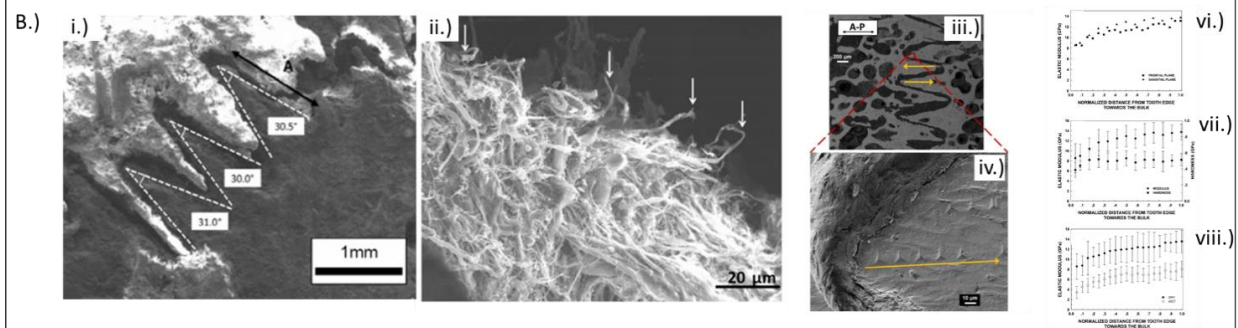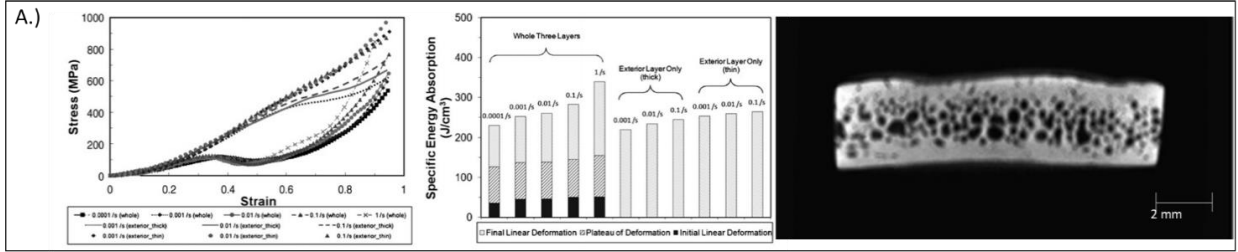
The turtle carapace also has a porosity gradient through the cancellous layer, which is hypothesized to prevent stress concentrations at the interface of the porous and non-porous layers. The bones, called ribs, are fused together to form the turtle's shell and are connected by a soft, unmineralized collagen; the interface forms a suture structure and is highly flexible as seen in Figure 2.7B (i). Under small loads, these interfaces allow the shell to flex and deform but lock together and stiffen under higher loads. These sutures are thought to trap and arrest laterally propagating cracks. When pulled apart the collagen network connected the interlocking sutures, stretched and ruptures absorbing energy in the process. Figure 2.7B (ii) shows the ruptured collagen network after tensile tests. White arrows indicate torn collagen fibers [74]. To prevent fracture of the suture teeth during impact, another gradient, this time in stiffness, was measured between the flexible suture material and the rigid bone in the center of the carapace. Figure 2.7B (iii, iv) shows the path of nanoindentation tests that produced the plots shown in Figure 2.7B (vi-viii). These tests revealed a steady increase in elastic modulus from the tip of the teeth towards the bulk of the turtle shell, even under wet conditions [49]. This gradient is also thought to induce more intimate entanglement of the sutured interface, creating better interlocking under high loads. Finally, the cortex layers have different fibrous structures. The upper cortex layer is close to the point of impact on the shell and thus is thought to be optimized to toughen the shell and prevent cracking while the lower cortex layer is believed to mainly provide structural support. The upper layer is composed of a randomly oriented osteon network embedded in an interwoven fibrillar array. This disordered arrangement hinders crack initiation and confines larger cracks from spreading through the material. The lower cortex layer has orthogonally aligned fibers which provide biaxial support at the base of the shell, but are likely less impact resistant [49].

The full ramifications of a bony sandwich structure under impact have been further

explored in testing on the human skull, which has a thicker, trabecular layer with irregular pores sandwiched between high-density cortical bone [42] [121]. Under impact, Wu et al.[121] observed that, at low velocities ~3-4 m/s, round impactors simply rebounded off of the skull, failing to puncture the firm external cortical bone. As impact speed increased though, the skull absorbs more energy, just as the turtle carapace does – this is in part due to the ability of the skull structure to widen the impact region. At high velocities, the damage area of the skull bone grows, indicating that more material becomes involved in absorbing energy and resisting the impact [121]. Brown et al. [44] performed shear punch tests at strain rates of $0.001s^{-1}$ and $0.1 \ s^{-1}$ on the human skull to better understand its dynamic shear strength and deformation. They found that shear strength of the individual layers of the skull had minimal dependence on strain rate, but when tested together, the skull had a higher shear strength at higher strain rates. In general, the porous trabecular bone determined the shear strength of the specimens. At both strain-rates they observed pore collapse and densification in the central region of the skull bones. A conical damage and densification zone was also observed beneath the impact surface (Figure 2.7C), indicating that the porous structure of the skull spreads the impact over a larger and larger area as the energy moves through the skull thickness. This recruits more material to resist the stressed state and prevents damage [44].

Additionally, the skull has a gradient in its porous arrangement [42]: Brown et al. [44] reported a pore volume fraction of the inner and outer layers of the skull to be ~ 10% which gradually increases to nearly 50% in the center of the skull bones [44]. Similar to porous gradients in fruits and nuts discussed earlier, this gradient decreases stress concentrations and the likelihood of delamination between layers of differing properties.

The woodpecker skull has been widely investigated with respect to impact [122]. Dissimilar to mammalian skulls, the sandwich structure is filled with air to reduce its weight for

flight. Spongy porous bone coalesces at the countercoup position of the beak and is expected to evenly distribute impact stress preventing damage to the brain [123]. There exists a gradient in Young's moduli across the skull from 4.0~11.0 GPa which has been modeled to minimize the peak stress during impact [124–126]. There is an additional impedance mismatch in the hyoid apparatus (the bone which suspends the tongue and wraps around the back of the skull) in the transverse and longitudinal directions. This gradient, along with the geometric tapered effect, and the surrounding viscoelastic tissues have been shown to mitigate the stress wave propagation through viscoelastic dampening [127,128].

The woodpecker beak can be imagined as a sandwich structure with three layers: (1) the rhamphotheca composed of compliant keratin surrounding, (2) spongy trabecular bone with (3) compact bone in the center. At the micro-scale, the keratin cells in the rhamphotheca stack up in layers along the impact direction and neighboring cells have an interlocking suture interface that are on the order of nanometers. The waviness (the height-to-width ratio) of the suture is ~1. The hardness and elastic modulus mismatch between the three layers in the beak help to dissipate internal stress. Additionally, the viscoelastic muscles in the neck and legs dampen the impact energy.

The elk antler has a similar structure to that of bone, with vascular channels (~15-25 μm diameter) surrounded by concentric bone lamellae, collectively referred to as osteons. Using drop tower experiments, Lee et al. [83] determined that elk antler had higher impact strength than nacre. Launey et al. [90] claimed that the main energy dissipation mechanisms in the elk antler arise from microcracks that form at these lamellar boundaries. These microcracks lead to crack deflection and bridging, in a similar fashion to nacre. Unlike nacre, the cracks in the elk antler twist when they reach these interfaces, which absorbs more energy [90].

2.7.2 Marine organisms

The conch shell has a similar composition to that of the nacre found in abalone; however, it has a hierarchical cross-lamellar structure that makes it an order of magnitude tougher. Similar to nacre, the conch shell is made of mineralized calcium carbonate sheets glued together by a protein phase, however it has three different hierarchies of lamellar layers which crisscross the layers above and below [9]. This leads to a compartmentalization of cracks which are arrested at the rotated interface between layers. In quasi-static testing, the shell also dissipates energy by forcing cracks to meander (similar to the phenomenon found in nacre) and by allowing microcracking to occur in the weaker phase which delocalizes damage [7]. However, unlike nacre which performs poorly during impact [83], the conch shell has several strain-rate strengthening mechanisms that are not observed during quasi-static tests. At a strain rate of $10^3 \, \text{s}^{-1}$, the conch shell has a 67% higher fracture strength than when tested at a strain rate of $10^{-4} \, \text{s}^{-1}$. Under impact loading, the third order lamellae (the smallest of the hierarchical lamellae) fracture and splinter away from the rest of shell. Under rapid loading, fracture no longer occurs along lamellar interfaces but instead cracks through the lamellae creating a powder of fragmented rods on the scale of single microns. Within a given third order lamella, impact strain rates were shown to induce rotation in nanoparticles which can block dislocation activities and improve fracture strength. Further, trapped edge dislocations were observed after impact suggesting strain-rate dependent defense mechanisms that are not seen during quasi-static tests [11].

One of the most remarkable impact resistant biological structures is the dactyl club of the mantis shrimp, which strikes its prey at a velocity of up to 23 m/s. Beneath the dactyl club's highly mineralized surface are oriented chitin fibers that form a twisted Bouligand structure. The Bouligand structure is composed of superimposed layers of fibers whose orientation is rotated

relative to the layers above and below, thereby creating a helical, stacked plywood arrangement. These are visualized in Figure 2.7D. Early pioneering work by Bouligand and Giraud-Guille [129] described this twisted, layered arrangement in a wide variety of organisms ranging from crustaceans to insects to bacteria, but more recent work has probed the mechanical functions of these structures. When this underlying phase in the mantis shrimp begins to fracture, cracks travel in a helicoidal path between the layers of fibers. Another implication of this structure is that crack fronts twist as they propagate creating larger fracture surfaces which absorb more energy than flat cracks [60].

2.8 Acknowledgements

Chapter 3: Bioinspiration from impact resistant design motifs in nature

It is evident that natural materials profit from the combination of different design elements and many levels of hierarchy which are constructed via self-assembly. However, this makes it difficult for testing to probe the role of individual structural designs (i.e., sutures, tubules, etc.) within a biological material. Many researchers have turned to computer modelling and additive manufacturing to recreate and test simple materials with only a single structural feature that is observed in impact resistant biological materials, before moving on to more complex models. This allows researchers to better understand the role of each design element and the synergistic effects that arise when they are combined. This section will cover the specific architectures noted at the bottom of Figure 2.2 which are some of the most important design motifs for impact resistance in nature. Table 3.1 shows the occurrence of these structures in different natural systems.

Table 3.1 Occurrence of different design motifs in impact resistant systems in nature.

Biological System	Sandwich	Tubular	Layered	Suture	Gradient	Hierarchical	Composite	Interfacial	Porous	Viscoelastic/ Viscoplastic
Pomelo	+	−	+	−	+	+	+	+	+	+
Coconut	+	−	+	−	+	+	+	+	+	+
Wood	+	+	+	−	+	+	+	+	+	+
Hooves	+	+	+	+	+	+	+	+	+	+
Horns	+	+	+	−	+	+	+	+	+	+
Pangolin Scales	−	−	+	+	−	+	+	+	+	+
Tendon	−	−	+	−	−	+	+	+	+	+
Ligament	−	−	+	−	−	+	+	+	+	+
Cartilage	−	−	+	−	+	+	+	+	+	+
Bone	+	+	+	−	+	+	+	+	+	+
Turtle Carapace	+	−	+	+	+	+	+	+	+	+
Human Skull	+	−	−	+	+	+	+	+	+	+
Woodpecker Skull	+	−	−		+	+	+	+	+	+
Woodpecker Beak	+	−	+	+	+	+	+	+	+	+
Elk Antler	−	+	−	−	+	+	+	+	+	+
Conch	−	−	+	−	−	+	+	+	+	+
Mantis Shrimp	−	−	+	+	+	+	+	+	+	+

3.1 Sandwich Structures

The sandwich structure is a common lightweight, impact resistant design for both high and low strain rates across many biological systems: avian beaks, bones, skulls, turtle shells, horns, pomelo peel, nuts, and wood. Two strong, stiff outer layers (faces) are separated by a softer, compliant layer (core). This arrangement accomplishes multiple goals; the hard-exterior face prevents puncture and resists repeated low strain rate impacts while the core dissipates energy and prevents cracks from bridging the two outer layers. The ultimate goal is to prevent catastrophic failure under impact. The low-velocity energy absorption mechanisms occur in the faces and the

core synergistically as follows: (1) cracking, wrinkling, fracture, and delamination in the top face, (2) core buckling, (3) debonding from the faces and the core, (4) core densification and compaction, (5) shearing and cracking of the core, (6) fiber pullout in the faces, and (7) damage initiation in the bottom face [130–134]. These energy absorbing mechanisms are strongly dependent on the material properties of the faces and core (e.g., stiffness of the faces, density and degree of cross-linking in the core) and geometry (e.g., aspect ratio, face thickness to core thickness ratio, cell structuring in the core). Overall, the sandwich structure increases the amount of strain energy a material can absorb while spreading the force of the impact over a large area and arresting cracks at pore and layer interfaces.

3.1.1 Introducing wavy cell structure increases energy absorption

Inspired by the wavy interface found in woodpecker beaks, Ha et al. [135] used finite element modeling to probe the effects of a wavy honeycomb wall (BHSP) compared to a conventional flat wall (CHSP) on energy absorption during impact with a velocity of 10 m/s (Figure 3.1). Both BHSP and CHSP had the same core volume, wall length (9 mm), and wall height (15 mm), with varying thickness. The bioinspired wavy honeycomb wall had a wave amplitude (A) of 1 mm, wave number (n) of 2, and wavelength of 4.5 mm, and a thickness (t) of 0.1 mm. For the conventional honeycomb wall case-one (CHSP-1) the wall thickness was 0.1 mm and case-two (CHSP-2) the wall thickness was 0.132 mm.

The wavy bioinspired sandwich is able to withstand greater peak forces before deformation than the conventional (CHSP-1) with same wall thickness (Figure 3.1(A-D)). However, a similar peak force was obtained for CHSP-2 having a thicker wall. The specific energy absorption (energy absorption per unit mass) is used to describe the structures' ability to dissipate energy upon impact through plastic deformation. The wavy honeycomb wall showed an increase in specific energy

48

absorption by 125% when compared to CHSP-1 and an increase in 63.7% when compared to CHSP-2 (Figure 3.1C). This is primarily due to competing deformation mechanisms. The conventional honeycomb is limited to cell-wall buckling, while the bioinspired-wavy honeycomb not only buckles, but bends and shears at the peaks and troughs of the wave allowing for an increase in plastic deformation without catastrophic failure. Additionally, the specific energy absorption can be tailored by adjusting the wave number and amplitude.

Figure 3.1 Impact modeling of bioinspired sandwich and tubule structures. A-D) Impact modeling of a wavy bioinspired honeycomb cell compared to a conventional honeycomb cell. A) Schematic of the conventional honeycomb cell with flat walls (CHSP-1). B) Schematic of the bioinspired cell with wavy walls (BHSP). C) The three investigated designs (CHSP-1, CHSP-2, and BHSP) and deformation at various strains. D) The deformation of the cell walls of the three designs zoomed in at a strain of 16% [135]. E-J) Impact testing of bioinspired tubules structures. E) Schematic of the cuticle layer with tubules (holes) supported by larger tubules (hollow columns). F) Deformation of the cuticle layer without tubules (holes). G) Deformation of the cuticle layer with tubules (holes). H-J) Deformation of the tubule structure with increasing inner diameter [50]. K-O) Impact results of the tubular structure with increasing hierarchical order. K) Impact response and von Mises stress of the three orders of hierarchy. L) Impact response and von Mises strain of the three orders of hierarchy. M) Deformation map of the first order single tubule. N) Deformation map of the second order which is a tubule with seven tubules within. O) Deformation map of the third-order structure [136].
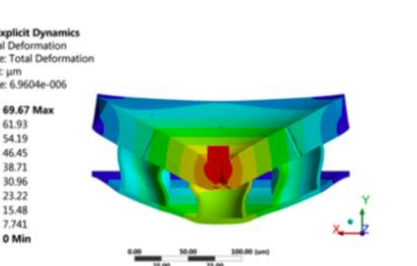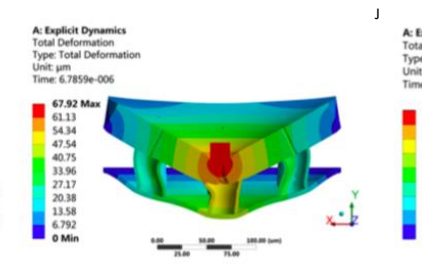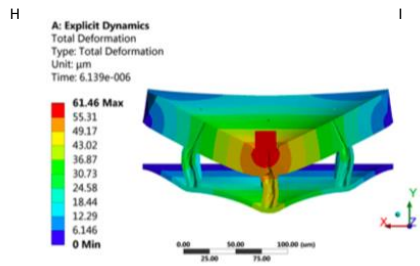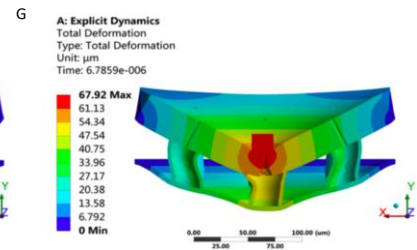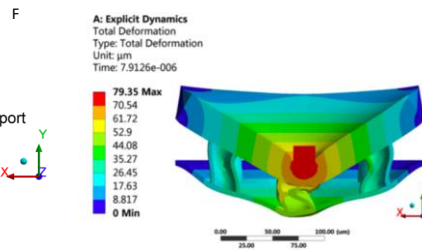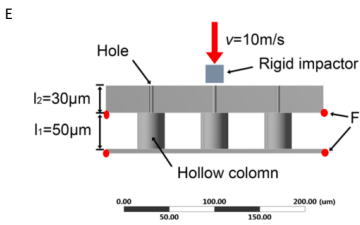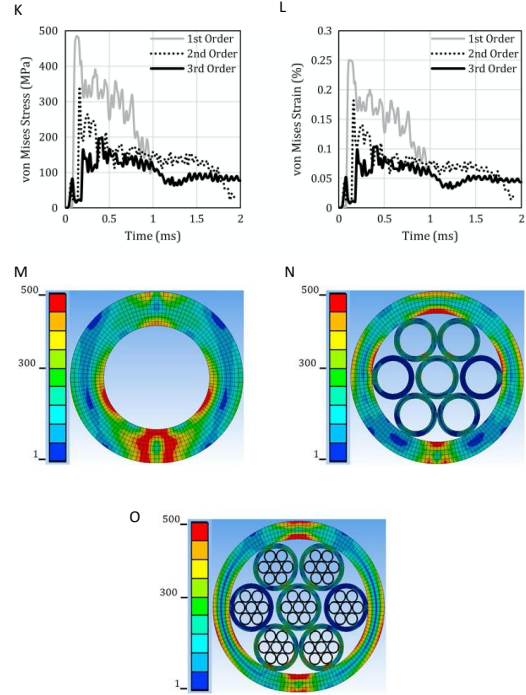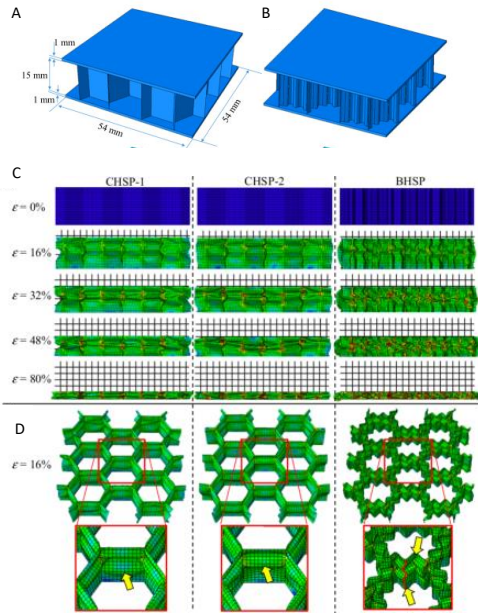
3.1.2 Fluid-filled honeycomb increases energy absorption

Hydration is a hallmark of biological materials and the presence of fluid has important mechanical implications for impact response. Inspired by the fluid-filled cells found in fruit peels such as the banana, Clark et al.[137] investigated the role of non-Newtonian fluid added to honeycomb structures and their ability to absorb impact energy. An impacting ram with an average kinetic energy of 0.9644 J was used for testing. With use of a high-speed camera the deceleration of the empty honeycomb and six layers filled with the shear-thickening fluid was 277.8 m/s^2 and 634.9 m/s^2, respectively. This corresponds to an increase in 52.38% energy absorption upon impact for the fluid-filled honeycomb structure with respect to the sample without fluid. The shear-thickening fluid stiffens upon impact and acts to redistribute the stress reducing global damage. Investigating shear-thickening fluid in sandwich structure cores for impact response has recently been popularized and the general consensus is their ability to absorb impact energy and suppress damage enhances impact response for sandwich structures [138–140].

3.2 Tubular Structures

The tubule architecture is defined by having hollow or fluid-filled channels organized along a similar direction. Many remarkable energy absorbent materials found in nature including bones, teeth, exoskeletons, horns, and hooves are known to harness this design strategy. Radius, volume fraction, wall thickness, orientation, material composition, and degree of reinforcement are important factors that influence mechanical response. Typical energy absorbing mechanisms for the tubule structure are buckling, bending, collapse, delaminating, vibration, and inhibiting crack propagation. Ultimately, tubules enhance impact resistance by increasing energy absorption via these plastic deformation mechanisms and by deflecting cracks.

3.2.1 Tubule thickness and deformation mechanisms

Inspired by the cuticle of the elytra beetle, Hao and Du [50] investigated the role of tubules within the thickness of the cuticle (pores) and larger hollow tubules that support the cuticle and their relative deformation mechanisms under impact with use of numerical modeling. This can be viewed as two orders of the tubule structure where the diameter of the tubule in the cuticle is much smaller than the supporting tubule beneath (Figure 3.1(E-J)). Hao and Du performed impact tests on structures with and without tubules in the cuticle layer. The presence of tubules in cuticle helps to absorb energy upon impact. This is explained by its ability to resist catastrophic deformation. In the case without cuticle pores, the support tubule buckles and collapses. However, with the tubule in the cuticle layer, the support tubule only slightly buckles as impact energy is used to split the cuticle pore and expand the upper diameter of the support tubule (Figure 3.1(F,G)).

Additionally, Hao and Du [50] investigated the influence of the inner diameter in the support tubules on impact deformation, while the wall thickness remains constant (Figure 3.1(H-J)). For all cases the cuticle pore remains the same size and deforms by delaminating and expanding at the base. For small diameters, the support tubule buckles in an "s" shape. The medium-diameter has an expansion with only slight buckling while the largest diameter buckles the least and has the greatest expansion. This behavior can be explained by changes in the moment of inertia and resistance to bending. Increasing the diameter and keeping the wall thickness constant allows for an increase in strain. This suggests that larger diameters may absorb more impact energy through conversion to strain energy.

3.2.2 Increasing tubule hierarchy increases energy absorption

Inspired by the hierarchical organization of tendons, Tsang and Raza [136] simplified fiber bundles as hollow tubular sections to investigate the role of hierarchy on impact absorption using

numerical modeling. The collision was modeled with an impact mass of 200 kg and a velocity of 20 m/s. Three orders of hierarchy were investigated where the first order is a simple hollow tube with each sequential order fitting seven hollow tubes within one larger tube (Figure 3.1(K-O)). Under impact loading, peak von Mises stress, strain, vertical displacement, contact force, and total energy all decrease with increasing hierarchy (Figure 3.1(K,L)). The peak von Mises stress occurs just below the point of contact and reduces from 485 MPa to 337 MPa to 198 MPa from first- second- and third-order hierarchy, respectively (Figure 3.1(M-O)). There is reduction in total energy of 73% and 89% for the second- and third- order, respectively, when compared to the first-order hierarchy. With each increasing hierarchy there is greater surface area to better distribute the load allowing for delocalization of stress and strain.

3.3 Layered Structures

Layered composite arrangements are a hallmark of biological materials. These are abutted layers of material that have different properties, often with the goal of creating a weak sacrificial interface between them. This sacrificial layer frequently serves to deflect cracks that propagate during impact, forcing them to take tortuous, energy-absorbent paths. This structure is found in a wide range of organisms and can be both made of both mineralized and unmineralized tissues. In a review of impact resistant mammalian structures for bioinspiration, McKittrick et al. [141] determined that the microdeformation mechanics of lamellar structures such as microbuckling and delamination made them the best energy absorbent designs. The combination of beneficial fracture dynamics and energy absorbent deformation modes have made natural lamellar materials an exciting topic of research in the past half century. Layered structures come in a variety of different arrangements which create tortuous fracture paths and crack arresting interfaces, while also dissipating energy through delamination and buckling.

3.3.1 Effect of Additional Levels of Hierarchy and Interface Angle

Gu et al. [142] 3D printed cross-lamellar structures inspired by the conch shell. They made two different models, one with a single level of hierarchy consisting of three stacked layers orthogonal to each other and one with an added level of hierarchy and a crossed lamellar structure with layers at a 45° angle to each other. These are shown in Figure 3.2A (top). The same crack deflection patterns as noted in quasi-static testing of the conch shell were seen in the impact testing of these biomimetic samples with crack deflection at the interfaces and delocalized damage as various sections of architecture worked in concert to resist catastrophic failure. Figure 3.2A (bottom) shows the effectiveness of the conch design, with minimal impactor penetration and hardly any visible damage. Gu et al. [142] also used finite element analysis to recreate impact conditions on both models. The crossed-lamellar arrangement proved to be 70% more impact resistant than the simple orthogonal geometry and 85% better than a bulk slab of the stiff phase with the same dimensions. In numerical simulations, distributed microcracking in the soft phase, which has been observed during quasi-static tests on the conch shell, was observed in the complex model, while localized damage created holes and caused catastrophic failure in the model with a single hierarchy. Gu et al. [142] calculated that cracks will deflect along the soft phase, when the interface angle is below a critical angle of 50°. This makes the 45° angle found in the conch shell optimal for deflecting cracks and preventing failure at high strain rates.

3.3.2 Effect of Layered Arrangement

Jia et al. [143] performed split Hopkinson bar testing on a range of 3D printed biological structures that mimic renowned impact resistant biological materials. These included layered, hexagonal concentric, brick and mortar, cross-lamellar, and rotated plywood structures representing the microstructure of the sea sponge, bone, nacre, conch shell, and mantis shrimp,

respectively. These microstructures are visualized in Figure 3.2B, along with comparative results for each. The layered structure had the best energy dissipation and critical energy (energy required to induce failure), but had a lower stiffness and response time (time needed for the impactor to complete rebound at velocities below the critical velocity). Digital image correlation was used to observe that much of this energy dissipation was the result of shear deformation between the layers. The rotated plywood structure and cross-lamellar were stiffer and more responsive than the layer section alone. However, while the cross-lamellar structure fractured at a critical energy 50% higher than the hard phase alone, the rotated plywood structure did not perform better than the hard phase. Jia et al. [143] suggested that the rotated plywood structure is effective as a crack arrester but allows easy crack initiation. This makes it effective in conjunction with other design elements that prevent cracks from initiating, where it can be used as a safeguard to prevent catastrophic failure once cracking has begun. The final two designs, brick and mortar and hexagonal concentric showed significant improvements in toughness, flexibility, and energy dissipation compared to the hard phase and stiffness, toughness, strength, and response time compared to the soft phase. Observations of these structures showed highly localized strain and microcracking throughout the material. The localized strain leads to magnified energy dissipation in the soft phase and higher stress which boosts strength and response time. The microcracking spreads damage over a larger volume, improving the overall toughness [35,143].

Ghazlan et al. [144], mimicked the polygonal bricks and mortar structure of nacre to investigate the performance of a bio-inspired composite panel under blast loading. Compared to a monolithic panel of equal mass, the nacre-like panel dissipated a significant amount of energy which was attributed to crack deflection and bridging by the mortar-like bonds. In the same way, Flores-Johnson et al. [145] mimicked the staggered structure of nacre to simulate the behavior of

a bio-inspired composite panel under impact loading, which showed a notable reduction in the residual velocity of the impacting projectile compared to an equivalent monolithic panel. Tran et al. [146] also developed a nacre-inspired composite panel by mimicking the interfacial waviness between adjacent bricks in nacre. They observed well-distributed damage at the interface of the composite by underwater blast loading, which results in prominent energy dissipation. Ghazlan et al. [147] developed an analytical model to capture the influence of nacre's interfacial geometry on its energy absorption capacity. They employed a typical lap joint modeling approach used in structural engineering, which assumes that tension through the bricklike tablets is transferred via shear through the interface. The results indicated that the waviness of the nacreous tablets amplifies the energy absorbed by the composite whilst improving the distribution of shear forces along the interface. Miranda et al. [148] used Finite Element Modeling (FEM) to test a variety of differently-shaped armors composed of non-overlapping alumina epoxy tiles under ballistic impact. They found that hexagonally shaped tiles performed better than diamond, square, and circular tiles, providing the most uniform levels of protection, best reduction in projectile speed, and one of the smallest areas of damage. These results are unsurprising since many natural armors, like that of the armadillo and boxfish, have evolved arrangements based on hexagonal scales.
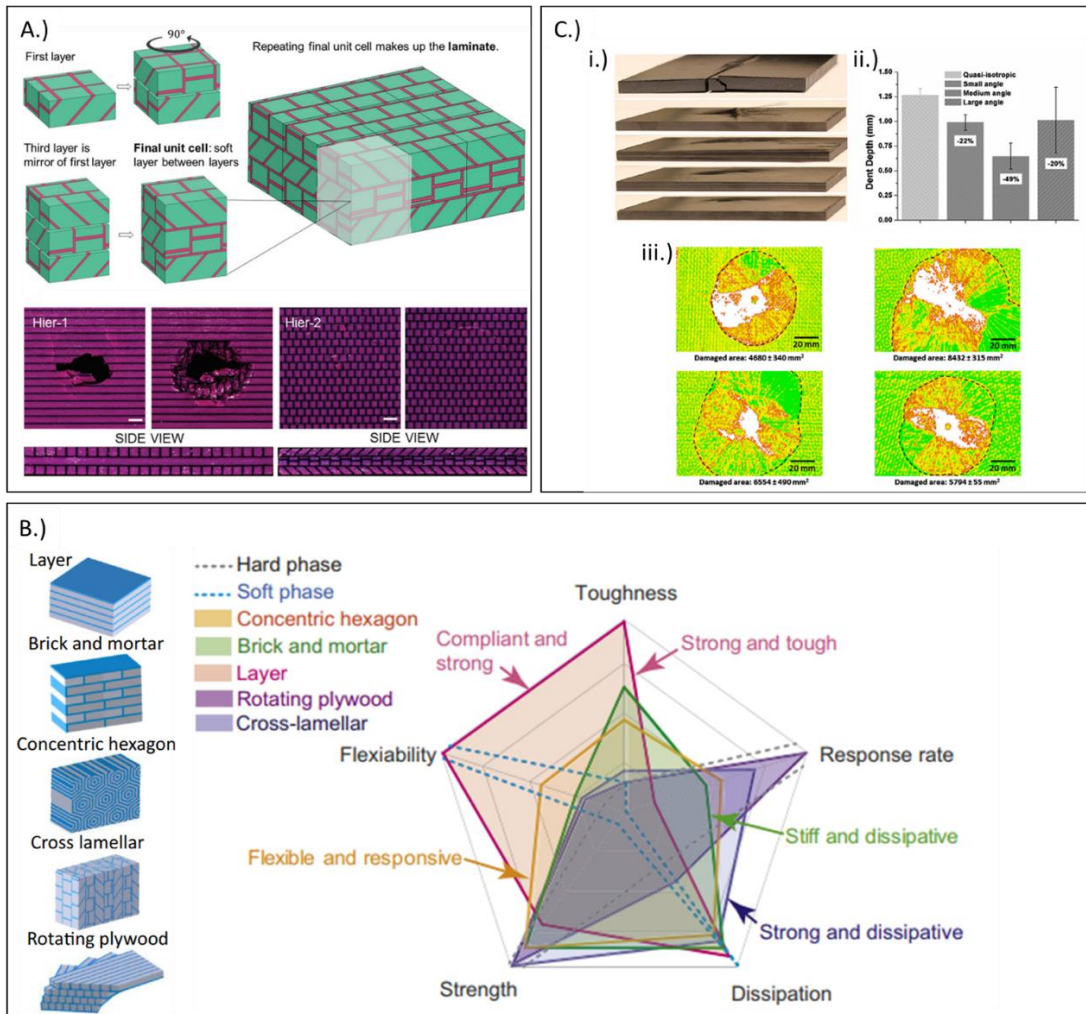
Figure 3.2 Bioinspired layered structures. A.) (Top) Visualization of 3D printed samples inspired by cross-lamellar structure of conch shell with a layer-by-layer construction of the repeating unit cell that forms the final structure. (Bottom) The single level of hierarchy and the conch-inspired designs after impact from a top and side view. Minimal damage is seen in the conch-inspired design with two levels of hierarchy [142]. B.) Comparison of properties of five different 3D printed lamellar arrangements [35]. C.) (i) Impact damage in fiber reinforced composite samples with different layup arrangements. From top to bottom the samples are unidirectional, quasi-isotropic, small-angle helicoidal, medium-angle helicoidal, and large-angle helicoidal. (ii) Comparison of dent depth from drop tower indenter across the bottom four samples in (i). The isotropic sample was completely fractured. (iii) Image from ultrasonic C-scan indicating the extent of internal damage in the quasi-static (top left), small-angle (top right), medium-angle (bottom left), and high-angle (bottom right) samples [61].

3.3.3 Layered Composites with Helicoidal Fiber Arrangement

Apichattrabrut et al. [149] tested helicoidally arranged carbon-fiber composites and found

that they performed significantly better than unidirectional and $\pm 45°$ fiber reinforced composites

in both quasi-static tension and bending tests as well as impact tests. In quasi-static tests, crack propagation in the engineered twisted composite proved to be similar to those observed in similar biological materials, where cracks propagate in a helicoidal pattern that mimicked the pattern of the fibers. Impact testing was performed using a vaguely bullet-shaped polycarbonate rod propelled at the samples at 55 m/s. Each layer of the $\pm 45°$ composite delaminated under impact and cross cracking was observed between fibers while the projectile remained embedded in the sample once it came to a stop. In the helicoidal composite, the projectile did not penetrate the sample. Localized damage was observed on the surface and only a single layer of delamination was apparent within the composite [149]. More in-depth testing on helicoidal composites inspired by the mantis shrimp dactyl club affirmed the beneficial impact resistance of the Bouligand structure. Figure 3.2C (i) shows images of five composite samples with different ply orientations after drop tower impact testing. The top sample is a unidirectional composite with all fibers aligned in the same direction and the second is a quasi-isotropic sample with fibers oriented at $0°$, $\pm 45°$, and $90°$ to each other. The bottom three samples have helicoidally arranged fibers with angles between adjacent layers of 7.8°,16.3°, and 25.7°. The unidirectional samples failed completely after impact testing. The helicoidal samples had a smaller dent depth (ii) after impact, which was attributed to an in-plane spread of damage. This is affirmed in Figure 3.2C (iii), which shows ultrasonic C-scans of the damaged composites and indicates a larger damage area in the helicoidal samples relative to the quasi-isotropic samples [61]. These results have been confirmed by other researchers and some have also noted that helicoidal composites have a higher extent of delamination during impact [64]. Further experiments involving 3D printed composites, composites fabricated from prepregs, and simulations under quasi-static bending showed that the crack twisting mechanism of Bouligand structures can delay catastrophic failure despite competing

failure mechanisms, such as delamination and crack branching [63].

Helicoidal nanofiber arrangements have also been tested in nanofiber film applications. Chen et al. [150] performed falling ball experiments on epoxy films without nanofibers, with orthogonally oriented nanofibers, and with electrospun nanofibers oriented in a helicoidal arrangement. The drop height necessary to fracture the helicoidally arranged fibers was four times that of the neat epoxy film and twice the height of the orthogonal nanofiber samples. As with larger samples, a zigzag fracture pattern was observed in the helicoidal samples indicating the crack was forced to follow a tortuous path. When the film was coated on a glass slide, it outperformed toughened glass films and resin films under impact.

3.4 Gradient Structures

Often interfaces in materials are weak points that concentrate stress and lead to failure. To effectively transfer energy to a new phase of material with different mechanical properties, biological materials will often gradually change the properties of the material, rather than produce a discrete boundary [151]. This gradual change in mechanical properties is frequently referred to as a gradient structure and falls into the classification of Functionally Graded Materials (materials that change in composition, constitution, or structure continuously through its thickness). These materials have garnered significant interest for armors meant to resist impacts in the ballistic regime. Multilayer ceramic armors are commonly used for bullet proofing in military applications. These materials often delaminate as the tensile wave caused by a bullet reaches the interlayer where there is a mismatch in mechanical properties. Functionally graded ceramic armor reduces this mismatch and creates an optimal impact resistant material [152]. Long before the first ceramic bulletproof vests were being prototyped for the Vietnam War, nature was optimizing structural gradients in a host of biological materials. While interfaces can arrest cracks, they can also act as

initiators where internal stresses are focused. Gradients in material properties eliminate these local concentrations and can also lead to crack tip blunting and deflection.

3.4.1 Compositional Gradients

Graupner et al. [153] created composite samples that mimicked the compositional gradient of the coconut pericarp. They produced samples out of cellulose fiber reinforced polylactide acid (PLA), using fibers of different strengths, stiffness, and elongation at failure embedded in a PLA matrix to recreate the steady change in mechanical properties found in the coconut. Samples with three and five layers were tested alongside reference samples to understand the effect a gradient in mechanical properties would have on the material's impact resistance. They found a threefold improvement in impact strength between the gradient structure and neat composites with the same fiber fraction, indicating that the gradient does in fact boost impact strength. Further, impact testing revealed that the five-layer composites performed significantly better than the three-layer composites, which suggests that a more gradual gradient results in better impact resistance. Graupner et al. [153] suggested that this was due to the smaller difference in properties at the interface, which decreases stress concentrations and increases the load transfer capabilities of the material.

Gradient structures improving impact resistant properties may seem to be antithetical to the improved impact resistance found in lamellar structures, which capitalize on sudden changes in material properties and significant soft-hard interfaces. However, Mirzaali et al. [154] studied the impact resistance of 3D printed materials with continuous gradients in hardness compared to materials whose hardness was a stepwise function and found that each were effective in different ways. Continuous gradients showed a higher fracture energy for cracks along the gradient direction, while stepwise functions showed better crack resistance as the hard-soft interfaces arrest

crack development. Intriguingly, Mirzaali et al. [154] also found that as the transition zone between the soft and hard regions varied from 100% to 5% of the sample length nearly all fracture properties of the material increased.

3.4.2 Porous Gradients

Bamboo and palm trunks have attracted significant attention in recent years due to their impressive energy absorption mechanisms and low density [155]. Zou et al. [156] confirmed that the gradient in vascular pores improves the impact resistance with drop tower tests before creating a bionic model that replicated the porous gradient through bamboo's cross section. This model was numerically tested and showed improved lateral impact and bending strength over models that did not contain the functional porous gradient. Chen et al. [157] 3D printed samples with a gradient in vascular pores and performed drop tower testing on the them. They discovered that the gradient increased the amount of energy that could be absorbed by the cylinders but that they also increased the peak force experienced by the structure. This occurs because the cross-sectional pores collapse and interfere with each other which allows the structure to absorb more energy, but can also prevent further deformation that is seen when there are the same number of pores throughout the material. It has also been determined that pore shape, pore size, wall thickness, rib thickness, rib angle, and a number of other parameters are intertwined with the porous gradient in making bamboo impact resistant [156–160].

3.5 Suture Structures

Suture interfaces are defined as a compliant interlocking junction that connects adjacent components allowing for regional control over strength, stiffness, and energy absorption. They are found across a diverse range of biological materials including those that are known to withstand large impact forces: human skull [161,162], woodpecker beak [163], turtle shells [74,164], boxfish

plates [165], pangolin scales [29], and horse hooves to name a few. The suture structure is incorporated in both mineralized (e.g., skull) and non-mineralized materials (e.g., hoof). Typically, there also exists a viscoelastic material within the gap of the suture interface, often collagen, that holds the plates together. Thus, there exists a dependence on performance with material properties such as elastic modulus. Additionally, there is a wide range of geometrical features that span across biological materials including degree of interdigitation, shape (triangular, trapezoidal, sinusoidal, etc.), and hierarchical ordering. Therefore, both the material properties and geometry of the suture structure are important in determining its ability to dissipate energy during impact. Suture structures improve impact resistance by creating a flexible joint that can dissipate energy under impact without failing, while also limiting the total deformation of the junction when the interlocking mechanism catches.

The response of suture structures to impact is widely studied with respect to human skulls due to the implications of traumatic brain injuries. This is primarily accomplished through parametric studies on material property and geometry with the use of finite element analysis and/or mechanical testing of 3D-printed prototypes. The suture structure is often simplified and reduced in complexity to isolate the design features of interest (e.g., interlocking angle, waviness, hierarchical order).

3.5.1 Increasing Suture Hierarchical Order Effectively Attenuates Stress

For example, Zhang and Yang [41] used a sinusoidal model with two orders of hierarchy in a two-dimensional finite element model to describe how suture morphology influences stress attenuation and energy absorption under dynamic loading conditions. The first order of hierarchy is a simple sinusoidal function (model B) and the second order of hierarchy contains the pure sinusoidal function with an additional sinusoidal wave on a smaller length scale (model C) (Figure

3.3A). Analysis was also performed on a flat interface as a control labeled as model A (Figure 3.3A). Each interface joined two neighboring bone pieces labeled L-bone and R-bone (left and right respectively). An impulsive load q (50 kPa) was applied on the outer surface of L-bone for 0.04 µs which represents physiological dynamic loading conditions.

The sectional stress was measured at R-R' (labeled in Figure 3.3A) and plotted in Figure 3.3B to highlight the influence of suture morphology and hierarchical order. The flat interface has the largest average von Mises stress while the second order hierarchical suture has a significant reduction in stress (Figure 3.3B). This suggests that the higher ordered suture structure acts as a transmission barrier to better attenuate the impact stress. This agrees with stress wave theory as increasing the hierarchy effectively increases the contact area with the transmitted stress wave. The suture morphology is also important in efficiently distributing the stress uniformly across the entirety of the bone (Figure 3.3C). This is caused by scattering at the interface. The higher order hierarchy also correlated to an increase in the strain energy ratio implying its ability to store energy during impact. Additionally, this study evaluated the effect of elastic modulus on strain energy and demonstrated that as elastic modulus of the suture increases the strain energy decreases. This indicates that stiffness can be tailored to optimize strain energy storage. This study purposefully omitted the viscoelastic response that is typically associated with the suture interface to isolate the dependence on morphology.

Figure 3.3 Bioinspired suture designs. A-C) Hierarchical suture morphology and stress attenuation. A) Describes the three different suture morphologies and loading conditions. Model A is the flat interface. Model B is the simple sinusoidal suture. Model C in the second-order hierarchy sinusoidal suture. B) Average Mises stress at position R-R' for the three different morphologies. C) Illustrates the time dependence and stress distribution among the different morphologies [41]. D-G) Stress distribution mechanism in sutured interfaces. D) Schematic of the suture and flat interface and their corresponding loading conditions. E) Stress with respect to time for suture and flat interface. F) Respective orientation of incident and reflected stress waves. G) Strain energy as a function of time in the gap of the sutured and flat bar [166].
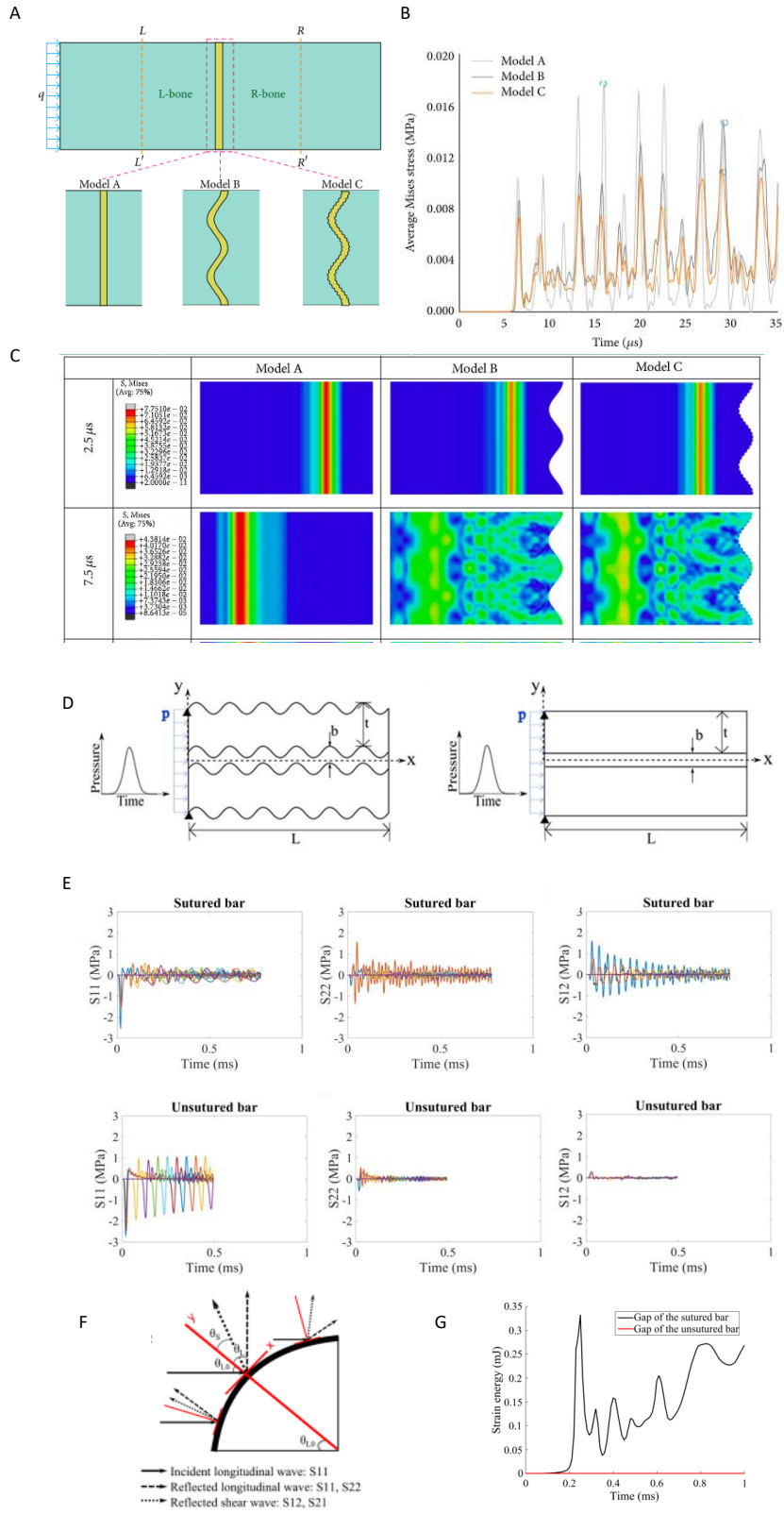
3.5.1 Mechanism for Stress Distribution in Suture Interfaces

While Zhang and Yang [41] formally described the ability of sutured interfaces to attenuate stress, there was a lack of understanding of the exact mechanisms at hand. Lee et. al [166] used a similar two-dimensional finite element analysis under dynamic loading conditions to compare how stress waves were mitigated between a sinusoidal suture interface and a flat interface. In contrast to Zhang and Yang [41], Lee et. al [166] applied a loading direction perpendicular to the interface (Figure 3.3D). They examined the damping capabilities and showed that the flat interface was able to reduce the initial pressure wave by 53% while the sutured interface had a reduction of 90%. The dominating mechanism at hand is the conversion of compressive waves (S11) to shear waves (S12) and orthogonal flexure waves (S22) due to scattering at the interface as shown in Figure 3.3E. Another attenuation mechanism was described by the viscoelastic response within the gap of the suture that allowed for strain energy storage (Figure 3.3G).

3.5.2 Geometric Influence on Stress Wave Mitigation

Lee et al. [166] performed a parametric study across a range of geometrical constraints including waviness, ratio of the suture height to the thickness of the bar, gap thickness, and type of boundary. The one geometric design that was shown to have the most effect on damping was the ratio of the suture height to the bar thickness. The pressure loss was the greatest in the sample that had the largest height of the suture when bar thickness was conserved. Interestingly, they did not see a huge influence with respect to waviness (wave height divided by wave period). They analyzed damping due to waviness from 0.25 to 1.5 while a higher range is seen in nature, 1 (woodpecker) and 2.4 (bison) [166].

3.5.3 Effect of Loading Direction

While the two aforementioned studies [41,166] prove that suture interfaces are more superior than flat interfaces in damping and attenuating stress despite loading direction (parallel vs perpendicular), it is necessary to compare how loading direction influences the impact response. The contribution of Maloul et al. [167] demonstrates the distinction between loading direction (parallel vs perpendicular) and strain energy. Loading parallel to the suture interface resulted in the highest strain energy output. This suggests that the parallel direction is more efficient in absorbing energy. For both loading directions, the highest stresses are observed at the peaks of the sutures. While the loading conditions in nature are much more complex and difficult to predict, this study provides the basis for tailorable design for specific applications under dynamic conditions.

Overall, there are limited studies that have investigated the geometrical and material property relationship found in sutures under dynamic loading conditions, and the studies that do exist rely heavily on FEA. These few studies have shown the important role that sutures play in distributing stress and dissipating energy under high strain rates. There is clear evidence that suture geometry, elastic modulus, viscoelastic properties, and loading direction work synergistically to enhance performance under dynamic conditions.

3.6 Time-Dependent Behavior

Due to their biopolymeric constituents (collagen, keratin, cellulose, hemi-cellulose, lignin, and chitin) biological materials demonstrate time-dependent behavior with respect to elastic modulus, strength, and post-yield behavior. Depending on the polymer, increasing strain-rate can influence changes in mechanical behavior. For keratin, with increasing strain rate the mechanical behavior transitions from elastic to ductile-plastic to brittle fracture [168]. This is attributed to the

time scales that are required to rearrange, slide, and stretch fibers through the breaking of intermolecular forces and chemical bonds [103,169]. Generally, biopolymers become stiffer and stronger and show decreasing breaking strain as strain rate increases (Figure 3.4 (A,B)). Figure 3.4 (A,B) demonstrates key strain rate sensitive biopolymers collagen/hydroxyapatite (cortical bone and elk antler)[77,170], keratin (bighorn sheep horn and horse hoof)[76,78], and cellulose/hemi-cellulose/lignin (spruce wood)[171] and their sensitivities to elastic modulus and ultimate compressive strength. This rate-dependent behavior has important implications for impact resistant biological materials which suggests that under dynamic conditions these materials can withstand greater stresses and have different failure mechanisms when compared to quasi-static conditions. Additionally, temperature, hydration, and loading orientation are shown to influence the degree of strain rate sensitivity. Temperature can change the activation barrier for structural transformations (e.g., sliding and rotating) of polymeric units to occur. Hydration or the increase in water content leads to an increase in viscosity of the material and its ability to dampen the travelling stress waves [76]. For the bighorn sheep horn, it was shown that at lower strain rates ($10^{-3} - 10^{-1}$ s^{-1}) there is a significant difference in the compressive stiffness with respect to loading direction (longitudinal and transverse were greater than the radial direction), while there was no significant difference between all three directions at higher strain rates (4×10^3 s^{-1})[76].

Inherent material properties are important determiners in providing energy absorption mechanisms that allow for impact resistance with a primary dependence on viscoelasticity and viscoplasticity. Viscoelastic materials are characterized as having both an elastic and viscous response. A purely elastic material stores mechanical energy during deformation and upon unloading the stored energy is released allowing the material to return to its original shape. Viscosity describes a materials resistance to flow and upon loading energy is dissipated as heat.

Viscoelastic stress-strain behavior is time-dependent. Viscoelastic materials work to isolate impact by attenuating shock and damping vibration. During impact, energy can be stored and dissipated as viscoelastic deformation. Viscoelasticity is described by the loss modulus (stored elasticity), storage modulus (energy dissipated as heat), and tan(δ) (the ratio between storage modulus and loss modulus which represents damping). For structural materials, it is advantageous to have high stiffness for rigidity with high mechanical damping (tan(δ)) [172]. Figure 3.4C shows the relationship between stiffness and damping of conventional materials and highlights the excellent performance of biological materials. Viscoplastic materials are time dependent and deform permanently. Such permanent changes may be due to sliding of interfaces, microcracking, and delamination, leading to energy dissipation.

Many impact resistant biological materials utilize viscoelasticity as a way to effectively store and dissipate energy under dynamic conditions. The viscoelastic response of the muscle and tissues surrounding the hyoid apparatus found in the skull of the woodpecker is known to reduce stress waves during free vibration induced by pecking [173]. Articular cartilage, when subjected to high-speed loading, behaves as a viscoelastic material which provides a mechanism for energy dissipation that limits potential damage to the matrix or surrounding tissues [174]. While all biological materials have some degree of viscoelasticity, there are competing energy absorption mechanisms at high strain rates that often dominate over viscoelastic deformation. For example, while wood has a strong viscoelastic response under quasi-static conditions, the structuring of layers and voids ultimately determines its energy absorption mechanisms under impact [12].

Fruits such as pomelos [175] and apples [52] absorb dynamic waves when dropping from tress and the capacity to dissipate energy is shown to depend on the viscoelastic properties of the protective layers. Ahmadi et al. [52] performed finite element analysis to study the dynamic

70

behavior of an apple and its corresponding layers (skin, cortex, and core) under impact loading (Figure 3.4(D-F)). The skin was modeled as an elastic material (E: 12 MPa, ν: 0.35), while the cortex (E: 5 MPa, ν: 0.35, G_0:0.15, β: 1/800) and core (E: 7 MPa, ν: 0.35, G_0:0.15, β: 1/800) was represented as viscoelastic material. The apple collided with a rigid plate at a velocity of 1 m/s. As shown in Figure 3.4E and F, the skin has the largest stress and acceleration under impact, while the cortex and core stresses are minimized due to their viscoelastic response. Here, viscoelastic deformation and energy dissipation are important in reducing localized damage.

3.6.1 Relationship between Impact Toughness and Damping Behavior

Ranganathan et al. [176] investigated the relationship between impact toughness and viscoelasticity of polypropylene (PP)-jute composites with the use of viscose fiber (rayon fiber from regenerated cellulose). Charpy impact testing and low-velocity drop-weight impact tests were used to determine impact resistance and dynamic mechanical analysis was used to quantify viscoelasticity. The addition of viscose (PP-J30-V10) increased the Charpy impact strength from 3.2 kJ/m^2 to 7.5 kJ/m^2 and decreased the residual impact velocity from 1.7 m/s to 0.9 m/s (Figure 3.4(G,H)). Images of the front and back sides of the low-velocity falling-weight impact tests show less damage for the composite with added viscose. Dynamic mechanical analysis showed that the addition of the viscose fibers decreases the storage and loss modulus softening the material and making it more deformable and increases the loss tangent (tan(δ)=loss modulus/storage modulus), which describes the dampening behavior. The addition of the viscose fibers improved impact performance by effectively dampening energy. While there is much more to take into consideration, such as microstructure and interfacial properties, this study sheds light on how viscoelastic response can influence impact toughness by improving the materials dampening ability.
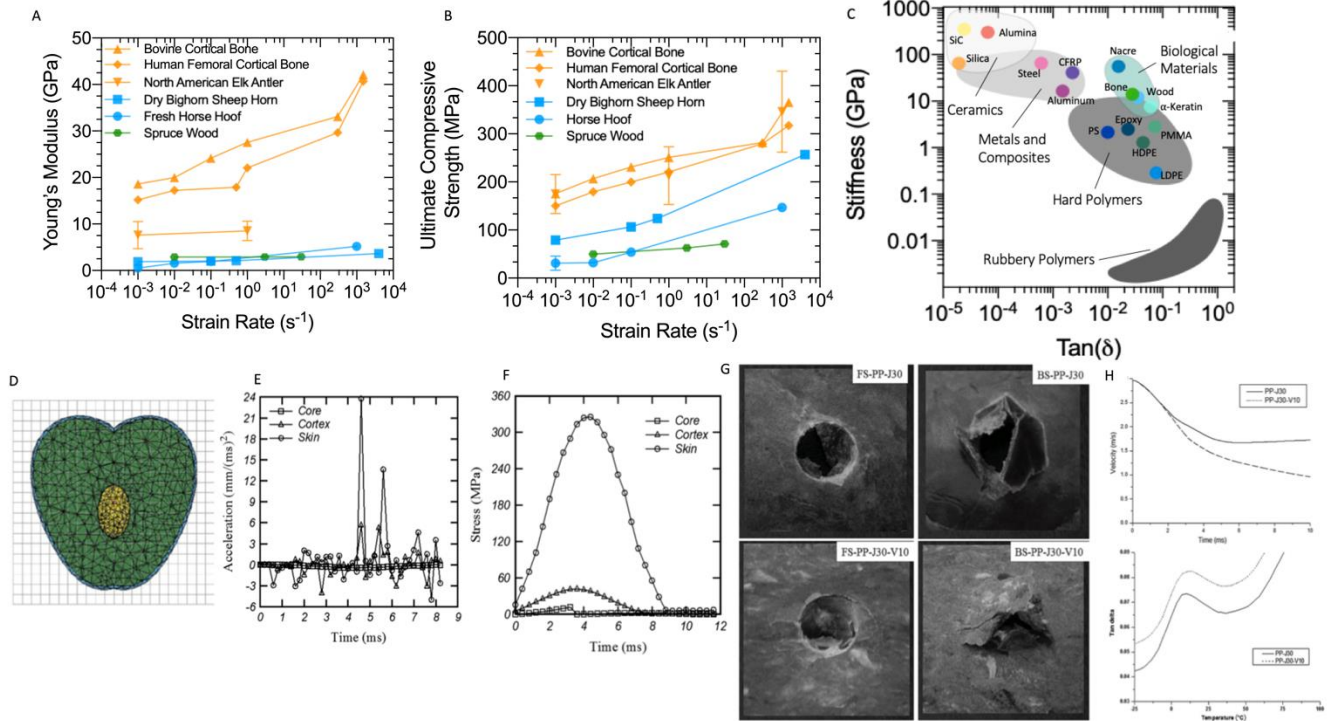
Figure 3.4 Inelastic behavior of biological materials. A) Strain-rate dependence with respect to Young's Modulus for representative biological systems. Hydroxyapatite/collagenous systems of bovine and human cortical bone and elk antler (yellow), keratinous systems of bighorn sheep horn and horse hoof (blue), and cellulose/hemi-cellulose/lignin system of spruce wood (green) B) Strain-rate dependence with respect to ultimate compressive strength. C) Ashby plot of stiffness and damping ($\tan(\delta)$) which indicates the enhanced performance of biological materials compared to engineering materials. D-F) FEA of apple layers under impact loading (1 m/s).D) Organization of the three layers: skin (light blue), cortex (green), and core (yellow). E) Acceleration with respect to time of the three layers. F) Stress with respect to time of the three layers [52]. G-H) Addition of viscose fibers to PP-jute impact response and viscoelasticity. G) (Top) Front side (FS) and back side (BS) of PP-jute after low-velocity falling-weight impact test. (Bottom) Front side (FS) and back side (BS) of PP-just added viscose after low-velocity. H) (Top) Impact velocity with respect to time. Indicating how the addition of viscose fibers decreases residual velocity. (Bottom) Tan delta with respect to temperature. Indicating how the addition of viscose fibers increases the damping ability [176].

3.6.2 Relationship between Impact Toughness and Damping Behavior

Ranganathan et al. [176] investigated the relationship between impact toughness and viscoelasticity of polypropylene (PP)-jute composites with the use of viscose fiber (rayon fiber from regenerated cellulose). Charpy impact testing and low-velocity falling-weight impact tests were used to determine impact resistance and dynamic mechanical analysis was used to quantify

72

viscoelasticity. The addition of viscose (PP-J30-V10) increased the Charpy impact strength from 3.2 kJ/m^2 to 7.5 kJ/m^2 and decreased the residual impact velocity from 1.7 m/s to 0.9 m/s (Figure 3.4 (G,H). Images of the front and back sides of the low-velocity falling-weight impact tests show less damage for the composite with added viscose. Dynamic mechanical analysis showed that the addition of the viscose fibers decreased the storage and loss modulus softening the material and making it more deformable and increased tan(delta) which describes the dampening behavior. The addition of the viscose fibers improved impact performance by effectively dampening energy. While there is much more to take into consideration, such as microstructure and interfacial properties, this study sheds light on how viscoelastic responses can influence impact toughness by improving the materials dampening ability.

3.7 Current Engineered Impact Resistant Materials

There is an increasing demand for lightweight materials and structures with high energy absorption capacity in automotive, naval, aerospace, construction, defense, personal protection, sports, and other industries. Engineered materials, such as steels and other alloys (titanium, aluminum, magnesium) and composites are being continuously developed, with performance tailored to crashworthiness, internal damping, and improved crack resistance. Also, designs often combine different classes of materials to achieve superior performance. The Chobham armor is a splendid example of a multi-component system designed to resist defeat by shaped charges, high explosive anti-tank rounds, and kinetic energy penetrators [177]. The armor is composed of ceramic tiles encased within a metal framework and bonded to a backing plate and several elastic layers. Thus, it contains ceramic, metal, polymer, and composite elements. Many other current technological applications and challenges involve similar structural and material complexity.

Body armors have been used for centuries to protect against penetration by weapons and disperse impact energy [178]. Standard features of these armors are ballistic fibers which are woven in two- or three-dimensional arrays. Fiber architectures, including their density, stiffness, and interfaces control the speed of stress waves and their dispersion [179]. Multi-layered systems absorb energy through interfaces. Shear thickening fluids have also been used to enhance friction and dampen waves [180–182]. High-performance fibers include synthetic choices (e.g., Kevlar) or natural fibers (e.g., cotton, wool, sisal, jute, silk). Natural fibers have high energy-absorbing capacity. Their other advantages include availability, cost-effectiveness, biodegradability, and environmental safety [179]. Highly effective designs in mediating impacts, are composite sandwich-like structures, as in the Chobham armor. The designs include a robust outer layer, soft-fill middle layer, and a plastic backplate. The outer sheet, usually made of ceramic, dissipates energy by brittle failure and fragmentation and deflects or damages the impactor. The core consists of a laminated composite which delaminates or a foam which deforms inelastically to absorb and dissipate energy. Metal (or composite) backing further dissipates energy by deforming plastically and contains armor's and impactor's fragments. Ceramics outer cores are made of alumina, boron carbide, titanium diboride, silicon carbide, and other high hardness materials [183]. Such sandwich designs are similar to a turtle shell or skull structure.

With the goal of reducing greenhouse gases and improving fuel efficiency, many have begun to investigate lightweight and sustainable energy absorbing materials. In the automotive industry, engineers are replacing steel with aluminum and magnesium alloys, composites, and foams [184]. The vital design consideration in designs of automobiles, trains, aircraft, boats, and ships is crashworthiness and penetration resistance. The energy of the impact needs to be dissipated in a controlled manner before it enters the passenger compartment. Composite materials and

plastics with synthetic and natural fibers as reinforcements are increasingly being utilized. Interest in natural fiber composites is growing due to environmental considerations and cost. Polymer-matrix composite materials are of particular interest to aerospace, automotive, naval, defense, and wind power industries also due to their high strength/stiffness to weight ratio. Composites are reinforced with fibers in various forms, such as short fibers, long fibers, and mats, with filler sizes ranging from microns to nanometers. The properties of composites depend on properties of matrix and fillers, filler shape and arrangement, interfacial bonding, and size of fillers. Polymer-matrix composites have excellent energy absorption characteristics due to their viscoelastic properties and various energy dissipation mechanisms. The damage mechanisms include delamination, matrix cracking, and fiber/yarn breakage. Drawbacks are that such internal damage degrades the material properties and reduces the load-carrying capacity of the structure [185]. Thus, more damage-tolerant composite materials are needed for high end and multi-use applications.

Nanocomposite materials, which are composites with nano-sized fillers, can have superior performance to traditional composites with micro-sized fillers [186]. Much larger interface surface area of nanocomposites provides enhanced energy-absorbing mechanisms in the form of interfacial slipping and debonding. Also, local properties and interfacial interactions are altered since the nanofiller size is of the same order of magnitude as molecular structure of a polymer, leading to additional toughening mechanisms [187]. Nanocomposites can reach higher strength and strain to failure than composites with micron-sized fillers [188]. Mineralized biological materials such as bone and enamel, which are examples on natural nanocomposites, similarly achieve high stiffness/strength and toughness. Nanofillers have also been added to composites to enhance matrix-fiber bonding and strengthen interfaces between plies in laminated composites, leading to

composites with hierarchical structures [189–191]. Hierarchical structures are one of the key characteristics of biological materials contributing to their robust properties.

The construction industry utilizes concrete, which is the most widely used material [192]. Concrete structures serve under conditions of frequent or occasional impact loads (winds, waves, blasts). Examples include airfield runways subjected to dynamic aircraft landing forces, buildings exposed strong winds and earthquakes, offshore structures subjected to waves, protection barriers, and dams. Conventional concrete has limited deformation and low energy-absorption capacity, which poses a challenge to the safety of these structures under impact loading conditions [193]. Thus, high-performance fiber reinforced concrete that can absorb energy has been utilized. Ongoing research addresses various energy absorption components to optimize the impact resistance of concrete. For example, granulated rubber particles added to concrete improved impact resistance of concrete [194].

Synthetic cellular materials such as honeycomb-like materials made of parallel prismatic cells or closed-cell random foams are utilized in automotive and aerospace industries for energy absorption due to impact. Polymeric foams, such as Styrofoams, are used for packaging. Foams are also used for thermal insulation, structural functions, buoyancy, and other applications such as filters, water repellent membranes, antistatic shields, and others. Foaming allows a broader range of properties. Foams allow designing lightweight and stiff components such as sandwich panels, portable structures, and floating devices. Low thermal conductivity of foams yield cheap thermal insulators, low stiffness makes them ideal for cushioning, low strengths, and large compressive strains give energy absorption [195,196].

Various cellular materials' architectures are being explored, ranging from honeycomb to truss-like structures, to auxetic structures with unusual properties (e.g., negative Poisson's ratio),

not achievable by traditional materials. Functionally graded materials (FGM), which spatially changing composition and structure (e.g., porosity) are being tailored for desired performance [197]. Applications include energy-absorbing structures, heat exchangers, optoelectronic devices, and medical implants for automotive, aerospace, medical, and other industries. Advancements in additive manufacturing provide freedom in their design and facilitate their manufacture. Compared with multiphase composites, FGMs have properties changing less abruptly, which helps to minimize stress concentrations, hence improving the durability of load-bearing structures. Porosity graded lattices have shown excellent energy absorption characteristics, making them candidates for various technological applications, particularly for multifunctional structures and devices [198–203]. Functionally graded structures are found in many impact-resistant biological materials, including bone, articular cartilage, and hoof wall.

Impact-resistant materials and structures are desired in various technological applications. The current state-of-the-art is addressing these pressing technological and societal needs, but it has limitations. Bioinspiration offers a multitude of ingenious ideas on designs of new, highly impact-resistant materials. Nature has masterfully created intricate architectures, but engineers have a much more extensive range of starting materials to utilize. Bioinspiration, combined with advancements in materials synthesis, manufacturing, and computational modeling (e.g., topology optimization), opens numerous exploration opportunities. These attributes make it a fertile area for new designs and material discovery.

3.8 Conclusions

Through analysis of successful impact-resistant biological systems, clear trends in structural arrangement emerge. This study has led to a classification of impact-resistant design elements in biological materials into sandwich, layered, sutured, tubular, and gradient structures.

This study has also explored ubiquitous traits of biological materials that are vital factors for impact resistance including hierarchical, composite, porous, interfacial, and viscoelastic/viscoplastic characteristics.

The most common deformation mechanism among biological materials subjected to low-velocity impact is delamination at interfaces at different structural scales, where kinetic energy is converted to free surface energy. Densification and collapse of tubules or other pores to generate strain energy is another predominating mechanism. Table 3.2 summarizes these biological systems, their structural elements, impact energies, and deformation mechanisms reviewed here. While many biological systems have been studied under the impact, it is not easy to de-couple the contributions of their individual structural elements.

Table 3.2 Summary of Impact Resistant Biological Systems . Sandwich (Sw), Tubular (T), Layered (L), Suture (Su), Gradient (G), Hierarchical (H), Composite (C), Interface (I), Porous (P), Viscoelastic/Viscoplastic (V)

Biological System	Impact Velocity (m/s)	Impact Energy (J)	Design Elements	Failure Mechanisms	Reference
Pomelo	14	490	Sw, L, G, H, C, V, I, P	Densification of pores, viscoelastic dampening, strain energy storage	[53]
Coconuts	19	250	Sw, L, G, H, C, V, I, P	Fiber stretching, densification of pores	[53,55]
Wood	40	4,300	Sw, T, L, G, H, C, V, I, P	Delamination, fiber bending and pullout, helical unwinding	[12,94]
Horse hooves	2.2	4,800	Sw, T, L, Su, G, H, C, V, I, P	Delamination, tubule buckling and collapse,	[26,78,100,79–82,96–99]
Horn	9	4,600	Sw, T, L, G, H, C, V, I, P	Delamination, tubule collapse, densification	[25,26,76,83,104]
Elk Antler	11	--	L, H, C, V, I, P	Delamination	[83]
Pangolin scales	--	--	L, S, H, C, V, I, P	Delamination, fracture, brittle failure,	[29]
Tendons and Ligaments	--	--	H, C, V, I, P	Transmit tensile loads, sliding and delamination, viscoplastic	[106,109,110]
Cartilage	--	--	L, G, H, C, V, I, P	Fluid pressure gradients, viscoelastic/viscoplastic	[106,111,113]
Bone	--	--	Sw, T, L, G, H, C, V, I, P		[106,114–119]
Turtle carapace	--	--	Sw, L, Su, G, H, C, V, I, P	Compaction pores,	[46,49,120]
Human skull	--	--	Sw, L, Su, G, H, C, V, I, P	Densification zone, pore collapse,	[42,44,121]
Woodpecker skull	7	0.6	Sw, H, C, V, I, P	Dampening, hyoid apparatus stress attenuation	[122–128]
Woodpecker beak	7	0.6	Sw, Su, L, H, C, V , I, P	Shearing of wavy keratin scales, densification pores, penetration resistance	[163]
Nacre	--	--	L, H, C, V, I, P	Brittle failure	[15,83,204,205]
Conch	--	--	L, H, C, V, I, P	Splintering, inter/intra-lamellar fracture	[11]
Dactyl club of the mantis shrimp	23	1.5	L, Su, G, H, C, V, I, P	Crack deflection	[60,129]

The grand challenge is to develop, from the analysis of biological structures and by classifying the fundamental mechanisms of bioinspired impact-resistant designs through advanced manufacturing techniques, appropriate mechanical testing and modeling. The generation of tunable designs via geometry and material properties allows for the investigation of how these structural elements deform, absorb, and dissipate impact energy. Through the use of modeling, many of these elements are shown to avoid catastrophic failure through stress attenuation and redistribution. These bioinspired design elements, their energy-absorbing mechanisms, and tailorable designs are summarized in Table 3.3.

Table 3.3 Summary of impact resistant design elements and material properties

Impact Design Element/Material Property	Energy Absorbing Mechanisms	Tailorable Designs	Reference
Hierarchical	Each layer works synergistically for an enhanced overall effect. Any of the energy absorbing mechanism detailed below can be found across multiple levels.	Increasing hierarchical ordering, incorporation of multiple structural elements, and length scale	[6,34,35]
Sandwich	Fracture and wrinkling in the top face; core buckling, densification, and shearing; viscoelastic dampening, strain energy storage	Face thickness to core thickness ratio, geometric cell structure of core, addition of fluid to the core, gradient in density and cell size	[130–135,137–140]
Tubular	Buckling, collapse, delaminating, crack deflection	Size, shape (circular vs elliptical), volume fraction, addition of reinforcing layer, gradients in density and size, loading direction	[50,136]
Layered	Microbuckling, delamination, crack deflection, shearing between layers, microcracking	Lamellar arrangement (layered, hexagonal concentric, rotated plywood etc.), geometry of the interface (wavy)	[61,64,141,142,144,145,147–150]
Gradient	Fracture energy, crack deflection, localized pore collapse	Continuous gradient, step-wise gradient, porosity gradient,	[151–160]
Suture	Attenuate impact stress, Reduction of pressure waves through the conversion of compression to shear,	Geometry of suture (sin wave, triangular, trapezoidal), Degree of waviness (Amplitude, wavelength, frequency), loading direction, additional hierarchies	[41,166,167]
Viscoelastic and Viscoplastic	Viscoelastic and viscoplastic deformation, vibrational dampening	Ratio between elastic and viscous response, degree of hydration, temperature	[12,52,173–176]

3.9 Future Directions

Development of impact-resistant materials remains an enterprising challenge that is strongly dependent on two fronts: (1) understanding structure-composition-property relations accompanied by a sufficient database for tailorable design and optimization and (2) use of advanced manufacturing techniques to accomplish design requirements.

Here we suggest details that are important to achieving these two facets.

- **New manufacturing techniques**
  - New developments in additive manufacturing accounting for complex bio-inspired architectures. The needs include printing of a wider range of materials, including multiple materials, achieving sufficient resolution and printing flexibility to manufacture hierarchical and composite structures.
  - New hybrid systems, combining more than one manufacturing technique to create new complex structures, with added flexibility.
  - Incorporation of biological materials, which achieve such excellent properties, into synthetic components to obtain new bioinspired materials.
  - Creation or implementation of new synthesis methods to create new materials.
- **Establishment of relationships between quasi-static and dynamic testing and material and structural responses**. While not shown here, there have been extensive studies on the quasi-static response of these biological materials with an attempt to explain what is happening dynamically. To what extent can quasi-static results be extrapolated to the dynamic regime?
- **Advancements in testing and modeling of biological and bioinspired materials under dynamic loads.** More impact testing and modeling of biological materials and bioinspired

designs is needed. Our review shows that there is limited testing of various structural elements. For example, there has been very limited studies on the effects of tubules on impact resistance, even though they are important structures in horns and hooves, and they show impressive impact resistance. Another open topic is the role of interfaces in biological and bioinspired composites.

- **Investigation of the effects of multiple structural elements acting in synergy.** How does the interaction of multiple elements in one bioinspired architecture influence impact? For example, what is the effect of combined tubules and layered structures seen in the hoof and the horn?

- **Understanding of the role of self-healing and self-repair on impact-resistance of materials and structures**. Nature can repair materials if a catastrophic failure occurs, such as breaking of bone, for example. How does such repair play a role in the impact resistance? Can regrowth be another mechanism or structural feature contributing to material response? Biological materials might allow damage to initiate regrowth. How does such process work in time, and what can we learn from it and implement in future designs?

- **Understanding of the role of structural hierarchy on materials' impact resistance**. How does hierarchy of structures contribute to the impact resistance? How do the different length scales influence the impact resistance or biological materials? When designing future bio-inspired, impact resistant materials, what length scale is most important: nano-, micro-, meso-, or macro-?

- **Identification of design parameters that have the highest influence on the impact resistance of materials and structures.** Which impact-resistant structural design characteristics have the strongest influence on the impact resistance of materials and

structures? How strong can the contribution of material components be in comparison to the effects of structural designs?

- **Optimal use of materials and porosity.** How can one utilize porosity most effectively to mitigate high stresses, provide materials' resistance to loads, in particular dynamic ones?

- **Optimal use of fluids in the designs of impact-resistant materials.** How do fluids contribute to the impact resistance at different structural scales? How could fluid properties be tailored to achieve optimal impact resistance?

- **Creation and efficient utilization of databases for structure-composition-property relations for impact-resistant materials and structures.** Use of machine learning to guide designs of impact-resistant materials and structures.

- **Utilization of the concepts of computational materials design proposed in Materials Genome Initiative** [206] **to accelerate innovation and creation of the final products**. Creation of theoretical (analytical and numerical) models and make them available for research community to facilitate and accelerate new materials designs.

- **Creation of graphical charts to guide designs of new impact-resistant materials and structures**. Ashby diagrams or similar plots have been powerful tools to guide materials selection for various applications. However, very limited charts are available on properties linked to impact resistance, such as absorption energy.

- **Architectured, bioinspired materials and structures offer nearly unlimited possibilities of combinations of structural elements, specific dimensions, and materials choices**. How can such a large parameter space be captured effectively?

- **Preliminary research has shown that increasing the levels of hierarchy lead to improved impact resistance, but is there a limit to the effectiveness each added length**

scale? What are the tradeoffs of adding geometries on more length scales and at what point do faster impacts bypass the energy absorption mechanisms of these structures?

- **A handful of studies have examined impact induced stress waves within a biological material. However further research is needed to fully understand the role the structural features play in mitigating these wave effects.**

We listed above just some of the open possibilities, questions, and opportunities. The discussion here focuses on impact-resistant materials, but similar thinking applies to other classes of materials. These open scientific questions show nearly endless possibilities and present exciting opportunities for the discovery and creation of new materials. Materials play an integral role in the technological advancements of our society, with impact resistance having multiple important applications. Impact-resistant materials can be used for high-end applications (protection against meteorites in space, protective armors, and sports equipment) to lower end such as packaging. Additional considerations for designs could include sustainability and materials reuse and repair.

3.9 Acknowledgements

Chapter 4. The Multifunctionality of Keratin

Keratin is found in horns, hooves, whale baleen, and pangolin scales which are designed to resist dynamic loading. Lee et al. [83] performed impact tests on a gamut of biological materials

including abalone, elk antler, bovine femur, wood, armadillo carapace, as well as ram and steer horn and determined that the keratinous horns had the highest normalized impact strength. In fact, steer horns had an impact strength nearly ten times that of the inimitable abalone shell. However, a vast range of biological materials are composed of keratin. It is most commonly found in relatively soft integument such as hair, feathers, and nails and is an important constituent in skin. In these roles it does more than just provide mechanical stability, filling numerous other roles including reversible adhesive, thermal insulator, and hydrophobic substrate. Often times, engineers view natural materials as monofunctional, but this is simply not the case. To fully understand keratin's capabilities its multifunctionality in nature needs to be taken into consideration. This chapter will review the structure and properties of keratin and will discuss the many functions it plays in nature including its role as a mechanical component.

4.1 Structure and Properties of Keratin

4.1.1 Structure of Keratin

The term keratin originates from the Greek word 'kera,' which means horn. Historically, keratin denoted proteins extracted from modifications of skin such as horns, claws, and hooves. However, with an increased understanding of its structural and chemical characteristics, keratin now refers to all intermediate filament-forming proteins with specific physicochemical properties that are produced in any vertebrate epithelium [207]. These proteins form the bulk of cytoplasmic epithelial and epidermal appendageal structures (i.e., hair, wool, horns, hooves, and nails)[168]. They are also present inside cells as intermediate filaments, which provide structural stiffness, together with actin fibers and microtubules. The term "keratin" will be used to describe this material at the nanoscale (macrofibrils) and below. In contrast, "keratinous material" will be used to describe the larger-scale structures that are composed of these keratin fibers.

Keratins are broadly classified as having either α- or β- ultrastructures (Figure 4.1). Typically, mammalian keratin is found in the α-keratin form, while avian and reptilian keratins are β-keratin types; however, one mammal, the pangolin, is known to have both α- and β-keratin domains in its scales [29]. Like all biological materials, both α- and β-keratinous materials form hierarchical structures with geometries ranging from the atomic scale to the macroscale, as shown in Figures 4.1 and 4.2. Both α- and β-keratin are built from amino acids at the atomic level. In α-keratin, the amino acids form a right-handed α-helix secondary protein structure stabilized by hydrogen bonds [208–212]. These protein structures, also referred to as polypeptide chains, are approximately 45 nm in length and form the basic building block of an intermediate filament at the sub-nanoscale. Two polypeptide chains twist together in a left-handed rotation to form a dimer, referred to as coiled-coil [213]. The dimers are also approximately 45 nm in length and have a diameter of ~2 nm. It is believed that the coiled-coil structure increases the stability of the filament compared to a single α-helix [214]. Terminal segments of the dimer constitute an amorphous head and a tail domain. Both the head and tail regions aid in the dimer's self-assembly. The two coiled-coil dimers then aggregate together to form a tetramer which bonds lengthwise (with disulfide bonds) to create protofilaments. Two protofilaments align to form a protofibril. Four protofibrils then connect to create an intermediate filament (IF) [215]. The IFs, which are ~7 nm in diameter for α-keratin, are crystalline and are embedded in an amorphous keratin matrix. Crystalline IFs and the amorphous matrix form IF-matrix composites, which act as a basic structure for macrofibrils (~400-500 nm in diameter). In literature, keratins are often considered short fiber-reinforced biopolymers consisting of an amorphous matrix and crystalline fibers (IFs)[216].

Like α-keratin, β-keratin is composed of amino acids at the atomic scale and has a comparable hierarchical order (dimer to protofilament to IF) at the sub-nanoscale. The most

significant difference, compared with a-keratin, is that β-keratin has a different secondary protein structure characterized by pleated β-sheets [217]. In β-keratins, the antiparallel peptide chains are positioned side-by-side to form a rigid planar surface. These surfaces are slightly bent with respect to each other, creating a pleated arrangement [216]. The planarity of the peptide bond and the lateral hydrogen bonding accounts for the formation of the pleated sheet [218]. Similarly to α-keratin, the β-sheet self-assembles into a dimer, which forms the basis of the distorted β-sheet (called a protofilament). Protofilaments align to form the β-keratin intermediate filament, which is ~3 nm in diameter. For β-keratin, the terminal sections of the polypeptide proteins wrap around the filaments to form the amorphous matrix. Besides the differences between the α- and β-keratin at the sub-nanoscale, both keratin types form similar hierarchical structures up to the nanoscale (Figure 4.2). At the microscale, keratinous materials' architecture diverges for different organisms to optimize their structures for their specialized functions.
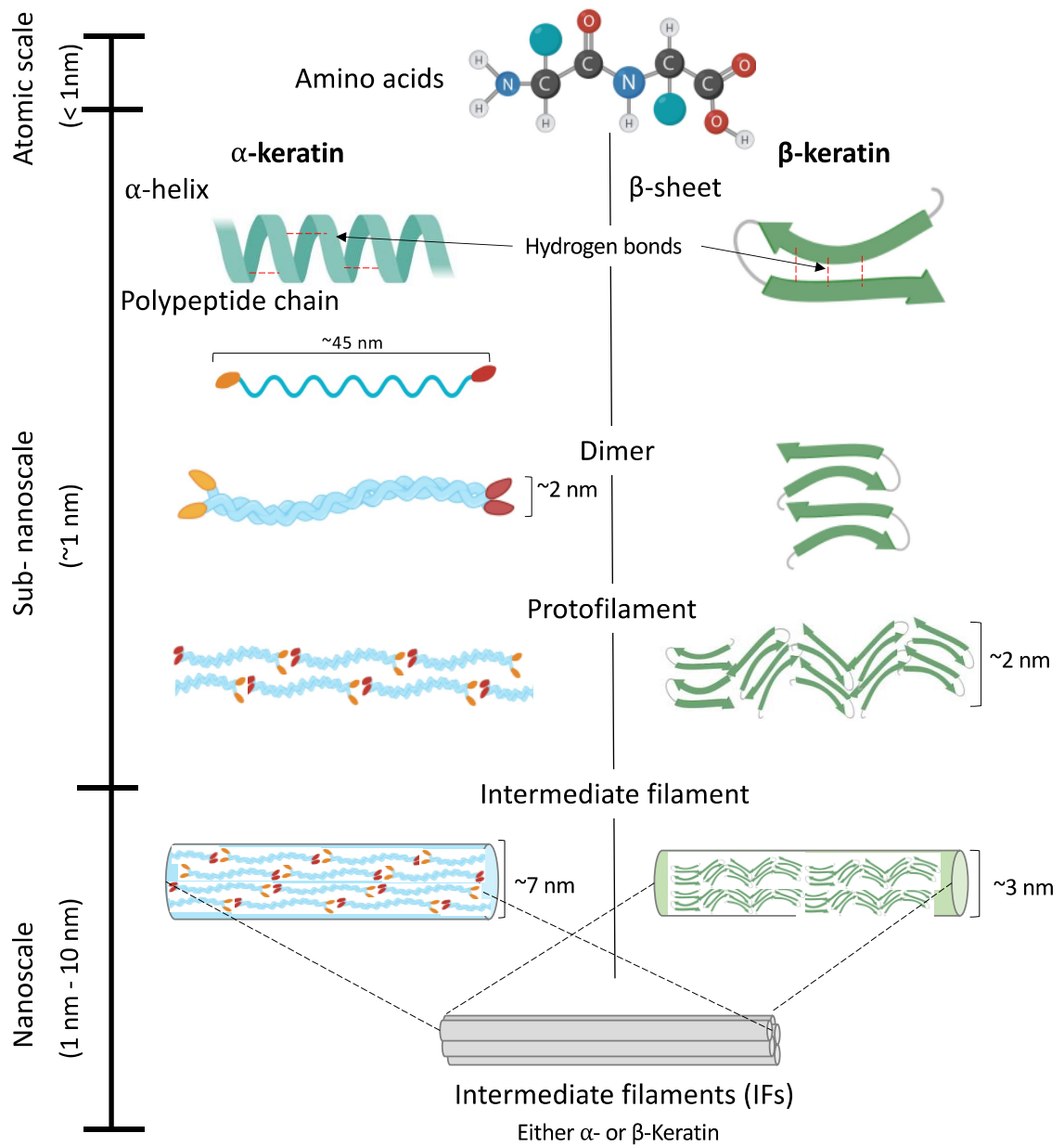
Figure 4.1 Comparison between the atomic-scale and sub-nanoscale of α- and β-keratin. Both α- and β-keratin, composed of amino acids, are similar at the atomic scale. The secondary protein structures are distinct for α (helix)- and β (sheet)-keratin at the sub-nanoscale. The subsequent polypeptide chains both form dimers which assemble into protofilaments and finally intermediate filaments. At the scale of IFs, both structures converge despite the differences in their diameters.
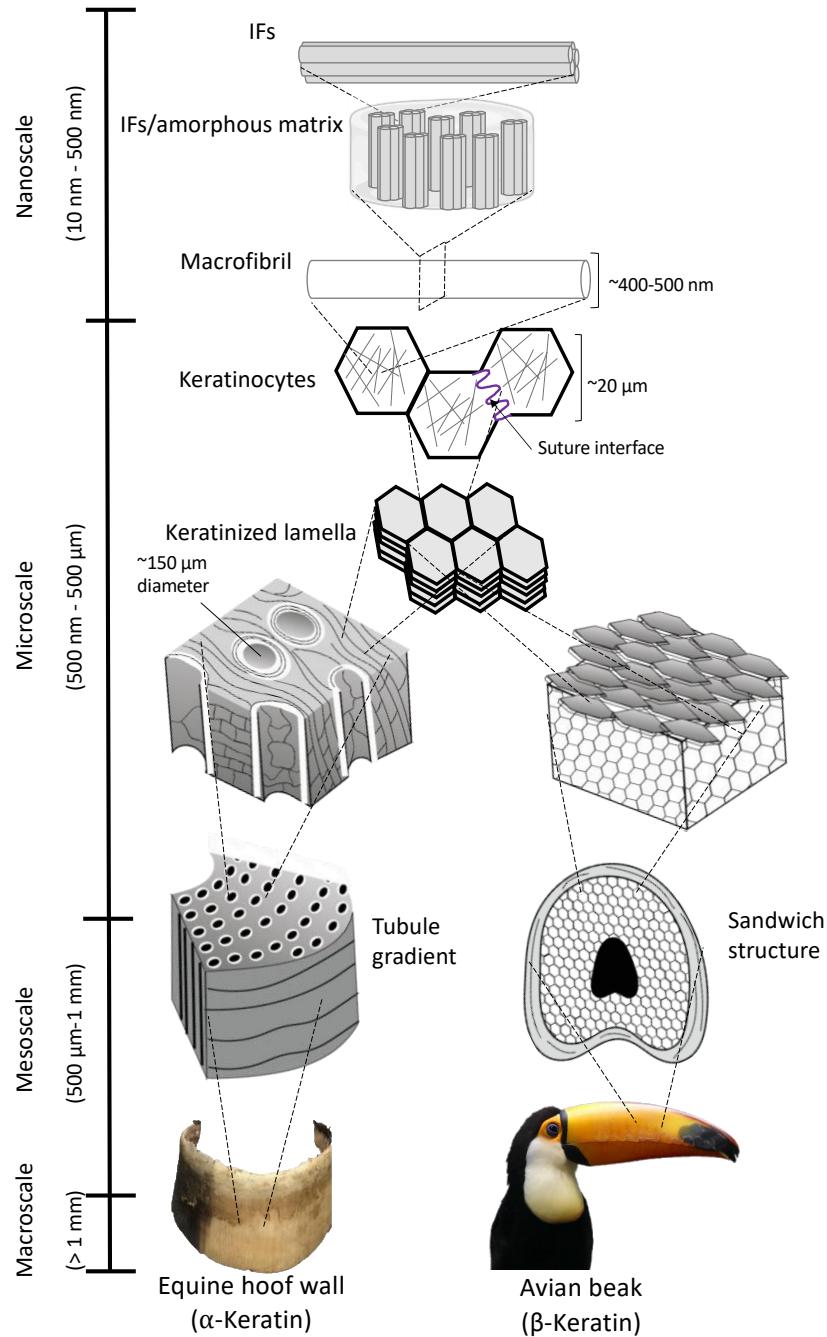
Figure 4.2 Once α and β keratin form IFs, their general structure converges again. The IFs embed in an amorphous matrix which then forms macrofibrils. These macrofibrils fill dead pancake-shaped keratinocyte cells, which stack on top of each other forming lamellae. From there, the structure of each keratinous system diverges to fulfil its specific function better. On the micro, meso, and macroscale, a vast range of designs and configurations are formed from the keratinous building blocks.

At the nanoscale, the IFs are embedded in an amorphous matrix in both α- and β-keratins. This IF-matrix nanocomposite structure subsequently groups to form macrofibrils (~400-500 nm in diameter) and then fibers (~6 µm). Variations in the IF alignment, volume fraction, orientation, and matrix properties account for the wide range of mechanical properties of keratin-based structures. Keratinocytes are the once-living cells that are filled with keratin fibers. Their formative boundaries encapsulate the orientation and can vary across organisms or locations within a specific organism. When stacked together, the keratinocytes form a layered structure at the microscale due to their inherent directional growth from the follicle. In some systems such as the horse hoof wall, woodpecker beak, pangolin scale, and bighorn sheep horn, the interface between neighboring keratin cells exhibits a wavy sutured morphology. Through their layered growth, keratin cells form laminated sheets. The hierarchical structure of many biological keratinous systems begins to diverge at this scale. This layered structure is a defining feature of keratin-based materials. The laminated sheets organize themselves into different arrangements at the mesoscale. For example, the laminated structure in some horns and hooves is characterized by embedded microtubules, whereas the lamellae in hair cuticles have an overlapping configuration. Even more so, at these larger length scales, some keratinous materials begin forming cellular solids such as the foamy centers of quills and feather shafts. The divergence of the structure at the meso and macroscales for each organism will be explained in greater detail in Section 2.

There are also morphological differences among different keratinocytes: in hair, they are elongated along the axis (one dimension much larger than the other two); in pangolin scales and many other places, they are pancake-shaped, with one dimension much smaller than the other two. There seems to be a preponderance of suture structures at the mesoscale. The surface of a cortical cell in human hair after tension exhibits a suture-like structure, which increases the contact area of

cortical cells and therefore increases the adhesion between adjacent cells and decreases splitting of hair along the axis. This suture structure is also found in the pangolin scale. It has a width between 250 and 450 nm and creates an interlocking effect. This structure has been studied and generalized by the Ortiz group [219–223]. Figure 4.3 shows the suture structures in hair and pangolin scale.
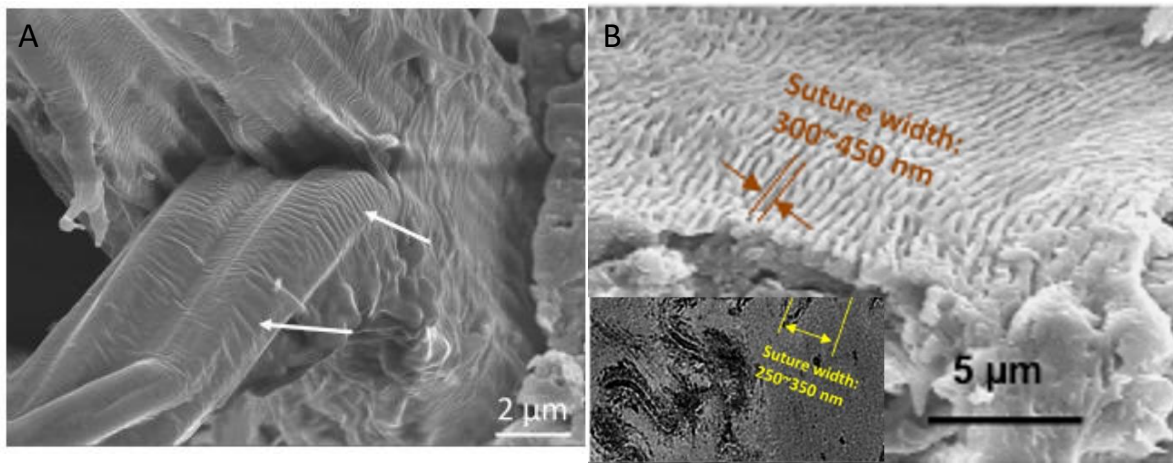
Figure 4.3 Intercellular suture structures. (A) Human hair. Reproduced with permission [224]. Copyright 2017, Elsevier. (B) Pangolin scales. Reproduced with permission [29]. Copyright 2016, Elsevier.

To fully capture the hierarchical structure of keratin, computational models have been developed for each length scale. Starting with the fundamental building blocks of amino acids, these models aim to analyze the mechanical properties and arrangement of molecules in IFs at the sub-nanoscale [214,225–227]. Chou and Buehler (2012) pioneered this effort by reconstructing heterodimers from an entire amino acid sequence of keratin proteins using molecular dynamics simulations. The geometric dimensions of the reconstructed dimer matched well with the experimental observations. Using this model, they compared keratin's mechanical properties with and without disulfide bonds and concluded that the disulfide bonds improve keratin's durability and strength [214]. This feature is similar to the one in elastomers, where vulcanization introduces

sulfur bonds between the chains and increases the performance markedly. Qin et al. (2009), from the same Buehler group, discussed the hierarchical structure of IFs and analyzed each hierarchical level's influence on the IF's mechanical properties. They divided the hierarchical structure of IFs at the atomic scale and sub-nanoscale (Figure 4.1) into additional eight hierarchical levels. Using molecular dynamics modeling, they concluded that each hierarchical level demonstrates a distinct deformation mechanism, which enables keratin to sustain prominent deformation at higher length scales (beyond the nanoscale) [225]. The dominant mechanisms at each hierarchical level and their description are summarized in Table 4.1. In another paper, Chou et al. (2015) demonstrated how information from atomic-scale models could be utilized to predict human hair's mechanical properties at the mesoscopic scale through a bottom-up approach [228].

Table 4.1 Key hierarchical levels and their corresponding mechanisms.

Length scale	Hierarchical structure	Key mechanism
Atomic scale	Amino acid ordering and hydrogen bonding	Hydrogen bonding forms at moderate temperatures and prompts formation of alpha-helices
Sub-nanoscale	Alpha-helix and Beta-sheet	Alpha-helical turns permit large tensile strains and extensibility due to uncoiling.
Sub-nanoscale	Dimer	Increased stability and resistance to mechanical deformation
Sub-nanoscale	Protofilament	Increased resistance to interfilament shear
Sub-nanoscale	Intermediate filament	Increased extensibility, stiffening, and superplastic properties
Nanoscale	IFs embedded in amorphous matrix	IFs provide rigidity while the amorphous matrix distributes the applied load
Nanoscale	Macrofibril	Increased rigidity and extensibility
Sub-microscale	Keratinocytes	Organization of macrofibrils by cell boundaries
Sub-microscale	Suture interface	Provides interlocking interface between neighbouring cells, enhances flexibility, and tailored stiffness.
Microscale	Keratinized lamella	Layered structure makes up the relative thickness of the material and distributes stress across the material. Allows for local flexibility and increases extensibility due to sliding of lamella.
Mesoscale	Dependent on material but can include tubules, sandwich structures, etc.	Dependent on structure. Tubules provide compressibility and crack deflection. Sandwich structures are lightweight yet stiff.

4.1.2 Mechanical properties of keratin

The polymeric nature of keratin lends itself to a wide range of mechanical properties that vary according to its amino acid composition, structure, and hydration level [97,168,216,229,230]. The amino acid sequence and corresponding residues dictate the availability of disulfide bridges. The amino acid cysteine has a thiol group which allows for a covalently bonded di-sulfide bond to be formed with another cysteine further along the chain and creates a fold in the protein. Chou and

Buehler (2012) showed that keratin's hardness is strongly correlated with the density of sulfur cross-links [214]. A low amount of sulfur indicates soft keratins (outer layer of skin, i.e., stratum corneum). In contrast, a high amount of sulfur leads to hard keratins (e.g., hair, nails, feathers, hooves) [214,231,232].

Based on the structural arrangement described in the previous section, keratin's amino acid chains can either curl into helices (α-configuration) or bond side-by-side into pleated sheets (β-configuration). The molecular arrangement associated with the alignment of IFs directly influences the mechanical properties of keratinous materials [216]. The stress-strain curve of a typical α-keratinous material consists of three distinct regions: linear elastic region, yield region, and post-yield region, as shown in Figure 4.4A. Figure 4.4A decomposes the contributions of both the IFs and the matrix to the properties of α-keratin fibers. The linear elastic region extends approximately up to a 2% strain. In this region, the stress increases linearly with an increase in strain [233]. Beyond 2% strain, the keratinous material enters the yield region in which it reaches critical stress beyond which the coiled-coil region of the α-keratin helices begins to unravel into the β-pleated sheet structure exhibited by β-keratin [234–236]. As a result, the stress-strain curve exhibits a large plateau. X-ray diffraction studies have shown that microfibrils open at various points and increase in length during the conversion [237]. However, atomic-scale simulations have demonstrated that the structure of the dimer assembles in a specific sequence [214]. The low increment in stress in the yield region can be explained by the Ciferri model [238]. Ciferri proposed that the low increment in stress is due to thermodynamic equilibrium existing between α-and β-structures. The α- and β-keratins coexist in equilibrium at a constant stress value dependent on temperature but not on each state's relative quantities. The plateau region exists up to ~30% strain, beyond which the material enters the post-yield region, where the stress again increases with an increase in strain.

The rise in stress can be attributed to the coupling between the matrix and IFs. Even though the α-keratin continues to convert to β-keratin until 70-80% of strain, the matrix starts resisting deformation at ~30% strain and thus begins to bear additional stress. As a result, a sharp rise in tangent modulus is observed [238].

Several attempts have been made to capture the mechanical properties of keratin analytically. The most notable ones are the two-phase model proposed by Feughelman [239] and the Hearle-Chapman model [233,240]. The initial two-phase model of Feughelman was later modified to incorporate additional features of keratin. In this revised model, the keratinous material comprises two phases: C and M. Phase C denotes long water-impenetrable and relatively rigid cylindrical rods. These rods are embedded in a water-absorbing matrix called phase M. Phase C represents a coiled-coil part of the polypeptide chain in α-keratin. This phase has lower sulfur content to interact with water. Phase M consists of non-helical parts of α-keratin (like its head and tail) and matrix structure surrounding polypeptide chains. These parts have higher sulfur content and can absorb water, giving rise to viscoelastic behavior in keratin. According to this model, the initial region (named the linear elastic region by earlier, less complex studies) of the stress-strain curve for α-keratin can be represented by a spring and dash-pot model (Figure 4.4B) where a spring (with a spring constant of E_f) is in parallel with another spring (with a spring constant, E_M) and dashpot (with viscosity, η). The spring constant, E_f, represents Young's modulus of the crystalline phase and therefore does not depend on moisture content. The E_M and η represent the properties of a viscoelastic amorphous matrix dependent on moisture and temperature. As evident from the spring-dashpot model, the non-linear viscoelastic behavior of keratin in the Hookean region is due to the matrix phase described as a weak "gel" structure [241]. As the gel structure is extended at a

fixed rate, the bonds progressively break down. If the extension is ceased, the broken bonds re-

form rapidly in equilibrium.
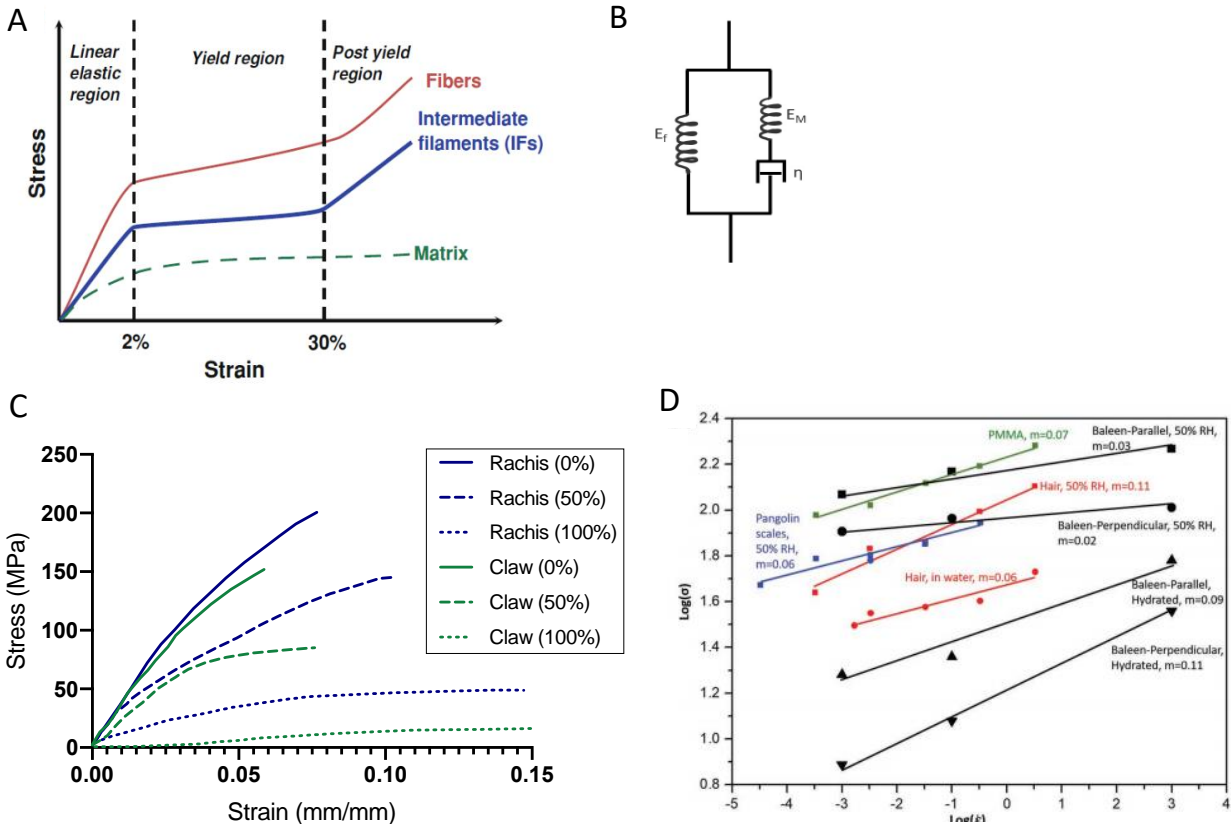
Figure 4.4 Mechanical properties of keratin and keratinous materials. A) Idealized stress-strain curve of α-keratin showing three distinct regions. This is a representative curve and does not take into account factors like viscoelasticity or structural deformation mechanisms. Still, it does highlight the plateau yield region and the range of these three phases of deformation. Reproduced with permission [216]. Copyright 2012, Springer. B) Spring and dashpot configuration of the two-phase model that is used to incorporate the hydration-induced viscoelasticity of the amorphous matrix. C) Tensile stress-strain curves of bird feathers and claws test at different humidities at a strain rate of 0.11 min⁻¹. Adapted with permission [242]. Copyright 2004, Springer. D) Effect of strain rate on biopolymers' strength (whale baleen, hair, pangolin) and the synthetic polymer PMMA. Reproduced with permission [243]. Copyright 2018, Wiley.

In the yield region, the α-helices in the crystalline phase C are extended to the fiber

structure's total length. As a result, they start unfolding to β-units at a nearly constant stress,

governed by a thermodynamic equilibrium between α- and β- units. Most of the force applied to

the keratinous material in this region is resisted by the IFs, whereas phase M resists only a small force that is nearly constant. The viscosity contributes to the time constant for the relaxation and provides resistance to folding and unfolding of α-helices.

When the α-helices transition to β-pleated sheets in the yield region, they extend in length. Figure 4.5A shows a full period of the α-helical structure consisting of the atomic sequence (-CCNCCNCCNCC-); its length is 0.52 nm. When this helix is fully rectified and extended (Figure 4.5B), its length becomes 1.39 nm. However, the assembly of polypeptides is such that a folded β-pleated sheet is formed; this reduces the length to 1.2 nm. Thus, the nominal strain of the α to β be calculated and is equal to 1.34. However, it is rarely achieved experimentally, and other processes are thought to take place.
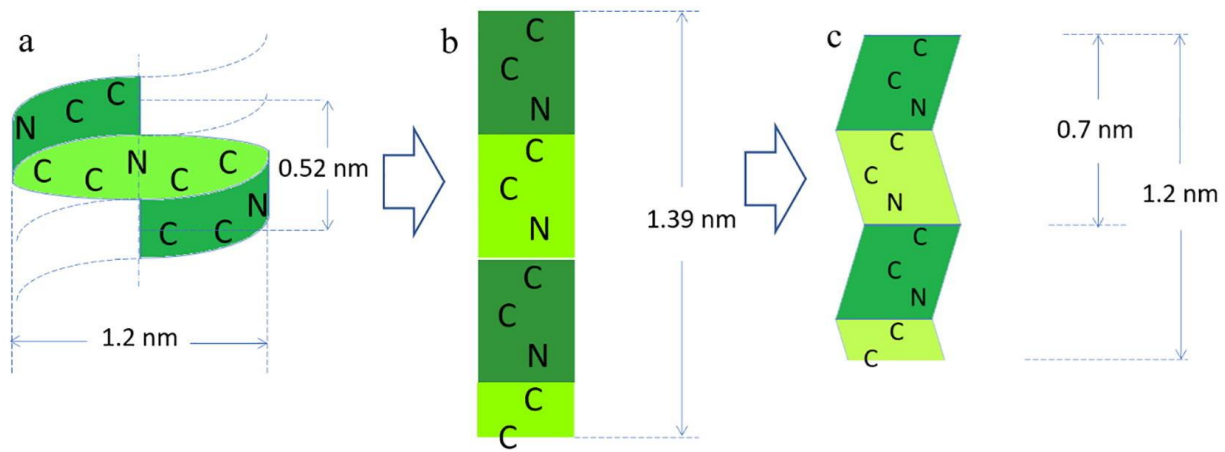
Figure 4.5 Full period (one rotation, corresponding to -CCNCCNCCNCC-) for α-helix (0.52 nm) and corresponding distance for β-pleated sheet (1.2 nm). The stretched β configuration with the same chain (-CCNCCNCCNCC-) has a length of 1.39 nm. The formation of pleats reduces the length to 1.2 nm. The theoretical strain corresponding to full transformation is equal to 1.34; this is seldom achieved in real cases. Reproduced with permission [224]. Copyright 2017, Elsevier.

At a larger spatial scale, the IFs parallel to each other start moving closer together, jamming the still unfolding α-helices against the matrix phase, which consists of globular matrix proteins. Due to the increase in length when the α-helices transition to β-pleated and the jamming of proteins

in the matrix, further extension of the material distorts matrix proteins. As a result, the matrix starts carrying more load resulting in an increase in stress with strain. The above is the essence of the Feughelman model.

Chapman [233] and Hearle et al. [240] independently extended the two-phase model to explain the zonal unfolding of α-helices in microfibrils by considering the effect of mechanical coupling between the fibril and matrix. They assumed that the single fibril is of infinite length. The matrix never enters the yield region and therefore behaves elastically as it bears only a small portion of the total force. Based on this model, they derived the equations to predict stresses and strains in different regions as shown below. We use subscripts f and M for the fiber and matrix, respectively.

Hookean region: $E_M \ll E_f$ thus, the stress is taken by the fibril

$$\sigma = E_f\varepsilon$$

At the yield point

$$\sigma = \sigma_c \text{ and } \varepsilon = \varepsilon_c = \sigma_c/E_f$$

Yield region: (once the transition of α-fibrils has started)

$$\varepsilon = \sigma/E_f + \varepsilon_2$$

$$\sigma_c = \sigma_e + E_M\varepsilon_M$$

End of post yield region

$$\sigma_0 = \sigma_e + E_M\varepsilon_b$$

$$\varepsilon_0 = \sigma/E_f + \varepsilon_b$$

100

where

$$\frac{1}{E_p} = \frac{1}{E_f} + \frac{1}{E_M - (\sigma_c - \sigma_e)/(2\varepsilon_b)}$$

E_M is Young's modulus of the matrix, E_f is an initial fibril modulus, σ and ε are the total stress and strain, respectively, in the material. σ_c is equal to the critical stress at which the unfolding of α fibrils begins. ε_2 is the strain due to unfolding of α fibrils, σ_e is the equilibrium stress for the transition between α to β fibrils, ε_M is the strain in the matrix, ε_b is the strain associated with α to β transition, and E_p is the effective modulus in a post-yield region. The detailed derivation for the above equations is given in Hearle and Chapman [233,240].

In general, α-keratin has a high tensile fracture strain, primarily due to the stretching and sliding of the polymer chains across many length scales. The hagfish slime threads have the highest tensile breaking strain of 2.2 when tested in seawater [244]. Despite large tensile breaking strains, there are significant variations in tensile strength across species due to structural orientation, hydration, and composition [244]. The tensile strength ranges from 2 MPa in the stratum corneum to 225 MPa in human hair to 530 MPa in the hagfish's dry slime threads. Mechanical properties of keratinous materials also depend on the orientation and volume fraction of intermediate filaments and hydration of the material: greater alignment in IF results in higher tensile strength. Thus, the tensile strength of human hair (where all the IFs in the cortex are aligned with the hair axis) is higher than that of human nails (where there are three layers in which the IFs are oriented at 90 degrees to each other).

The degree of hydration dramatically influences the mechanical properties of keratin. Increasing humidity and water content decreases the stiffness, strength, and hardness [28,168,245,246] This behavior, summarized in Table 4.2, is attributed to the interaction of water

molecules with the amorphous matrix, which breaks stabilizing hydrogen bonds and increases the mobility of the fibers within the matrix [247]. In equine hoofs, Young's modulus drops an order of magnitude between dry and hydrated conditions [82,97]. This increase in ductility in hydrated keratinous samples is associated with a higher tensile strain but lower tensile stress. Thus, hydration has a drastic effect on strength. The feather, for example, sees its tensile strength more than halved from 221 MPa to just 106 MPa when placed in 0% relative humidity (RH) environment vs. 100% RH environment [242]. These trends can be seen in Figure 4.4C, which shows the stress-strain curves of bird feathers (rachis) and claws under tension at different relative humidities. Additionally, the pangolin scale has been shown to exhibit a decrease in hardness with hydration, from 314 MPa to 148 MPa in dry and hydrated states, respectively [28]. Other systems like whale baleen, porcupine quill, horn, and claws also see drastic reductions in strength with increasing hydration.

Table 4.2 Mechanical properties of keratinous systems at various humidity levels. *% RH= % Relative humidity, perp. = perpendicular to longitudinal axis of the tubules, para. = parallel to longitudinal axis of the tubules.

Biological material	Humidity	Young's Modulus (GPa)	Strength (MPa)	References
Stratum corneum	10% RH	1	18	[248]
	100% RH	0.005	2	
Wool	0% RH	--	260	[249,250]
	65% RH	4.5	--	
	100% RH	2.5	180	
Quill	65% RH	2.7	146	[251]
	78% RH	1.9-2.3	61.3-167.9	
	100% RH	1.0	60	
Horn	50% RH	3.9	77	[104]
	Soaked in water	0.7	25	
Hoof	0% RH	14.6	--	[97]
	75% RH	2.63	38.9	
	100% RH	0.41	9.18	
Whale baleen	Ambient	1.8/3.1 (perp./para.)	80/116 (perp./para.)	[243]
	Soaked in water	0.1/1.1 (perp./para)	7/19 (perp./para.)	
	Soaked in water	1.2	30	[252]
Hagfish slime threads	Soaked in water	0.006	180	[244]
Feather	0% RH	3.7	221.0	[242]
	100% RH	1.5	106.3	
Beak	50% RH	1.3	47.5	[101,253]
Claw	0% RH	2.7	90.3	[242]
	50% RH	2.1	68.7	

Table 4.2 Mechanical properties of keratinous systems at various humidity levels. *% RH= % Relative humidity, perp. = perpendicular to longitudinal axis of the tubules, para. = parallel to longitudinal axis of the tubules. (Continued)

	100% RH	0.14	14.3	
Pangolin scale	50% RH	0.963	72.43	[29]
Snake epidermis	43% RH	3.42-4.73	--	[254]
Finger nail	0% RH	4.34	--	[255]
	55% RH	2.32	--	
	100% RH	0.47	--	
Hair	20% RH		~250	[256]
	50% RH	4.2	~175	
	Soaked in water		~165	
Gecko Seta	30% RH	3.7	262.5	[257]
	80% RH	2.13	237	

There are apparent variations in the mechanical properties of different keratinous systems. For example, the hoof, which has reinforced tubules, exhibits Young's modulus of 14.6 GPa at 0% RH, more than three times that of fingernails, claws, and feathers under the same humidity conditions. Even keratinous materials found in similar organisms, such feathers and claws, have noticeably different mechanical behaviors. These variations can also be observed in Figure 4.4C. These differences can result from deviations in both chemical composition (i.e., mineralization, degree of crystallinity, etc.) or structure (porosity, lamellar arrangement, fiber orientation, etc.)

Keratin is known to be highly strain-rate sensitive, which is related to its viscoelasticity and viscoplasticity, i.e., its time-dependent response [224,256]. This is typical behavior of polymers. Figure 4.4D shows the strength (s) versus strain rates ($\dot{\varepsilon}$) on a log-log scale for whale

baleen, hair, pangolin scales, and a synthetic polymer (PMMA); the similarity is evident. The strain rate sensitivities "m" (defined as $\frac{d(\log\sigma)}{d(\log\dot\varepsilon)}$) for biological materials (hair, pangolin, whale baleen) are comparable to those of PMMA, a synthetic polymer. In the case of whale baleen, the strain-rate sensitivity of the dry samples (m ≈ 0.02–0.03) is significantly lower than that of the hydrated ones (m ≈ 0.09–0.11). This difference is attributed to the hydrated specimens' increased viscosity, enabled by the water molecules penetrating the amorphous matrix and plasticizing it. In the dry specimens, the effect of the mineral phase becomes stronger.

The general trend for keratinous materials is that increasing strain rate increases stiffness and strength while decreasing the breaking strain [79,169,246,253]. Thus, most keratin materials undergo an elastic to ductile-plastic to brittle transition with an increasing strain rate, as was shown for the toucan rhampoteca [253] and pangolin scales [29]. This rate-dependent behavior has important implications for impact resistance, suggesting that these materials can withstand greater stresses under dynamic conditions and have different failure mechanisms than quasi-static conditions. The embrittlement at high strain rates is an important consideration.

Keratin is also one of the toughest biological materials, as seen in Figure 4.6 [168]. This characteristic is due primarily to its hierarchical structure. As demonstrated by Qin et al. (2009), different hierarchical levels can undergo distinct deformations that enable keratin to absorb larger amounts of energy before failure [225]. The matrix is primarily responsible for distributing the applied loads during large deformations while the fibers carry the most load and serve to arrest cracks. Some keratinous materials have optimized mesoscale features, such as tubules in horns and equine hooves, which enhance the material's toughness. Due to fiber orientation concentration and the presence of features like tubules along a specific direction, toughness is typically found to be anisotropic [80].

105
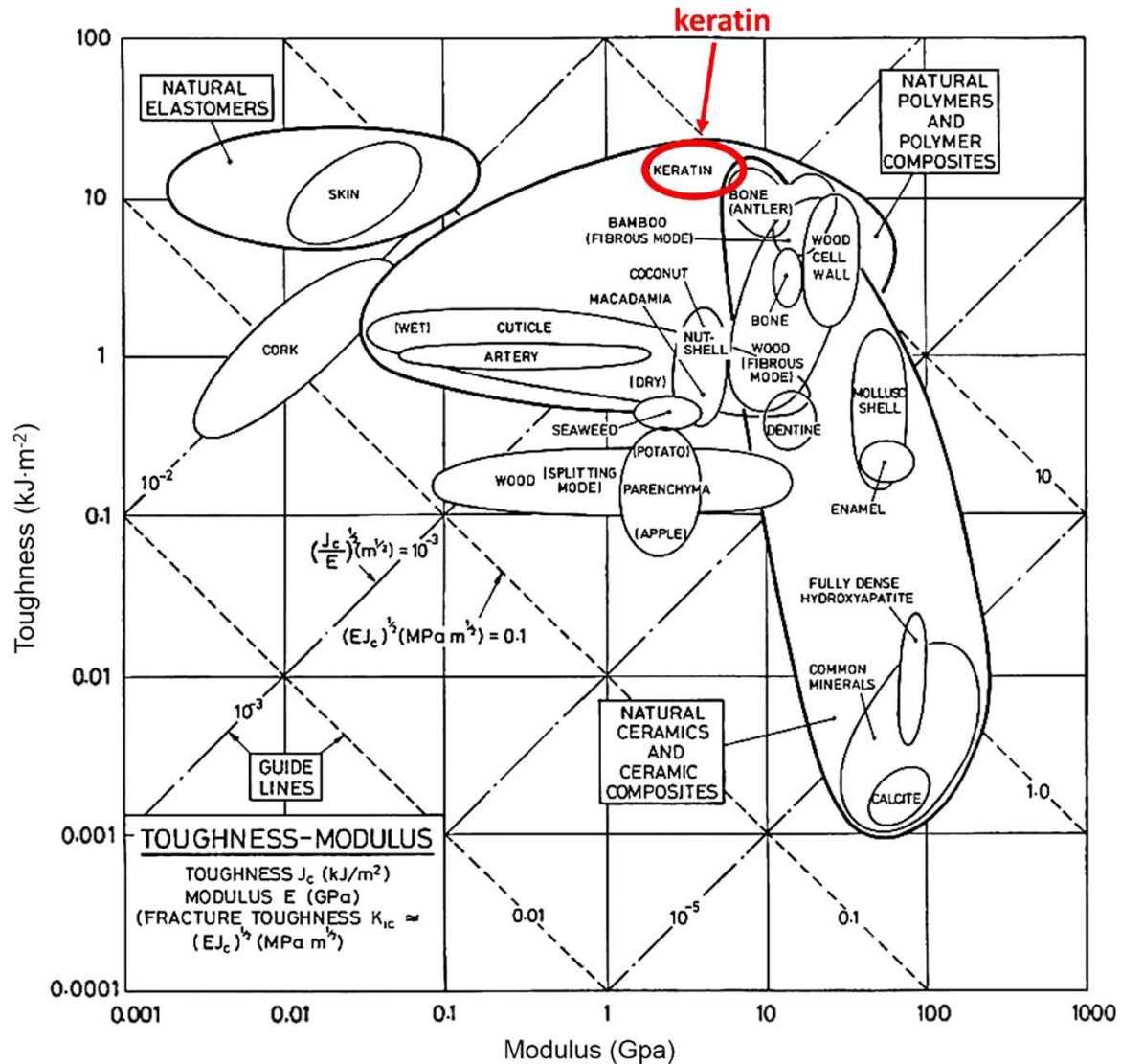
Figure 4.6 Ashby diagram demonstrating toughness vs. modulus for different biological material. Reproduced with permission [258]. Copyright 2016, Elsevier.

4.1.3 Hydration-induced shape recovery

Keratin systems often function as protective layers which undergo significant deformation. Many of these systems are permanent and cannot remodel or self-heal through biological processes after experiencing considerable deformation, such as in the bighorn sheep horn [259], feathers [260,261], and pangolin scales [262]. A solution to this lack of regenerative capacity is keratin's ability to undergo hydration-assisted shape recovery. This phenomenon was discovered by Liu et al. (2015b), who observed 98% shape recovery in compressed peacock tail feathers after seven

106

cycles of deformation to over 90% strain [260]. After the keratin is deformed plastically, the recovery process involves water infiltrating the amorphous keratin matrix, causing swelling, which forces the deformed crystalline regions of the IFs to regain their initial shape by breaking and reforming hydrogen bonds [259]. Also, the feather shaft was shown to have hydration-assisted shape and strength recovery. The feather shaft was subjected to bending and then allowed to soak in water for 24 hours, and after one cycle, it was found to recover its strength by ~80% [261]. The mechanism proposed by Sullivan et al. (2018) for the feather is shown in Figure 4.7 [261]. The Bighorn sheep horn was also shown to recover its shape by soaking in water after severe compression of 50% strain which was further assisted by the hollow tubules [259]. In a similar study by Liu et al. (2016b), the pangolin scale was shown to have hydration-assisted strength recovery after indentation, which simulated penetration-induced injury by a predator. The self-healing was attributed to the swelling of the keratin-based material allowing for an increase in flexibility of keratin fibers to reorientate and straighten [262].

The top sequence of Figure 4.7 shows the gradual restraightening of the feather shaft as it is hydrated. Plastic deformation causes permanent deformation of the amorphous matrix (bottom sequence), which is weaker than the IFs. The IFs undergo buckling on the compression side. Upon hydration, water molecules penetrate the amorphous matrix and cause swelling, which forces the crystalline IFs to straighten and realign. Upon drying, the matrix shrinks again, and the original configuration is established. These studies show that hydration actuates shape recovery in α-keratin and β-keratin, which is not surprising as both keratins have similar structures involving crystalline IFs embedded in an amorphous matrix.
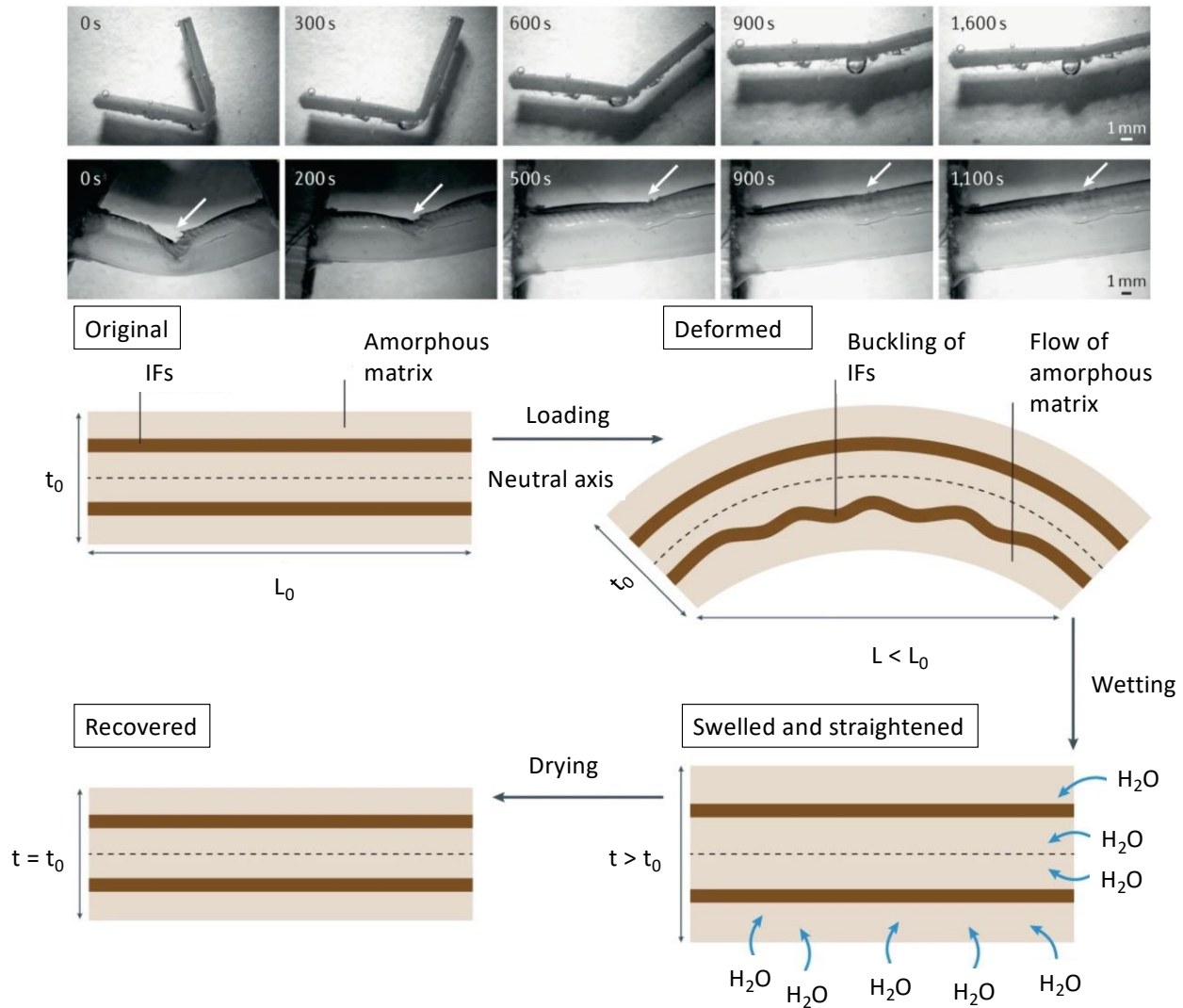
Figure 4.7 Reversible deformation of feather shaft induced by hydration; top: restraightening of a deformed feather with hydration and recovery of its initial shape; bottom sequence of events as the IF-amorphous matrix composite is first deformed and then hydrated. Adapted with permission [263]. Copyright 2021, Nature.

4.1.4 Thermal Properties

Another common function of keratin is to serve as a thermal insulating barrier in hair, wool, fur, and feathers, to name a few. Often the goal of these systems is to trap air pockets within the insulating layer. This method is very effective since air has an extremely low thermal conductivity of just ~0.0264 $Wm^{-1}K^{-1}$ [264]. As noted previously, the self-assembly process of natural keratinous materials has afforded some organisms with precisely controlled meso-, micro-, and

nanostructures. For thermal insulation, this ability has been utilized to generate lightweight systems that trap significant amounts of air with minimal material. Note that keratin by itself has a low thermal conductivity of just 0.19 $Wm^{-1}K^{-1}$. However, when arranged into low-density wool, the combined thermal conductivity is reduced to 0.03 W $m^{-1}K^{-1}$ [264]. Nature's ability to produce these intricate structures in abundance has made certain keratinous systems like feathers, wool, and fur some of humanity's most valuable thermal insulators to date. In humans, bipedalism concentrates exposure from the sun to the head, and this is exactly where capillarity is highest. The remainder of the body is only covered by vestigial hair, and this enables an increase in sweat glands, which enhances the ability of the body to regulate the temperature and has helped humans to develop an amazing ability to run for extended distances.

4.2 Bioinspired materials based on keratinous systems

Keratin is one of the most essential biopolymers found in nature, appearing in the integument of many vertebrates, as discussed in Section 1. Keratinous materials are especially intriguing due to their hierarchical structures, which vary widely across organisms and are found in a broad range of morphologies that are tuned for their specific functions. To show that these configurations give rise to the high performance of natural keratinous materials and can be a source of bioinspiration, these naturally occurring geometries are replicated in engineered materials by simplifying integral designs and scaling them to more appropriate sizes for processing and mechanical testing. Additionally, many of these studies rely on numerical and analytical models to better understand the mechanical behavior and deformation mechanisms of these bioinspired systems. This section will review these efforts through a bioinspired lens, focusing on how keratin-based systems and their structures achieve diverse functions.

The many functions of keratinous materials, shown in Figure 4.8, will lay the framework for reviewing their associated bioinspired materials. Table 4.3 highlights some common examples of systems for each function and their relevant structures.
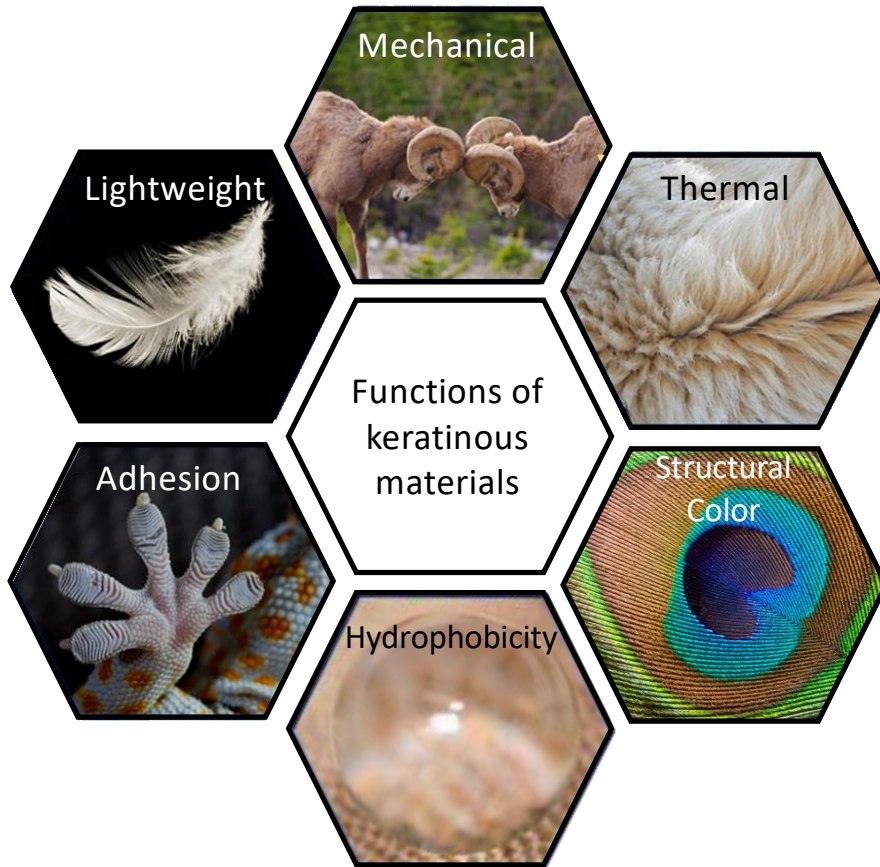
Figure 4.8 Keratin provides many functions in nature. In the following section, bioinspired designs based on keratinous systems will be broken down into the classifications shown in this figure.

Table 4.3 Keratin biological systems, their principal functions, and related structures.

Function	Biological Systems	Structures	References
Mechanical	Hooves, horns, bird beak, turtle scutes, pangolin scales	Tubules, sutures, layers, sandwich structures, articulated scales	[27,29,76,78,122]
Lightweight	Feathers, beak, porcupine quill	Sandwich structures, foam	[251,265,266]
Thermal	Hair, fur, and feathers	Large surface area, trapped air	[256,267,268]
Structural color	Feathers	Nanostructures	
Reversible Adhesion	Gecko setae	Branched structures, nanospatula	[269]
Hydrophobicity	Feathers, gecko skin	Spinules, hamuli, nanogrooves	[270,271]

4.2.1 Mechanical Applications

Keratin-based materials are frequently utilized in nature as structural load-bearing components that provide protection and withstand high impact forces. Keratinous systems perform admirably under such diverse mechanical demands, even compared to some of the most advanced engineered materials [83]. One reason is that keratin's mechanical properties can be tuned by hydration, providing a stiff (~10 GPa) load-bearing material when dry or a ductile rubbery material when fully hydrated (~0.1 GPa) [78,97,245,272]. Another reason is that keratin takes on the form of a wide range of structures with intricate geometrical features at multiple length scales that synergistically lead to high mechanical performance. This subsection will review keratinous systems with remarkable mechanical properties and instances where their structural features have been used as inspiration for synthetic materials.

One of the most common keratinous systems that has been studied for bioinspiration is the hoof wall of horses and bovines [26,78,79,81,82,97,98]. Horse hooves hit the ground at a speed of

~8m/s [96] and can experience impact forces of ~16.1 N/kg (deceleration of ~56 g) [273,274]. The hoof wall is composed of dead keratinocyte cells that cannot repair themselves yet can survive many regular impacts. This characteristic has made the hoof wall a prime candidate for designing bioinspired materials with high impact resistance and energy absorption capabilities. The hoof wall has an intricate hierarchical structure, depicted in Figure 4.9A, that has been shown to augment keratin's bulk properties. At the mesoscale, the hoof has hollow cavities (~40 micrometers in diameter) surrounded by relatively stiff elliptical regions (with a major axis of ~200 micrometers and a minor axis of ~100 micrometers) that run parallel to the surface of the hoof wall [78]. These tubules are embedded in a lamellar matrix composed of stacked, microscale, pancake-shaped cells (keratinocytes). These two geometries work in concert to provide the hoof with high fracture control [80–82] and impact toughness [78,79].
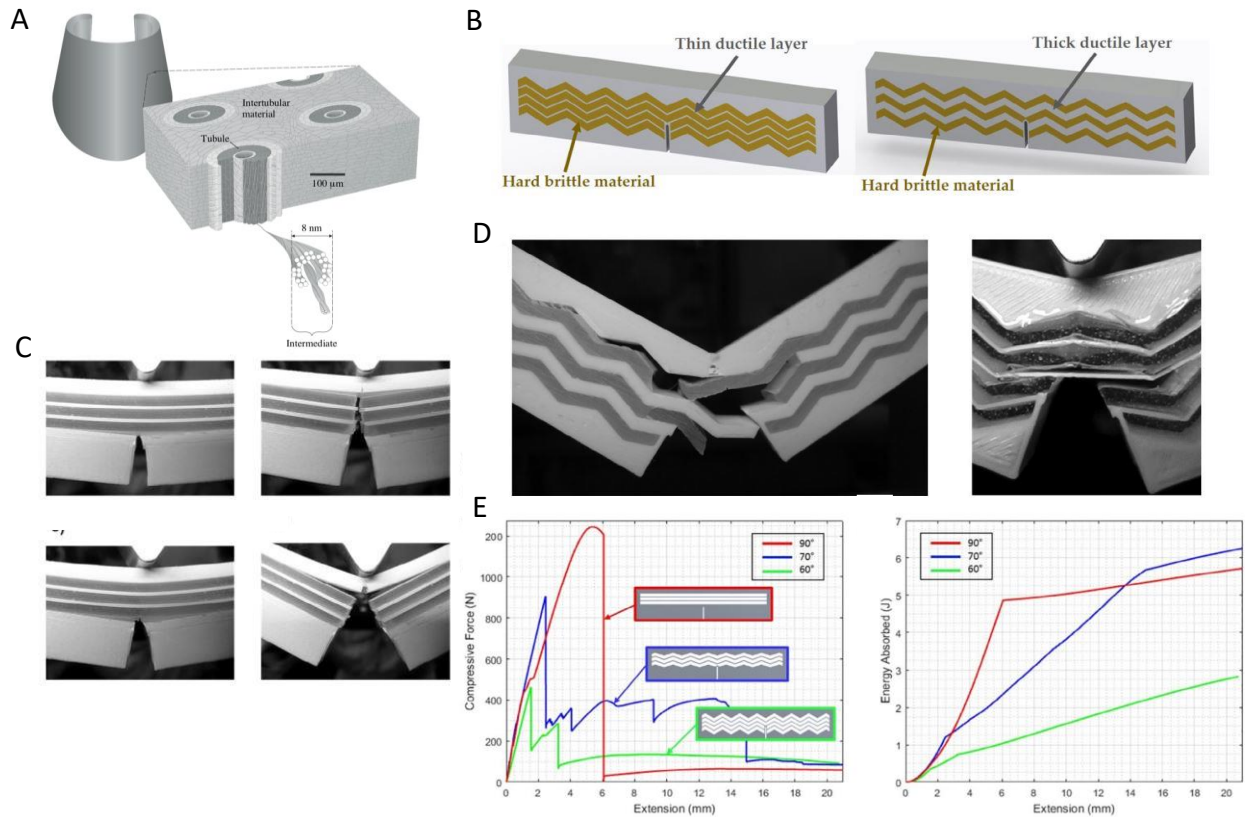
Figure 4.9 Horse hooves have been a great source of inspiration for tough materials with fracture control properties. A) A schematic of the horse hoof's micro and meso structure showing reinforced tubules embedded in layers of pancake-shaped cells. These cells are filled with IFs. Reproduced with permission [82]. Copyright 1999, Company of Biologists. B) Schematic showing different epoxy arrangements infiltrated PLA samples inspired by the hoof's layered structure. C) Crack propagation through flat layered samples before peak stress (top left), at peak stress (bottom left), during failure (top right), and after failure (bottom left). D) Failure pattern of zig-zag layered samples. E) Schematic showing how cracks interact with a jagged layered structure. F) Force-extension curve (left) and energy absorption-extension curve (right) of samples with layered structures of different angles. Reproduced with permission [275]. Copyright 2019, Elsevier Ltd.

Rice and Tan [275] drew inspiration from the lamellar structure found in the horse hoof's intertubular matrix to design improved composite materials. In hooves, the lamellar structure has shown strong retardation of fracture propagation by causing cracks to divert along the interlayer interfaces away from the living tissue at the hoof's interior [80–82]. To harness this fracture control

mechanism for engineered composites, Rice and Tan [275] manufactured a layered material with alternating soft (ductile) and stiff (brittle) regions, composed of 3D printed PLA layers infiltrated with epoxy or resin, as shown in Figure 4.9B. Their goal was to demonstrate that this bioinspired structure could successfully be utilized in synthetic composites and explore the effects of layer thickness, layer angle, and notch location on crack propagation. Single-edge notched bending tests on monolithic samples of resin, epoxy, and PLA showed that cracks traveled directly through the material with negligible deflection. Similar results were found for samples that contained flat lamellae and thin PLA layers, as shown in Figure 4.9C. The shear stress near the crack tip initiates debonding between the soft and hard layers; this gives rise to a crack-deflection mechanism similar to those found in hooves. Maximum shear stress develops at 45° to the original notch tip, while the lowest shear stress occurs at 90° to the notch. So, flat layers (layers oriented at a 90° angle to the notch like those in Figure 4.7C) experience the least debonding and exhibit minimal crack deflection. However, these samples have the benefit of being very stiff and require high peak forces to failure. Figure 4.9D shows how the introduction of angles into the lamellar structure can affect the crack path through the material. As the angle of the layers relative to the crack tip nears 45°, more shear stress builds up between the soft and hard layers causing the crack to deflect along the interface of the two materials. Figure 4.9E compares the force-extension curves of samples with layer angles of 60°, 70°, and 90°. Layers at 60° begin to debond at very low forces, while layers at 90° do not exhibit any debonding. Lamellar structures oriented at 70° are an ideal compromise, providing some stiffness and resistance to fracture before absorbing energy by debonding along the zig-zag interface. Figure 4.9E also shows each model's energy absorption curves and indicates that after 14 mm of extension, the 70° model absorbs more energy than the traditional 90° model. One final factor that was found to be very important for this configuration is the layer thickness.

When the ductile PLA layer was too thin, the crack fractured through it, and minimal deflection was observed. Higher peak forces and energy absorption were found for thicker ductile layers.

Several researchers have also explored the characteristic tubular structures found in hooves. B. Wang et al. (2020) 3D printed simplified tubular arrangements based on bovine hooves [276]. The tubules were modeled as hollow hexagonal prisms with varying angles that are inspired by the different angles of the intertubular layers found in the hoof. Three different configurations, shown in Figure 4.10A, were prepared for single-edge notched bending tests. The first model (G1) had no internal structure and was composed of bulk PLA. The second model (G2) had three rows of tubules, each offset from the previous row by 22.5°. The final model (G3) had the same structure as G2, but the tubules had a deflection of 15°. The introduction of tubules significantly improved the mechanical performance of the material with an increase of 39% in K_{IC} and 55% in G_{IC} from the G1 model to the G2 configuration. Figure 4.10A shows the K_{IC} and G_{IC} results normalized by volume, which indicates the superiority of the G2 design. The samples with tubular elements had a confined fracture pattern, which was given credit for the enhanced toughness and energy absorption of the G2 and G3 models.

Huang et al. (2018) combined reinforced tubular and lamellar structures to understand the impact-resistant synergy that these arrangements provide. Four different models were created using a multi-material 3D printer. These can be seen in Figure 4.10B. Single-phase samples were made out of stiff and brittle VeroClear®. A softer, more ductile polymer called TangoBlackPlus® was used to print the black, interlayer regions on the models. Both of these phases are proprietary materials produced by Stratasys, Ltd. Each sample was impacted with 100 kJ/m^2 of energy, and the results are shown in Figure 4.10B. The single-phase samples failed and fractured into many pieces. While the other three samples all remained intact, only the double-phase tubule reinforced

sample prevented cracking from reaching the sample's corners. Optical microscopy images of the damaged samples are shown at the bottom of Figure 4.10B, where the tubules' crack arresting capabilities can be observed [100].
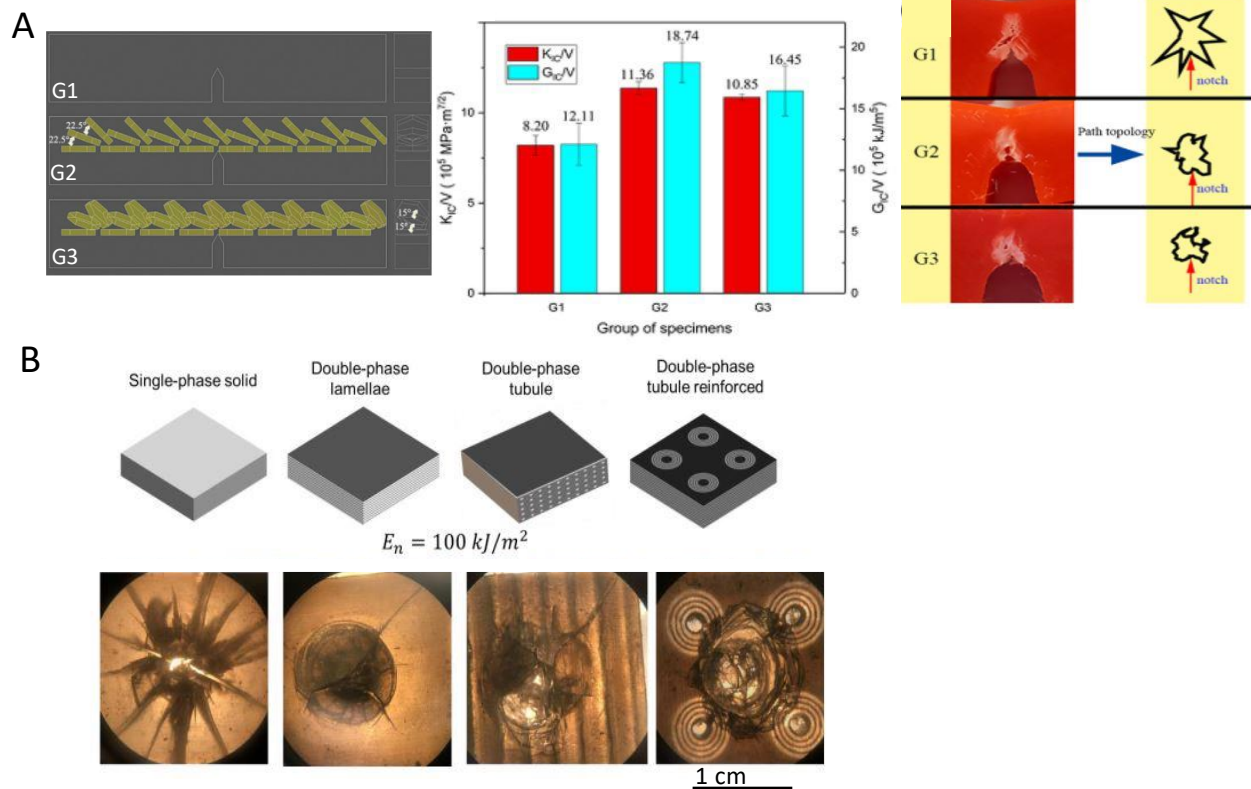
Figure 4.10 Tubular structures in hooves have attracted significant attention for bioinspired designs. A) Schematic of different tubular arrangements modeled after the hoof with tubules (yellow) represented as hexagonal prisms [276]. B) Image of notched three-point bending test of different models (top), graph normalized K_{IC} for each model (middle), and representative images of the damage zone for each model after testing (bottom). Reproduced with permission [276]. Copyright 2020, Elsevier B.V. C) Schematic of different models with increasing complexity culminating in double-phase tubules embedded in a layered structure (top). Images (middle) and optical micrographs (bottom) of the different samples after drop tower tests where the impact energy was 100KJ/m^2. Open Access [100].

Ma et al. (2020) formed tubular structures inspired by the equine hoof wall's architecture to achieve outstanding crashworthiness. As shown in Figure 4.11, they modified traditional square tubes by replacing the vertices with the unit geometrical structure. The conception of these structures was inspired by the tubular geometry present in the keratinous equine hoof wall. They

also modified the side walls to corrugated plates, inspired by secondary epidermal lamella in an inner lamellar layer. The samples were manufactured using the aluminum alloy AA6061-0. Ma et al. (2020) demonstrated that the hoof-inspired geometry (HCT) could significantly improve crashworthiness using compression tests and finite elemental analysis. The HCT provided a 269% increase in energy absorption and 124% increase in specific energy absorption over traditional square tubules in compression testing [277].
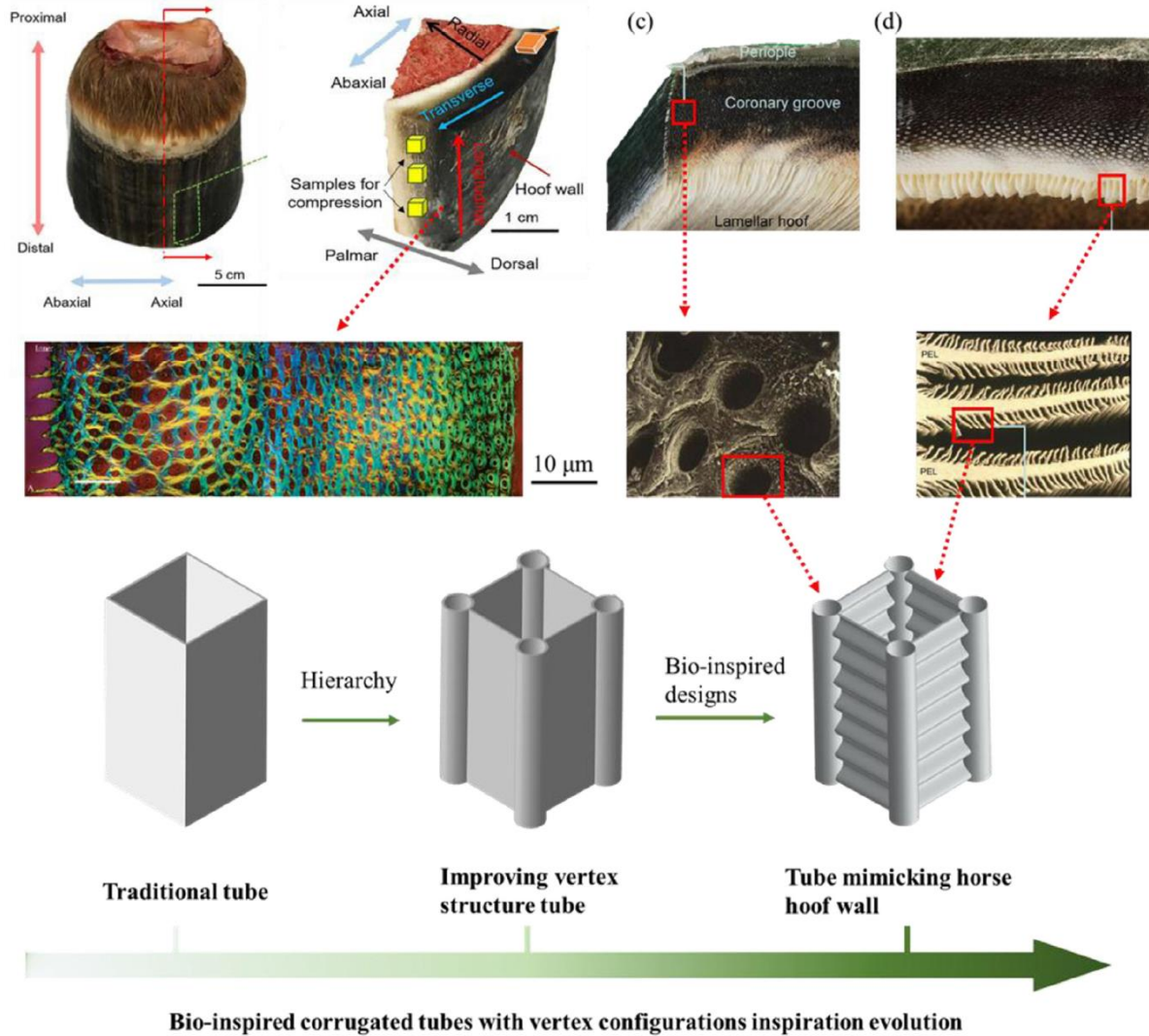
Figure 4.11 Crashworthy structures inspired by the horse hoof wall. The top two rows of images show the naturally occurring horse hoof, while the bottom row shows designs of increasing complexity that incorporate the tubular and lamellar microstructure of the keratinous hoof sheath. Reproduced with permission [277]. Copyright 2020, Elsevier Ltd.

Horns have a very similar structure to hooves with hollow tubular elements embedded in lamellar stacks of flat cells. However, the tubules in horns are perpendicular to loading at the impact zone and lack the reinforced region surrounding the tubules that is found in hooves. Figure 4.12A shows SEM images of the tubular and lamellar structure of the bighorn sheep horn alongside 3D printed models of the horn, including a single-phase block of stiff VeroClear® with and without an array of tubules and two-phase lamellar structures (the second phase being ductile

118

TangoBlackPlus®). Figure 4.12B shows how the bioinspired models compare to horn samples under compression. When samples were compressed with the loading axis parallel to the lamellae, they showed much lower strength. This behavior is due to delamination between the soft and hard phases, similar to the response found in horns. When samples were compressed perpendicular to the tubules, the hollow cavities collapse, leading to a slight decrease in stiffness and strength but an increase in plastic deformation and final compressive strain. Again, this performance mirrored that of real horns, suggesting that this structure could also have good energy absorption capacity under impact [100].
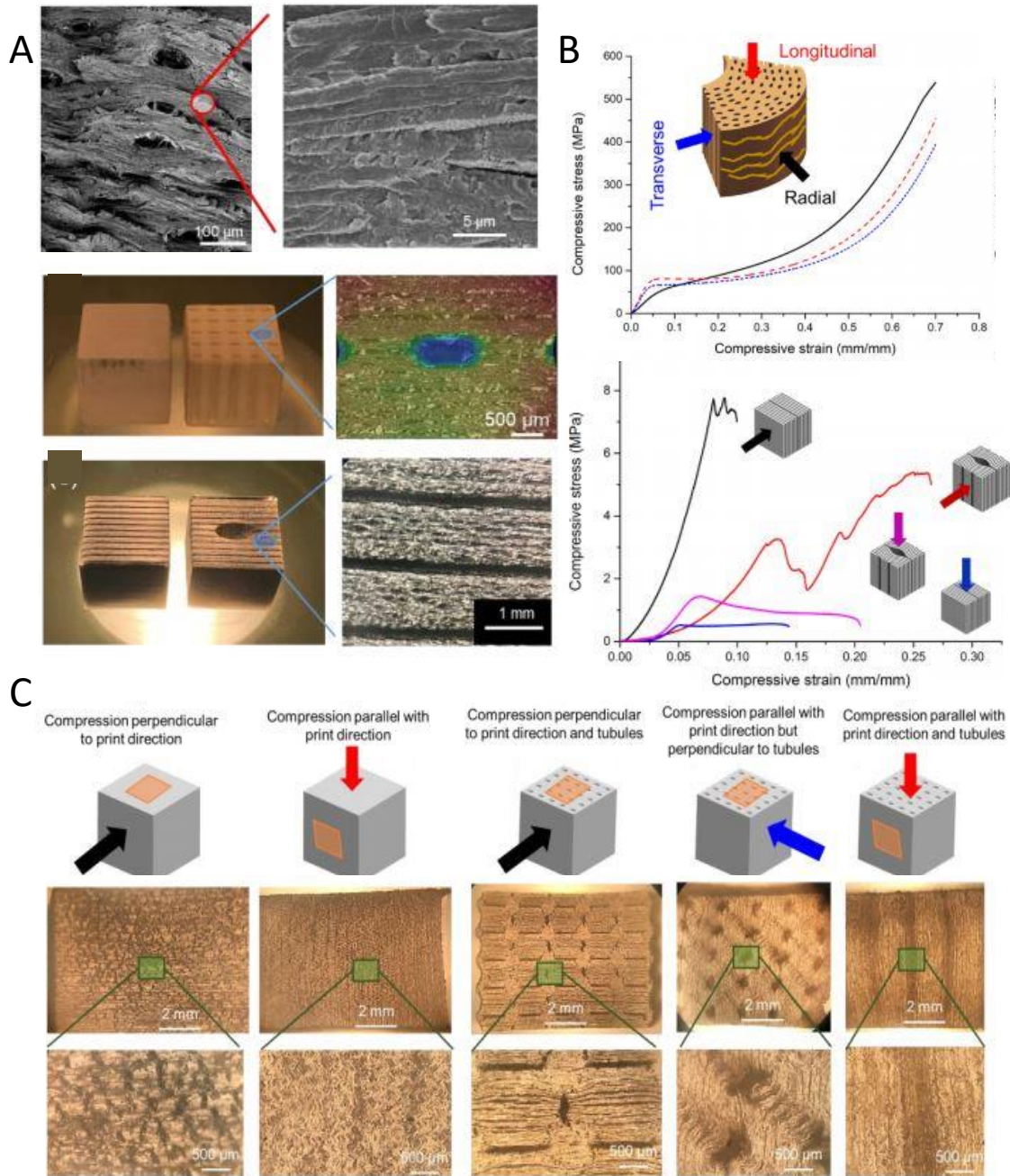
Figure 4.12 Bighorn sheep horns can endure tremendous impacts and have been the muse for several impact-resistant bioinspired designs. A) The horn's structure (top) with SEM images of its tubular and layered structure. Schematics and images of bioinspired designs with unreinforced tubules embedded in a layered configuration. The layers relative to the tubules' orientation are the opposite of the hooves while the orientation of the tubules to the impact direction is also reversed. B) Stress-strain curves of the horn and bioinspired samples in different orientations. C) images of failure mechanisms of bioinspired samples when compressed in different orientations with respect to print direction. Open Access [100].

120

However, 3D-printed polymer models of keratinous structures have been limited by their inability to capture these systems' full complexity and mechanical functionality. While the shape of the stress-strain curves of the printed samples and horn samples are similar, Figure 4.12C shows that their failure mechanisms are quite different. For example, the 3D printed samples developed stress concentrations around the tubules leading to cracking when compressed perpendicular to the tubules. This behavior was not observed in the horn, which was able to distribute stress more uniformly [76]. Also, when horn samples were compressed parallel to the tubules, tubule buckling was observed. In the 3D printed samples, it was the lamellae that buckled rather than the tubules. These differences are likely due to disparities in material properties between printed and natural samples, the lack of lower-order hierarchical structure in the printed models, and processing restrictions that create weak interfaces and residual stress in 3D printed components. The print direction additionally influences the mechanical response. While 3D printing biomimetic structures have huge potential, this example underscores some of this technique's limitations [76].

Huang et al. (2018) also tested the recoverability of compressed 3D printed samples inspired by bighorn sheep horns. Dynamic and quasi-static recovery tests on horn samples showed that, when exposed to water, keratinous materials can regain much of their initial shape after compression. In keratin, this process is highly dependent on hydration, which disrupts the hydrogen bonds within and between the macromolecular chains and allows them to be reformed in a recovered position once the load is released. A similar process can be achieved in synthetic polymers by raising the specimen's temperature over the glass transition temperature. After being compressed to 50% strain, the 3D printed samples were exposed to 62° C for 15 minutes. Similar to the horn results, damage from compression in the longitudinal and transverse directions was irrecoverable due to lamellae buckling and shear band formation. However, in the radial direction,

much of the structure and the stress-strain curve was recovered in subsequent compression cycles, suggesting that keratinous materials can also provide a structural blueprint for shape recovery materials [100].

Kassar et al. (2016) produced foam liner material for motorcycle helmets inspired by the microstructure of horns. Helmets and horns both have an outer structure that is mainly responsible for energy absorption during impact. Soft inner tissue that distributes the load increases the deceleration distance and thus protects the head. Following a similar principle, they designed solid foams with varying tubular porosity. As observed in horn structures, the tubules' porosity was varied from 0%, near the head, to 10% in the middle and ~30% on the outer shell [278]. This spatial change in porosity is a classic example of a gradient structure, one of the hallmarks of biological materials [151]. Figure 4.13 shows the bioinspired design. To assess the design, modified drop tower tests according to "United Nations Economic Commission for Europe Standard" for motorcycle helmets ECE 22.05 were performed using the foam manufactured by EPS material. The design was able to meet safety thresholds far below the limits stipulated by the ECE 22.05 motorbike helmet testing standard.
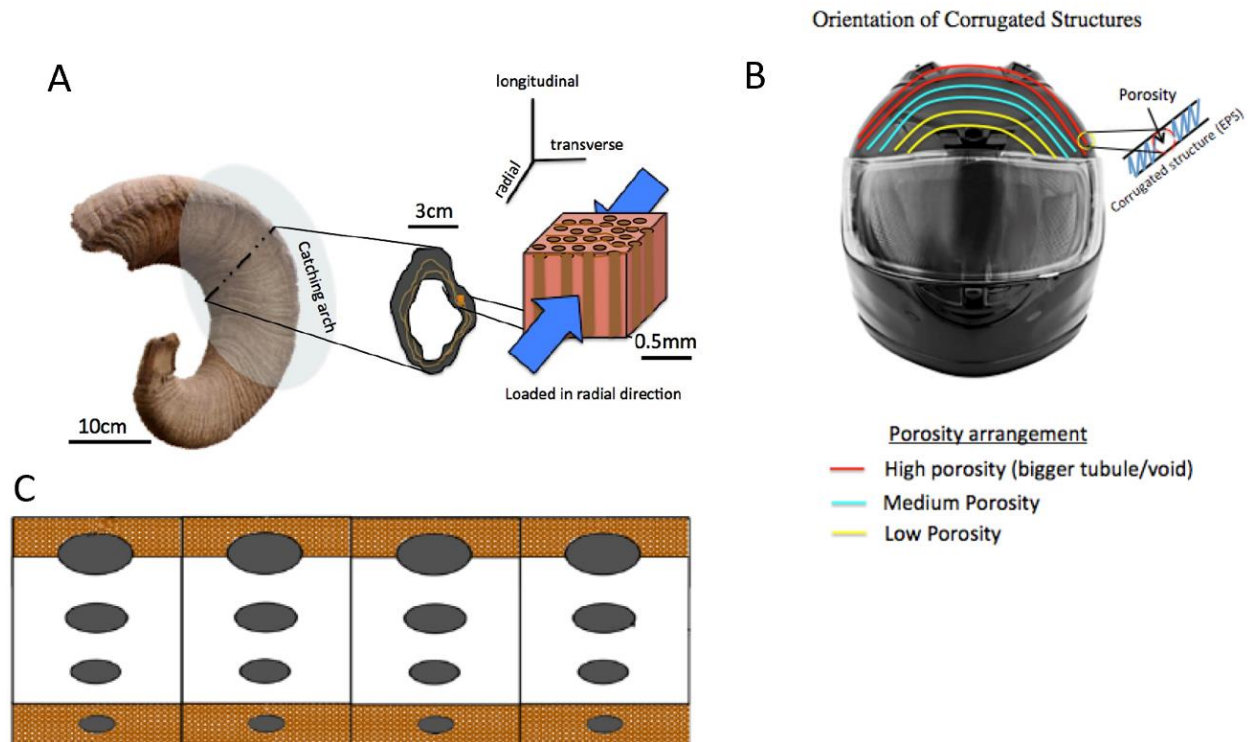
Figure 4.13 Bighorn sheep horns absorb tremendous impacts in nature, so researchers envision helmets inspired by the horn's microstructure. A) Visualization of the hierarchical structure with an emphasis on the microstructure of the bighorn sheep horn. B) Conception of a helmet with a gradient in tubular porosity between the interior and exterior. C) Cross-section of the protective tubular region showing a variation in tubule size through the helmet's thickness. Reprinted with permission [278].

The above efforts have taken bioinspiration from microscale structural elements of hooves and horns. However, Sun et al. (2014) designed rear under-run protection devices (RUPD) for heavy trucks inspired by the macroscale geometry of the sheep horn. The RUPD prevents the entry of small-scale vehicles under the rear end of the heavy truck. The design was analyzed using a finite element analysis. The authors concluded that, compared to the normal RUPD of the same thickness, the bio-inspired design could provide better protection when rear-end accidents happen; this is due to its enhanced energy absorption and structural strength [71]. Zhang et al. (2008) took inspiration from buffalo hooves to design impellers for a paddy field. They studied the buffalo hooves' curvature that allows them to maneuver through the field with relative ease. The impeller

designed with similar curvature has a 38% increase in pull force and was more efficient than standard blades [279].

Baleen is the filter-feeding system found in the oral cavity of baleen whales, some of the largest animals on the planet, and is composed of highly mineralized keratin. To withstand the forces associated with filter-feeding, some whales have evolved baleen with complex structures that provide remarkable fracture toughness. The baleen plates contain a tubular sandwich structure that can be seen in Figure 4.14A. The tubular region has a structure that is reminiscent of hooves but has a much higher mineral content that arises from hydroxyapatite nanocrystals embedded among the keratin intermediate filaments. The sandwich structure, composed of a solid shell around the tubular zone, provides high flexural stiffness and strength relative to the material's weight. Much like the tubule lamellae found in hooves, the concentric layered arrangement around the hollow cavities serves to deflect cracks and increase fracture toughness. This structure is highly anisotropic. The differences that arise from different loading directions can be seen in Figure 4.14B. Loading parallel to the tubules gives higher Young's modulus but less ductility than the loading perpendicular to the tubules. This anisotropy has a profound effect on fracture toughness [243].
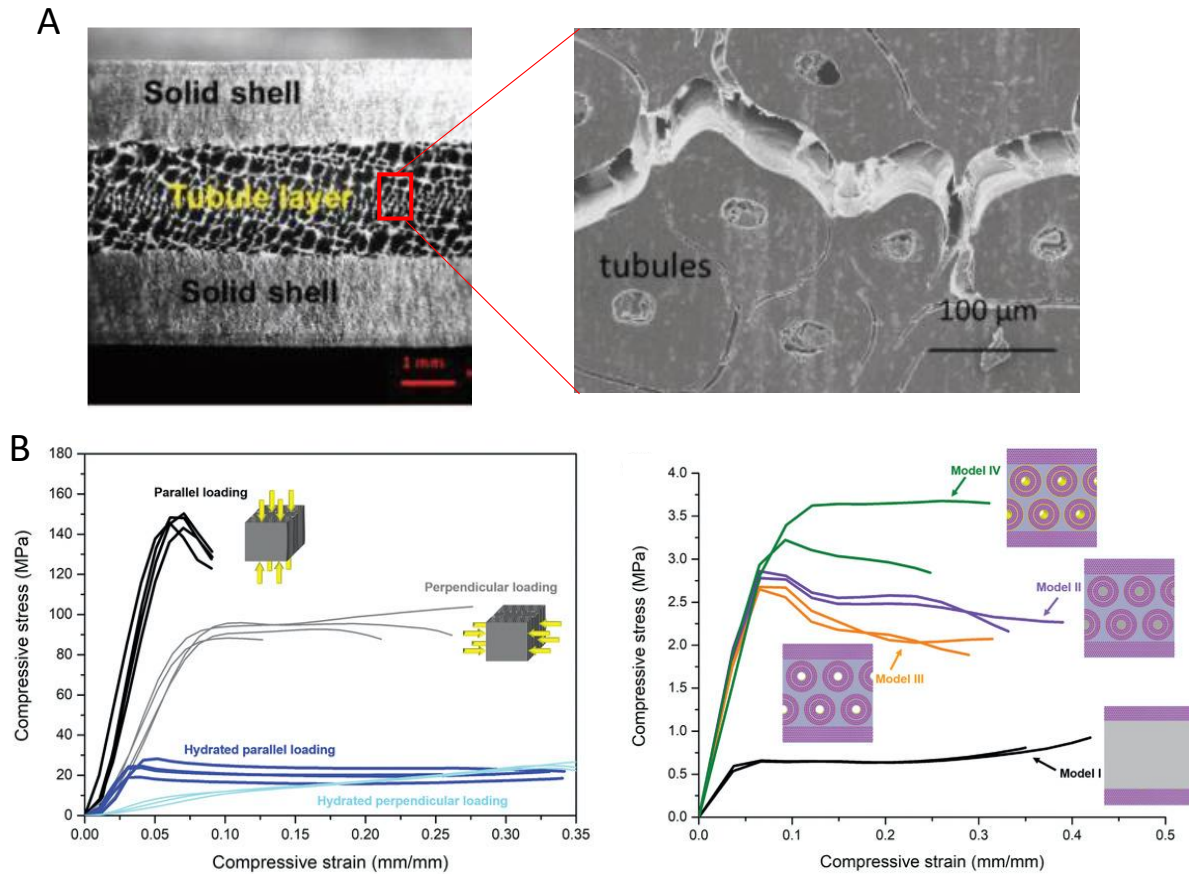
Figure 4.14 Whale baleen is a part of the filter-feeding apparatus of baleen whales and is able to withstand high pressures and impacts from fish that get sucked into the whale's mouth. Bioinspired models have shown that the structure of the baleen helps endow it with admirable properties. A) Image of a cross section of whale baleen showing the tubule layer sandwiched between a solid shell of keratin. B) Stress-strain curves of the baleen in each orientation showing significant differences in response based on loading direction. Stress-strain curves of the bioinspired models, indicating the design's superiority with all of the features incorporated in tandem in model iv. Reproduced with permission [243]. Copyright 2018, WILEY-VCH Verlag GmbH & Co. KGaA.

Four 3D printed models were fabricated to investigate the role that each of these features plays in the baleen. The most complex model (model IV) printed using three different materials most closely represents baleen. The mineralized lamellae were simulated using a stiff polymer and the matrix using a ductile polymer, while a polymer of intermediate stiffness represented the unmineralized lamellae filaments. Each successive model adds a new design element. Model I

125

contains just a sandwich structure of soft material between two stiff layers; model II adds the concentric filament structure; model III includes the hollow cavity at the center of tubules. Model IV combines all of these features with the stiff lamellar rings shown in yellow. The addition of filaments raised the samples' stiffness, while the hollow cavities slightly decreased the sample strength at strain rates of 0.28 s^{-1} and 10^{-4} s^{-1} but increased it at strain rates of 10^{-2} s^{-1}. The addition of the stiff lamellar rings unsurprisingly increased the models' stiffness and strength and led to significantly more strain-rate stiffening and strengthening. These phenomena were also observed in the natural baleen. Wang et al. (2019) concluded that model IV provides the best mechanical performance showing that the features found in keratinous whale baleen can be utilized as beneficial structural design elements [243].

In summary, bioinspired research on mechanical keratinous tissue has focused on several features: tubules (as found in the hoof, horn, and baleen), lamellar structures (found in all keratinous materials), and macroscale geometry (like hoof curvature or horn shape). When composite materials incorporate tubules or lamellae, they find improved fracture toughness due to crack interactions at these structures' interfaces. Similarly, macroscale geometries are practical but largely unexplored avenues of inspiration for specific functions like impellers or bumpers.

4.2.2 Thermal Insulation

Keratinous systems are some of nature's best insulation by virtue of their elaborate structures that trap air. Many synthetic fibers are more inherently resistant to heat transfer. However, with their hierarchy of air-trapping features, natural keratinous systems are still some of the most superb thermal insulators. The popular and unsurpassed down jackets use feathers. As a result, researchers have tried to recreate these natural insulators' configurations in engineered materials to harness their desirable thermal capabilities.

126

Some organisms, like polar bears and penguins, can thrive in the most extreme conditions on earth due to their keratinous thermal protection [280,281]. Polar bear hairs consist of a hollow porous interior that provides superior thermal properties surrounded by a shell of aligned fibers, which supplies mechanical stability. SEM images of these hairs are shown in Figure 4.15A. Individual hairs are approximately 200 micrometers in diameter, while the interior pores measure 15-20 micrometers across. The length scale of these pores is significant because it allows the hairs to trap substantial amounts of air, providing a thermal buffer between the bear's living tissue and the surrounding arctic temperatures that can reach as low as -45º C.

Since 3D printing cannot manufacture architectures on the scale of micrometers, Cui et al. (2018) used freeze spinning to create bioinspired synthetic fibers that could mimic the polar bear hair. This process is similar to freeze-casting in that it harnesses directional ice crystal growth to create a porous lamellar structure within an aqueous solution. However, freeze spinning performs this technique within a stable, extruded liquid wire. Once the wire is frozen, the material is freeze-dried to preserve the intricate microstructure formed by the ice crystals, and the completed porous fiber can be woven into a textile [268]. This process is visualized in Figure 4.15B.
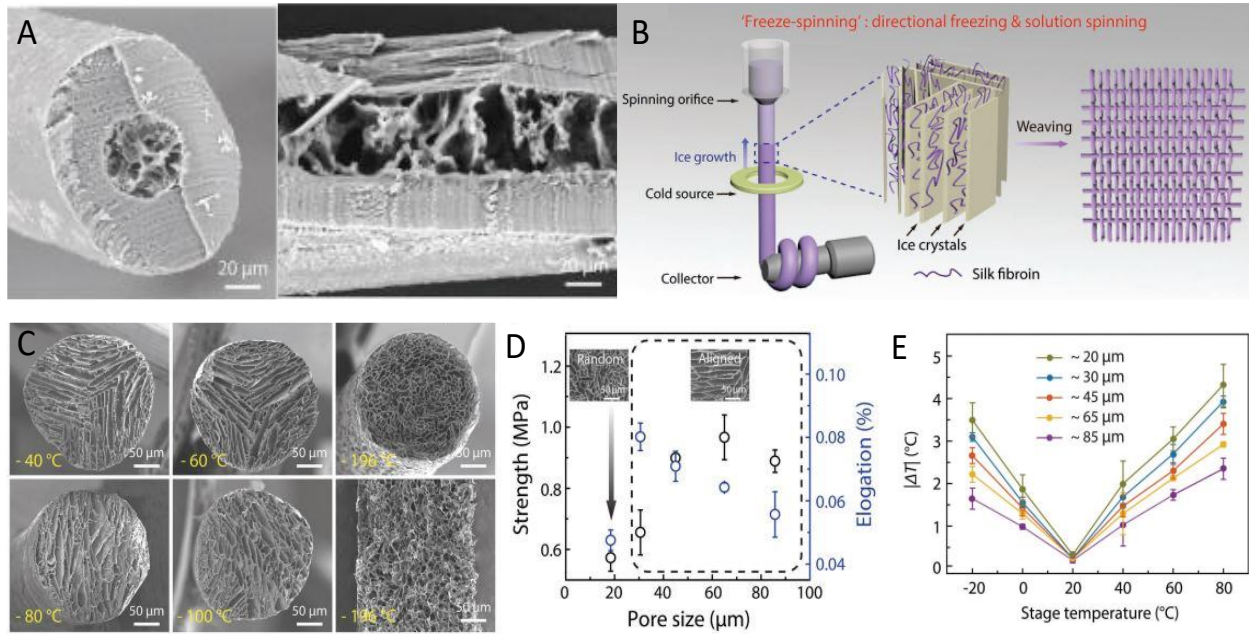
Figure 4.15 Polar bears can survive in some of the harshest environments on earth, largely due to their warm fur. Bioinspired models based on porous hairs have been fabricated to harness the remarkable thermal properties exhibited by polar bear hair. A) SEM images of polar bear hair radial (left) and longitudinal (right) cross-sections. B) Design set up for freeze spinning system used to fabricate bioinspired polar bear hairs fibers. C) SEM images of bioinspired hair cross-sections fabricated at different temperatures. D.) Plot of average pore size vs. fiber strength in the bioinspired fibers. E.) Plot of difference in heat between the top of fibers and bottom of fibers with varying average pore size when placed on a heated stage over a range of temperatures (-20 ºC - 80 ºC). Reproduced with permission [268]. Copyright 2018, WILEY-VCH Verlag GmbH & Co. KGaA.

As with freeze-casting, numerous parameters can be adjusted to control the production, such as solution viscosity, extrusion speed, and freezing temperature. For the latter, Cui et al. (2018) found that the temperature at which the ice crystals are formed can be used to control the pore size and orientation in the fiber, as shown in Figure 4.15C. As the temperature is lowered from -40 Cº to -196 Cº, more ice crystals are formed, but the freezing process occurs quickly, giving the crystals less time to propagate through the solution. The result is more pores that are smaller. When the fiber is frozen in liquid nitrogen, a random porous network is produced, but when crystals are formed at higher temperatures, the pores align in the crystal growth direction. The pores' alignment and size have a significant effect on the fibers' tensile properties, as seen in

Figure 4.15D. Aligned pores provide better strength and elongation than a random porous network [268].

In comparison, fibers with larger pores tended to have higher strength but lower average elongation than fibers with smaller pores.   Smaller pores, however, provide better thermal properties. This behavior was determined by heating fibers with different pore sizes on a stage and measuring the temperature on fibers' surfaces using IR images. These results are summarized in Figure 4.15E. This biomimetic material also showed promising results for thermal cloaking and, when embedded with carbon nanotubes, electro heating [268].

Feathers are among the most ubiquitous materials used as thermal insulators due to their extreme lightweight and durability. Different types of feathers are distinguished by their structure and location on the bird: contour (body feathers) and plume (down feathers). Down feathers are primarily responsible for thermal insulation, which is attributed to their hierarchical foam-based structure creating large surface areas for trapping heat. Some academics have posited that Eiderdown, in particular, is the most thermally insulating natural material in the world [282]. Down benefits from an impressive strength-to-weight ratio [267,283], compressibility [284], and compression recovery [285], making it invaluable as bodily insulation in extreme environments. The first use of down jackets was seen in expeditions to Mount Everest in 1922 and by 1933 in down sleeping bags, which have become a staple of mountaineering in the harshest of climates. While this application of keratinous tissue is hardly bioinspiration, a discussion of keratin's multifunctionality would be incomplete if it did not mention the pervasiveness of feathers in a vast range of textiles from common bedding to elite sub-zero clothing [286]. Even before down became popular, other keratin sources such as wool and animal fur have played a dominant role in the human race's ability to inhabit some of the coldest regions on earth.

One of the driving enterprises of the industrial revolution was the production of textiles. With such vast commercial implications, research on manufacturing cheap, synthetic fabrics with properties similar to wool and fur has been evolving for centuries. Modern clothing is often a mix of natural materials such as wool or cotton and synthetic fibers like polyester. In some cases, natural fibers have been replaced entirely. Examples include synthetic cashmere, which is usually a combination of rayon, nylon, and polyester, and fleece, typically composed of PET. Ultimately, many of our modern textiles are bioinspired materials that are attempting to replicate the success of traditional but expensive, labor-intensive keratinous systems.

In summary, keratinous materials' thermal insulation revolves around hierarchical surface texture or internal pores that are meant to trap air pockets and create a buffer between the animal and its surroundings. Efforts to recreate these structures using synthetic materials have been quite successful, highlighting that this is a fruitful area of study.

4.2.3 Reversible Adhesion

Reversible or non-destructive adhesion allows for repeated attachment and detachment cycles that do not damage the substrate. Nature employs a variety of reversible adhesive strategies: mechanical interlocking, friction, chemical bonding, dry adhesion (i.e., van der Waals), wet adhesion (i.e., capillary), and suction (i.e., pressure differential). Often, organisms will use a combination of the above attachment methods to adhere to surfaces successfully. These processes are strongly dependent on the environment (predominantly wet vs. dry and smooth vs. rough). Mechanical interlocking, friction, dry adhesion, and wet adhesion are strongly dependent on having nanostructured surfaces. The hierarchical nature of keratin lends itself well to forming nanostructured and intricate designs. While the field of reversible adhesion is extensive [287,288], our focus here is on materials inspired by keratin-based systems to highlight the diverse

functionality that keratin offers. We will focus on the mechanical attachment found in the feather vane and dry adhesion found in gecko setae and their respective bioinspired designs. Claws and talons use a more conventional design principle, a relatively large hook, and will not be treated here.

The feather vane is directionally permeable, which effectively helps it capture air for lift [289,290]. This mechanism is controlled by the branching barbs' geometry and stiffness and interconnecting barbule network, which ultimately forms the feather vane [289,290]. Barbs, which branch from the rachis, are further branched into barbules. The barbules have hooklets (hamuli) on their extremities, which fit into the neighboring barb's groove, creating a highly ordered lattice of interconnected adjacent barbs (Figure 4.16A). Having multiple hooklets increases both the adhesion and the probability that two neighboring barbs will stay connected. The interconnected network of the feather vane, provided by this adhesive mechanism between the barbs and barbules, is credited as the essential element that allows birds to achieve flight [290].

Figure 4.16 Progression of bioinspired designs based on the attachment mechanism found in the feather vane. A) SEM micrograph of the feather vane showing a branched network of barbs, barbules, and hooklets. B) First hook and groove-inspired sample. C) Modified hook and groove structure with a closer match in stiffness to the actual feather vane. D) Advanced replication of the feather vane to incorporate membrane flaps for directional permeability. E) The first groove-only unidirectional sliding structure. F) Two-dimensional sliding structure, which shows textile-like behavior. G) Cubic sliding structure which provides tailored stiffness in three dimensions. Adapted with permission [291]. Copyright 2019, Elsevier.

A

B

Groove

Barb   Hooklet

C

1 cm

D

Grooved Barbule

Hooked Barbule

E

Closed channels

Open channels when stretched

F

Closed channels

Open channels

G

133

Several 3D printed bioinspired designs based on the reversible adhesive mechanism of the feather vane have been developed by Sullivan et al (2019). These 3D printed structures not only serve to understand better the mechanisms operating in the feather but extend beyond the scope of the intended function in nature to suggest innovative solutions for deployable structures, next-generation chainmail, and smart foams. The initial interlocking barbule bioinspired design was intended to mimic the attachment mechanism by scaling the dimensions to an appropriate size for 3D printing and mechanical testing. The first design in Figure 4.16B helped demonstrate the feather vane's adherence through hooks and grooves that slide along each other. This feature is similar to the mechanism found in Velcro but is more organized and directional. While the first design served as a simplified model, the 3D printed material used was much stiffer than the feather vane. It did not accurately mimic the feather vane's elasticity and ability to re-adhere. The second model attempted to reduce the elastic mismatch by printing with a more flexible material which helped to elucidate how the material properties and the hook's geometry can enable sufficient adhesion that is damage-tolerant and can re-adhere readily (Figure 4.16C). Development of subsequent designs based on the barb and barbule interaction further increased in complexity to represent the feather vane with the inclusion of flaps that act as one-way valves (Figure 4.16D). These models suggest that two existing modes allow for tailored air permeability: (1) membrane flaps allow air to flow through space between barbules dorsally but not ventrally, and (2) the sliding of hooks along the grooves offers expansion within the feather vane (when hooks are closer to the base of the groove the vane is tighter, i.e., less permeable than when the hooks are at the tip of the groove). The purpose of this effort was to offer a simplified visualization of the complex nature of reversible adhesion and directional permeability in the feather vane [291].

The subsequent iterations of designs expanded beyond just mimicking the feather vane by extracting fundamental design principles to optimize the interplay of tailorable, expansive materials. The ideas involved removing the hooks, which were shown to be the weakest point of adhesion from previous designs (Figure 4.16 A-D), and creating an exclusively grooved-based structure that had stoppers at the end to prevent complete detachment (Figure 4.16E). In the first groove-based structure, sliding was only able to occur in one direction. In this direction, sliding enabled an increase in flexibility while the perpendicular direction remained rigid. The design was further altered to allow sliding in both directions, which led to textile-like behavior when stretched open (Figure 4.16F). Finally, a cubic structure was developed, which allowed for sliding and manipulating the modulus in all three dimensions (Figure 4.16G). This progression in development highlights the importance of bioinspired design as a creative process reaching beyond the limitation imposed on nature to develop innovative materials.

The gecko setae are a most striking example of reversible adhesion in nature. Over the past two decades, these keratinous nanopillars have stirred up a tremendous amount of scientific interest, leading to the publication of hundreds of research papers and enough articles to be the topic of their own review [292–299]. However, interest in the gecko stretches back through the past century. Piquantly, geckos' mysterious ability to climb vertical walls and even to hang upside down on ceilings was correctly interpreted in 1902 by Franz Weitlaner [300]. Since then, great strides in bioinspiration have come with vast amounts of research, and many groups have succeeded in making reversible dry adhesives based on the gecko setae structure. Here, we will only broadly cover this burgeoning area of study.

The gecko's adhesive pads utilize van der Waals forces and, to a lesser extent, capillary forces generated by the hierarchical broom-like geometry of setal arrays [298,299]. The setae

found on the gecko adhesive pad are arranged on lamellae and branch into hundreds of individual spatula-shaped tips (typically referred to as spatulae), as shown in Figure 4.17A. Van der Waals forces require extremely close contact (<10 nm) to generate a significant force, and this is accomplished by the flexible, branched nanostructure of the gecko pad. As the setae divide into smaller subdivisions with higher aspect ratios, their effective elastic modulus decreases, allowing them to conform easily to smooth and rough surfaces [299]. In the aggregate, the spatulae generate significant adhesive forces in the normal direction and frictional forces in the lateral direction, both of which are vital to the locomotion of the gecko [296]. Further, these fine subdivisions have the added benefit of confining crack propagation if a single seta begins to fail [298].

Figure 4.17 Geckos use van der Waals forces generated by densely packed setal arrays on the feet to climb even the sheerest surfaces. Many researchers have attempted to replicate this structure to create reversible, dry adhesives. A) SEM image of the branched gecko setal array. The inset image shows the split-fiber endings with tilted, spatula-shaped tips [301]. B) SEM image of synthetic gecko-inspired adhesive composed of polymer micropillars with densely packed carbon nanotubes glued to the end. Open Access [301]. Copyright 2013, the authors. C) SEM image of bioinspired, tilted micropillars composed of polyurethane that mimic the gecko setae's directional gripping strength. Reproduced with permission [302]. Copyright 2009, Wiley-VCH Verlag GmbH & Co. KGaA. D) SEM images of three hierarchical tiers of mushroom-shaped pillars composed of polyurethane that mimic the hierarchical branched structure found in the gecko pad. Reproduced with permission [303]. Copyright 2009, American Chemical Society.
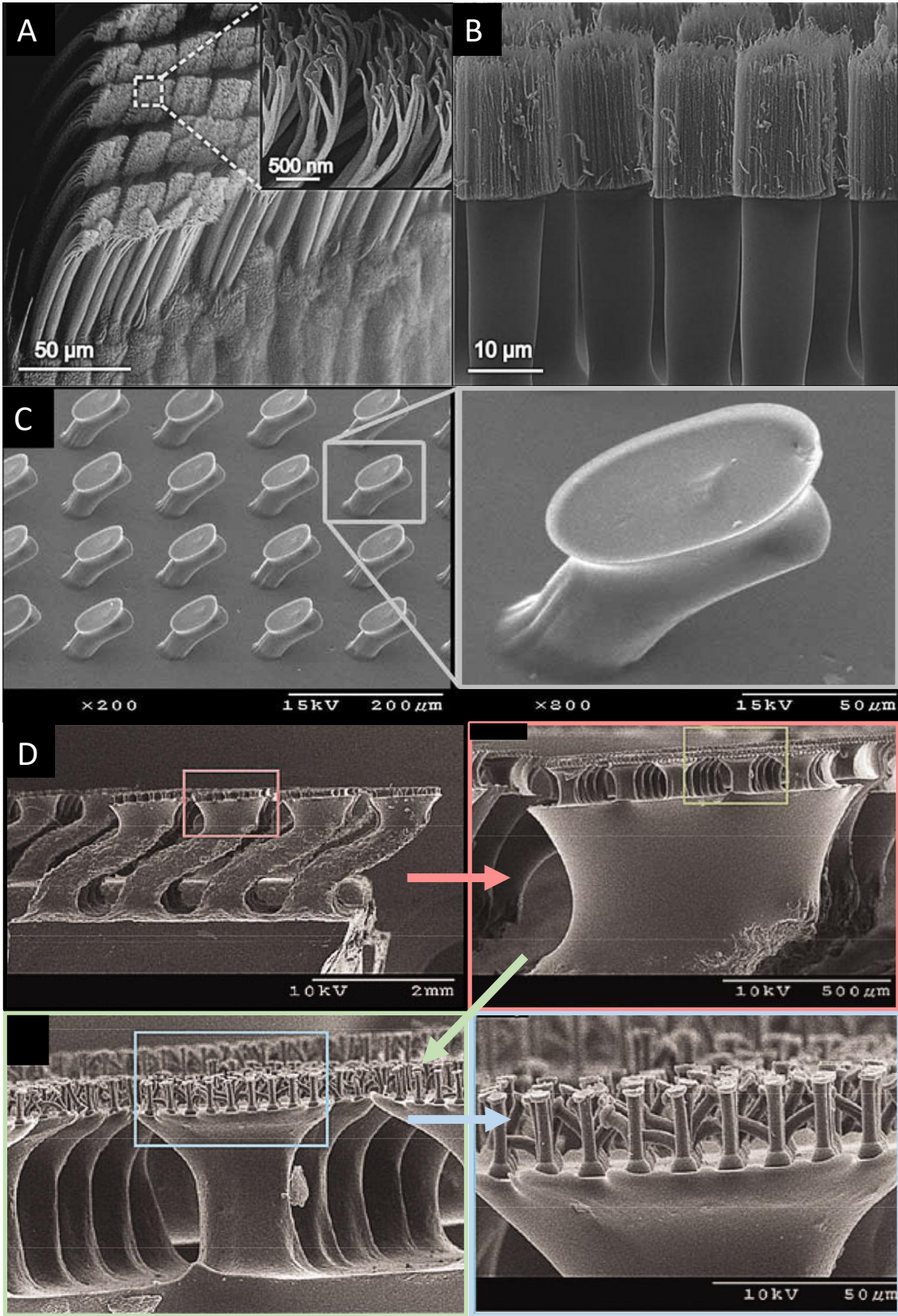
There are several additional characteristics of the gecko pad that make them particularly alluring to researchers. One of the gecko pad's most enticing features is its controllable and reversible adhesion, allowing it to be reused and not leaving behind any residue on the locomotive surface. The setal spatula-shaped tips attach to a surface when the gecko pulls its toes downward and inward, creating a small pulling angle between the setae and the surface. To detach from a substrate, the gecko pushes its toes upward and outward; this has the dual effect of increasing the pulling angle past the critical detachment angle (~30°), and squeezing the setae increases their effective elastic modulus and decreases their conformability to the surface [298,299,304]. This process can be actualized in a matter of milliseconds allowing for rapid, reversible adhesion. Other unique properties provided by the branched setal arrangements include self-cleaning characteristics and adhesion in challenging environments like underwater and on surfaces with different polarity and roughness [297,299].

Several research groups have hypothesized that the self-clean capabilities of the gecko-pad arise directly from the nanostructure of the setal configurations. Hansen and Autumn (2005) suggest that the primary reason for self-cleaning is the energetic disequilibrium between the substrate and the setae, but state that other factors like locomotion, particle rolling, and particles wedging between the setae could play a role [305]. Follow-up studies have confirmed that each of these mechanisms improve self-cleaning [306,307], particularly when particles bond more strongly to the setae than the substrate. Xu et al. (2015) postulated that the dynamic motion of gecko toes (referred to as digital hyperextension) allows geckos to tune the pull-off velocity of the setal arrays [308]. Since the adhesive force between dirt particles and the substrate is velocity-dependent, and the force between particles and the setae is largely velocity-independent, increasing the pull-off rate can dislodge bonded particles from the surface of the toe pads. This velocity-

controlled self-cleaning technique was applied to synthetic biomimetic materials with great success, achieving an ~80% chance of particle detachment at high velocities (>1000 $\mu m\,s^{-1}$) compared to the 0-40% chance of detachment beneath this threshold.

Many different approaches [309] have been utilized to fabricate nanostructures capable of generating dry, reversible adhesion inspired by the gecko setae. These include soft lithography [310–312], injection molding [313–316], hot embossing [317], photolithography [318–322], plasma etching [321,323], electron beam lithography [324], carbon nanotubes (an example of which is shown in Figure 4.17B)[301,325–327], nanodrawing [328], micro/nanomolding [329–332], dip-transferring [302,303], two-photon lithography [333], nanoimprint lithography [334], and many more. As research groups have aimed to mimic the gecko pad's intricate structure more closely, the complexity of their fabrication processes has increased. Early techniques focused on only manufacturing a dense network of nanopillars. However, these studies showed that other design parameters need to be considered to truly capture the gecko pad's functionality.

For example, the natural setae are tilted, which creates much larger shear forces in the gripping direction than in the non-gripping direction, effectively enhancing the gecko pad's reversible adhesion [296]. Figure 4.17C shows tilted polyurethane fibers fabricated via inclined exposure and dip coating to capture this parameter. Another essential variable for gecko-inspired adhesives is the shape of the tip of the nanofibers. Many different arrangements have been investigated, but mushroom-shaped tips have proven to be the most successful design [299].

Del Campo et al. (2007) compared biomimetic arrays with various pillar shapes and found the mushroom configuration to have a pull-off strength 30 times that of cylindrical pillars [335]. Spatular tips provided an intermediate degree of adhesion, while concave tips and spherical tips were slightly better than flat cylindrical pillars. Spuskanyuk et al. (2008) hypothesized that part of

140

this larger adhesive force is due to the fact that mushroom-shaped tips are less adversely affected by edge defects than flat or cylindrical pillars [336]. Further, stress concentrations are reduced at the contact interface [298]. Several other papers [316,337–340] have examined the mushroom shape both experimentally and numerically and concluded that it is one of the best pillar designs for adhesion. Fleck et al. (2017) and Balijepalli et al. (2017,2016) considered fibril detachment as a crack propagating along the pillar-substrate interface and found that mushroom-shaped pillars reduce the corner stress intensity of the contact zone, thus reducing the likelihood of detachment [339] [338,340]. Review papers on the subject [293,294,296,298,299] have also noted several other benefits of the mushroom shape, including improved adhesion enhancement via contact splitting and increased crack trapping compared to flat cylinders.

Figure 4.17D shows a three-layered hierarchical arrangement of polyurethane fibers with mushroom-shaped tips. This arrangement was manufactured with soft-lithography and capillary molding. Fiber aspect ratio, fiber radius, hierarchical branching arrangements, and material selection are all important factors as well. Figure 4.17 shows some of the tradeoffs that come with different manufacturing processes. While the polyurethane tips in Figure 4.17D have controlled tip geometry, their aspect ratio and fiber density are much lower than that of the carbon nanotube tipped design in Figure 4.17B. Neither of these designs was able to incorporate the tilted structure shown in Figure 4.17C. The gecko pad's ability to optimize all of these different parameters simultaneously provides just another example of why natural keratin can be so impressive relative to manufactured materials and how there is so much for engineers to learn from nature.

The applications for gecko-inspired, dry, reversible adhesives are seemingly endless. One of the most popular uses of this emerging technology is soft robotics [341]. The reversible dry adhesion is ideal for (unsurprisingly) climbing and gripping. It has been utilized for numerous

commercial devices (like Onrobot's soft gripper and GECOMER's pick-and-place robotic systems) as well as countless academic pursuits [342,343,352–355,344–351]. Furthermore, several products utilizing adhesive materials based on the gecko pad are now commercially available from Geckskin, nanoGriptech, and Gottlieb Binder GmbH.

By way of their tunable and hierarchical structure, keratinous materials have evolved diverse methods to achieve reversible adhesion. In the feather, this is accomplished through the mechanical interlocking of hook-shaped barbs and barbules, while the gecko pad adheres to surfaces with van der Waals forces generated by its branched setal arrangement. These features have been translated to scaled up to macroscopic engineered systems (as in the feather-inspired 3D prints) and biomimetic nano and microscale structures (for the gecko setae).

4.2.4 Lightweight Structures

In engineering applications, sandwich structures are used for their ultra-lightweight, energy absorption capabilities, and comparable mechanical strength relative to bulk materials. Sandwich structures can be tailored by controlling the properties of the face (outer cortex) and core (foamy center) and their geometry. Typically, sandwich structures are constructed with a high modulus face and a low modulus core to achieve a lightweight yet stiff material with rectangular cross-sections. Sandwich structures are not limited to engineered materials and are found in abundance in keratin-based systems, including beaks [101], feathers [265,356], quills [251], baleen [243], and spines. Unlike engineered materials, the faces and core of biological materials are frequently made of the same material but occur in distinct phases: the face being more compact while the core is more porous. Here, we will review how the lightweight yet mechanically robust, keratin-based sandwich structures implemented in porcupine quills and hedgehog spines serve as the basis of lightweight bioinspired designs. While sandwich structures are not limited to keratinous materials,

its prevalence highlights the structural and functional diversity found in keratin systems that lend themselves to developing bioinspired structures.

The porcupine quill is composed of α-keratin and is a lightweight yet buckling-resistant structure that undergoes significant compressive and flexural loads during its service as a protective mechanism. The sandwich structure of the porcupine quill consists of a thin-walled cylindrical cortex enclosing a closed-cell foam. Some porcupine quills contain an additional structural element that reinforces the foamy center, which is referred to as a stiffener. The stiffeners have been found to increase the compressive strength and buckling resistance of porcupine quills [251]. Inspired by the stiffeners present in the porcupine quill, Tee et al. (2021) developed several 3D-printed cylinders with varying infill structures from uniform to non-uniform designs to mimic the radial structures found in the porcupine quill. However, mechanical testing was not performed, and little information is known on the degree of reinforcement the stiffeners provide and how their structure can be tailored [357].

Hedgehog spines are similarly structured to porcupine quills and contain reinforcing stiffeners, further classified as longitudinal stringers and transverse plates [358,359]. Despite their structural similarities, porcupine and hedgehog spines serve different functions. Hedgehog spines are adhered to within the skin and are primarily used as shock absorbers upon falling from great heights, while porcupine quills can readily detach from the body and serve as a defensive mechanism. Due to their high stiffness and capabilities for impact resistance, hedgehog spines are a suitable inspiration for developing lightweight yet mechanically robust bioinspired designs.

Drol et al. (2019), using X-ray microcomputed tomography, were able to capture the key internal structural design elements found in hedgehog spines, which were then used to create computational model abstractions in ABAQUS and compared to analytical models to better

understand the role that stringers and plates play in the spine's flexural performance. Ten models with increasing complexity were generated. The most basic level is a simple hollow cylinder (level 1) and builds up to most realistically represent the spine (level 10) with a complex arrangement of longitudinal stringers and periodically arranged branched transverse plates. The beam models were subjected to 3-point bending with a displacement-controlled boundary condition in which the bending stresses, the normalized bending stresses, and the Von Mises stress contours were quantified. The hollow tube, the simplest case, is reported to have the highest specific stiffness; however, the lack of stiffeners limits its ability to reduce buckling. The model with the next highest effective stiffness is model 10, the most complicated and representative model of the spine. Model 10 contains longitudinal stringers and branched transverse plates with the smallest spacing between the central plates and the longitudinal stringers and a more accurate curvature connection between the stringers instead of a blocked fillet. The build-in model 10 allows for removing material while maintaining stiffness, creating a lightweight yet stiff structure. The longitudinal stringers aid in increasing the bending stiffness by localizing material further away from the central axis, which effectively increases the second area moment. The transverse plates provide reinforcement and help distribute the applied load evenly, minimizing buckling and localized failure. Furthermore, this study provides insight into how the structural organization of keratin-based materials, such as the hedgehog spines, can be directly translated to synthetic designs to develop tailored stiff and lightweight structures. This study's findings have even inspired the development of novel football helmet liners to help reduce traumatic brain injuries. This example illustrates how bioinspired designs stimulate innovation [360].

The feather shaft is another example of how keratin can be used to achieve a lightweight yet mechanically robust structure that is able to withstand aerodynamic loads during flight. This

behavior is primarily attributed to the sandwich structure of the feather shaft. The feather shaft is composed of an outer shell of compact keratin that surrounds a medullary center made of foamy keratin. Liu et al. (2015a) investigated the hierarchical structure and mechanical properties of the peacock tail feather shaft under tension and compression. They determined that the presence of the foam center enhanced failure resistance by delaying splitting and buckling of the cortex shell and exhibits overall improved compressive stability [356]. While there has been a significant amount of work dedicated to understanding the structure and mechanical properties of the feather shaft, there have been limited attempts towards the development of bioinspired sandwich structures based on the feather shaft. We suggest that this is an area of study for future work.

Many keratinous materials manage to achieve good mechanical properties while limiting their mass. Often this is accomplished with a sandwich structure consisting of foam surrounded by a stiff exterior face. Since low density is a highly coveted trait in engineered materials, these natural keratinous systems have served as the basis for bioinspired designs aimed to capture high strength to weight ratios.

4.2.5 Structural color

Besides the outstanding mechanical, lightweight, and thermal properties of avian feathers, these keratinous materials are also known to display a diverse range of vibrant colors. This property is in part due to structural coloration, which arises from the interactions of light with a submicron array of varying morphologies which include multilayer structures (as seen in the iridescent throat patch of the hummingbird)[361], two-dimensional photonic crystals (as seen in the peacock feather and the mallard) [362–365], or spinodal-like channel structures [366] (as seen in the Eurasian Jay Garrulus glandarius). These nanostructures self-assemble and can occur as a multi-layered structure of β-keratin and a pigment-based protein (e.g., melanin, carotenoids), as shown in Figure

4.18A. The combination of structural color from the sub-micron array of keratin and the absorption from the pigment is referred to as color mixing. β-keratin has a low refractive index (~1.5), but when implemented in a multi-layer structure, it allows for high reflectance and vivid coloration [367]. The presence of pigments strongly contributes to the vibrant coloration due to their high refractive indices and broad absorption spanning the UV-visible range. Structural color in avian feathers can occur as iridescent or non-iridescent and is strongly dependent on the underlying structure and organization. Typically, long-range order is responsible for producing iridescence, while short-range order is non-iridescent [368]. Thus, structural color in avian feathers is highly tunable and thus a desirable candidate for bioinspiration.

Figure 4.18 Structural color found in avian feathers and bioinspired analogs. A) Violet-backed starling and TEM micrograph of the multi-layered structure of hollo melanosomes and a thin film of keratin. B) Structural color produced by SMNPs. C) Micrograph detailing the arrangement of SMNPs as a thin film. Adapted with permission [369]. Copyright 2015, American Chemical Society.
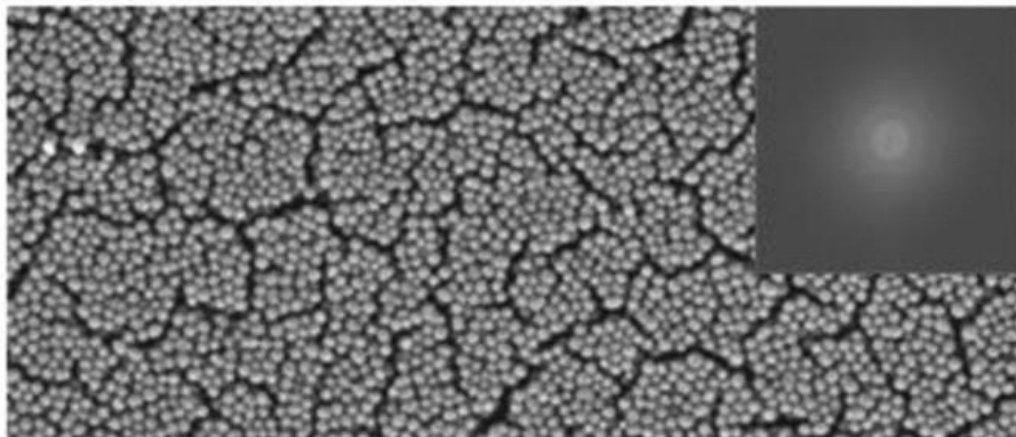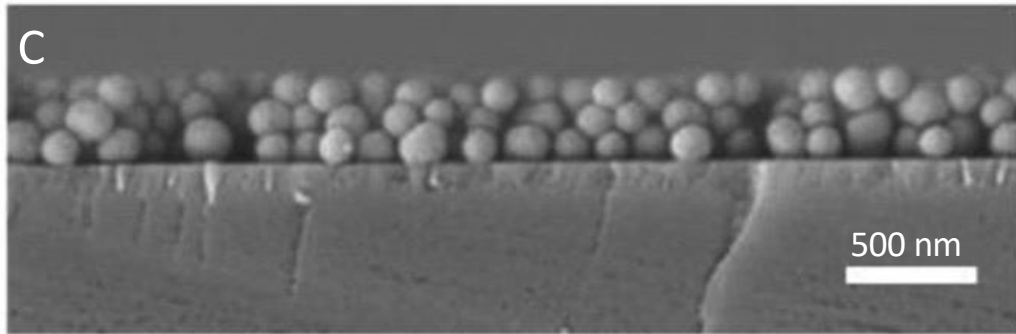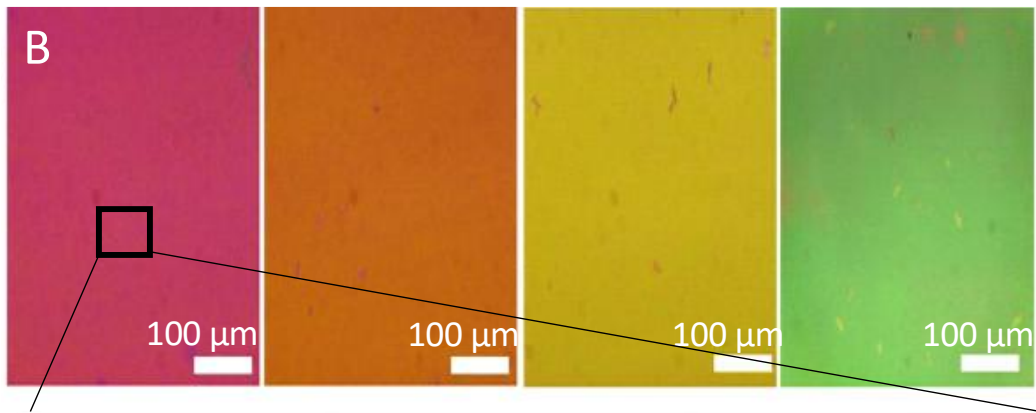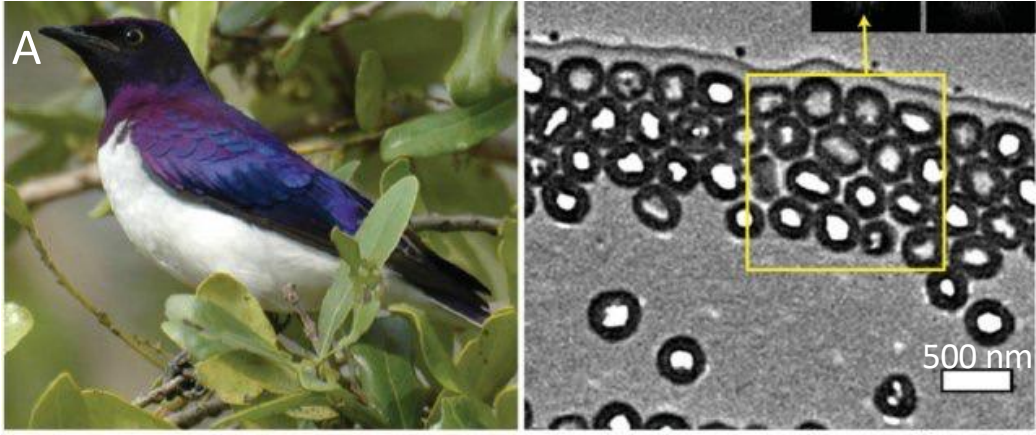
Despite the vast arrangement of keratin in combination with pigmentation and the subsequent multitude of colors with varying optical properties (iridescent vs. non-iridescent) found in bird feathers, there have been limited ventures at bioinspiration. The most prevalent study that draws inspiration from feathers is the development of structural color produced by self-assembly of synthetic melanin nanoparticles (SMNPs) inspired by the assembled melanosomes in avian feathers [369]. Xiao et al. (2015) used a vertical evaporation-based self-assembly method to develop thin films of SMNPs with a wide range of colors (red, orange, yellow, and green) (Figure 4.18 B,C). The coloration produced is attributed to the thickness of the thin film which can be controlled by the concentration and evaporation rate. Additionally, the morphology of the SMNPs influences the packing, and, therefore, the film thickness and coloration produced. In avian feathers, there exists a diverse range of melanosome geometries from spherical to oblong and hollow to filled. These morphologies can additionally tune the coloration produced, which is an exciting avenue for future work. The SMNPs have a broad absorption spectrum (high absorption at short wavelength and low absorption at long wavelengths) and a relatively high refractive index (~1.4-1.6 at 589 nm) which was found to be responsible for the enhanced color saturation and purity. In addition to the desirable optical properties, SMNPs are biodegradable and inherently biocompatible, making them suitable candidates for various applications [369].

Structural coloration is not limited in nature to keratinous materials and is additionally found in chitin-based materials such as the morpho butterfly and the exoskeletons of beetles [370]. These chitin-based systems have been extensively studied and have led to the development of numerous bioinspired structural colors [371–373]. Despite their lack of prevalence in bioinspired structural colors, there are still many opportunities awaiting to be explored in the field of avian

feathers. This highlights the importance of keratinous structural colors found in avian feathers and the vast potentials for these systems to serve as bioinspired candidates.

4.2.6 Hydrophobic surfaces

Hydrophobic surfaces are essential in both the engineering and the biological world. As such, researchers have been attracted to how living creatures can repel water by manipulating the contact angle of water droplets on their surfaces. Certain organisms, like ducks, excrete hydrophobic oils that can be spread on the surfaces of their feathers to repel water. Others, like the famous lotus flower, utilize nanoscale roughness to decrease the contact area of water droplets on their surface, with the two-fold benefit of keeping the organism dry while cleaning dirt and debris of the substrate as water droplets runoff. This phenomenon, dubbed the "lotus effect," has been observed in several keratinous systems as well, which is particularly intriguing because keratin itself is very water absorbent. It should be noted that, in nature, several hydrophobic strategies are often utilized in tandem. The duck feather, for example, also has significant surface roughness, which helps to repel water along with the oil excreted by its uropygial gland, while the lotus leaf's nanostructure is covered by a thin, hydrophobic wax film that helps prevent water from penetrating the epidermis. Thus, researchers have attempted to imitate the surface features found on hydrophobic keratinous systems to create synthetic, water-repellent materials.

Penguin feathers have not only superior thermal insulating properties but also remarkable anti-icing properties. Despite spending a significant amount of time in freezing temperatures and swimming underwater, ice crystals are not typically observed on penguins' feathers. The secret to the ice-phobicity of penguin feathers is in its rough micro and nanostructure, which traps air in grooves, preventing supercooled water droplets from adhering and coalescing. A schematic of this water repulsion mechanism can be seen in Figure 4.19A. This trapped air is also postulated to

provide a thermal barrier that reduces ice adhesion strength and heat transfer during icing. On the surface of the barbules and hamuli are grooves that are about 100 nanometers deep. These grooves are responsible for the surface roughness that creates the air pockets shown in Figure 4.19A [374].

Inspired by the penguin feather, Wang et al. (2016) used asymmetric electrode electrospinning to weave an anti-icing polyamide nanofiber membrane, as shown in Figure 4.19B [374]. The radially arranged fibers mimic the barb tips' structure, while other fibers randomly overlap this arrangement, creating a regular 3D network similar to that found in the feather. The fibers are densely packed near the triangular electrode compared to the fibers near the curved electrode, as shown in Figure 4.19 b1, b2, and b3. This fiber arrangement creates a gradient in the chemical surface structure. In the region of densely packed fibers, the static contact angle of water droplets was ~154° with a low adhesion force of ~37 μN. In this region, droplets struggled to permeate the tightly bound membrane. The few droplets that were able to adhere to the fibers coalesced with other droplets and resulted in self-propelled jumping, i.e., the droplets fell off the membrane naturally before freezing. As the distance between the fibers increases, more droplets were able to penetrate the membrane. The static contact angle and adhesion force of the water droplets were measured at 105.1° and 102μN, respectively. Figure 4.19C shows the gradual change in these values through the membrane's radius. Droplet coalescence and jumping did not occur when the fibers' distance was greater than the diameter of droplets. After 3-4 hours at -5°C, some frost and ice were found on the less densely packed fibers but not in the densely packed fibrous network. This result shows that by tuning the density of the overlapping nanofiber network, anti-icing properties similar to those found in keratinous penguin feathers can be achieved.
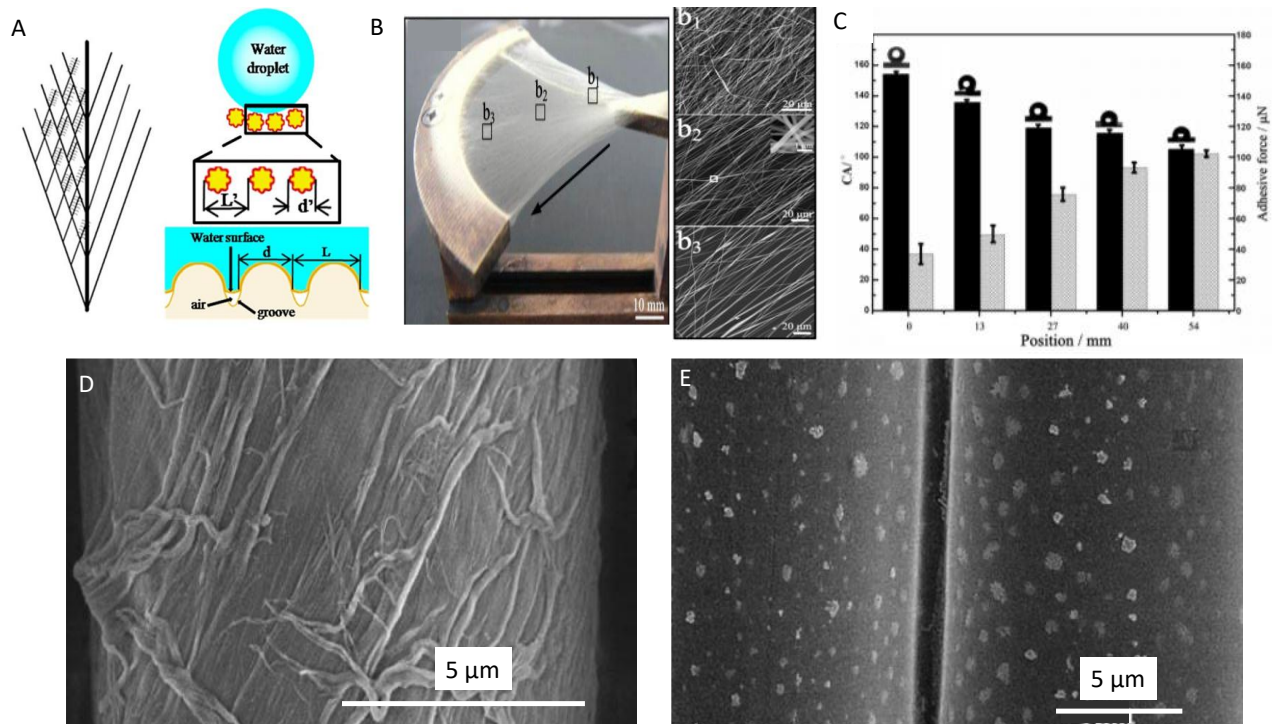
Figure 4.19 The multiscale surface roughness and fine nanoscaled grooves on feathers help them repel water. A) Schematic showing how the hamuli on penguin feathers trap air beneath water droplets creating an air cushion and minimizing the amount of material in contact with the water. B) Bioinspired polyamide nanofiber membrane fabricated via asymmetric electrode electrospinning. C) Chart of contact angle and adhesive force versus location on the polyamide membrane highlighting the effect of fiber density. Reproduced with permission [374]. Copyright 2016, American Chemical Society D) SEM image of cotton fiber with precipitated chitosan nanoribbons on the surface inspired by duck feathers. E) SEM image of polyester fibers with precipitated chitosan "nanoflowers" on the surface. Reproduced with permission [271]. Copyright 2008, IOP Publishing Ltd.

Waterfowl, ducks in particular, are so famous for their anti-wetting capabilities that the phrase "like water off a duck's back" has worked its way into our everyday lexicon. Until recently, it was generally thought that this extraordinary hydrophobicity arose from the low surface energy of preening oil excreted from glands at the base of their tail and spread over the feathers. However, recent studies [375] of preening oil on smooth surfaces have revealed that it is not that special after all and is less hydrophobic than several synthetic resins and oils. The feather's structure, coupled with preening oil, makes water run off of a duck's back so efficiently. Like penguin feathers, duck

feathers have multiscale textures, with the same branched structure and micro-sized surface features covered with nanoscale grooves and protuberances. Liu et al. (2008) mimicked this structure by precipitating chitosan nanostructures on the surface of textile microfibers. They did so by dip-coating fibers in an acidic solution containing chitosan before placing them in an ammonia gas environment. The ammonia is absorbed by the film, making the solution basic and causing the cationic polyelectrolyte chitosan to precipitate in nanofeatures on the textile substrate's surface. On cotton fibers, the chitosan formed long ribbons (Figure 4.19D), while on polyester fibers, the chitosan shrank down to nanosized flower shapes (Figure 4.17E). The result is a hierarchical arrangement of surface irregularities where the fibers themselves compose the microscale roughness, while the chitosan precipitates form the nano roughness. Once the fibers are dried, they are treated with polysiloxane to lower the fibers' surface energy (similar to the preening oil found on natural duck feathers). With just the polysiloxane treatment, the contact angle of a water droplet was 118° for cotton and 100° for polyester. When combined with the chitosan surface roughness, these values rose to 152° and 148°, respectively, showing how the combination of a low surface energy film and surface roughness, similar to feathers, can lead to the development of superhydrophobic materials [271].

The oberhautchen (thin outer layer) of many lizard and gecko skins is composed of β-keratin. Many geckos also have tiny keratin spinules upon this outer layer that serve to repel water and disrupt bacterial growth. Figure 4.20A (i-iii) shows images of the scales of Strophurus williamsi, a species of arboreal geckos found in Australia. Generally, these spinules are 0.5-4 μm long packed closely together with over 400 spinules per 10 μm². These spinules are mounted upon scales that have a honeycombed-shaped basal layer composed of intersecting ribs. The static contact angle of water droplets was similar to that of feathers, ranging between 151-155°.

Interestingly, gecko skin accomplishes such impressive superhydrophobicity from its spinule density rather than finer roughness structuring like the channels found on insect hairs or the hamuli in penguin feathers. These hairs not only prevent water from building up on the skin of the gecko but also allow the skin to clean itself, removing harmful bacteria and contaminants as droplets coalesce and run off the gecko with even the slightest tilt or perturbation [270].

Green et al. (2017) developed a benchtop biotemplating apparatus to fabricate synthetic replicas of gecko skin spinules with comparable hydrophobicity to emulate their antibacterial properties. To do so, negative molds were generated by coating shed gecko skin, which was adhered to a glass slide by a thin layer of water, with commercially available PVS. The water also served to inflate the spinules to mimic their natural state better. This negative mold was then used to fabricate gecko skin replicas from several different polymer solutions targeted towards various applications. These included a synthetic polystyrene solution and natural biopolymer solutions of chitosan, silk fibroin, fused bilayers of chitosan and alginate polysaccharides, and blended α-keratin hair extract [376].

Each solution was successfully used to form a replica of the gecko skin nanostructure; several images of the natural shed gecko skin compared with the polystyrene replica are shown in Figure 4.20A (iv-vi). Some of the solutions were able to more closely mimic the gecko spinules' dimensions, as visualized in Figure 4.20B. The curing process had a significant effect on the ability of each solution to closely resemble the geometry of the natural gecko spinules. For example, the polystyrene solution hardens slowly due to organic solvent evaporation, which resulted in stiffer spinules with less curvature. The metrics for measuring curvature in the spinules are shown by images "d" and "e" in Figure 4.20B. The chitosan-based replicas, on the other hand, closely mirrored the curvature of the nano tip, as well as the thickness and height of the natural spinules.

The biomimetic samples were only slightly less hydrophobic than the natural gecko skin obtaining a contact angle of about 134º. The synthetic spinule arrays also revealed notable anti-bacterial properties. Confocal microscopy showed that the spinules effectively disrupted bacterial cultures grown on the replicas removing as much as 95% of bacteria from the surface after water treatment. Vucko et al. (2008) developed a similar procedure using epoxy molds of live geckos to observe their oberhautchen without needing to kill and prepare them for SEM examination. This approach is highly applicable to other organisms and other research fields since it can be non-destructively performed on living creatures while generating finely detailed replicas for observation or functional use [377].
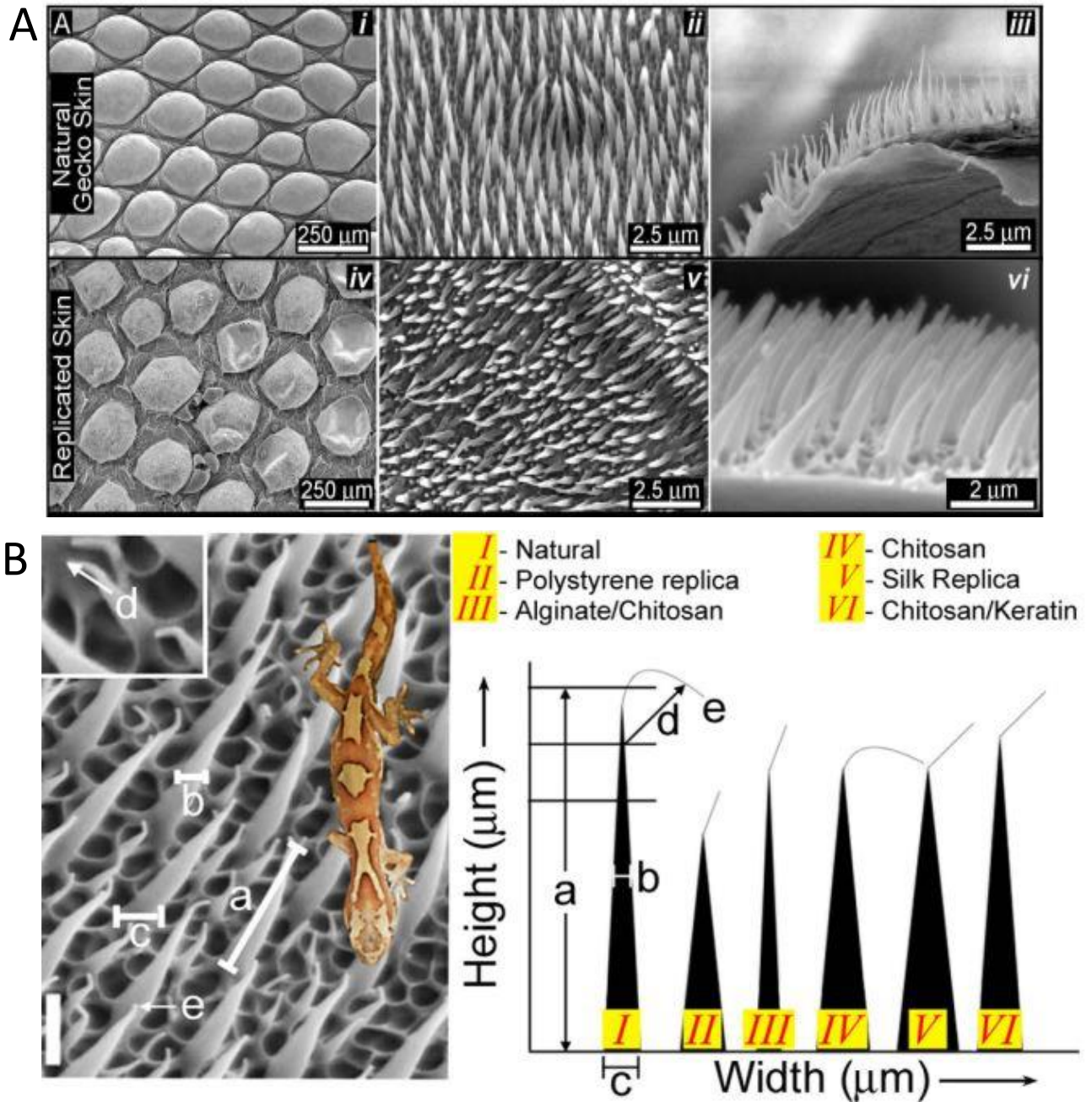
Figure 4.20 Much like the gecko pad, the outer layer of skin on the gecko has hydrophobic, self-cleaning properties due to its rough mesostructure, which researchers have attempted to replicate. A) SEM images of natural gecko skin (i-iii) alongside SEM images of biomimetic polystyrene replicas made via biotemplating (iv-vi). B) Close-up SEM images of gecko spinules and the different measurements used to characterize them (left). Various biomimetic replicas, like the ones shown in A iv-vi, were prepared using several polymer solutions. The resultant spinule shapes are visualized (right) and compared to the natural spinules found on the gecko. Open access [376]. Copyright 2017, the authors.

Many keratinous materials that provide thermal insulation also protect organisms from getting wet because significant surface roughness benefits both areas. In the case of hydrophobicity, this roughness comes in many forms in nature, such as hamuli, nano grooves, or spinules, but all have the objective of reducing the area in contact with water droplets allowing them to run off the surface efficiently. Like research on thermal insulation and reversible adhesion, studies on bioinspired surface roughness to achieve anti-wetting properties have shown great success and are a promising research area for bioinspiration.

4.3 Keratin as a Material for Engineered Systems

So far, we have seen how keratinous structures provide beneficial properties that can be used to inspire engineered designs. However, keratin itself has often been utilized as a material for various applications due to its unique intrinsic properties. Over the past few decades, many researchers have explored how to connect different technologies such as materials science, applied health sciences, and engineering. This section will discuss possibilities to use keratin for applications in the: i) biomedical, ii) composite, and iii) reversible material realms.

Historically, keratin was one of the first polymers used by humans before the plastics revolution in the 20th century. Keratin extracted from tortoise shells has been used to craft fine components, like hairbrushes, for hundreds of years, while baleen from whales was famously used to make corsets [216,258]. Hair (typically human or horsehair) has also had versatile applications ranging from paintbrushes to the torsional springs used in ancient Greek and Roman artillery. Researchers have recently explored natural macromolecules as candidates to perform biochemical, mechanical, and structural roles due to their appealing properties.

Keratin can be extracted from various sources (typically wool, poultry feathers, or hair) using different extraction methods. Common extraction methods include oxidative and reductive extraction, steam explosion extraction, or ionic liquids and eutectic solvents [378,379]. Studies involving oxidative technologies and reductive extraction were initially applied to animal horns and hooves but were also used to extract keratin from wool and human hair. Early studies on the properties of extracted keratin led to increased interest in exploring keratin for medical applications. Among the first innovations were keratin powders for cosmetics, fibers, composites, and coatings for drugs [380–383].

4.3.1 Biomedical usage

Recently there has been a significant increase in the number of biomedical studies related to using keratin-based biomaterials. This variety of applications includes bio-medicine, natural polymer flocculants, bioelectronics, bio lubricant formulations, and manufacturing bone scaffolds [384]. Keratin is widely used in biomedical applications due to its biocompatibility, lack of immune reaction upon transplant, good cellular interaction, and biodegradability [383,385].

Asia has taken the lead in keratin biomaterials research since the first medical application of pyrolyzed human hair by a Chinese herbalist dates from the 16th century [386]. In the modern age, scaffolds, hydrogels, powders, films, and fibers have been prepared, starting with early studies by Japanese scientists [387,388] in 1982 on vascular graft production with hemostatic properties. Researchers have also shown that keratin can be effectively used for peripheral nerve regeneration, drug delivery, hydrogel formation, and films that promote wound healing [383]. For medical applications, keratin has shown interesting characteristics, but its potential has not yet been fully explored. For example, areas such as wound healing, bone regeneration, peripheral nerve repair, antimicrobial activity, hemostasis, and cell adhesion of amino acid sequences (due to the Arg-Gly-

Asp and Leu-Asp-Val binding motifs) have led to increasing interest in keratin for medical applications. Though keratin-based biomaterials show wide promise, there can be significant costs associated with the extraction and processing of keratin and its post-processed mechanical characteristics. In 1983 and 1985, researchers from Japan and the UK, respectively, published papers speculating on the prospect of using keratin as the building block for new biomaterials [389,390].

Also, keratin biomaterials derived from wool and human hair have been shown to possess cell-binding motifs, such as leucine-aspartic acid-valine (LDV) and glutamic acid-aspartic acid-serine (EDS) binding residues, which are capable of supporting cellular attachment. Together, these properties create a favorable three-dimensional matrix that allows for cellular infiltration, attachment, and proliferation. Thus, the conservation of biological activity within regenerated keratin biomaterials could prove advantageous for controlling specific biological functions in various tissue engineering applications [383].

Reconstituted biopolymers often suffer from inferior mechanical properties, which can pose a challenge for processing and limit applications. This is especially true for biomaterials made from extracted keratin fibers, despite the stellar mechanical properties found in natural keratinous materials. Thus, many studies have targeted keratin films, focusing on the physical strength and flexibility of the films while maintaining their excellent biological activity [383]. The addition of other biopolymers such as chitosan or silk-fibroin improves the mechanical properties of keratin. The chitosan-keratin films also had beneficial anti-microbial properties and proved to be suitable substrates for cell cultures [391–393]. For silk-fibroin and keratin films, studies have shown that the two molecules interact synergistically and provide unique properties not found in pure keratin or silk-fibroin films. For example, the polarity of keratin's amino acids causes silk-fibroin to

159

rearrange from a random-coil to β-sheet configuration [394,395]. As a result of these unique interactions, the combined film is more biocompatible [396,397] and biodegradable [398] than its constituents.

Keratin has also been explored as a raw material for cell scaffolds and shows significant promise due to its ability to self-assemble into complex 3D shapes. A host of fabrication techniques from electrospinning [399], wet spinning [400], photomask micropatterning [400], and compression molding/particulate leaching [401] to freeze casting of aqueous keratin solutions [402,403] have been used to create keratin scaffolds. These scaffolds have many advantages, including a stable homogenous, interconnected, porous structure [402,403], free cysteine residues that can be used to bind bioactive substances to the scaffold surface [404,405], and resorbability [406] that make it a suitable material for tissue engineering and drug delivery [392,393,403,407,408]. These properties have also led to studies on keratin-based biomaterials for wound [392,399,409,410] and burn dressings [411].

Composite films of keratin and synthetic polymers have also been fabricated to create films with even better mechanical properties. For example, poly (diallyl dimethylammonium chloride) and poly (acrylic acid) were blended with keratin extracted from wool to fabricate thick films based on the principle of poly ionic complexation. This was accomplished using a layer-by-layer self-assembly method [412–414]. Keratin blends with poly(ethylene oxide) have also been explored for usage as scaffolds for cell growth, wound dressings, and drug delivery membranes, while keratin mixed with polyamide 6 has been envisaged as a practical material for biomedical devices, active water filtration, and textile fibers [415].

Keratin's emerging role as a medical biomaterial revolves around many of the same aspects that make it a successful biological material. Its tunable properties and architecture make it viable

for numerous different applications, while its abundance and natural origin make it appealing to researchers as an economical, sustainable, and biocompatible material. However, it is limited by the mechanical weakness of reconstituted keratin and the lack of cheap and scalable extraction techniques [378].

4.3.2 Composites

Composite materials have steadily grown in popularity over the past decades due to their lightweight yet mechanically robust properties. However, these synthetic materials are traditionally produced from petroleum-based plastics, which are increasingly expensive and environmentally harmful. Many researchers aim to tackle this problem with biodegradable, renewably sourced composites made of biopolymer matrixes and natural fibers. Knowledge of the properties of available biodegradable polymers and natural fibers is essential for manufacturing a biodegradable composite [416].

Polymers reinforced with natural fibers, commonly named "bio-composites," have started to be used industrially in the automotive and building sectors as well as the consumer goods industry. Green composites are a specific class of bio-composites where a bio-based polymer matrix such as a biodegradable polyurethane is reinforced by natural fibers such as keratin [417–419]. Väisänen et al. (2016) describe natural fiber-polymer composites (NFPCs) as renewable and sustainable materials since they are composed of natural fibers embedded in a polymer matrix which may also be of biological origin (e.g., polylactic acid, PLA) [420].

Recently, Conzanatti et al. (2013) reported on the valorization of keratin-based wastes, made of unserviceable poor quality raw wools from farm breeding, fiber byproducts from textile processing, and horns, nails, hair, and feathers from butchery. Zoccola et al. (2009) estimated that keratin wastes from breeding, butchery, and textile industry, made up of wool, hair, feathers, beaks,

hooves, horns, and nails, have been estimated worldwide to be more than 5,000,000 tons/year [421]. With an increasing demand for sustainable materials, these protein byproducts are beginning to be regarded as renewable resources worthy of better exploitation [422].

Extracted keratin has also gained popularity as a component for composite production as both a filler material and a fiber reinforcement. This interest is primarily driven by keratin's availability and environmental benefits (biodegradable, renewable, leftovers from other products) on top of their beneficial properties.

Donato et al. (2019) discussed the manufacturing of keratin-based composites with different polymers in detail [423]. To form efficient keratin-polymer composites, it is essential to have good adhesion between the fiber and polymer matrix. Since keratin fibers have numerous hydrophilic surfaces, this can lead to weak mechanical properties of the overall composite material. As a result, coupling agents are sometimes required to boost interfacial adhesion. For example, Song et al. (2017) used functionalized cellulose nanocrystals to crosslink keratin fiber while also serving as reinforcement. This interfacial treatment resulted in marked improvements in tensile strength, elongation to failure, and toughness of such a composite. Further, the incorporation of cellulose nanocrystals reduced the keratin's water sensitivity which is a barrier for many in-vivo applications [424]. More approaches to coupling agents and keratin-polymer composites are discussed in detail by Shavandi and Ali [425].

As attractive as synthetic polymers are, their use is coming under scrutiny due to the realization that petroleum reserves are finite and that oil prices are likely to rise steadily over the next few decades. Furthermore, with global environmental awareness at an all-time high, synthetic polymers have lost some of their luster. The synthetic fiber industry as it currently exists will ultimately decline and be replaced by an industry based on renewable feedstocks [426]. Recent

works on the mechanical properties of fibers isolated from hagfish slime suggest that these unique fibers may one day be replicated in a way that is environmentally sustainable and economically viable. These 'slime threads' consist of bundles of 10 nm protein nanofibers known as intermediate filaments, which form part of the cytoskeleton in most animal cells [427,428]. Keten et al. (2010) explored the nanoconfinement of β-sheet crystals in silk as a means to control stiffness, strength, and toughness. This study highlighted another feature that makes β-sheet crystals an attractive model: they self-assemble from soluble precursors into 10 nm filaments in aqueous buffers [429]. The key to the high strength and toughness of spider silk and hagfish threads are the β-sheet crystallites that simultaneously crosslink the protein molecules and arrange them into a structure in which 'sacrificial bonds' increase the energy required to break the material [427,429,430].

Pourjavaheri et al. (2018) developed a bio-composite from chicken feather waste and thermoplastic polyurethane. This composite material was fabricated via solvent-casting evaporation at eight different compositions. The thermo-mechanical properties of the composites were assessed using thermogravimetry, dynamic mechanical analysis, and stress-strain measurements with hysteresis loops. The results showed that keratin derived from a current waste product from the poultry industry could effectively and cheaply provide the thermo-mechanical properties required of composite materials [431]. Similarly, Tran and Mututuvari (2016) developed composite materials made from keratin, cellulose, and chitosan combinations. They found that adding cellulose and chitosan improved the mechanical and thermal stability of the overall material but hindered the reformation of α-helices. Instead, when combined with these biopolymers, the keratin preferred the extended β-sheet morphology or amorphous configurations [432].

4.3.3 Reversible materials

Another attractive characteristic of keratin as raw material is its mechanical reversibility. This reversibility can be found in keratin due to the transition from α-keratin helices to β-keratin sheets. This transition has been observed as a result of stress along the longitudinal axis of the α-helix as well as heat absorption or from a combination of the two [433–437]. Recently, Cera et al. (2021) have captured this reversible process using hydration as a trigger to fabricate 3D-printed, hierarchical shape-memory materials out of keratin extracted from animal hairs. Impressively, this material had a tensile strength and Young's modulus orders of magnitude higher than conventional water-triggered shape-memory materials [438].

Fibrillar keratin was extracted from ground Angora wool using LiBr to induce a solid-liquid phase transition of the crystalline keratin and DTT to cleave the disulfide bonds in the hair matrix at 90 C^o. The product was then filtered, cooled, centrifuged, and separated to obtain concentrated fibrillar keratin quantities. This extraction process is shown in Figure 4.21A. When subject to shear stress and spatial constraint, the extracted keratin protofibrils self-organized into a nematic crystal phase. Adding NaH_2PO_4 to the extracted keratin allows for tighter control of the nematic phase by introducing a charge screening effect which causes the keratin fibrils to interact more. This process makes the crystalized proteins stiffen and pack closer together with more alignment. The result is a shear-thinning, viscous, keratinous solution that is ideal for extrusion processing and whose properties can be tuned via the NaH_2PO_4 concentration.
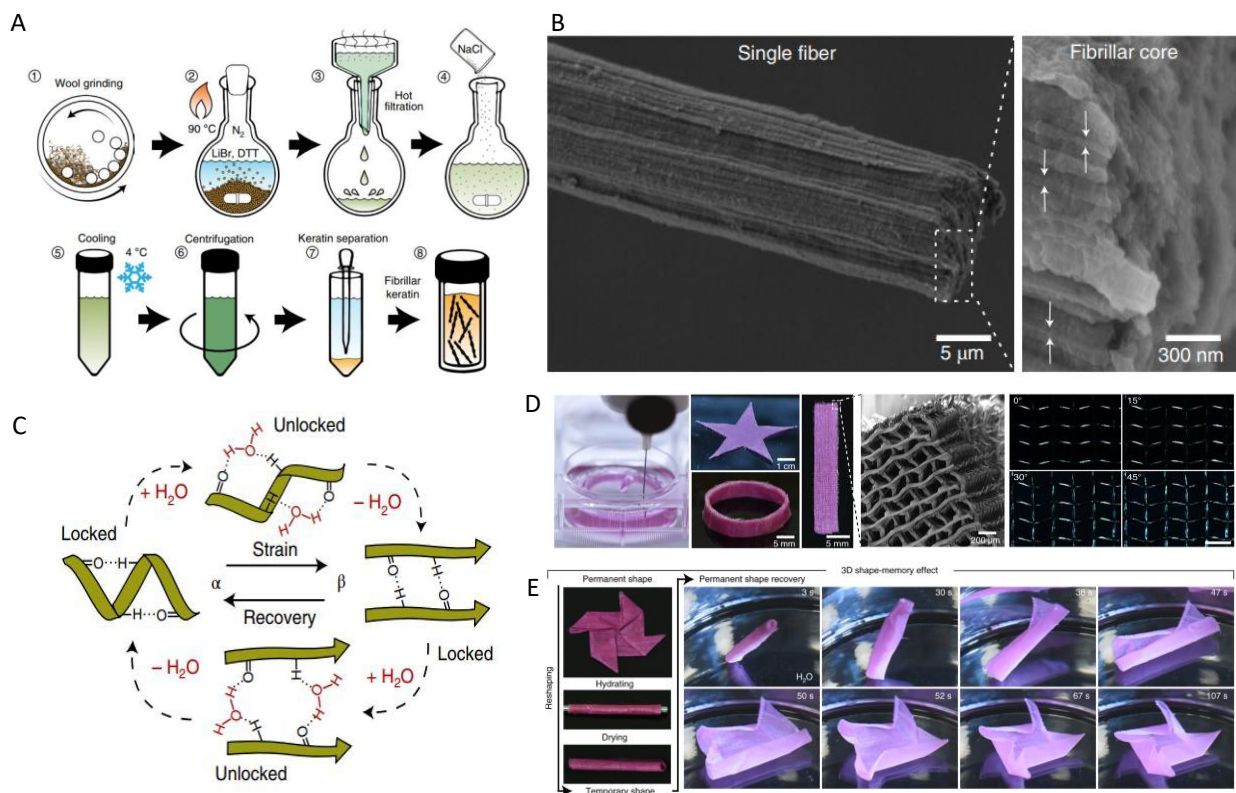
Figure 4.21 Advances in 3D printing technology have recently made printing different biological materials more feasible. Cera. et al. (2021) have recently utilized these advances to fabricate hydration-induced shape-memory components out of keratin. A) The keratin extraction process used to obtain printable, fibrillar keratin [438]. B) To obtain aligned fibrils, keratin fibers were fabricated using traditional wet-spinning. The resultant hierarchical structure is visualized here. C) Schematic of the atomic scale process for using water to lock and unlock the hydrogen bonds within α-helices or between the β-sheets. This mechanism endues the material with shape recovery properties. D) Images of the keratin printing process and final products (left); SEM image of the fine detail that can be obtained; birefringence images showing the alignment of the keratin fibers in the woven structure. E) Series of still images of the hydration-induced shape recovery of the printed samples composed of keratin, showing the prints returning to their initial form over a matter of seconds when submerged in water. Reproduced with permission [438]. Copyright 2020, the authors.

To maximize uncoiling when loaded and to improve tensile strength and strain-to-failure, α-helices were aligned using traditional wet-spinning. Spun fibers were exposed to hydrogen peroxide to restore the disulfide network of the keratin. Figure 4.21B shows that the keratinous fibers (~10 micrometers in diameter) maintained a hierarchical structure, with a core composed of fibrils that are approximately 50 nm in width. When stretched in the wet state, the α-helices unwind

into β-keratin sheets. As the fibers dry while under a constant load, hydrogen bonds begin to form between the β-sheets, fixing them in place and making them metastable. In fact, when stretched to 80% strain and held in place for 10 minutes at room temperature, the fibers only shrunk back to 77% strain, showing the efficacy of these hydrogen bonds for locking the keratinous fiber into its new fixed shape. Upon rehydration, the hydrogen bonds are disrupted, and the fiber can return to its original shape. This process is visualized in Figure 4.21C.

Due to the shear-thinning properties of the keratinous solution, small diameter extrusion needles can be used to print different geometries with textural features on a scale of 50 micrometers. The keratinous material was printed into a hydrogel which served as support as well as the coagulation bath. The keratin protofibrils aligned themselves along the print pathway, allowing finer control of the material's shape memory properties. Figure 4.21D shows the 3D printing process to fabricate a flat star, ring, and flat strip. The middle image shows an SEM of the fine details that could be produced. The images on the right are birefringence images that show the common alignment of the keratin protofibrils. Once the keratinous material has been printed, it can be further manipulated into new shapes before the disulfide network is reformed by exposing the print to hydrogen peroxide. Figure 4.21E shows a square print that was folded into an origami star shape before the disulfide network was reformed. Once the star shape is set with the hydrogen peroxide, water can be used to trigger shape recovery even when it has been deformed into a tube. In this case, it takes less than 2 minutes for the tube to recognizably transform back into the star origami arrangement, as seen in Figure 4.21E [438].

4.4 Conclusions

The aim of this chapter is to establish a link between keratin as a fibrous biopolymer and as a material of engineering interest due to its wide-ranging functionality. Keratin fills many

different niches in nature due to its inherent properties and its geometric tailorability on multiple length scales derived from its self-assembled hierarchical structure. We established the importance of each of these aspects by exploring keratin as a source of design inspiration alongside the keratin as a raw material for engineered systems.

Keratinous systems have been used to inspire materials with mechanical, thermal, reversible adhesive, lightweight, structural color, and hydrophobic characteristics. These bioinspired designs have not only been used to understand the success of biological materials better but have served also as a creative platform for researchers to extend natural design ideas beyond the limitations of nature, laying the groundwork for the next generation of functional materials. Keratin also has been used as filler or reinforcement in composites with an eye towards environmentally sustainable production and specific biomedical applications. Keratin's prolificity in the industrial world in wool and feathers alongside its beneficial material properties makes it a desirable constituent for expensive components like biomedical materials or fiber-reinforced composites.

4.5. Future Directions

Keratin has a lot to offer to the scientific and engineering communities, but several obstacles need to be overcome to convert its propitious potential into reality. Here we suggest several future directions to maximize the impact of keratinous materials on the engineering and scientific communities:

- **Material selection**
  - As discussed in Sections 1 and 3, keratin has a hierarchical structure that allows for tailorable material properties. When manufacturing bioinspired components, it can

be challenging to find a material that matches the properties (i.e., Young's Modulus, strength, toughness, viscoelasticity, conductivity, density, and others) of natural keratin. This can make translations of natural keratinous designs to synthetic systems challenging. Recent developments in the 3D printing of keratin [438] have the potential to eliminate this issue by allowing bioinspired designs to be printed using keratin.

- **Hierarchical Structure**

    o As shown in Figures 4.1 and 4.2, keratin has an inimitable hierarchical structure that plays an important role in its extensive functionality, i.e., atomic-scale hydrogen bonds in the amino acids make keratin's properties highly tunable via moisture alongside the nanoscale α-helices, which allow for a phase transition at 20% strain while mesoscale features like lamellae, spinules, or spatulae, toughen, repel water, or adhere to surfaces, respectively. Engineers have struggled to replicate the multiscale ordered arrangements found in keratinous systems that help them be so multifunctional, and this remains a major challenge for the field going forward.

- **Exploration of additional keratinous materials in nature**

    o While there has been significant research on various keratinous systems, there are other keratinous materials that have not yet been studied, particularly amongst reptiles and birds. Much of the research on keratin has revolved around its role in wool, hair, or human skin, which all possess the α-keratin. However, much less is known about β-keratin. Further, each keratinous system bears its unique structure

optimized for its role in an organism. Exploring more keratinous systems will continue to reveal new design motifs and inspiration for engineered materials.

- **More bioinspired designs**

  o Similarly, some keratinous systems have been explored, but few attempts have been made to replicate their structure in synthetic materials. These include pangolin scales, butterfly cocoons, nails, talons, claws, and beaks, amongst others.

- **Multifunctional bioinspired designs**

  o Harrington et al. (2016) eloquently state : "in the case of biological materials, a battery of selective pressures encountered over the evolutionary history of the organism influence the final product," and as such biological materials are always multifunctional [439]. However, engineers often replicate these materials with a singular objective in mind, ignoring the tremendous benefits of a multifunctional material. An exception is the gecko pad, where researchers have perused its reversible dry adhesion, self-cleaning capabilities, and toughness [296,298]. Taking a multifunctional approach to each bioinspired design could help to develop superior materials that can be used for numerous applications at once.

- **Focus on different length scales**

  o A vast majority of the work on bioinspired keratinous materials has been done at the macro, meso, or micro scale and is often scaled up for fabrication. An increased focus on generating these structures at their natural length scale could help recapture the original material's properties. Similarly, a broader thrust in exploring the nanoscale behavior of keratin could help develop hierarchical materials or

unlock further functional mechanisms that larger-scale experiments have not revealed.

- **Numerical and analytical modeling**
  - Modeling is a beneficial way to understand the structure-property relationships, particularly for a complex biopolymer like keratin. Improved models would help to understand better the hierarchical synergies in keratin and which design parameters are most important for different functionalities.

Listed above are just some of the possibilities for future work on keratin as an engineering material. However, this list is not necessarily specific to keratin. Many other biopolymers like collagen, elastin, and chitin have similar wide-ranging usages in nature. Uncovering what niches each of these biopolymers can fill, how they succeed in so many different environments, and using them in engineered materials will provide a wealth of knowledge to the engineering community. All of this comes with the added benefit of biopolymers being renewable resources. With so many different utilities, understanding and replicating keratin-like structures has the potential to touch every corner of society.

4.6 Acknowledgements

Chapter 5. Impact Resistance in Equine Hooves

5.1 Introduction

Each of the specific architectures identified by Lazarus et al. [75] are found in the horse hoof wall which has shown remarkable impact resistance and fracture control properties. These arrangements exist in a hierarchical assembly, meaning they are exhibited on multiple different length scales. While nature's intricate hierarchical designs are still outside of engineers' grasp, these types of configurations often bear more finely tuned mechanical properties including improved energy absorbance, higher toughness, and selective anisotropy [75]. The hoof wall also contains several other key design features that have proven to be vital for beneficial mechanical properties including a composite nature, viscoelastic behavior, and unique porosity distributions.

The hierarchical structure of the equine hoof wall can be seen in Figure 5.1. On the mesoscale, the hoof wall contains tubules that are approximately 40-100 μm in diameter [82]. The shape, size, and density of the tubules vary through the thickness of the hoof, gradually becoming more elliptical, smaller in cross-section, and more densely packed closer to the exterior of the hoof wall [99,440]. These tubules have a mostly hollow medullary cavity at the center, which is surrounded by a stiffer tubule wall. The wall is made of helical lamellae composed of thin pancake-shaped cells filled with nanoscale keratin intermediate filaments (IFs) [80,97]. The IFs are crystalline and act as fiber reinforcement for the hoof wall. Huang et al. [78] observed thin "bridges" within the medullary cavity but did not extensively study these structures. The tubules are embedded in a softer matrix composed of irregular, polygonal, keratin-filled cells [78]. These cells form lamellae that generally run orthogonally to the tubule axis but can also vary in

orientation throughout the hoof wall [81]. The surfaces of the cells that compose these lamellae are sutured, providing increased mechanical stability through physical interlocking of the ridged interfaces. The hoof wall also contains a gradient in stiffness from the exterior of the hoof wall to the interior (near the living tissue) that arises from a hydration gradient, changes in reinforcement (from the tubule arrangement), and possibly variations in the IF density [81,98,245,440].

Multiple studies have explored the mechanical properties of the hoof wall and uncovered intriguing structure-property relationships. The tubules, with their anisotropic intertubular lamellae, have been reported to deflect cracks, increasing fracture toughness and providing the hoof a degree of crack path control [79,80]. Kasapi and Gosline [79,81] noted tubule pullout during tensile tests but suggest that crack deflection is the primary energy dissipative role of the tubules. Further, they postulate that IF orientation dominates crack propagation in the hoof wall and nearly always causes cracks to deviate away from the interior of the hoof confirming the previous compact tension results of Bertram and Gosline [80]. Like other keratinous materials [26,28,29,78,230,245,249,259,272,441], the mechanical properties of the horse hoof are highly susceptible to hydration and strain-rate. Bertram and Gosline [97] measured an approximately 36 fold increase in tensile elastic modulus between samples held in a 100% and 0% relative humidity environment. Kasapi and Gosline [79] observed a 3 fold increase in elastic modulus between tensile samples tested at a strain rate of $1.6 \times 10^{-3}\,s^{-1}$ and $70\,s^{-1}$.

Despite the extensive research on the hoof wall's mechanical properties there are still numerous knowledge gaps. Many of the previous studies on the hoof wall's fracture control properties have focused on samples tested in tension [79–82,97]. While this can yield valuable results the primary loading mode of the hoof is in compression. Furthermore, nanoscale keratin experiences a transition from alpha helices to beta sheets when loaded in tension

172

[236,244,442,443] but this has never been reported in compression. Of the studies that have utilized compressive tests, they have either been performed with a single cross-head speed [98,440] or used narrow or less precise hydration ranges [78,98]. Only two studies have explored the hoof's response to non-quasi-static strain rates. Kasapi and Gosline [79] used a compact tension arrangement with the cross-head attached to a pendulum to generate tensile strains of ~$70s^{-1}$, while Huang et al. [78] used a split Hopkinson pressure bar to attain strain-rates of ~$1000s^{-1}$. Neither of these tests provide a realistic impact scenario for what the horse hoof would experience in-vivo.
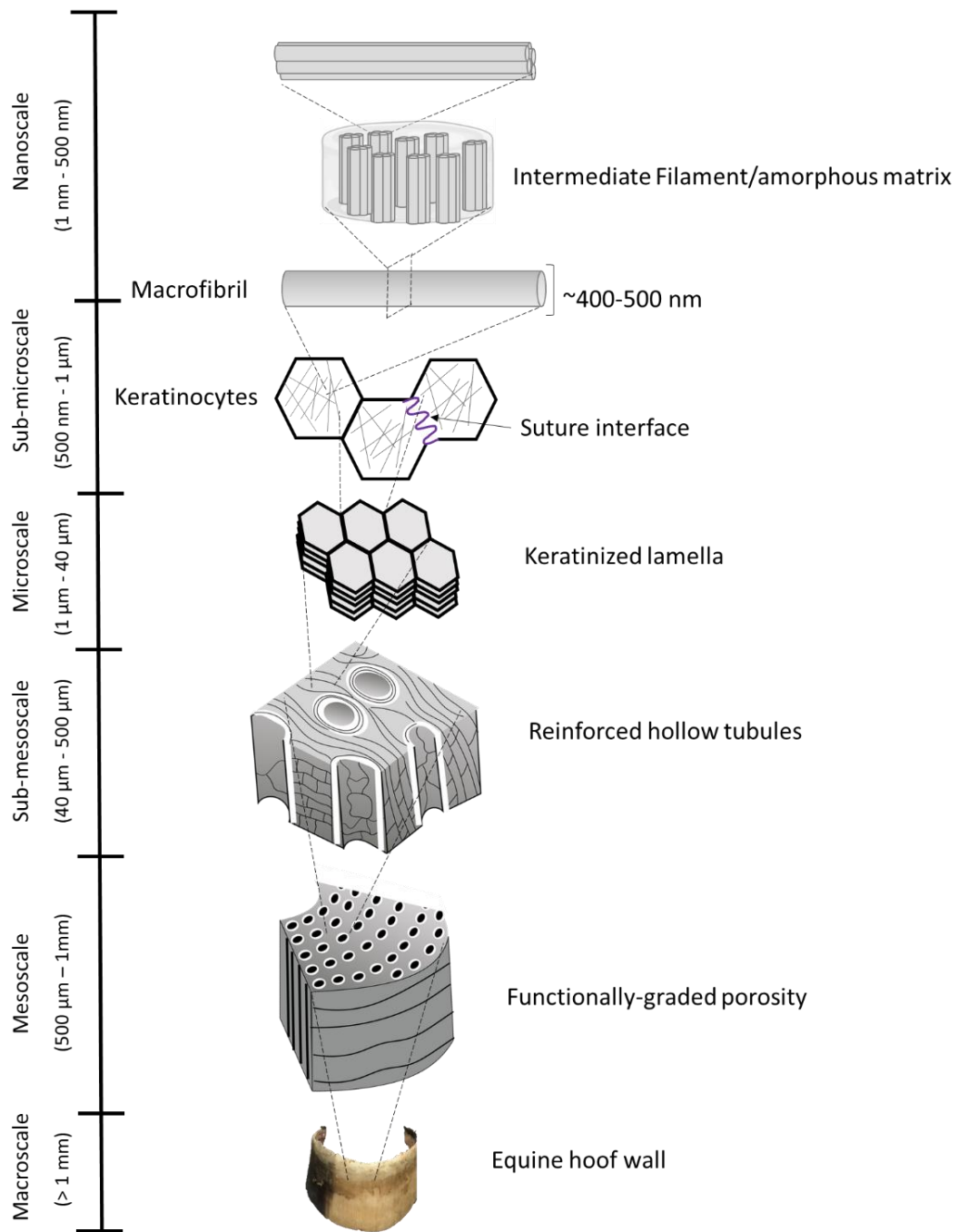
Figure 5.1 The horse hoof wall exhibits a complex hierarchical structure. Each length scale contains its own characteristic design that contributes uniquely to the mechanical functionality of the bulk material. Figure adapted from [441].

Several researchers have designed engineered structures with enhanced mechanical properties based on the meso, sub-meso, and microscale (1μm-1mm) features of the hoof wall. Rice and Tan [275] performed single-edged notched bending tests on lamellar structures composed of epoxy and PLA and found that lamellar orientation can be tuned to improve stiffness and energy absorption during fracture. Wang et al. [276] fabricated 3D printed structures containing tubular arrangements and found that K_{IC} and G_{IC} increased by 39% and 55%, respectively, relative to control samples. Huang [100] used multi-material 3D printing to fabricate samples with four tubules each and found that they helped to prevent damage in comparison with featureless samples. Ma et al. [277] fabricated crashworthy structures inspired by the tubular and lamellar structures in hooves and used finite element analysis and experimental compression tests to determine that bioinspired samples absorbed significantly more energy when compressed. Hoof-inspired corrugated tubules exhibited a 94% increase in specific energy absorption over traditional square tubes while achieving a 66% decrease in the undulation of load-carrying capacity (a metric used to determine the smoothness of the force-displacement curve, where a lower value indicates a smoother curve). A lower undulation of load-carrying capacity suggests a more efficient deformation process.

In this study, we present new results on the structural characterization of the hoof wall including measurements of the tubules, tubule bridges and their density, and the hierarchy of meso/microscale fibers in the hoof wall (Section 3.1). Expanding on the mechanical experiments of previous studies, compression tests at five different strain rates were performed on hoof samples hydrated to three different hydration levels. This wide range of testing conditions was used to capture the hydration and strain-rate sensitivity of the hoof wall and to determine the ductile to brittle transition of this biological material. To determine the viscoelastic properties of the hoof

wall, compressive creep and stress relaxation tests for different hydration levels were performed. The results are used to fit the hoof wall's response to a simplified Maxwell-Weichert model using a Prony series and are compared to another keratinous material, hair (Section 3.2). To supply an understanding of the hoof wall's fracture mechanics during a realistic impact, drop tower tests that closely resemble those experienced by the hoof wall in-vivo were performed and the resulting failure mechanisms are reported (Section 3.3). Based on these results and existing literature, unique multi-phase hoof-inspired structures were fabricated to show that elements of the hoof wall can be used to improve energy absorption and control crack propagation in engineered materials (Section 3.4).

5.2 Materials and Methods

5.2.1 Hoof samples

Hoof samples were obtained from the University of California, Davis, Veterinary Department. They were taken from six racehorses of mixed age and gender that died due to musculoskeletal injuries. Each horse weighed between 450-550 kg. The hooves were removed from the corpse within 4-24 hours and were then refrigerated for 24-48 hours before being frozen at -20 °C. The keratinous hoof capsule was removed from the hoof before being cut down to the required sample dimensions. Hoof samples were taken from the central portion of the toe region. Two different methods were used to obtain desired hydration levels. The relative humidity method was used for the drop tower samples and involved placing samples in a sealed chamber with a desired relative humidity until the weight of the sample equilibrated. The water content by weight technique was used for compression samples. This method involved drying samples in an oven at 110 °C until their weight reached equilibrium. Samples were then placed in 70 °C water and periodically weighed until they reached the desired water content. Samples were tested

176

immediately upon reaching the desired conditions. The relative humidity approach replicates better natural moisture conditions where water diffuses into a sample over an extended period of time at ambient temperatures. The water content approach is ideal for ensuring that all samples contain the same ratio of water. Since drop tower tests were intended to see how cracks propagate naturally in the hoof, relative humidity was chosen to modulate sample hydration. The compression tests, on the other hand, were meant to characterize the keratinous hoof wall at different moisture levels, so water content was chosen as a means of quantifying moisture in the hoof wall samples.

5.2.2 Bioinspired samples

Due to the promising mechanical performance of hooves reported by previous studies, bioinspired models were created to replicate the tubular, layered, and gradient structures found in the hoof. These different models aim to evaluate the mechanical properties and failure mechanisms imparted by its design motifs. Earlier studies have shown that the tubular structure in the hoof wall plays a vital role in its crack deflection mechanisms [79,81,82]. Thus, the tubular structure is of key interest for creating energy absorbent engineered materials. Models consisted of 64 tubules as a representation for the span of the hoof wall and focused on varying tubular shape gradients (elliptical to circular), density gradients (high density to low density), and the inclusion of soft intertubular lamellae. Dimensions of the tubules were drawn from Kasapi et al. [81] where the hoof stratum medium and externum were divided into six distinct regions. The average tubule shape, cavity size, and cross-sectional area reported for each region were scaled up enough to allow for 3D printing and replicated in the bioinspired models. Data for the density gradient comes from Reilly et al. [99]; it was adapted to fit 64 total tubules. For all models, the volume fraction of reinforced tubular area was held constant at 30% and the tubular cavity area at approximately 3% to match the values reported by Huang et al. [78]. Models were designed initially for drop tower

177

impact testing to study the effect of structural features, both isolated and in varied combinations. A multi-material 3D printer (Objet350 Connex3, Stratasys, Rehovot, Israel) was used to fabricate the drop tower models, using polymers FLX9095-DM for the matrix, VeroClear for the reinforced tubules, and TangoBlack+ for the lamellae.

These bioinspired designs were adapted for compact tension experiments to explore how the various arrangements affected crack propagation. The designs were implemented into a modified Plastic ASTM D5045 − 14 specimen geometry (W= 39.09 mm) with the tubules arranged orthogonal to the crack tip. The modifications consisted of re-positioning the pinholes for the sample to fit in the testing apparatus with enough clearance to avoid collision of the sample and the crosshead during ductile Mode I failure. The modification is not expected to have consequential effects on the results. The compact tension models consist of the same design but with the addition of two models; one which tests control Model 1 composed of the stiff reinforcing tubular material and a model which has uniformly distributed tubules with an elliptical reinforcing region. For the latter, a shape ratio of 1.62 was chosen as this correlated to the most extreme elliptical tubules observed in the hoof by Kasapi et al. [81]. The intertubular lamellar designs were not studied in compact tension due to the prioritized focus of studying the effect of the tubular structure on crack propagation.

5.2.3 Microcomputed tomography

5x5x5 mm^3 cubes were removed from the hoof wall and scanned using an Xradia MicroXCT 200 (Zeiss, Jena, Germany). Two sets of scans were taken at different magnifications. A low magnification set was taken with an optical magnification of 3.9692 and a pixel size of 4.001 μm. These scans had an exposure time of 1.5 seconds, a voltage of 80 kV, and a current of 88 μA. Higher magnification scans were taken with an optical magnification of 19.312 and a pixel

size of 1.1315 μm. These scans had an exposure time of 3 seconds, a voltage of 80 kV, and a current of 87 μA. The results were processed with Fiji/ImageJ (U. S. National Institutes of Health, Bethesda, Maryland, USA) [444] and 3D plugins [445,446] prior to measuring. The processing was customized based on the properties of the images, and consisted of brightness and contrast enhancements, noise reduction 3D filters, pixel thresholding, morphological 3D erosions and dilations, 3D hole filling, size-based object filtering, and object isolation from the stacks. Global 3D analysis of tubule morphology was conducted using the Volume Viewer plugin.

5.2.4 Compression tests

5x5x5 mm^3 samples taken from the hoof wall were tested using an Instron 3367 mechanical testing machine (Instron, High Wycombe, United Kingdom) with a 20 kN load cell. Despite bearing such large in-vivo loads, the hoof wall is only about 1 cm wide at its thickest, and this can vary between horses and even within the same hoof. The dimensions chosen for these tests were the largest possible ensuring that samples were composed exclusively of stratum medium (the central portion of the keratinized hoof wall). Samples were compressed in the longitudinal direction to 30% of their original height at three different hydration levels (10%, 20%, and 30% water content by weight) and five different strain rates (10^0s^{-1}, 10^{-1}s^{-1}, 10^{-2}s^{-1}, 10^{-3}s^{-1} and 10^{-4}s^{-1}). Five samples were tested for each condition. Stress relaxation tests were also performed on 5x5x5 mm^3 samples at each hydration condition. These samples were compressed to 90% of their initial height at a strain rate of 10^{-1}s^{-1} before a 10-minute relaxation period. Creep tests were conducted on samples of 20% and 30% water content. 5x5x5 mm^3 samples were compressed and held at a constant stress of 14.5 MPa (the average initial stress between the two hydrations for the stress-relaxation tests). The resultant change in strain was measured over a period of 700 s.

5.2.5 Drop tower tests

Drop tower impact testing was chosen as a characterization technique because it best recreates the natural localized impact that might be experienced by hoof when it lands on uneven terrain, such as a small rock, during locomotion. Hoof samples were tested in a drop tower specially made for testing biological samples described previously in detail [83]. For this study, the 1.2 kg impactor was raised to a height of 0.24, 0.48, and 0.72 m for impact energies of 2.8224, 5.6448, and 8.4672 J, respectively. Hoof samples were tested in two different hydration conditions of 25% and 50% relative humidity (RH). Five samples were tested for each impact energy at both hydration conditions. Samples were cut using a benchtop saw to be 17x8x3 mm^3.

Bioinspired samples were also characterized through drop tower testing. These tests were performed on a CEAST 9350 (Instron, High Wycombe, United Kingdom). The samples were impacted at 4 m/s ± 0.2 m/s by a 3.266 kg impactor (corresponding to ~26.1 J of impact energy) with a half-inch hemispherical tip. Force-displacement curves were measured, but no trends were observed for each type of sample, so they were not reported here. Instead, the analysis of these tests focused on the fracture surfaces and residual damage of impacted samples.

5.2.6 Fractography

Post-impact hoof samples were imaged using an FEI Apero FESEM (Thermo Fisher Scientific, Waltham, Massachusetts, USA) after being sputter coated (Emitech K575X, Quorum Technologies Ltd, East Sussex, United Kingdom) with iridium for eight seconds. Post-impact bioinspired samples were imaged using an Xradia microCT 200 (Zeiss, Jena, Germany). Scans were reconstructed and segmented in Amira 2020.2 (Thermo Fisher Scientific, Waltham, Massachusetts, USA) to obtain damage volume values.

5.2.7 Compact tension testing

Three samples of each bioinspired model were printed and tested. They were pre-notched using a razor blade and jig to ensure consistently sized and perpendicular cracks 2.5 mm ± 0.09 mm in length. All samples were tested using the Instron 3367 load frame under ambient indoor conditions (approximately 22 ºC and 75% humidity). Samples were tested at 10 mm/min as per ASTM and the displacement and load until failure were recorded. Raw data were exported from the universal testing machine and normalized to consider the first 90% of the displacement in plotting load versus displacement curves on MATLAB. The energy absorbed for each model was calculated by measuring the average area under the curve for the model trials. Standard deviations for each model were also calculated and plotted.

Measurements of the sample dimensions were made before and after fracture using digital calipers. Videos of each experiment were recorded, and digital images of each sample post-fracture were taken. Videos were used to correlate the physical deformation behavior to the measured curves. Digital images were used to measure crack length using ImageJ (U. S. National Institutes of Health, Bethesda, Maryland, USA).

5.3 Results and Discussion

5.3.1 Structure of the hoof wall

Tubular and fibrous arrangements reported by previous authors were confirmed by scanning electron microscopy (SEM) and micro-computed tomography (microCT). The gradients in tubule shape and density were consistent with previous observations of the hoof wall [81,82,99,245]. Figure 5.2A shows an image of an extracted tubule from a microCT scan. The scans show that the hollow medullary cavities at the center of the tubules are not continuous structures but are segmented by bridges that span the empty space dividing the cavity into hollow

pockets. These features have been noted before but never quantified [78]. Averaged measurements of bridge width, bridge density, cavity cross-sectional area, porosity of the central hoof wall cross-section, tubule density, and volume of an individual pocket are summarized down Table 5.1. Measurements of the tubule density agree with Reilly et al. [99] and Kasapi and Gosline [81], who found, respectively, 11-22 tubules/mm^2 and 10-25 tubules/mm^2 in the central region of the horse hoof wall. The average value for porosity (0.77±0.3%) was lower than those measured by Huang et al. [78] (~3%). The measurements of the bridge width, bridge density, and average pocket volume are novel and have not been previously reported.

Table 5.1 MicroCT measurements of hoof features

Bridge width(n=301[x])	$10.3 \pm 2.4 \, \mu m$
Bridge density (n=16[y])	0.009 ± 0.002 bridges/μm
Pocket cross-sectional area (n=226[y])	$365.8 \pm 18.2 \, \mu m^2$
Pocket volume (n=43[z])	$40633.5 \pm 12820.5 \, \mu m^3$
Porosity (n=226[y])	$0.77 \pm 0.3\%$
Tubule density (n= 226[y])	15.91 ± 0.4 tubules/mm^2

x- Bridges, y-Tubules, z- Pockets

SEM scans of fibers extracted during the cutting process show the hierarchy of fibers found in the hoof wall ranging from macrofibers on the scale of 100 micrometers down to

embedded fibers that are just hundreds of nanometers in diameter. These features are shown in

Figure 5.2B.
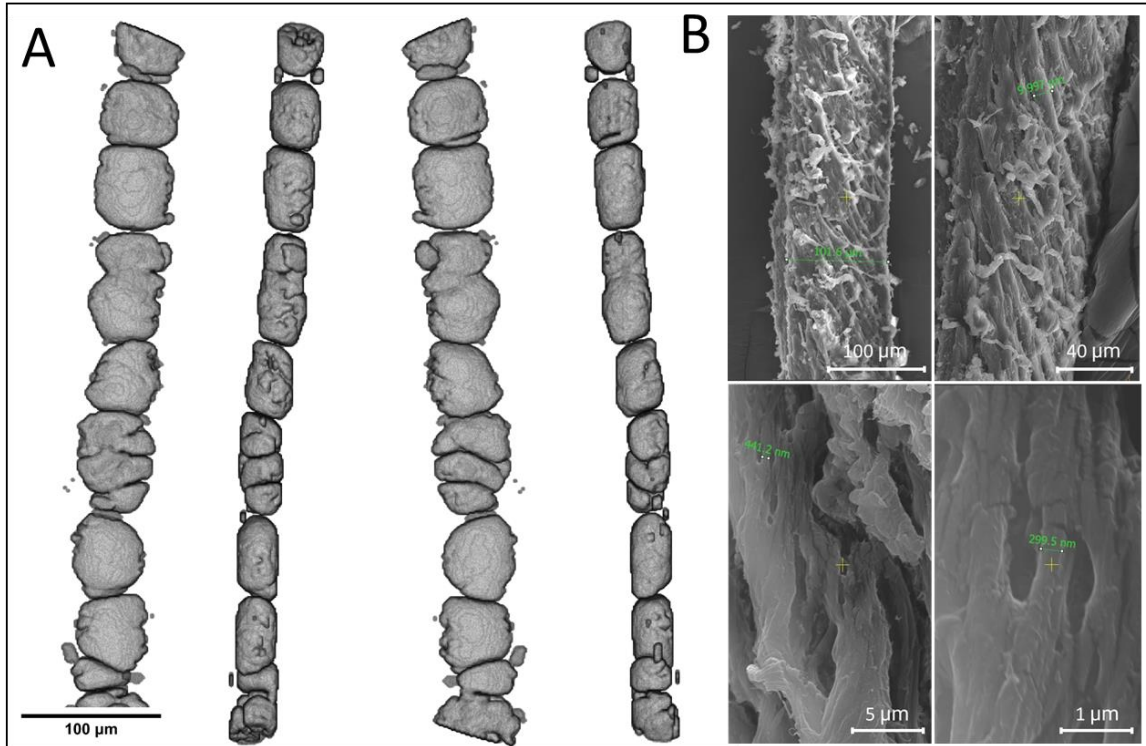
Figure 5.2 A) Tubule structure extracted from microCT scans of the horse hoof. B) Hierarchy of fibers in the horse hoof.

5.3.2 Compressive response of the hoof wall

Keratin's mechanical properties are very hydration dependent, a phenomenon that has been

reported in hooves [78,98,440] and numerous other keratinous systems such as horns, whale baleen

[243], and hair [168,244,246,259,263]. Stress-strain curves for hoof samples compressed at five

different strain rates for three different hydration conditions are shown in Figure 5.3A-C. In these

curves the areas between like samples are shaded in to establish a range of results and to better

illustrate the trends observed under different testing conditions. A ductile-to-brittle transition can

be observed with the decrease in hydration as well as increasing strain rate. Samples hydrated to

10% water content began to fracture around 0.15 strain and showed severe plastic damage after

being compressed to 0.7 strain. Due to this brittle behavior, a very wide variability in the curves was observed between samples as shown in Figure 5.3A, where the ranges for each strain rate show a significant amount of overlap. In this condition, brittle fracture dominates; it is determined by discrete microplastic buckling and fracture events, and there is no clear strain-rate sensitivity. For drier samples, these catastrophic events determine the material response. Indeed, the fracture stress of brittle materials is strain rate insensitive up to strain rates in which the crack velocity is hindered by the load application rate.

For the most hydrated samples (30% water content) there is a noticeable and consistent strain-rate effect. A linear shift in stress levels at specific strains can be seen with increasing strain rate. Samples tested at $10^{-4}s^{-1}$ fit this trend well initially but then diverge at higher strains, likely due to drying effects during testing. As such, the reported stress levels for this strain rate are likely inflated due to inconsistent hydration conditions during testing.

At 20% water content by weight, samples tested at the highest strain rate continue to show a brittle behavior. This response is visualized by the green shaded region in Figure 5.3B where there is a long elastic regime, reaching a high stress of 50-65 MPa, followed by a precipitous drop in stress, signifying plastic damage and fracture. When loaded at $10^{-1}s^{-1}$, the samples exhibited a similar initial behavior as the samples loaded at $10^{0}s^{-1}$. However, they did not fail in a brittle manner between 0.1-0.2 strain and were able to exceed the maximum stress of samples tested at the faster strain rate. On the other hand, samples tested at $10^{-2}s^{-1}$, $10^{-3}s^{-1}$, and $10^{-4}s^{-1}$ express elastomer-like behavior. Thus, the ductile-to-brittle transition is captured at 20% water content by weight. Such a ductile-to-brittle transition with increasing strain rate is consistent with previous observations for toucan rhampotheca [101] and pangolin scales[29].

As mentioned above, all of the samples hydrated to 30% water content by weight display ductile behavior and are significantly softer than those in the other two hydration conditions. The stress-strain curves at $10^0 s^{-1}$ and $10^{-1} s^{-1}$ are shifted upward relative to the other strain rates. Only a marginal difference between $10^{-2} s^{-1}$ and $10^{-3} s^{-1}$ is observed for this hydration condition, but the curves for the latter strain rate tend to be comparatively shifted down. As previously mentioned, samples tested at $10^{-4} s^{-1}$ have higher stress values than expected, likely due to drying during testing. Samples hydrated to 30% water content also showed very little visible damage and even exhibited noticeable shape recovery after the load was released. This shape recovery has been previously observed in feather [261] and horn [259] keratin. The strain rate sensitivity, defined as $m = \partial \ln\sigma / \partial \ln\dot{\varepsilon}$ is displayed in Fig. 3D and ranges from 0.072 to 0.087. These values are in line with other keratins: baleen (0.09 to 0.11)[243], pangolin scales (0.06)[29], hair (0.06)[224]. These biopolymers have a response similar to synthetic polymers, such as PMMA (0.07) [243].
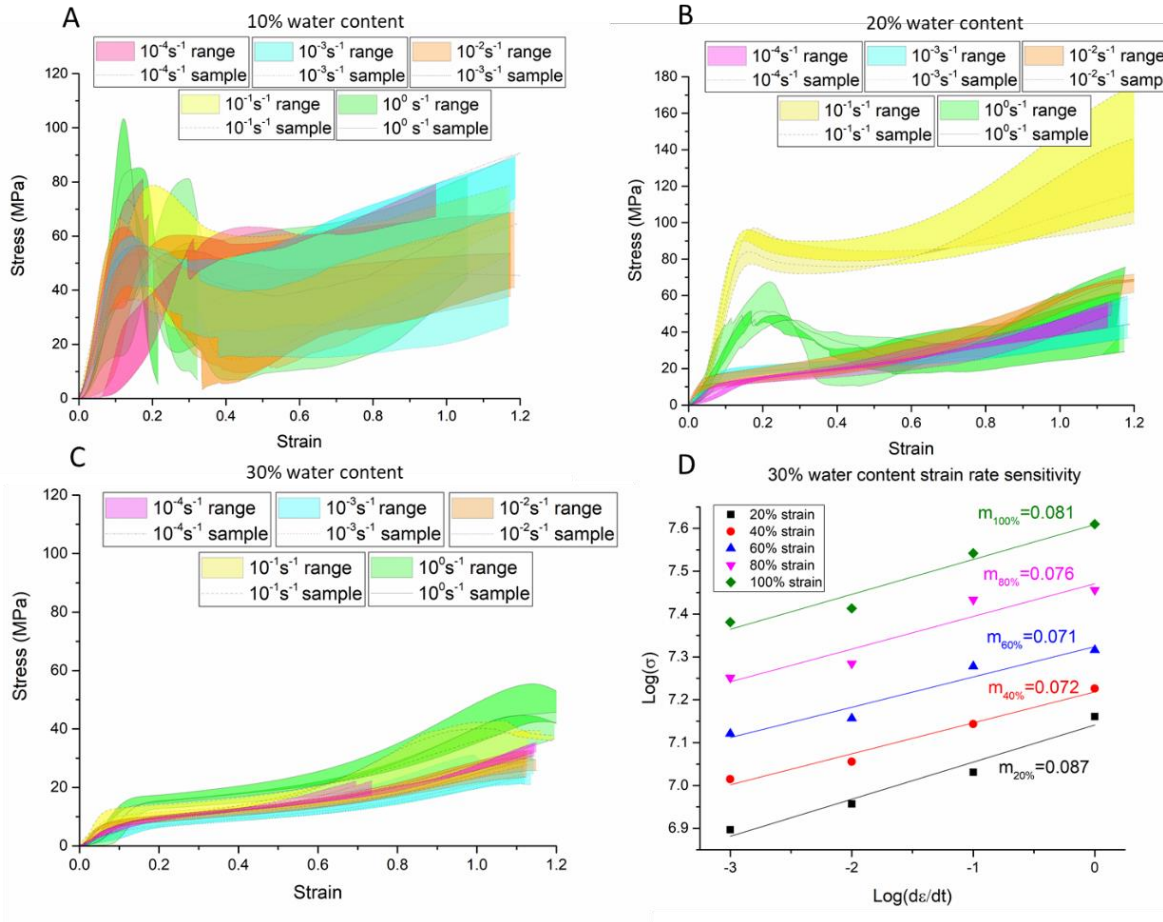
Figure 5.3 Stress-strain curves of hoof samples compressed at five different strain rates (10^0s^{-1}, 10^{-1}s^{-1}, 10^{-2}s^{-1}, 10^{-3}s^{-1} and 10^{-4}s^{-1}) for hydration states of A.) 10%, B.) 20%, and C.) 30% water content by weight.

The elastic modulus decreases with increasing hydration and generally increases with increasing strain rate, in agreement with previous work [98,440]. Table 5.2 shows the measured elastic modulus for each condition. The linear elastic regime, seen in Figure 5.3A-C, shrinks with increasing hydration. The water molecules in the hydrated hoof act as a plasticizer. The hydrogen bonds that stabilize the α-helix structure of the keratin molecules and weakly crosslink adjacent polymer chains are interrupted, reducing the stiffness of the material dramatically [447]. At low hydrations, the keratinous hoof wall behaves like a hard plastic, exhibiting plastic deformation at relatively low strain. This behavior results in a stress plateau beginning at ~0.15 strain as the

damaged material is less capable of resisting stress once fractures have been introduced. At higher hydrations, the material behaves more like an elastomer. It exhibits a short initial elastic regime before a slow, steady increase in stress up to approximately 45% strain. At this point, most of the pores have collapsed, and the densified material sees a steep increase in stress with increasing strain. However, very few fractures are observed, and the onset of plastic deformation is significantly delayed.

Table 5.2 Elastic modulus values for hoof samples tested at different hydrations and strain rates

Strain rate	10% $\pm$ 1% water content	20% $\pm$ 2% water content	30% $\pm$ 2% water content
$10^{-4}s^{-1}$	547.4 $\pm$ 251.9 MPa	105.1 $\pm$ 22.5 MPa	48.4 $\pm$ 26.4 MPa
$10^{-3} s^{-1}$	600.0 $\pm$ 99.1 MPa	281.5 $\pm$ 40.1 MPa	56.6 $\pm$ 25.8 MPa
$10^{-2} s^{-1}$	774.9 $\pm$ 188.4 MPa	439.3 $\pm$ 90.3 MPa	169.2 $\pm$ 51.1 MPa
$10^{-1}s^{-1}$	743.4 $\pm$ 151.1 MPa	512.8 $\pm$ 120.5 MPa	105.1 $\pm$ 35.1 MPa
$10^{0}s^{-1}$	1218.9 $\pm$ 171.5 MPa	941.9 $\pm$ 120.7 MPa	164.6 $\pm$ 17.3 MPa
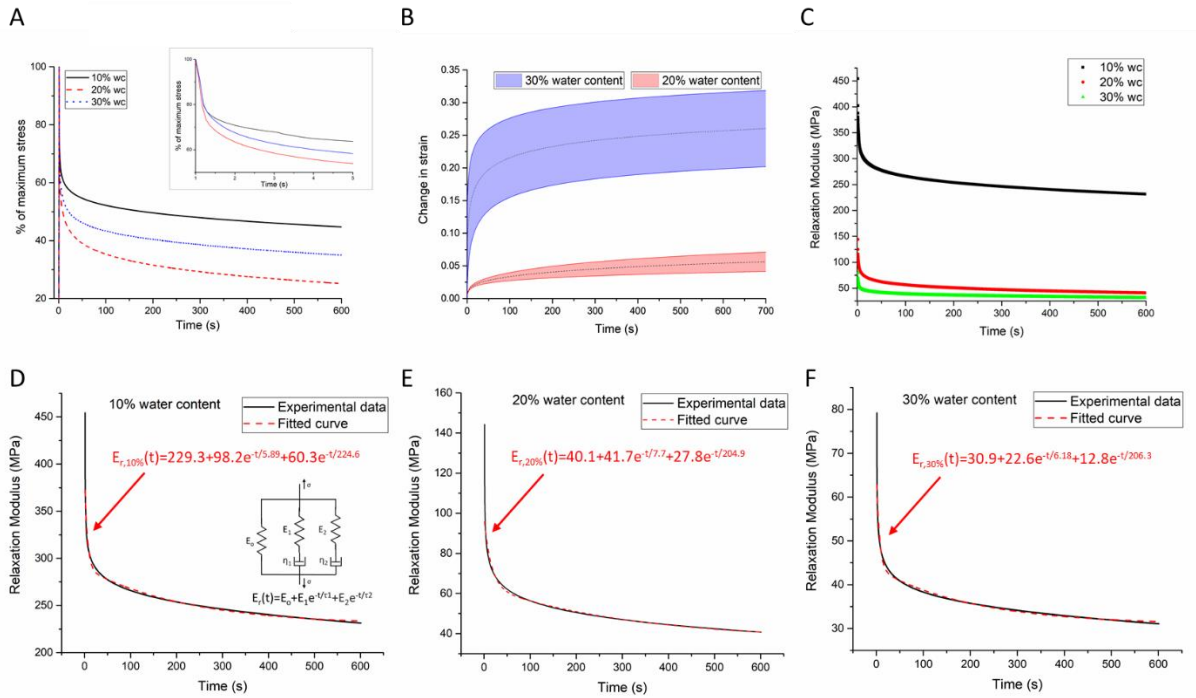
Figure 5.4 When compressed, the hoof wall displays viscoelastic behavior that varies with hydration. A.) Normalized relaxation data vs time. Inset shows initial relaxation period. B.) Creep test of hoof samples hydrated to 20% and 30%. C.) Relaxation modulus for each hydration state as a function of time. Fitted curves of three-term Prony series compared with experimental data for D.) 10% (and Simplified Maxwell-Weichert model with generalized equation used to model viscoelastic behavior of the hoof wall) E.) 20%, and F.) 30% water content by weight.

Figure 5.4A shows the averaged curves (N=5) of stress relaxation tests over a range of 600 seconds. To better compare samples, the percentage of maximum stress was plotted versus time. Interestingly, the middle hydration level of 20% water content by weight exhibits the most relaxation relative to its initial stress level, losing nearly 75% of its maximum stress over a 10-minute relaxation period. Meanwhile, the 30% water content by weight samples approached a 65% decrease in stress, while stress in the 10% water content by weight samples only dropped by about 55%. It stands to reason that the dry samples would exhibit less viscoelastic relaxation, but the results of the 30% water content by weight samples seem anomalous. This is likely due to the higher absolute stress level present in the 20% water content samples when they are compressed to the same strain, since the 20% water content samples have elastic modulus values ~2-5 times

188

higher than those of the 30% water content samples. This notion was confirmed by creep tests on the two sets of samples hydrated to 20% and 30% water content, where the samples are loaded to the same stress level and then the change in strain over time is measured. The results of these tests are displayed in Figure 5.4B and suggest that samples hydrated to 30% water content are significantly more viscoelastic, with an average change in strain of $26.02 \pm 5.83\%$ after 700 seconds compared to that of the 20% water content samples which had an average change in strain of just $5.62 \pm 1.48\%$ over the same time period.

Water, by infiltrating in the structure, disrupts hydrogen bonds that stabilize the keratin structure, allowing the keratin fibers to slide past each other and rearrange more easily. This behavior has interesting implications for the naturally occurring hydration gradient in the hoof wall. Kasapi and Gosline [81], Bertram and Gosline [97], and Douglas et al. [98] discuss how this gradient leads to a decrease in strain differential between the stiff hoof wall and the soft interior tissue; however, the authors do not explore or discuss the viscoelastic implications of this hydration gradient. Unfortunately, there is no clear consensus for the natural hydration condition of the horse hoof in-vivo. For example, Leach [440] reported an average of 20.0% water content at the outer wall and 27.6% at the inner wall, while Douglas et al. [98] reported a moisture content of 27.9% at the outer wall and 35.5% at the inner wall. In either case, it seems that the stiffer exterior portion of the hoof wall may have an optimal water content for increased stiffness while maximizing the viscoelastic nature of keratin that improves its energy dissipation and durability. Furthermore, even with the gradual gradient identified by previous studies, one would expect the hydration difference and therefore stiffness difference through the thickness of the hoof to give rise to internal shear stresses as the hoof is. However, the more rapid viscoelastic recovery of the hoof when hydrated to 20% water content likely helps overcome this issue. For instance, when compressed to 10%

strain, hoof samples hydrated to 20% water content experience an average stress 1.77 times that of samples hydrated to 30% water content. However, this ratio drops to 1.67 after 1.5 seconds and then 1.57 after 22 seconds. After 10 minutes this ratio is reduced to just 1.31. Meanwhile, samples hydrated to 10% water content experience an initial stress 5.67 times larger than that of the 30% water content samples. After 1.5s, 22s, and 10 minutes this grows to 6.11, 6.61, and 7.44, respectively. An exterior hydration of ~20% water content allows the hoof to harness the benefits of a stiff exterior while also minimizing internal shear stress via rapid viscoelastic relaxation. Of course, these tests only account for variations in hydration, but not any of the structural differences that occur through the hoof wall thickness, which may further improve this optimization.

A closer look at the initial phase of relaxation can be seen in the inset of Figure 5.4A. Immediately after the stress relaxation begins, the samples experience a linear drop in stress before entering a region of gradual decay. The samples hydrated to 20% water content experience the steepest drop in stress in this linear region, followed by the 30% water content samples and finally the 10% water content samples. Several of the relaxation curves for the 10% water content samples lack the smoothness seen in the other two sets of curves. In these samples, a sudden change in the relaxation rate can be observed between 3-4 seconds, and this is reflected to a lesser degree in the averaged curve. This behavior is likely the result of shifting plastic deformation that occurred during loading.

The viscoelastic behavior of keratinous materials has previously [224] been quantified using a simplified version of the Maxwell-Weichert model (Figure 5.4D) which uses two Maxwell elements (a spring and dashpot in series) and a spring in parallel. The relaxation modulus of the system can be represented by the following three-term Prony series:

$$E_r(t) = E_o + E_1 e^{-t/\tau 1} + E_2 e^{-t/\tau 2}$$

where t is the time elapsed since the beginning of the relaxation period, E_1 and E_2 are the elastic moduli of the springs in the Maxwell elements, E_o is the elastic modulus of the remaining spring, and τ_1 and τ_2 are characteristic relaxation constants defined as the ratio between the viscosity, **η,** of the dashpot and the elastic modulus, E, of the spring in each Maxwell element. The two-step relaxation process observed in keratin has been attributed to two distinct mechanisms at different hierarchical levels. The shorter relaxation time, measured to be between 11s and 14s in hair [224], is the result of relaxation of the larger scale features such as cells, lamellae, and tubules while the longer relaxation time, determined to be about 207s in human hair, is thought to be the result of nanoscale features, like the IFs. Figure 5.4C shows plots of the relaxation modulus for each hydration condition. These curves were then fitted to the generalized Maxwell-Weichert equation. The calculated curves are plotted alongside the experimental data in Figures 5.4D-F. The resulting equations are:

$$E_{r,10\%}(t)=229.3+98.2e^{-t/5.89}+60.3e^{-t/224.6}$$

$$E_{r,20\%}(t)=40.1+41.7e^{-t/7.7}+27.8e^{-t/204.9}$$

$$E_{r,30\%}(t)=30.9+22.6e^{-t/6.18}+12.8e^{-t/206.3}$$

The hoof wall samples hydrated to 20% had the largest short-term relaxation constant and the smallest long-term relaxation constant. Studies on hagfish slime threads suggest that the amorphous matrix in which the IFs are embedded is likely the most susceptible to hydration sensitivity [244,448]. In this context, it makes sense that the more hydrated samples would have a noticeably lower long-term relaxation constant which is associated with nanoscale structures. Meanwhile the driest samples, hydrated to 10% water content, exhibit the fastest short-term

relaxation time due to plastic relaxation of minor cracking and delamination that occurred during loading.

Human hair has characteristic relaxation times of ~207s and ~11s [224]. The larger relaxation time is remarkably consistent with the results of this study (224.6s, 204.9s, and 206.3s). The results agree well with the assumption that this relaxation time represents keratin's nanoscale features which should be similar in both systems [78,168]. The shorter relaxation time, however, is significantly different. This finding also makes sense, considering that the hoof has significantly different mesoscale features than hair. With a lower short-term relaxation time (5.89-7.7s), the tubule reinforcement/intertubular lamellae in the hoof seem to relax quicker than the cortical structure of hair (11s). Furthermore, in the hoof, the Maxwell-element moduli for the large-scale features, E_1, are 1.5-1.75 times larger than the moduli of the smaller features, E_2, whereas in hair, this is reversed, with E_2 being 1.5-1.75 times larger than E_1 [224]. This finding indicates that the hoof has a steeper initial decay of stress and that the short-term relaxation that arises from the hoof's mesostructure is more dominant than in other keratinous materials. For example, after 3 seconds, the E_r for hair drops to 95.9% of its initial value while that of hooves drops to 89.7%, 87.4%, and 86.6% for 10%, 20%, and 30% water content, respectively. After 10 seconds these values become 89.5% (hair), 78.6%, 71.1%, and 71.7% (hoof). With just a matter of seconds between each footfall for a galloping horse [449,450], being able to dissipate compressive stress via viscoelastic relaxation more quickly is advantageous for preventing the build-up of stress during the repeated loads of locomotion. These tests suggest that hooves can improve this capability over other keratinous materials with their mesostructural features, highlighting yet another benefit of the hoof's unique configuration.

5.3.3 Impact performance of hoof wall

Similar to the quasistatic compression experiments, there was a dramatic effect of the degree of hydration on the impact response. Figure 5.5A shows sample dimensions and extraction location from the hoof wall. Samples hydrated at 50% RH (Relative Humidity) showed almost no damage regardless of impact energy. Many of these samples simply bent under impact, rather than fracturing or cracking. These samples were so ductile that they were able to bend in half and squeeze into the lower aperture upon impact. They could be removed and straightened to their initial shape with minimal noticeable damage. Only one sample impacted at the highest energy exhibited cracking after being bent to nearly 180°. The samples hydrated at 25% RH, however, showed significant damage regardless of impact energy. This is indicative of a ductile-brittle transition between 25% RH and 50% RH for the hoof wall. The severity of damage in the samples also increased with increasing impact energy. Figures 5.5B and C indicate the damage observed in the samples after drop tower testing at different impact energies for 25% RH and 50% RH, respectively.
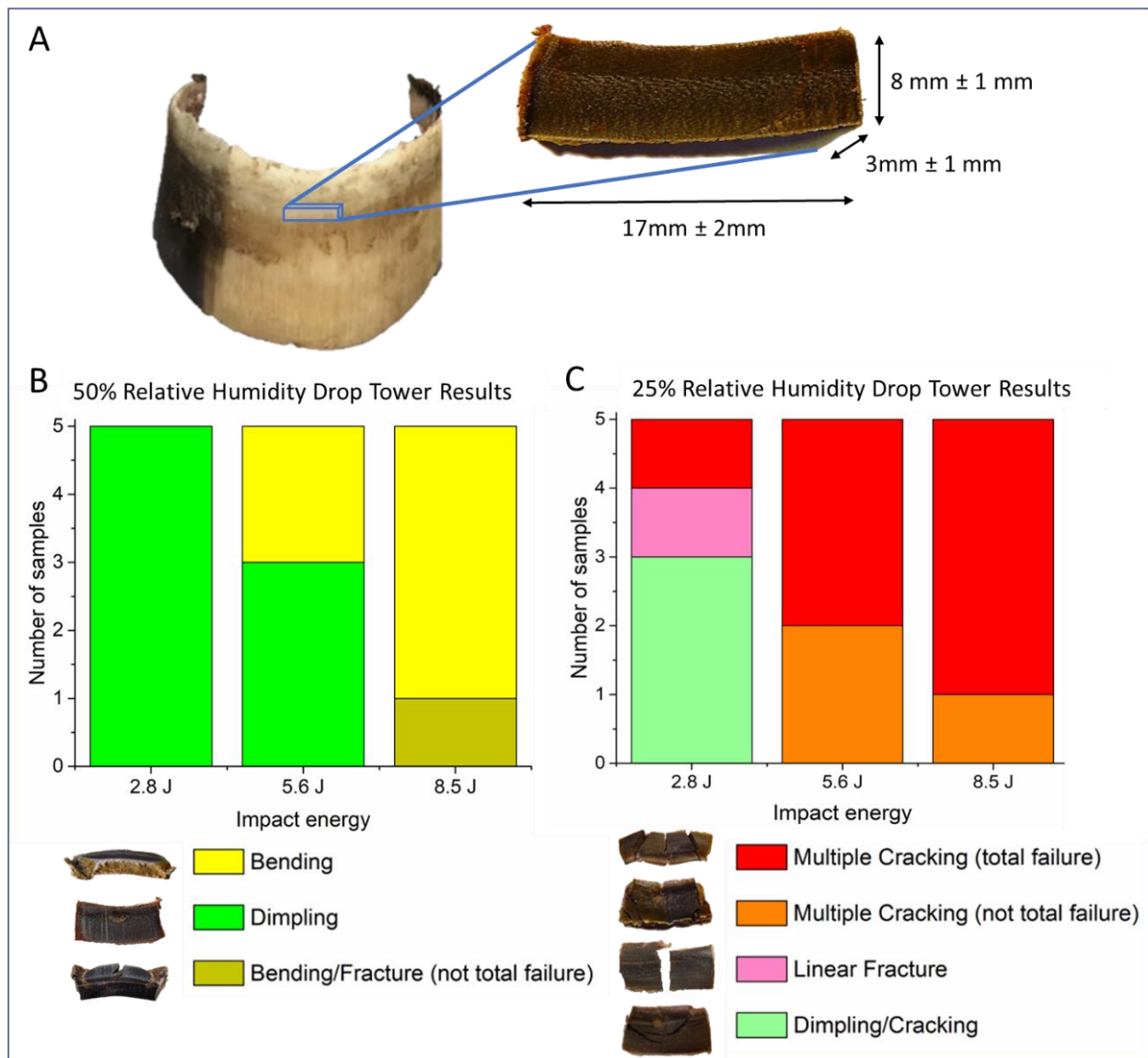
Figure 5.5 Drop tower experiments were performed on hoof wall samples. A) Sample dimensions and location of extraction. Failure mechanism histograms for different impact energies for samples equilibrated at B) 50% RH and C) 25% RH.

The fracture morphology depends, by virtue of the anisotropy of the structure, on the orientation of the propagation path. For the drop tower fractured specimens, the state of stress is complex and not controlled, and so is the fracture path. Nevertheless, it was possible to identify some important characteristics. Figure 5.6A shows two principal fracture planes: parallel and perpendicular to the orientation of the tubules in agreement with previous studies [79–81,97].

When the crack front is perpendicular to the tubules, it forms steps aligned with weak planes in the intertubular matrix. For the other extreme case, where the crack plane is aligned with the tubules, the crack front tends to meander between the tubules, since the peritubular material has a higher strength than the matrix (Figure 5.6B). These different modes of fracture corresponded to varying impact energy with fractures tending to form perpendicular to tubules at higher impact energies and along the tubule axis at lower ones. Kasapi and Gosline [79] do not mention these phenomena during their fractography analysis of compact tension tests at different strain rates, instead only making note of differences due to location in the hoof wall. At the next spatial scale, (Figure 5.6C-E) there is also a distinct effect of strain rate. At low impact energies cracks develop between tubular and intertubular fibers. When the material fails these cracks eventually propagate longitudinally along the tubule as shown in Figure 5.6A. At intermediate impact energies, crack initiation phenomena similar to the low impact energy samples were observed; however, longitudinal tubule pullout could also be seen. At high impact energies, individual tubules were shorn laterally from the matrix while cracks traveled in a stepwise pattern through the intertubular

material. Finally, on the microscale and below, failure of the horse hoof involves rupturing the hierarchy of fibers shown in Figure 5.2B.
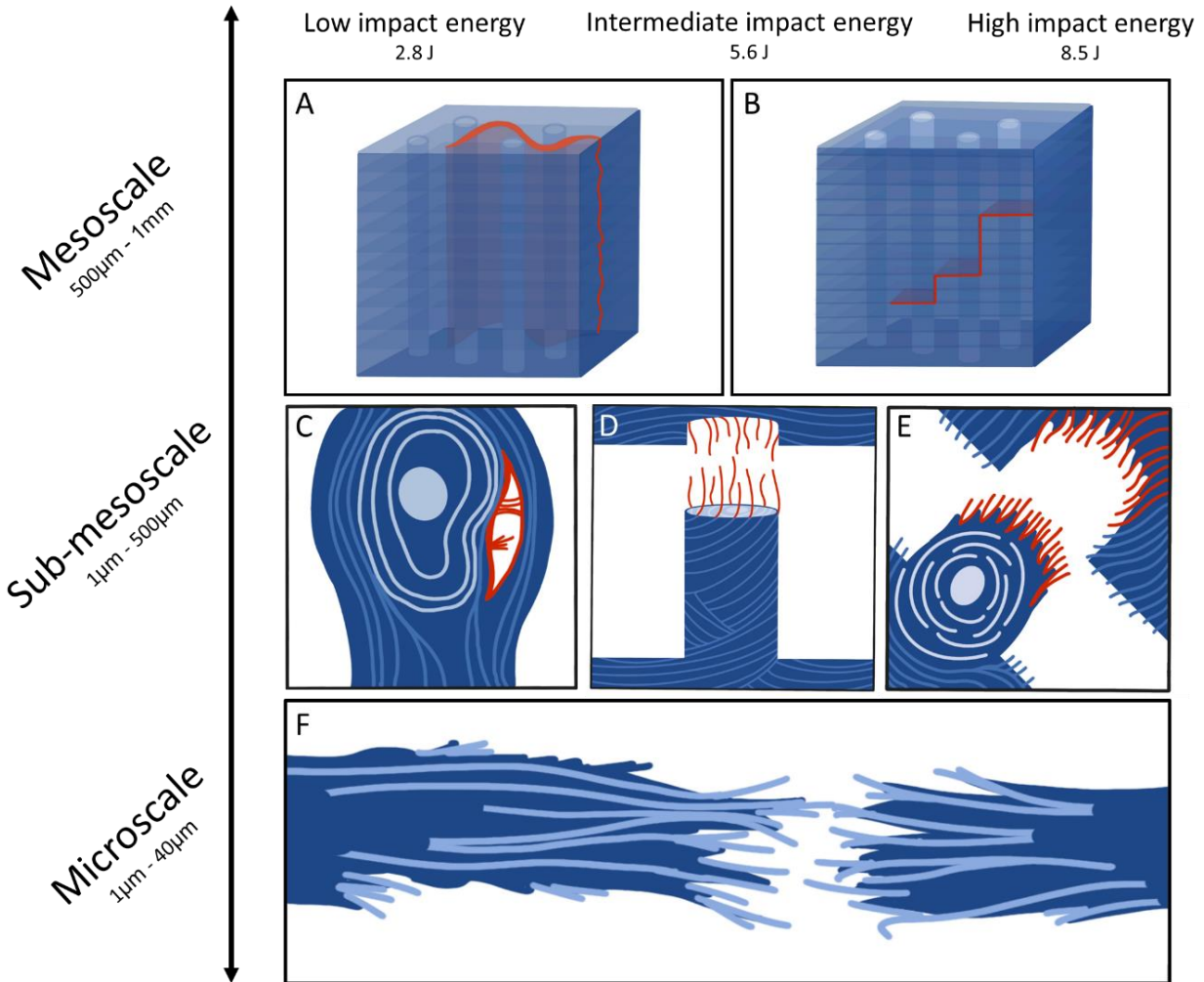
Figure 5.6 Schematic showing the failure mechanism of each length scale's characteristic structures at different impact energies. The microscale depicts the ubiquitous fiber rupture, the sub-mesoscale shows tubule splitting/cracking, tubule pullout, and tubule tearaway, while the mesoscale depicts crack deflections at the tubular (low and intermediate impact energies) and lamellar (high impact energies) interfaces. Red lines indicate points of failure such as fiber rupture or cracking, light blue lines indicate tubular fiber orientation, and dark blue lines correspond to fiber orientation in the intertubular matrix. Figure by Brooke Stephenson.

Figures 5.7-9 provide observations that elucidate the mechanisms of fracture propagation and toughening at the meso and microscale. SEM images of the post-impact crack interfaces of

the 25% RH samples reveal that the failure mechanisms depend on impact energy and highlight some of the features that make the hoof so energy absorbent under impact. At the lowest impact energy of ~2.8 J, cracks formed in several samples. SEM images of these crack interfaces show that significant deflection occurred along the tubule/matrix interface (Figure 5.7). These deflections cause the crack to take a meandering, energy-absorbent path. This result is similar to that of Mirkhalaf et al. [451] who determined that introducing planes of weakness into a brittle material can be used to create tortuous crack paths and improve toughness. Small cracks were also observed around some of the tubules which suggest the onset of delamination between the tubule cortical layers and the surrounding matrix. Several other fracture mechanisms centered around the tubules were observed, including tubules arresting cracks and bridging cracks, as shown in the right-most image in Figure 5.7. In the instance of tubule arresting, cracks were halted when their tip reached a tubule interface. Meanwhile, in the case of tubule bridging, cracks passed through the tubules, but the two surfaces of the crack were held together by the intact tubule structure. This extrinsic toughening mechanism has been observed with perpendicular fibers spanning cracks in biological systems such as bone [452], but not as a result of tubules running parallel to the crack interfaces. Horse hooves are unique since they have high-aspect ratio reinforcing elements (tubules) that are physically intertwined with the surrounding fibrous matrix. This feature will be discussed in greater depth later in this section but is important for understanding how tubules are able to span fracture surfaces and arrest crack growth.
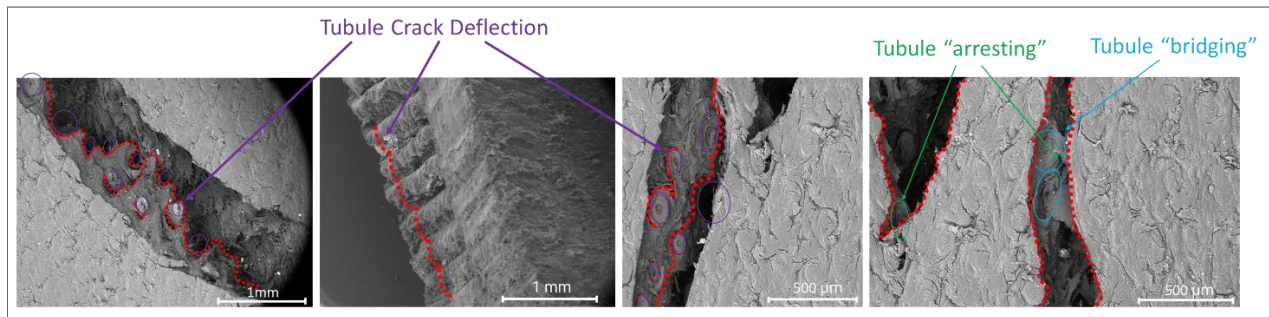
Figure 5.7 At the lowest impact energies the tubules cause significant crack deflections resulting in tortuous fracture surfaces. Tubules were also noted for the first time to bridge cracks, providing an extrinsic toughening mechanism, and arresting crack interfaces in their fibrous cortical layers.

At the intermediate impact energy of ~5.6 J, tubules not only cause crack deflections but also begin to delaminate entirely from the surrounding matrix. This mechanism is similar to the fiber pullout observed in synthetic composites [95,453–455] and has been noted in other composite biological materials like wood and bone [12,94]. As the hoof wall flexes under impact, significant stress concentrations build up at the interface between the reinforced tubules and the softer matrix. These magnified stresses cause the tubules to debond and slip out of the matrix. Several examples of this behavior are noted in the top images of Figure 5.8. An example of a pulled-out tubule can be seen in the bottom left pane of Figure 5.8 while the remnant matrix is shown in the bottom right.
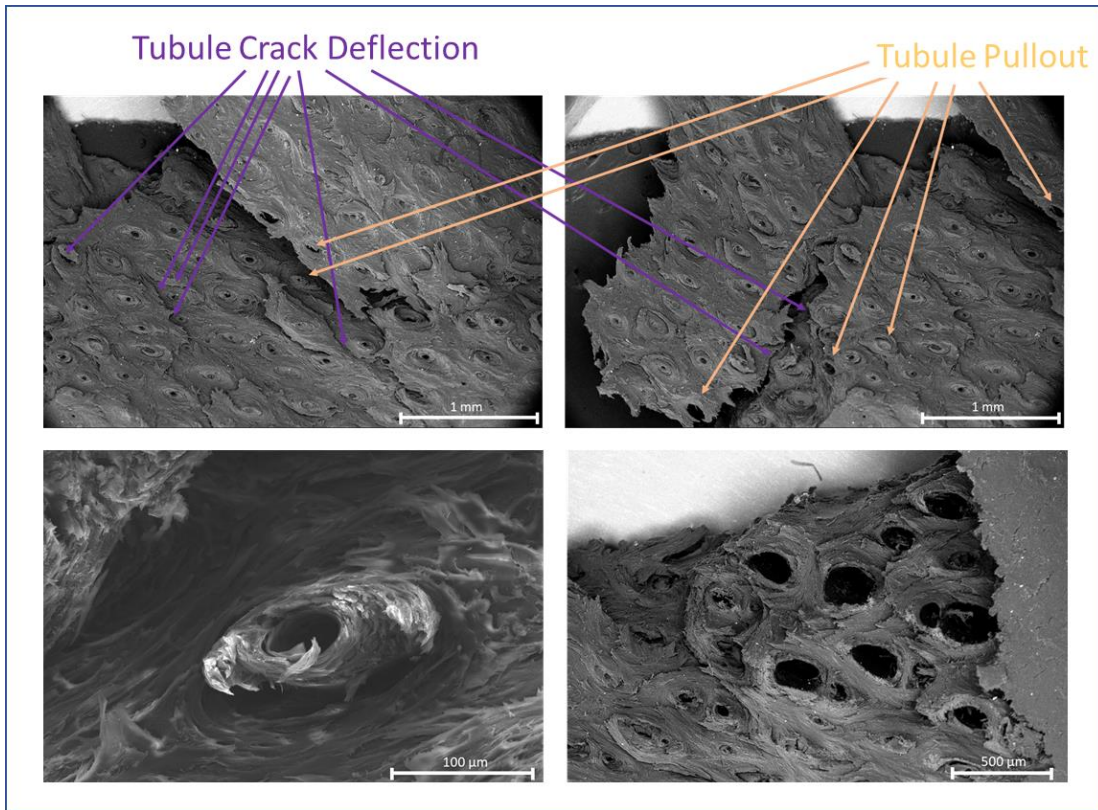
Figure 5.8 At the intermediate impact energy tubules cause crack deflections and pull out of the matrix. The top two panels show SEM images containing multiple examples of these phenomena. The bottom two panels show a tubule that has debonded from the matrix in the longitudinal direction (left), as well as the remnant matrix.

Another important implication of the hoof wall's tubular reinforcement is the way in which the tubules adhere to the surrounding matrix. Unlike most synthetic fiber reinforced composites, which grip the matrix with friction, the tubular reinforcement in the hoof is physically attached to the matrix with intertwined fibers that span the tubule/matrix interface. Therefore, to induce tubule pullout or tubule tear-away the bonds that hold these fibers together need to be overcome. Torn fibers between the matrix and tubule after impact can be seen in Figure 5.9A-C. Figures 5.9D-F show the hierarchy of torn fibers on the surface of a tubule that has ruptured from the surrounding matrix with each successive image revealing a finer embedded fibrous structure. We hypothesize that this physical attachment can increase the value for κ, the bond modulus of the reinforcement,

as well as increasing the amount of energy that is dissipated when tubules rupture from the surrounding matrix. In synthetic composites, the degree of bonding across the interphase region (the interface between fiber and matrix) is vital and can govern the mechanical potential of fiber reinforced composites [456,457]. Significant research has gone into improving the adherence of fibers to the matrix including the use of fiber surface modifications via dip coating [458], functionalized nanoclay grafting [459,460], nanofiber chemical vapor deposition [461,462], and chemical sizing agents [463–465]. The hoof's bottom up self-assembly allows it to create fiber reinforcement that is physically attached to the surrounding matrix with a hierarchy of fibers. This structural motif can serve as inspiration for future designs of fiber reinforced composites.
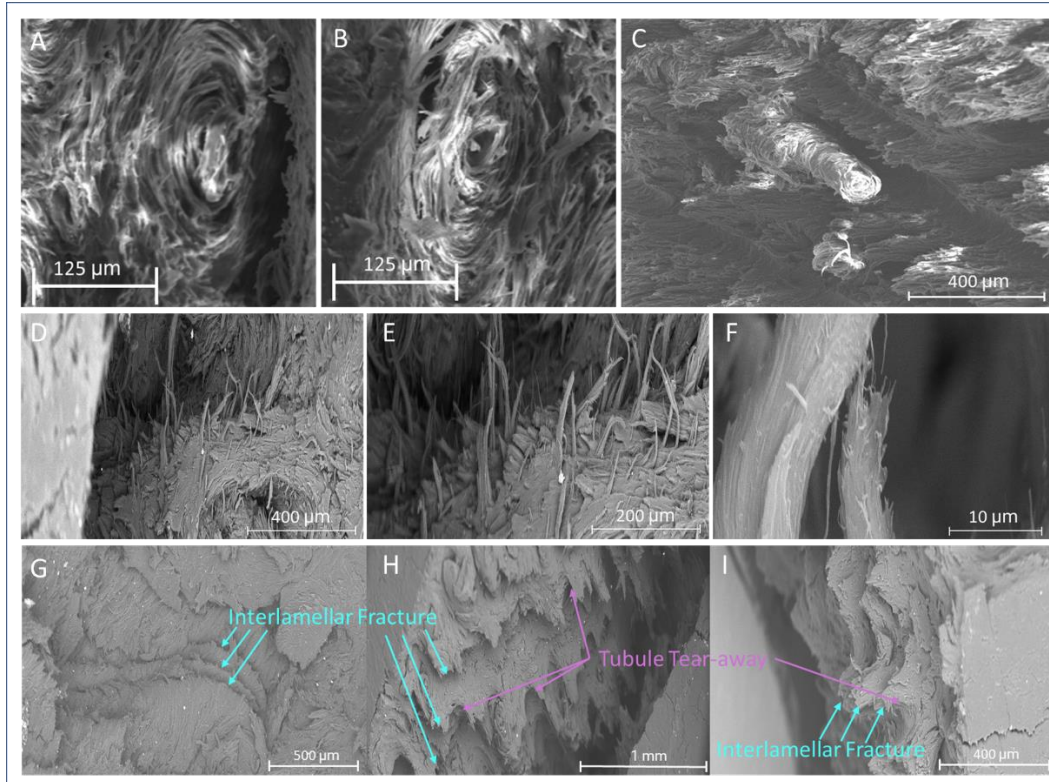
Figure 5.9 Unlike engineered composites, the hoof wall's reinforcing elements are physically attached to the surrounding matrix. A-C) SEM images of post-impact specimens showing torn fibers that once connected the reinforced tubules to the matrix. D-F) SEM images of the same ruptured tubule showing the hierarchy of fibers involved in the interphase connection. G-I) At the highest impact energies, the intertubular lamellae dominate the fracture path as cracks propagate along the boundaries between the layers. At these impact energies, tubules rupture from the matrix laterally rather than longitudinally.

The critical force, P_{crit}, required to induce fiber pullout in engineered composites is often based on the assumption that the bonding between the reinforcement and surrounding matrix is purely frictional. In the case of the hoof, where additional force is required to fracture the fibers that traverse the interphase boundary of the reinforcement, an additional term can be added: $P_{tubule} = \sigma_{fibers} * A_{fibers} * \rho_{fibers} * 2\pi r l$, where σ_{fibers} is the tensile strength of the keratin fibers, A_{fibers} is the average cross-sectional area of the fibers, ρ_{fibers} is the density of fibers per unit area, r is the radius of the tubule, and l is the length of the tubule. However, as previously noted, many of the

tubules in the hoof are elliptical rather than circular in cross-section, which increases the surface area of the tubules and therefore the number of fibers that can span the interphase region.

At the highest impact energy of ~ 8.5 J, the intertubular lamellae begin to play a more dominant role in the fracture path of the hoof wall. Figure 5.9 G-I shows several of these fracture surfaces. This failure pattern increases the surface area of fractures in the sample as cracks move horizontally through the sample rather than traveling down along the tubule axis. At the highest impact energy, the tubule-matrix interaction also begins to change. Rather than pulling tubules out of the matrix in the longitudinal direction, the impact causes tubules to tear away from the matrix in the transverse direction.

These findings generally agree with higher strain rate compact tension tests performed by Kasapi and Gosline [79]. However, they differ in that samples impacted at higher energies do not have more smooth fracture surfaces. These results also differ significantly from quasi-static tests [80,81] on the hoof wall which showed that the intertubular material nearly always dominates the fracture path. One feature that was noted by Kasapi and Gosline [81] is the variation in IF alignment through the hoof. Under quasi-static loading, this IF arrangement led to crack deviations away from the living tissue at the interior of the hoof. A similar phenomenon was observed after drop tower impacts but to a much lesser extent. In nearly all fractured samples, cracks traveling toward the interior exhibited a sharp bend at the same location. Several examples of this deflection can be seen in the images on the left half of Figure 5.10. SEM images, shown on the right of Figure 5.10, revealed that this deflection occurred in the region where there was a change in fiber alignment. Since the IFs are aligned within the macrofibers, the change in macrofiber orientation corresponds well to the crack deflection mechanisms found by previous studies. However, likely due to the higher impact energies of the drop tower tests, this change in orientation was not enough

to fully deflect the crack away from the interior, but only to cause a minor deviation in the crack path. Regardless, this suggests that macroscale fracture control properties of the hoof arise from its fibrous composition. Another cause of this deflection could be the change in tubule shape and density in this region that was reported by Kasapi and Gosline [81], Reilly et al. [99], and Leach [440]. Here, there is a transition from smaller partially elliptical tubules to large circular ones which may lead to the change in crack path.

Figure 5.10 Fiber orientation within the hoof leads to crack deflections during fracture. (Left) images of samples after drop tower testing showing crack deviation near the interior of the hoof wall. Crack path is highlighted by the dotted red line. The deflection is emphasized by the yellow arrow. (Right) SEM images taken around the deflection zone showing a change in the orientation of the fibers. In the top image, taken above the yellow line, fibers are oriented perpendicular to the cross-section. In the bottom image, taken below the yellow line, fibers run parallel to the cross section, as shown by the green arrows. The middle image shows the transition region where the orientation of the fibers changes.
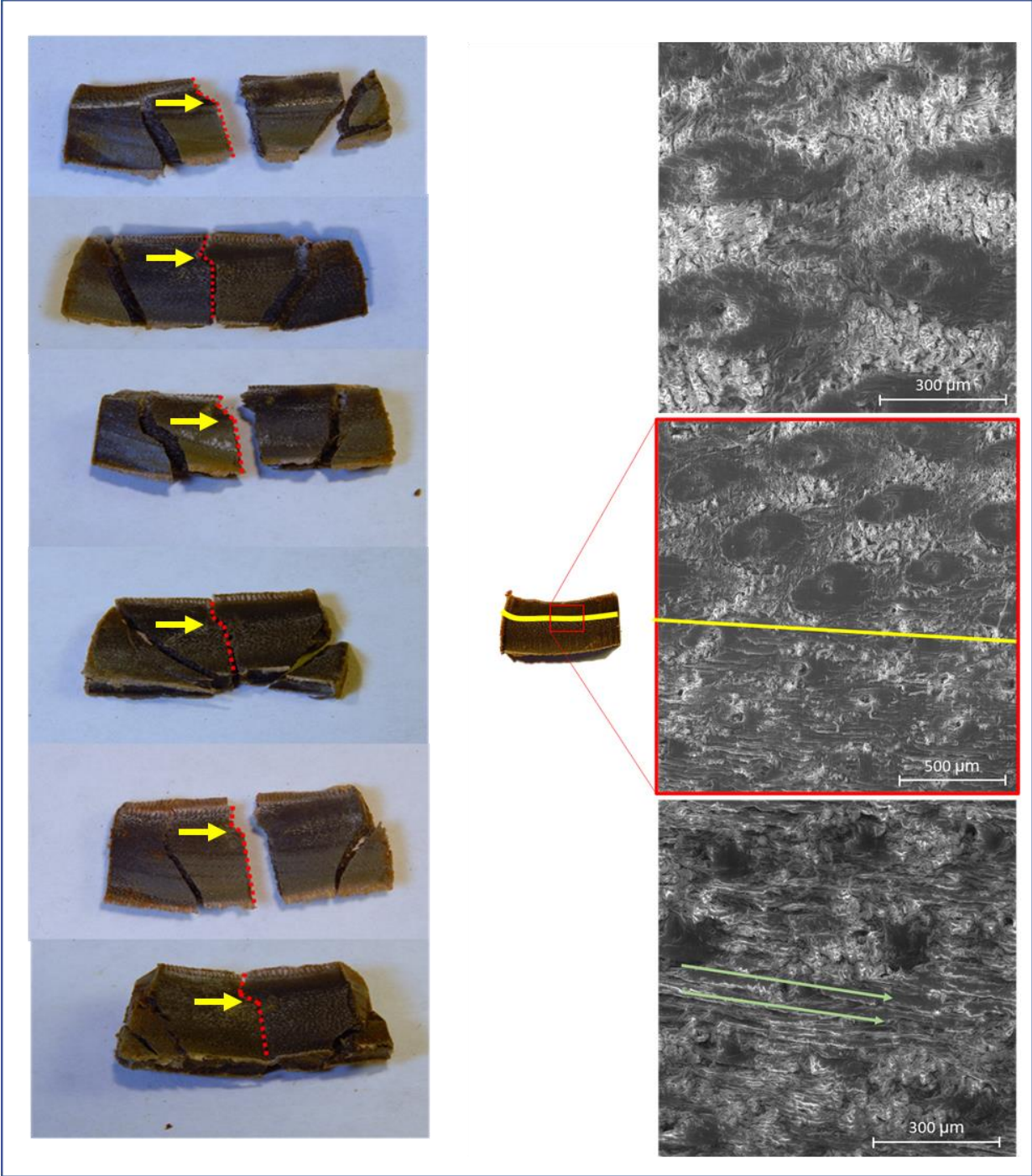
Huang et al. [78] observed fibrous bridges spanning the hollow medullary cavities of the tubules and hypothesized that these increased stability of the tubule. Indeed, these bridges do seem to play a structural role in the hoof as many were found fractured after impact while the rest of the tubule was left mostly intact. Several SEM images of this phenomenon can be observed in Figure 5.11.
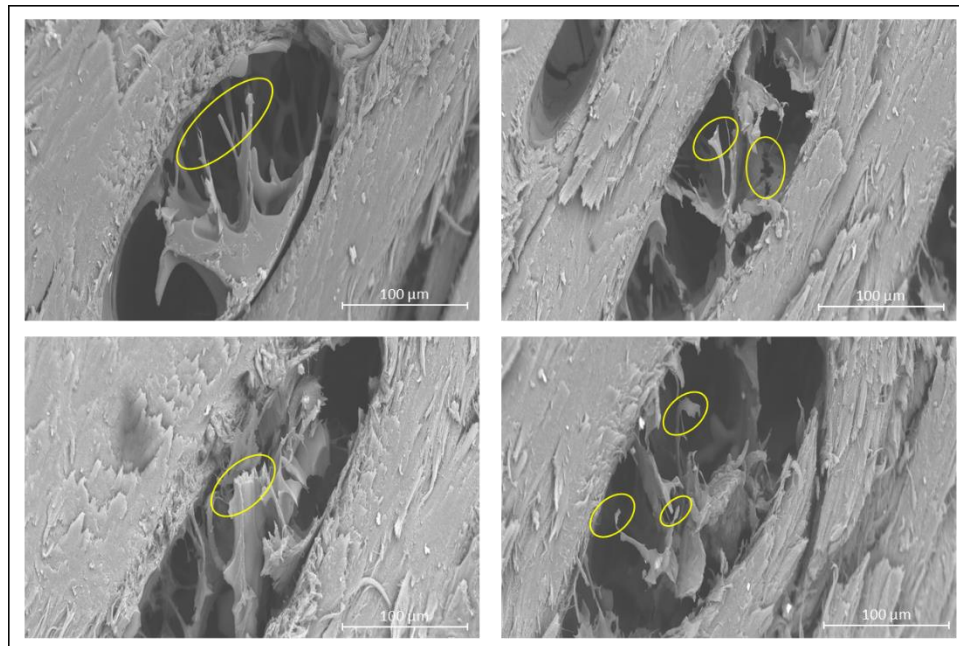
Figure 5.11 SEM images of fractured tubule bridges. These structures fractured prior to the rest of the hoof wall suggesting they play an important role in the structural stability of the hoof wall.

5.3.4 Bioinspired designs

These designs were generated to test the hypotheses developed as a result of the observations of the fracture retardation mechanisms made in the drop tower tests. Several simulated mesostructures created by additive manufacturing were tested in the drop tower setup and subsequently in a more controlled geometry in which a crack was generated with well controlled orientation (quasistatic fracture toughness tests).

5.3.4.1 Dynamic tests (Drop tower)

Computer aided design depictions of each model is shown in Figure 5.12A. Model 1 serves as a control sample with no features and consisting only of matrix material. Model 2 incorporates uniformly distributed hollow cylindrical cavities, representing the medullary cavities found in the hoof wall. Model 3 incorporates the tubular density gradient found in the hoof wall, with the hollow cylinders more congested towards the 'exterior' end of the sample and fewer near the 'interior'. Model 4 maintains the same uniform tubular arrangement as Model 2 but incorporates reinforcement material around each cavity. Model 5 maintains the same uniform distribution but adopts the shape gradient feature as outlined in Kasapi et al. [81], which shows that tubules in certain regions are more elliptical than in other portions of the hoof. Model 6 incorporates the shape gradient as well as the density gradient and has a tubular structure most similar to the actual hoof. The final two models were designed to test the intertubular lamellar features by emulating a 3:1 matrix to soft layer ratio. Model 7 incorporates the soft layers into a featureless matrix with no tubules. Model 8 has the same realistic tubule arrangement as Model 6 but adds soft lamellae into the intertubular matrix. Care was taken to ensure that each multi-material model consisted of the same volume fraction of tubular reinforcement in spite of the design differences.

The introduction of tubules into single phase samples led to an appreciable increase in damage volume between the featureless Model 1 and the uniformly distributed tubules in Model 2 as can be seen in Figure 5.12A. However, the addition of a gradient in tubular density in Model 3 significantly decreased the damage volume to below that of Model 1. Wei and Xu [466] found that cellular gradient structures inspired by nacre distribute load better and allow for greater bending deformation before failure. A similar phenomenon occurred in these bioinspired samples where the asymmetric porosity leads to a gradient in effective elastic modulus. Double material

samples (Models 4-6) containing reinforced tubules predictably sustained the most damage as samples were embrittled by the addition of the stiffer reinforcing phase. The gradient features, both in tubule density and tubule shape, again led to a decrease in observed damage after impact. The increased soft material in the impact zone blunts the damage while the reinforcement on either side resists the spread of damage. The soft ductile layers further reduced residual damage. Model 8 had the same tubular arrangement as Model 6 but included soft ductile layers. This combination of tubular density and shape gradient alongside ductile lamellae led to the lowest damage volume of the reinforced tubules, providing a positive optimization of stiffness and damage reduction.

A closer look at the segmented damage volume itself revealed how each sample failed under impact. Figure 5.12B shows microCT images of the back face of impacted models as well as extracted subvolumes of the damage in each model. The damage volume of Model 1 forms a cylinder near the impact surface before spreading into a conical shape with very smooth fracture surfaces. The tubular features of Models 2 and 3 create more asymmetric damage in the samples as cracks "reach" for tubules that are farther away from the impact zone. This leads to delocalization of damage. In Model 2, cracks extend out from the damage zone before terminating at hollow tubules. In Model 3, the fracture is controlled by the tubular density gradient. Damage occurs preferentially on the more densely porous side of the sample. The unreinforced tubules near the impact zone act as flaws, initiating cracks, while those farther away act as crack arresters; with so many densely packed tubules the crack path is constricted and does not extend past the first row of tubules adjacent to the impact. On the less dense side of the model, fractures behave similarly to those in Model 2, traveling through the matrix towards nearby tubules. Much like the damage mechanisms observed in the horse hoof [79,81,82], this arrangement allows the samples to control the crack propagation.

Figure 5.12A shows that Model 2 sustains more damage than Model 1 while Model 3 experiences noticeably less. This is a result of the gradient in density. With tubules near the impact zone acting as crack initiators, the uniform distribution of tubules leads to an increase in damage relative to the neat, featureless samples. The benefits of cracks arrested by distant tubules are outweighed by tubules near the impact zone weakening the material. Mirkhalaf et al. [451] observed a similar phenomenon in glass, noting that when intentional crack deflecting flaws were concentrated too densely they could significantly reduce a material's overall toughness rather than enhancing it. Meanwhile samples with a gradient in tubules get the benefit of tubule crack arresters while there are fewer tubules near the impact zone to act as crack initiators. Previous authors have postulated about the role of the gradient in tubule density and shape within the hoof. Kasapi and Gosline (1996,1997) suggest that the denser tubules near the exterior are meant to act as an initial barrier for cracks propagating inward from the outer wall of the hoof, to resist bending, or to provide increased stiffness near the wall's exterior surface. Our results suggest that this design is meant to incorporate crack arresters near the edges of the material, which prevent cracks from propagating entirely through the material, causing complete failure. Instead, the damage is localized in the middle of the sample where the tubules are least dense. This is supported by drop tower tests on the hoof itself, where damage to hydrated samples was contained in the central portion of the sample. In the hoof, this corresponds to the mid-wall where Kasapi and Gosline (1996,1997) identified fiber orientation-related crack deflection mechanisms during non-impact tests that direct damage away from living tissue at the hoof's interior. This observation suggests that if damage occurs from impact in-vivo in the hoof, it is contained in the mid-wall by the tubular arrangement while further propagation of these

cracks from quasi-static loading (say walking or standing on the hoof) will be redirected towards the exterior.

Model 4 sustained the most damage of any design. Unlike Model 1, damage in Model 4 immediately began to spread into a conical damage shape starting at the impacted surface. In Models 5 and 6, the initial cylindrical shape near the impact surface was once again observed. This is likely the result of having less stiff reinforcement near the impact zone. However, a notable feature of the damage volume for these two models is their jagged fracture surfaces. The denser reinforcement on either side of the impact restricted the spread of damage and deflected fracture interfaces. In some of the tubules near the damage front microcracks were observed in the tubule reinforcement but were arrested at the tubule-matrix interface. Furthermore, the reinforcement reduced the number of cracks traveling through the matrix, resulting in more symmetric, localized damage. The use of tubular gradients is likely meant to strike a balance between stiffness and impact resistance. Without sacrificing the amount of reinforcement, the hoof can improve its impact resistance over uniformly distributed tubules features with this arrangement. In Models 7 and 8, the soft lamellae dampened the impact and absorbed energy via delamination. The back face of Model 7 exhibited very little damage other than a few cracks. The segmented damage volume shows that the conical damage was arrested at one of the lamellar interfaces and only narrow cracks were able to penetrate to the bottom of the sample. The tubular gradient once again controlled the damage volume seen in Model 8, with irregular, asymmetric fracture patterns that indicate deflection at tubular interfaces. Figure 5.12C shows a cross-section of the internal cracking of Model 8 compared to Models 1, 4 and 7. In Models 1 and 4, relatively little microcracking was observed, with most damage concentrated in the conical shape directly below the impact. In Model 7, several horizontal cracks were observed along the soft-hard lamellar

interfaces, with some fiber bridging occurring. In Model 8, many horizontal cracks initiated along the lamellar interfaces and radiated outward.

These tests show that many beneficial failure mechanisms identified in the horse hoof wall can be translated into engineered materials by utilizing bioinspired designs. These include deflections at tubular interfaces, tubular gradients as a means of fracture control, and soft lamellar arrangements dampening impacts and delocalizing damage. However, there are features unique to the hoof that are very challenging to replicate. For example, the hierarchically intertwined fibers of the tubular reinforcement found in the hoof would be very difficult to recreate in a man-made structure. Also, certain failure mechanisms commonly observed in post-impacted hoof wall, such as tubule pullout, were not observed in the bioinspired designs. This could be a result of the scale difference between the biological structures and the 3D printed designs or from differences in sub-tubular scale features and properties.
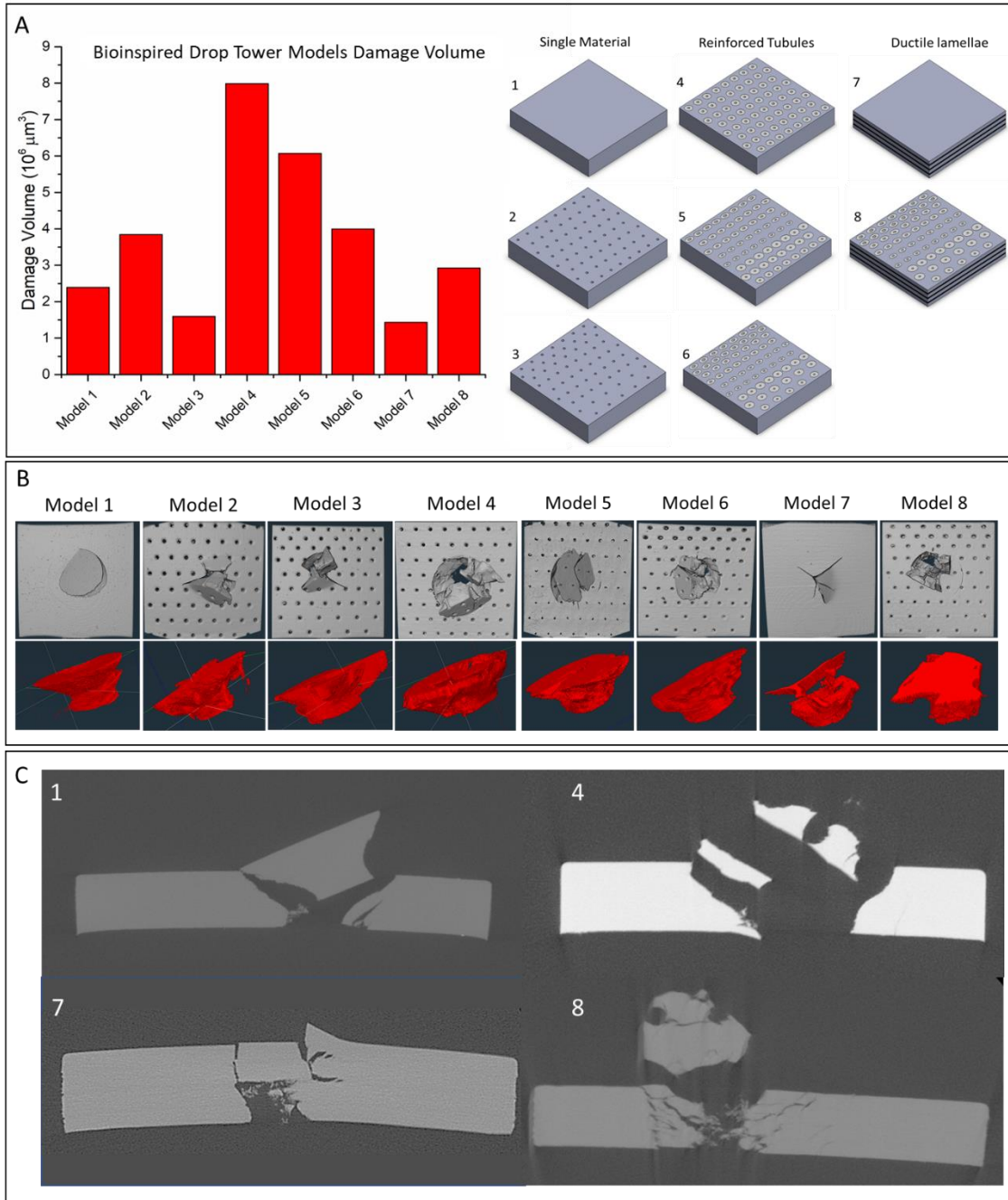
Figure 5.12 A) Damage volume after drop tower testing for each of the bioinspired samples, B) Visualizations of the damage volume for each model showing how the different arrangements control crack propagation, and C) Orthogonal slices through the damage zone of four different samples showing the different crack propagation mechanisms.

5.3.4.2 Quasistatic tests (Compact Tension)

Computer aided design depictions of the compact tension models are shown in Figure 5.13A. The compact tension models consist of the same model designs from dynamic drop tower bioinspired designs, but with the addition of two models; one which tests control Model 1 composed of the stiff reinforcing tubular material and a model which has uniformly distributed tubules with an elliptical reinforcing region. For the latter, a shape ratio of 1.62 was chosen as this correlated to the most extreme elliptical tubules observed in the hoof by Kasapi et al. [81].

All fractured samples are shown in Figure 5.13B. Models 1-3, with no reinforcement, maintained a relatively straight crack through the sample while Models 4-7, with tubular reinforcement composed of the stiffer VeroClear phase, experienced torturous crack deflection around tubular regions. Particularly in Models 2 and 3, the crack passes directly through the medullary cavities where the cavities act as flaws. Resulting load versus displacement curves provide insight for the performance of the models. The averages for each model were plotted in Figures 5.13C and 5.13D for control Models 1a and 1b and Models 1a, 2-7 respectively. For the control models, Model 1a maintained a smooth curve representing the expected ductile nature of the printed material. The stiff Model 1b experienced brittle fracture almost immediately after the experiment began. Models 2 and 3, with no reinforced cavities, rendered curves with smaller maximum loadings as the crack propagated through the cavities. The maximum loads and overall curves for Models 4-7 were greater than for Models 1a, and 2, and 3. The introduction of cavities into the bioinspired hoof structure dramatically decreased the mechanical toughness of the samples, as noticed by comparing Model 1a to Models 2 and 3, since the cavities act as flaws guiding the crack relentlessly through the material. This observation supports Kasapi and Gosline's [467] theory that the hollow cavities are either a manufacturing constraint, meant to reduce the

weight of the hoof, or resist co-operative buckling of the individual reinforcing elements under longitudinal compression rather than as a means of improving fracture toughness.

The reinforced tubular structure caused crack deflection that led to torturous crack paths, which is attributed to its high energy absorbing behavior. Furthermore, the density gradient feature in combination with the reinforced tubular structure exhibited consistent fracture control properties due to the congestion of tubules near the crack tip and further implied crack path manipulation. Through video correlation, the ridges in the curves of Models 2-7 were caused by a tubule or cavity acting as obstacle interface for the propagating crack. When the specimen's crack path was halted by a tubule in the crack path, a ridge was formed in the curve as it required an extra amount of load to deviate around or through the tubule. This hypothesis is reinforced by the curve in Model 1a and 1b, with no tubular features, maintaining a smooth curve throughout.

The energy absorbed by each model is compared in Figure 5.13E. Models 4-7 rendered energy absorption that was nearly two times larger than the control Model 1a, nearly four times larger than Models 2 and 3, and nearly six times larger than Model 1b, the stiff tubular material alone. While the reinforced tubular structure appeared to have aided in increasing energy absorption, another notable result was regarding fracture control. Samples of Model 7 had very similar curves and took the same crack path in all three trials generating significantly similar curves as shown in Figure 5.13F. On Figure 5.13E, intervals marked on each bar represent standard deviation with Model 7 rendering the smallest standard deviation out of the multiple material models, trailing behind Models 2 and 3 where their lower standard deviations are most likely due to the nonreinforced cavities guiding the crack path. Model 7's consistency could be due to the density gradient feature. By congesting the number of tubules towards the front of the model, the crack was guided by the reinforced tubules down a particular ideal path. Model 7, which is most

like the hoof, did not absorb as much energy as Models 4-6 did. However, this may indicate a tradeoff relationship between fracture control and toughness of a structure. The very slight decrease in energy absorption may be a small price to pay for unique fracture control properties.

Lastly, crack deflection was further quantified by finding the initial angle deflection, the angle measured from crack initiation to 50% displacement of the specimen as noted in Figure 5.14A. Average calculated initial angle deflection for each model is listed Figure 5.14B. Larger angles imply greater crack deflection occurring and propagating through a more torturous path rather than a straight line. Models 4-7 had overall greater angle deflection, implying that crack deflection was highly present during fracture due to the reinforced tubular structure. Likewise, the average crack length of each Model was measured and displayed in Figure 5.14C and the average crack length was greater by about 3 mm for Models 4-7 than Models 1-3, which likewise implies greater crack deflection. Crack deflection can also be generally attributed to the increased energy absorbing properties of the tubular structure. While each of the models with reinforced tubules had relatively similar crack lengths, the model with all elliptical tubules had the longest crack length, likely due to the larger deflections required to circumvent the longer perimeter of each ellipse. Kasapi and Gosline [81] suggest that the elliptical nature of the tubules is meant to withstand bending or to prevent tubules from collapsing due to circumferential stresses that arise at the edge of the hoof wall. However, the elliptical tubules may also play a beneficial role in resisting the propagation of orthogonal "quarter-cracks" (an issue in distorted hoof capsules where cracks run parallel to the tubules and can cause lameness and infection [468]) by increasing crack tortuosity at the exterior portion of the hoof. Meanwhile, the large, circular tubules in the interior, further from the location that cracks would be expected to initiate, would be better able to resist longitudinal bending and buckling.

Figure 5.13 A) Computer aided design models of the compact tension samples. B) Post-fracture image of samples. C) Averaged Load(N) vs. Displacement(mm) of Model 1a and 1b. D) Averaged Load (N) vs. Displacement (mm) of Models 1a, 2-7. E) Bar graph of average Energy Absorbed (MJ) for each model with intervals indicating standard deviation. F) All trials plotted in Load(N) vs. Displacement(mm) for Models 1a, 2-7.

A

		2. Standard	3. Applied Density
	1a. Control Matrix		
	FLX9095-DM (gray)		
	1b. Control Tubular		
	Veroclear (white)		

4. Standard Multiple 5. Elliptical Shape 6. Applied Shape 7. Applied Shape & Density

B

1a 1b 2 3 4 5 6 7

no reinforcement **reinforced stiff tubular phase**

C

D

E

F
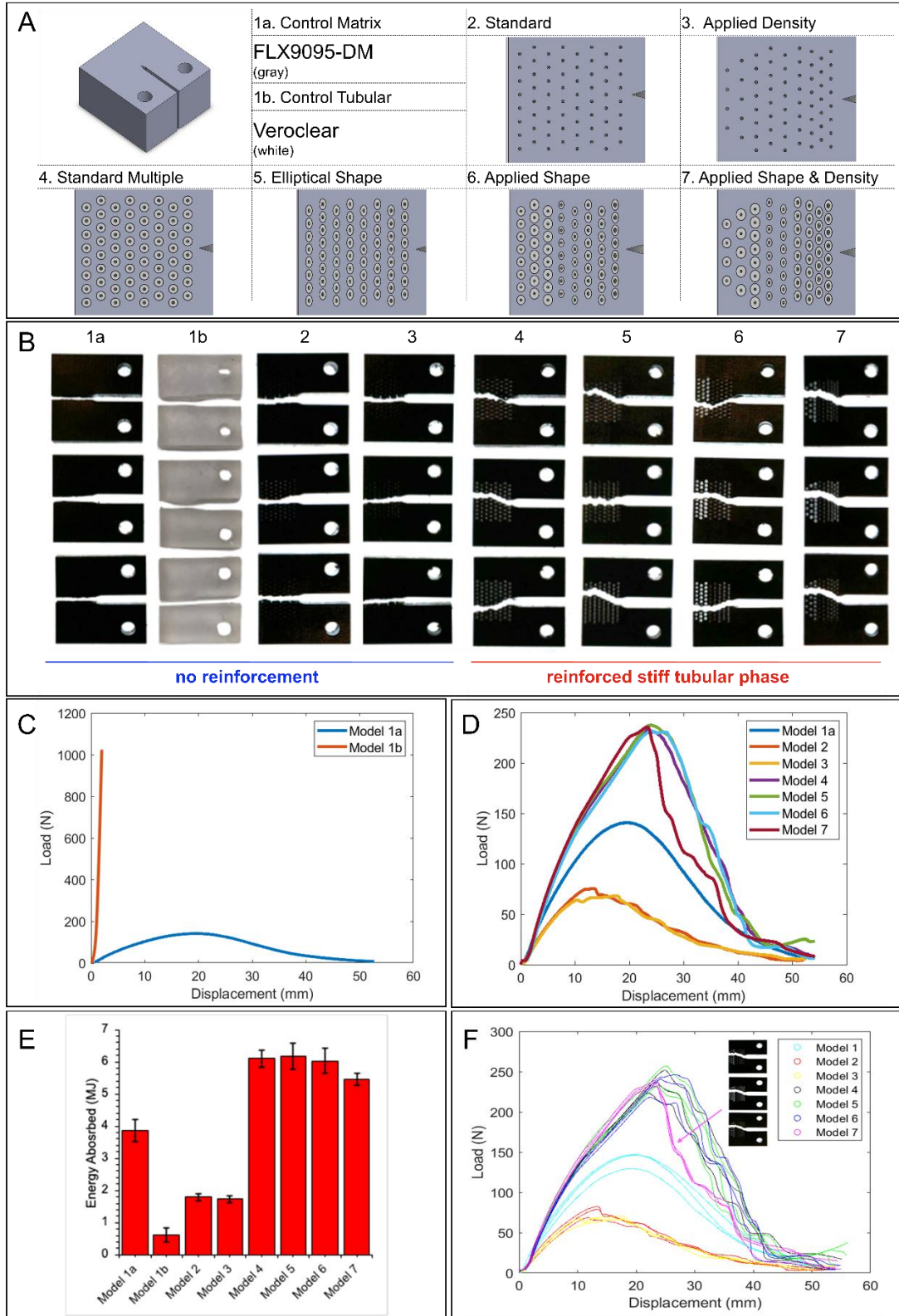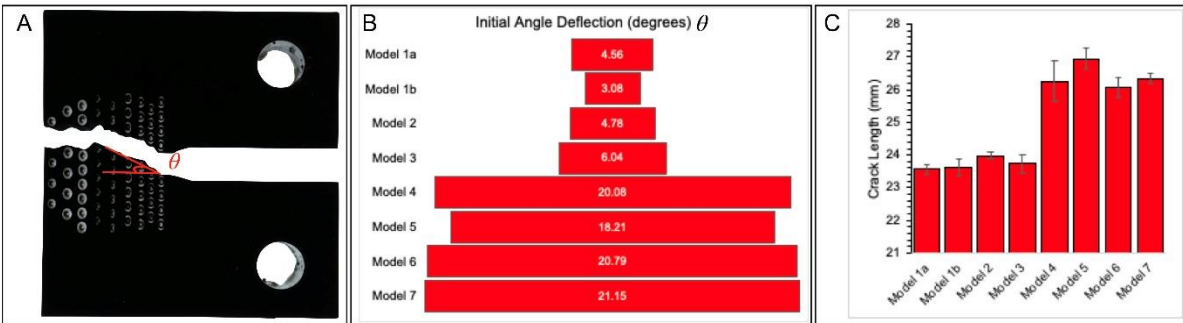
Figure 5.14 A) Initial Angle Deflection indicated on a fractured sample. B) Funnel graph of initial angle of deflection. C) Average Crack Length (mm) measured per each Model from crack start to end of sample.

5.4 Conclusions

The load bearing horse hoof wall has evolved a unique design and properties to survive the demands placed on it in-vivo. Previous authors have identified this evolutionary marvel as a remarkable material for engineers to learn from, yet knowledge gaps surrounding the hoof wall's architecture and it's relation to the compressive, viscoelastic, and impact behavior of the wall remained. This study reaches significant conclusions that expand our understanding of the structure and mechanical response of the horse hoof wall:

1. Several features in the hoof wall are quantified and characterized using microCT and SEM. Results from previous studies on porosity, tubule density, and tubule cross-section were confirmed while new values such as average tubule bridge width and bridge density are reported for the first time.

2. Drop tower tests suggested that these previously unexplored features play a mechanical role in the hoof wall, stabilizing the hollow medullary cavity, and being the first part of the tubule to crack during an impact scenario.

3. Other fracture mechanisms observed by previous authors were noted after drop tower tests such as tubule pullout and deflections at the tubular and lamellar interfaces.

However, our impact fractogaphy results contradict the analysis of tensile fracture presented by Kasapi and Gosline [79,81] and Bertram and Gosline [80,97] who suggest that cracks nearly always prefer to propagate along the intertubular IF orientation. While the intertubular fiber orientation leads to a slight deviation in crack path during impact, the tubules dominate the fracture pattern, particularly at lower impact speeds. At higher impact energies, cracks more commonly propagate between the intertubular lamellae, but fractures still traveled through the sample along the tubular axis.

4. A hierarchy of fibers were also identified within the hoof wall. During cracking these fibers play a key role by intertwining the tubular reinforcement with the matrix. These observations reveal unique mechanisms that are not normally observed in synthetic composites such as tubule bridging or arresting where tubules extrinsically toughen the hoof by spanning crack interfaces or by arresting propagation at the tip altogether. The fibrous entanglement with the matrix also strengthens the interphase zone of the composite, requiring more energy to induce delamination or pullout of the reinforcing phase since fibers need to be ruptured to do so. This architecture is challenging to replicate but offers an ingenious design motif to improve composite materials, which can be limited by the ability of the reinforcement to adhere to the matrix.

5. To test the role of hydration on the impact resistance of the hoof, drop tower tests were performed at two different hydration states. The samples equilibrated at 50% relative humidity showed minimal damage with most samples exhibiting a small dimple at the impact zone. All samples in the 25% relative humidity environment developed cracks with most samples cracking through the thickness of the sample in multiple places.

6. Quasi-static compression was used to build a better understanding of the ductile-brittle transition in the hoof. Samples hydrated to 30% water content exhibited a ductile behavior across all strain-rates ($10^{-4}s^{-1}$-$10^{0}s^{-1}$) while samples hydrated to 10% water content consistently showed brittle behavior dependent on catastrophic events that began around 0.15 strain. Young's moduli and strain-rate sensitivity were also determined and were in range with those of other keratinous materials.

7. Relaxation tests revealed that samples hydrated to 20% water content dissipated more stress, faster than samples hydrated to 10% or 30% water content. In the hoof, this is a very useful trait, since there is a hydration gradient, and therefore stiffness gradient, that exists through the hoof's thickness leading to loading differentials and internal stresses between the interior and exterior. Twenty percent water content by weight seems to be an ideal optimization for the hoof's exterior that maximizes relaxation speed (reducing internal stresses) while increasing stiffness.

8. Fitting the relaxation data to a Maxwell-Weichert model using a Prony series showed that this quicker relaxation was due to the hoof's mesostructural features. Further, the hoof's relaxation due to mesofeatures is faster than that of other keratinous materials, such as hair, where being able to quickly recover from loading may not be as evolutionarily important.

To show that the benefits of the hoof wall's design can be translated to engineered materials, bioinspired designs were fabricated using a multi-material, 3D printer to replicate the tubular, lamellar, and gradient arrangements found in the hoof. These specimens were subjected to drop tower and fracture toughness tests which showed the interaction of matrix and tubules:

1. Drop tower tests on single material samples showed that tubules act as both crack arresters as well as crack initiators. In samples with uniformly distributed tubule cavities the material weakness introduced by the cavities outweighed the benefits of cavities arresting cracks. With the introduction of a gradient in tubule cavity density, a decrease in damage was observed. This likely results from the fact that fewer tubules are located near the impact zone to act as initiators while more densely packed tubules further from the impact zone continue to arrest crack propagation. The introduction of a more brittle reinforcing phase predictably increased the total damage observed in the samples. However, the application of a gradient again led to a decrease in damage relative to samples with a uniform tubule distribution. This highlights that a gradient in reinforcement density can be used to improve impact resistance without reducing the amount of reinforcement in the material. The addition of soft lamellae further reduced the overall damage of the samples. Much like the drop tower tests performed on hoof samples, impact tests on the 3D printed samples led to crack deflections along the tubular and lamellar interfaces.

2. Compact tension fracture toughness tests on 3D printed samples showed a large increase in crack deflection angle and crack length for samples with reinforcement. While gradient samples showed a slight drop in energy absorbed, they produced predictable fracture patterns with very little deviation in mechanical response between samples.

The present study shows that the hoof contains several unique structure-property relationships that enable it to survive its environmental demands. Its mesostructure improves impact resistance while also allowing it to reduce internal stresses via rapid viscoelastic relaxation.

The importance of several architectures such as cavity bridges and reinforcing elements that are physically intertwined with the matrix were identified and these features offer inspiration for future study. Other previously identified aspects of the hoof wall such as tubules, lamellae, and gradient configurations show significant promise as design elements in engineered materials and warrant continued research, particularly as designs to be used in tandem.

5.5 Acknowledgements

Chapter 6. In-situ Microcomputed Tomography of the Horse Hoof

6.1 Introduction

The horse hoof wall is an incredibly impact resistant biological material which contains many design motifs that provide impact resistance [75]. One of the most characteristic structures

of the hoof wall are the hollow reinforced tubules which provide stiffness [78,100] as well as

fracture toughness [80–82] and impact resistance [79,469]. The role of the tubules has been well-

studied with regards to fracture propagation and crack control. Several studies have shown that

tubules can redirect cracks away from the living tissue at the interior of the hoof and create tortuous

fracture paths within the hoof wall [81,82,469]. Yet, there are still open questions regarding the

configuration of the hoof wall's tubules. For example, the hoof wall contains a well-documented

gradient in tubule dimensions with densely-packed, smaller, elliptically-shaped tubules near the

hoof's exterior and spaced-out, larger, circular tubules near the interior. Previous authors have

debated whether this is meant to create a barrier for cracks initiating at the hoof's surface [81,99],

provide a smooth transfer of energy through the hoof wall [470], resist bending of the tubules

[467], or is simply a residue of manufacturing constraints at the proximal generative tissue [467]

but no definitive conclusion has been put forward. Furthermore, while Huang et al. [78] showed

that tubules completely densify by 60% longitudinal strain, correlating to a steep increase in the

stress-strain curve of hoof wall material, the highly anisotropic hoof wall experiences multi-

directional loading conditions owing to its complex shape [98,450]. Little is known about the

behavior of the tubules when loaded in the transverse and radial directions, which could unlock

the mystery of the complex reinforced-composite design of the hoof wall. Previous authors have

also debated why the tubules are hollow, suggesting that this design would perform better if solid

and arguing that its structure is merely a manufacturing constraint [81,82].

Bridges traversing the hollow medullary cavity at the center of the tubules in the hoof wall

were first observed by Kaspai and Gosline [467] and later Huang et al. [78] however the authors

offer no hypothesis regarding the role of these features. Lazarus et al. [469] identify and quantify

tubule bridges providing a bridge density (~111 μm between bridges) and an average bridge

thickness (10.3 μm). The same study also used post-impact fractography to suggest that these bridges play a role in stabilizing the tubule. The results showed that bridges are one of the first features in the hoof to rupture and that their failure absorbs impact energy which helps keep the tubular reinforcement intact. However, this provides an incomplete understanding of the mechanical role of bridges in the tubule and their behavior during loading. Furthermore, this failure mechanism was only observed in the dry state and it has been repeatedly shown that the hoof behaves quite differently when hydrated.

Many other systems in nature such as bone, dentin, antler, and wood have evolved tubular structures that play an important mechanical role in resisting compressive loading. Yet, amongst these the hoof is unique. It is composed of dead cells with sutured interfaces (shown in Figure 6.1A) that are filled with keratin fibers (shown in Figure 6.1B and C) and are incapable of repairing and remodeling if the hoof is damaged. And, unlike its bony counterparts, is not mineralized and therefore can be much more ductile, particularly when hydrated. As such the structure of the load-bearing hoof wall has deviated from the architectures of these other materials, incorporating unique design gradients and bridging elements. In this study, 4D microCT is used to provide insight into some of the decades old questions surrounding the hoof wall's microarchitecture and to provide blueprints for the design of engineered composite materials. This technique affords researchers the opportunity to observe the microstructural deformation behavior of a material as it is occurring, instead of trying to piece together what occurs during loading retroactively by observing the surfaces of failed samples. As a result, time-dependent phenomena such as buckling and bending, which may relax after testing or be interrupted by rupture and critical failure, can be observed.
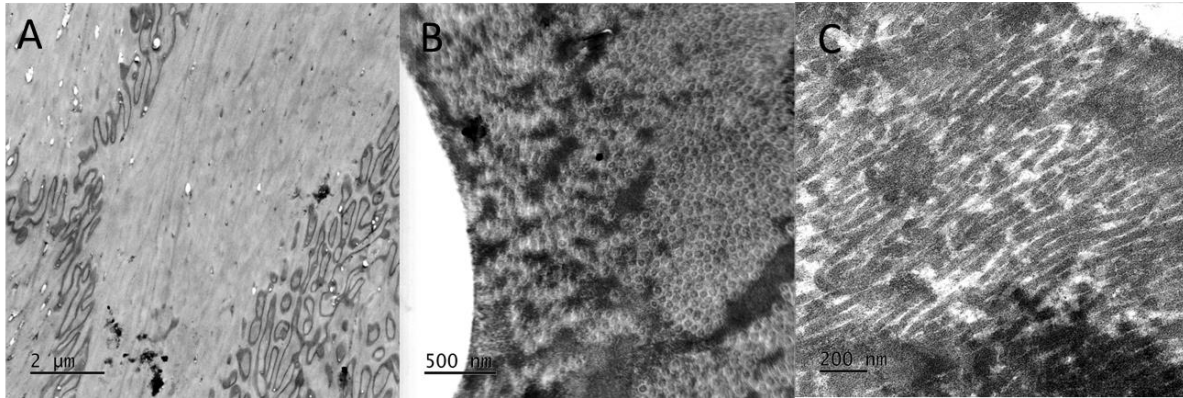
Figure 6.1 TEM images revealing the A.) cellular structure with its sutured interfaces as well as B.) cross-sectional and C.) longitudinal views of the intermediate filament structure in the hoof wall.

Furthermore, in-situ microCT testing can be used to capture time-dependent relaxation behavior to understand the structure-induced viscoelasticity of a material. Lazarus et al. [469] modelled the viscoelastic nature of hooves under compression and found that meso and microscale features of hoof keratin allow it to relax faster than other keratinous materials like hair. Using in-situ microCT we can directly observe the relaxation behavior of hoof features and attach the microstructural deformation events to the macroscale behavior. A similar approach can be used to visualize how cracks propagate through the hoof wall and how this plays into the results of previous authors [79,81,82,469].

This chapter is broken into three parts. The first uses compressive in-situ microCT to test the effect hydration, loading orientation, and location (interior vs exterior) have on the deformation behavior of the hoof wall's features. The second portion focuses on the relaxation behavior of the hoof wall and how the features in the hoof behave after a loading event. The final section utilizes in-situ compact tension tests to analyze the fracture behavior of the hoof wall.

6.2 Methods and Materials

6.2.1 TEM

TEM samples were prepared from slices of hoof taken from the central toe region. Samples were fixed a in 2% glutaraldehyde solution in sodium cacodylate (CaCO) buffer for a period of two hours at room temperature. Samples were then washed in a CaCO buffer three times for ten minutes each. Samples were post-fixed in a 1% osmium tetroxide solution, with 0.8% potassium ferricyanide and 5 mM calcium chloride in CaCO buffer, for an hour, protected from light. Samples were then washed again in the CaCO buffer three times for ten minutes each. Following the wash, samples were dehydrated in a series of increasingly concentrated (30%, 50%, 70%, 90%, and 100%) acetone solutions at room temperature for 10 minutes each step. The final step was performed twice before the sample was submerged in super dry acetone. Samples were then infiltrated with PolyBed 812® resin at room temperature and constant slow agitation, for at least 6 hours each, in the following proportions:

- Resin/super dry acetone molar ratio 1:2;

- Resin/super dry acetone molar ratio 1:1;

- Resin/super dry acetone molar ratio 2:1;

- Resin/super dry acetone molar ratio 3:1;

- Pure resin.

Each sample was assembled in a Beem capsule® and polymerized for 60 hours in an oven at 60 °C. Samples were scanned using a JEOL (Tokyo, Japan) TEM-1230 transmission electron microscope.

6.2.2 In-situ microcomputed tomography

In-situ microcomputed tomography experiments were performed at the Lawrence Berkeley National Laboratory Advanced Light Source on beamline 8.3.2. Three different tests were performed on hoof samples; compression tests, relaxation tests, and compact tension tests. Scans were taken at 22 keV using a camera exposure of 225ms, an Optique 10x lens, 20 μm LuAGb scintillator at 130 degs, focus of 17.345mm, and a tilt of .579um. Scans took around 7 minutes to run. The projections were reconstructed with a custom software (https://microct.lbl.gov/software) produced by ALS beamline scientists. Reconstructed stacks had a pixel size of 0.64 μm and were analyzed with ImageJ/FIJI and the Volume viewer plugin. Two series of tests were performed. The first consisted of compression and compact tension tests. Relaxation tests were executed during the second round of experiments. To increase consistency and precision, an improved hydration technique was used during the second round of experiments.

6.2.3 Compression tests

5x5x5mm^3 samples were taken from central toe region of the hoof wall. For compression tests, samples were scanned at compression intervals of 10% or 20% strain either until 80% strain or until the sample failed. Samples were tested at three different hydration levels; hydrated, ambient conditions and dry. All samples were oven dried at 100 °C for 72 hours. Immediately after being removed from the oven, dry samples were sealed in two plastic bags with desiccant for transportation. Hydrated samples were soaked in water for 24 hours prior to testing while ambient condition samples were allowed to equilibrate for several weeks prior to testing. Ambient condition samples were prepared to be tested in each of the three axial directions; longitudinally (along the tubule axis), radially (along the exterior-interior axis of the hoof), and transversely (sometimes referred to as circumferentially, this is along the hoof wall's thickness). To understand

how the different tubule geometries and configurations that exist through the hoof wall's thickness behave during loading, samples were taken from the interior and exterior of the hoof wall and compressed along the longitudinal axis for comparison.

6.2.4 Compact tension tests

Compact tension samples were machined out strips of the hoof following ASTM D5045 with the crack oriented along the radial axis using a Haas TM1 (Haas, Oxnard, CA, USA). Aluminum jaws were used to cut a pocket in the shape of the sample and then an endmill to cut the pieces. Care was taken to ensure that small cuts were made, and samples were cooled with water during cutting. Owing to the narrow thickness of the hoof wall, samples could only consistently be cut to be 10x10mm. To facilitate tomography scans, 1mm thick samples were used allowing a good signal to be transmitted to the detector. A precrack was introduced at the end of the slit using a razor blade. Custom made clevis grips were prepared to attach the sample to the tensile rig in the microCT beamline. Scans were performed at intervals of 100 μm until the crack propagated entirely through sample. Hydrated, dry, and ambient condition samples were tested.

6.2.5 Relaxation tests

5x5x5mm^3 samples were taken from central toe region of the hoof wall. Samples were scanned prior to testing (the initial samples), then loaded to set strains (20%, 40%, 60%, and 80%) and scanned immediately after compression, and then scanned again after a 5-minute period of relaxation. One sample was also compressed in a scaled fashion, reaching 80% strain in 20% strain increments with incremental relaxation periods between loadings. Samples were also tested at two different initial hydration conditions (dry and hydrated) and two different relaxation conditions (ambient or water immersed). All samples initially were oven dried at 100 °C for 72 hours and then sealed similarly to compression test samples. Hydrated samples were soaked in

water prior to experiments, until the samples reached a water content of 17.5% ± 1.26, calculated by comparing the weight of the sample dry versus after soaking. In ambient relaxation conditions after loading, the samples were left in an open container exposed to ambient conditions. In water immersed relaxation condition during loading, there was an attempt to consistently wet the sample during the beamline experiment by covering a wet, hydrated sample with plastic wrap. After loading, the sample was then submerged in water. Sample dimensions were tracked in recovery using digital calipers, routinely for the next twelve hours.

6.2.6 Finite Element Analysis

Using images obtained from the tomography experiments, digital 3D models were created in Solidworks 2021, replicating observed tubule bridges. Models were direct interpretations of imaged cavity bridges with secondary models created that emulated the same cavity but without the bridge. Modeled cavities were embedded in a thin plane, drawn roughly to scale. These models were then imported into Ansys Workbench 2022 R2 for simple, static structural simulation. A custom material library for hoof wall was created and applied using previously reported elasticity properties. Ansys Mechanical was used to set Fixed Support and prescribed Displacement conditions, pinning, and compressing the model varying in the radial and transverse loading directions and with or without bridge cavity support. Total strain energy was calculated by the model simulations and reported.

6.3 Results and discussion

6.3.1 Compressive behavior

When compressed, tubules tend to behave as a cohesive unit, likely due to the reinforcement that surrounds the medullary cavity, buckling into an "S" shape. In untested hooves, tubules often exhibit some waviness along their longitudinal axis, undulating back and forth in

both the radial and transverse directions (a schematic of the hoof wall's axes nomenclature is shown in Figure 6.2A). This initial waviness (Figure 6.2B) provides a template for the tubules' motion during compression. The bowed portions of the tubules become exaggerated, and the amplitude of the waves increases as the hoof is compressed longitudinally. Buckling is the most common failure mode of engineered composite materials in compression, and it generally is accompanied by shear band kinking, where lateral cracks develop in the reinforcing elements [471–473]. Such failure mode leads to a precipitous drop in stress and the overall toughness of the composite. However, in hydrated and ambient hoof samples, the tubules buckled significantly without exhibiting kinking. This behavior has been reflected in the stress-strain curves measured in previous studies, where the stress level continues to rise throughout compression. Such a constitutive response is likely because the reinforcement is composed of a relatively soft and ductile polymeric material. Generally, composite engineers try to avoid failure from buckling, since shear-induced fractures occur at lower stresses than those that form during uniaxial fiber crushing. However, in hooves, this tradeoff may not be the case.
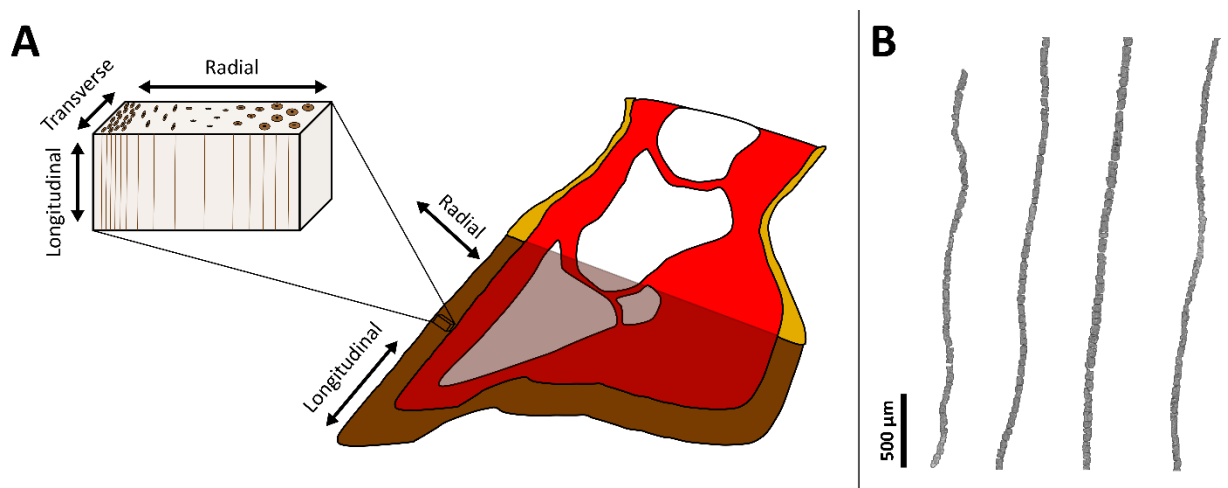
Figure 6.2 A) Schematic of the hoof showing the orientation of the different axes in the hoof and their nomenclature. B) Individual tubules extracted from microcomputed tomography (microCT) scans showing the wavy nature of the tubules.

The cavity bridges provide a degree of resistance to tubule collapse during compression. Figure 6.3A shows a longitudinal cross-section of the same interior tubule being compressed radially at different strains. After 10% strain, small amounts of bridge and tubule wall deformation can be seen throughout the tubule, with slightly more seen in the top portion of the tubule where the bridge density is lower. By 20% strain, nearly the entire tubule has collapsed in the region with fewer bridges, while small pockets survive between the compacted bridge material in the lower portion of the tubule. Figure 6.3B shows a perpendicular cross-section of several exterior tubules compressed in the transverse direction. Much like the radially compressed tubules shown in Figure 6.3A, these tubules collapsed more in areas with less bridging and experienced buckling of the tubule wall in the unsupported pockets. Meanwhile, in regions with more bridge support, bridges were observed buckling and deforming into characteristic "S" shapes, while the tubule walls maintained their geometry.
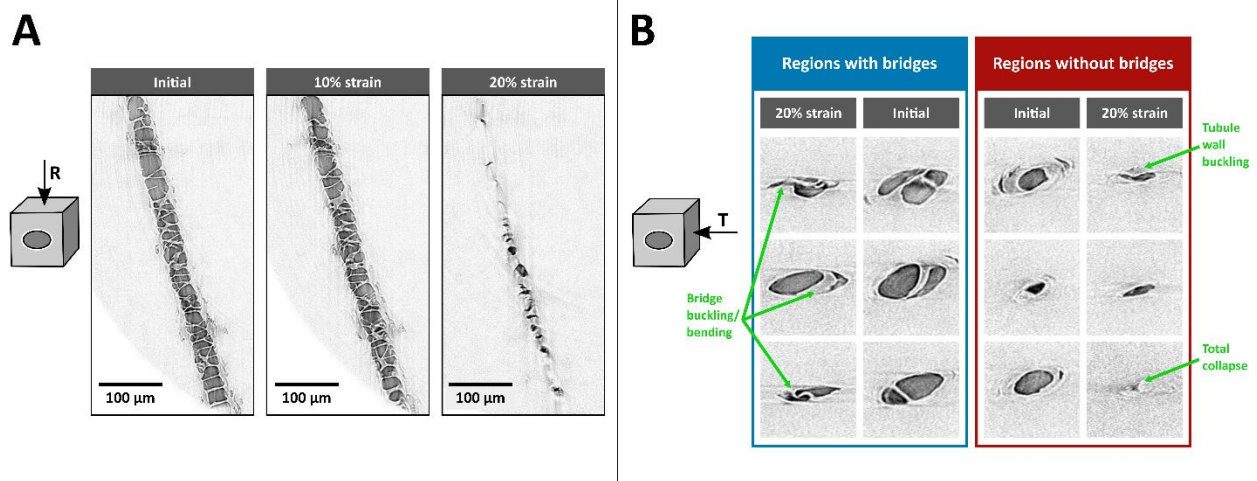
Figure 6.3 A) Microcomputed tomography (microCT) scans of tubules hydrated at ambient conditions compressed radially, showing how the tubules collapse first in regions with less dense bridging. B) MicroCT scans of tubules compressed in the transverse direction, highlighting how bridges can help prevent collapse, relative to regions without bridges (scale: each of the microCT images shown in this panel is a square of 100 μm × 100 μm).

Thus, the bridges play an important role in helping the tubules maintain their structural integrity while also increasing the amount of energy the hoof wall can absorb when compressed. Figure 6.4A depicts a typical interior tubule with a bridge compressed in the radial direction, and Figures 6.4B-E portray a finite element analysis of this scenario with and without the bridge compressed in the radial and transverse directions. When compressed in the transverse direction, the bridge, understandably, only has a minor effect on the strain energy absorbed. However, when compressed in the radial direction, the model with the bridge absorbed over 50% more strain energy than the model without.
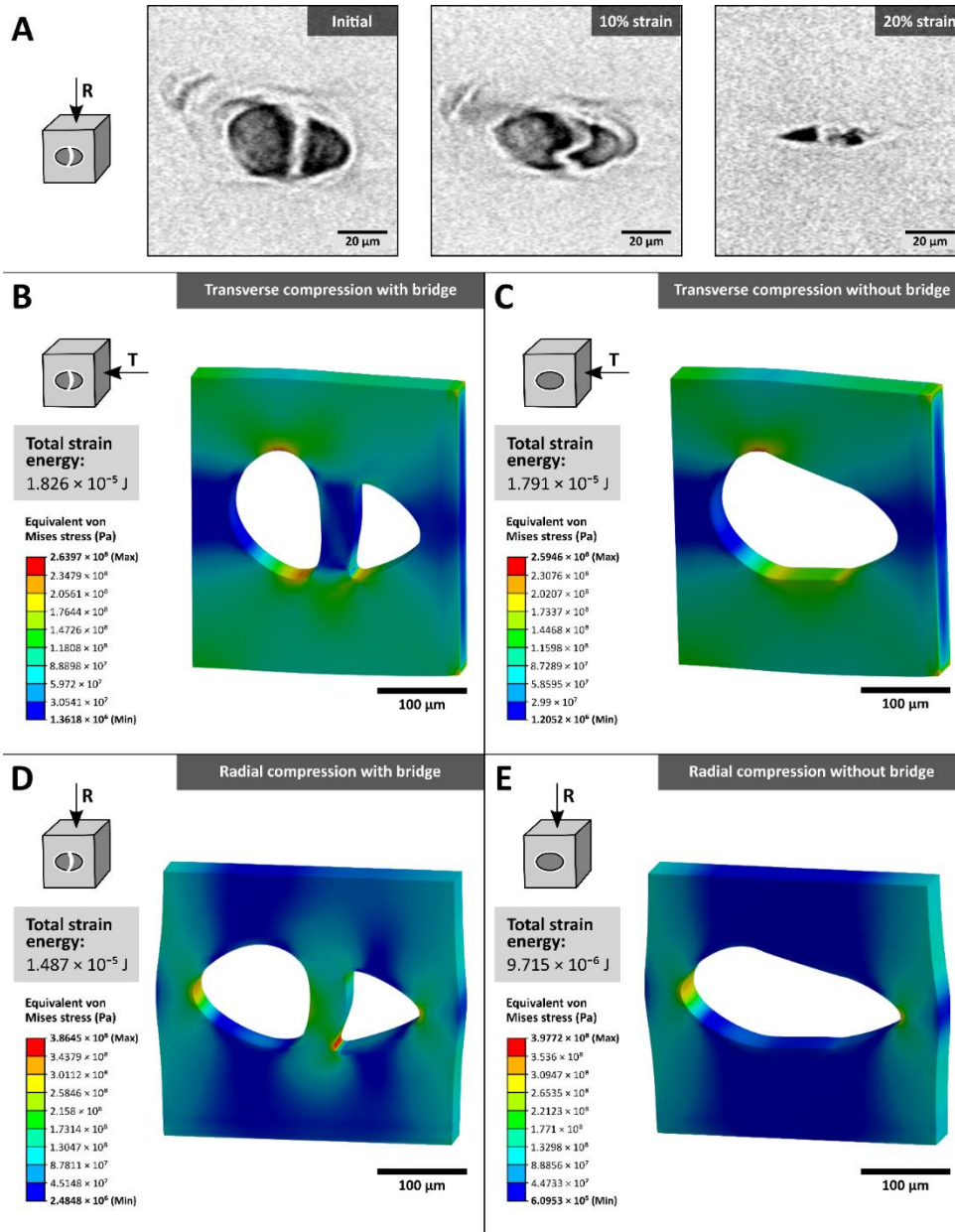
Figure 6.4 A) Microcomputed tomography (microCT) scans showing an example of a radially compressed tubule and bridge. This example was used as a blueprint for finite element analysis (FEA) models examining samples compressed in the transverse direction B) with and C) without the bridge, as well as in the radial direction D) with and E) without the bridge. The total strain energy absorbed during compression was calculated and is listed in each panel.

6.3.1.1 Variations by water content
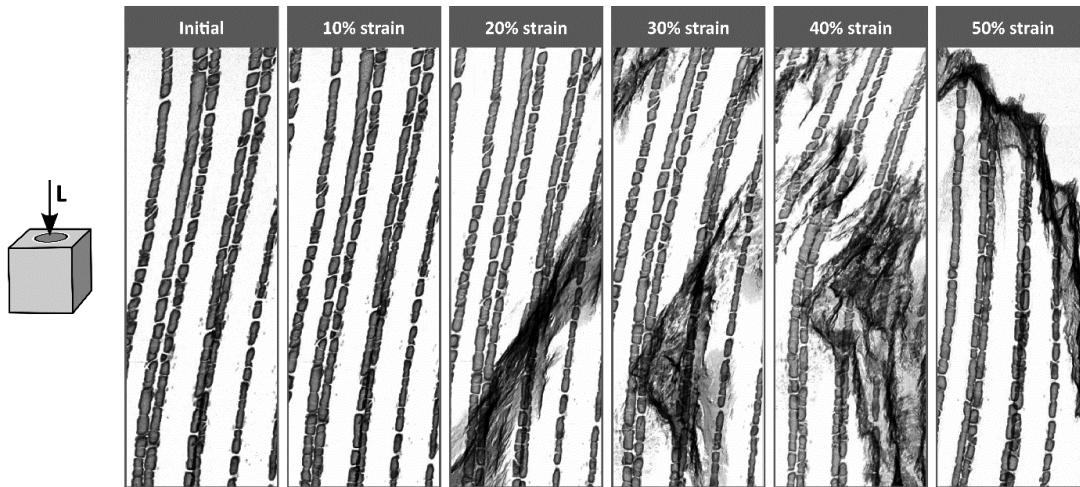
Figure 6.5 Three-dimensional renderings of microcomputed tomography (microCT) scans taken of dried hoof wall samples compressed in the longitudinal direction at intervals of 10% strain. Dark jagged features beginning at 20% strain are cracks propagating within the sample.

The water content of the hoof appears to affect the hoof's mode of failure strongly. In agreement with [3,8], it is found that hydrated hoof tubules will buckle under compression, whereas a dried hoof will crack before the microfeatures experience much deformation. Figure 6.5 shows the progression in increments of 10% strain of a dry hoof sample cracking under compressive load. Formation of large black splotching are cracks weaving between the tubules and tubule bridges and begin to initiate between 10% and 20% strain. Tubules begin to bend

towards the top of the field of view at around 30% strain until a clean fracture occurs at 50% strain, shearing off the tops of the tubular cavities.
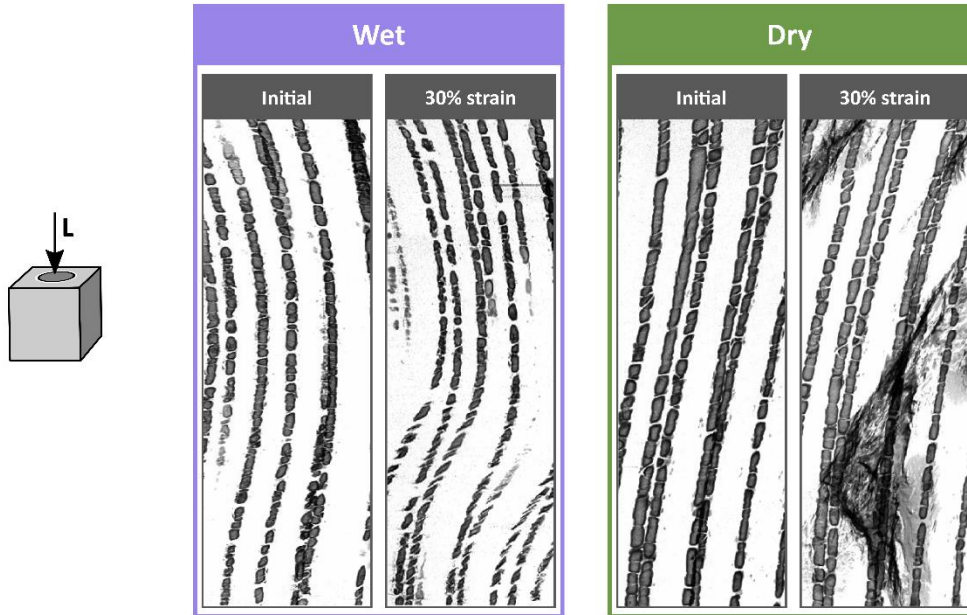
Figure 6.6 A side-by-side comparison of microcomputed tomography (microCT) scans of wet and dry samples compressed to 30% in the longitudinal direction. Wet samples exhibit much more tubule buckling and cavity collapse, while dry samples form diagonal cracks.

A direct comparison of a wet and dry hoof is demonstrated in Figure 6.6, showing the initial tubular cavities and their configuration at 30% strain. At 30% compressive strain, the dry hoof cavities show minimal deformation, but cracks form around the cavities. As for the wet hoof sample, no cracks are observed. Instead, parts of the cavities begin to densify as the tubules deform

into an "S" shape. Very little deformation was observed in the bridges of dry samples, even just before the onset of fracture, as shown in Figure 6.7.
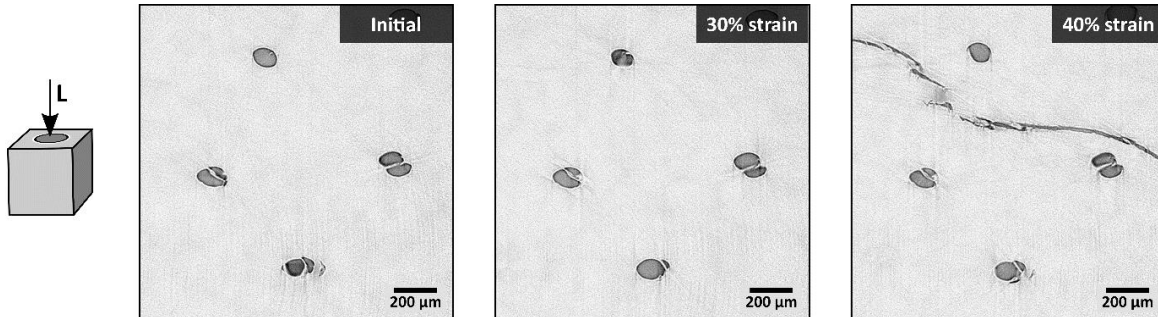
Figure 6.7 Microcomputed tomography (microCT) scans of a dry sample compressed in the longitudinal direction showing cracking but minimal deformation of the tubule bridges.

6.3.1.2 Variations by location

The density, size, and shape of the tubules vary based on their location within the hoof wall. In the interior, tubules tend to be less densely packed, larger, and more circular (although all tubules are elliptical in shape) compared to the exterior portion of the hoof. Leach [440] found that the inner wall had a much lower modulus of elasticity than the outer wall, reaching values of 62.5% when compressed along the tubules and just 51% when tested in the other two directions. Leach also suggests that the outer wall has a resilience that is 1.5-2 times greater than that of the inner wall.
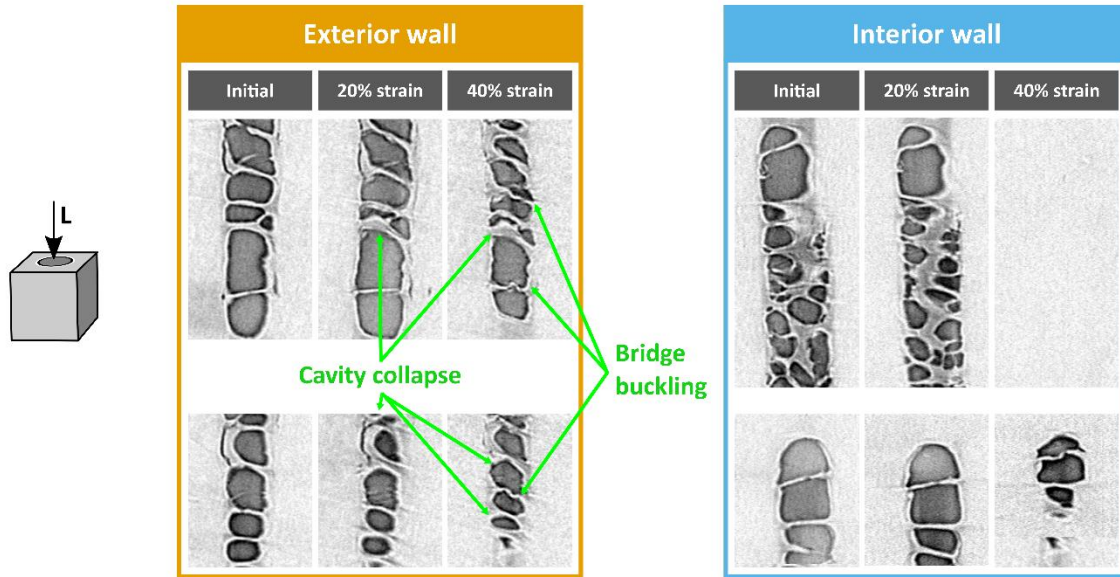
Figure 6.8 Images extracted from in-situ microcomputed tomography (microCT) scans showing longitudinal cross-sections of samples compressed along the tubule axis. Images on the left show individual tubules from exterior samples, while those on the right show those of interior samples (scale: each of the microCT images shown in this panel is a rectangle of 100 μm width).

The in-situ microCT results showed that tubules in interior samples compressed longitudinally collapsed at lower strains, being nearly completely densified by 40% strain. Meanwhile, exterior samples were often able to maintain their internal features until 60% strain. Interestingly, tubule features in the exterior of the hoof wall show noticeable, progressive damage during compression, including cavity collapse and bridge buckling. Interior samples, however, exhibited minimal deformation before collapse. These phenomena can be seen in Figure 6.8, which shows tubules compressed in the longitudinal direction. However, this trend is consistent amongst tubules compressed in all directions. This observation supports the mechanical findings of Leach [18]. One possible explanation for this behavior could be the effect the difference in tubule size and shape has on the bridge behavior. In the larger interior tubules, the bridge span is longer, particularly in the radial direction (along the minor axis of the more elliptical tubules), which could

reduce the resistance provided by the tubule bridges relative to the smaller, elliptical tubules at the exterior.

6.3.1.3 Variations by loading orientation

Thomason et al. [12] used strain gauges mounted on living horses' hooves to determine that the hoof wall experiences significant lateral biaxial deformation during locomotion. Biaxial strains primarily arise due to heel-spreading and load transfer between the exterior and interior portions of the hoof. The authors regard the hoof as a multi-directional composite that can withstand strains in every loading orientation. Leach [18] and Huang et al. [3] found that the hoof's properties vary by loading orientation and that, surprisingly, the hoof can be stiffer perpendicular to the hollow, reinforcing tubules. Thomason et al. [12] suggest that this behavior is meant to resist these biaxial loads. Further, Huang et al. [3] found that the hoof wall absorbs more energy when compressed in the radial direction relative to the other two orientations. However, beyond these macroscale mechanical observations, there is little understanding of why this behavior arises from the hoof wall's microstructure.

In-situ microCT scans revealed that the tubules compressed in the radial direction collapse at a lower imposed deformation than the others. Figure 6.3A shows how tubules compressed in the radial direction are nearly entirely densified by 20% compression, while Figure 6.3B (transverse) and Figure 6.8 (longitudinal) show tubules compressed in different directions retaining most of their structural integrity at 20% strain. A cross-section of this phenomenon can also be seen in Figure 6.9A.

The scans also revealed that regardless of the compression direction, tubules almost always prefer to collapse along the radial axis (which corresponds to the minor axis of the elliptical tubules). This behavior is particularly surprising in samples that are compressed in the transverse

direction (Figure 6.9A). Much like samples compressed in the radial direction, bridge buckling was observed, while regions without tubules collapsed at lower strain values. This finding suggests that the tubules are more resistant to loads in the transverse direction. There are several possible factors that could lead to this modality. One reason is that the elliptical tubules have more reinforcement along the transverse axis than in the radial direction, increasing the transverse stiffness of the tubules in that direction. Beyond the sheer quantity of reinforcement, the configuration of the reinforcement might also play a key role. Kasapi and Gosline [6] observed variations in the intertubular intermediate filament orientation through the hoof wall's thickness. However, regardless of location, tubular fibers tend to "flow" around the hollow medullary cavity. The result of this arrangement is that more fibers that compose the tubule walls are oriented in the transverse direction and form a reinforced arch along the major axis of the tubule, further stiffening the tubules against transverse loading (Figure 6.9B). During radial compression the tubule collapse easily along the flattened curves (emphasized in green) formed by fibers along the tubule's long side (Figure 6.9C). This behavior likely occurs during transverse compression as well because the softer intertubular matrix material is more easily compressed than the fibrous arches along the major axis (emphasized in pink). As the matrix compresses, it expands laterally, pushing on the walls of the tubule in its weakest orientation, the radial direction (Figure 6.9D). These results align with the findings of Huang et al. [3] and Leach [18], who found that macroscale hoof samples are stiffer in the transverse direction than in the radial direction. Furthermore, their results show that during compression in the longitudinal and transverse directions, samples plateau at around 50 MPa between ~2.5%-40%. Radially compressed samples, on the other hand, experience a linear increase in stress over this interval before experiencing a steeper stress-strain relation, which aligns well with the assertion that tubules densify more easily in this orientation.
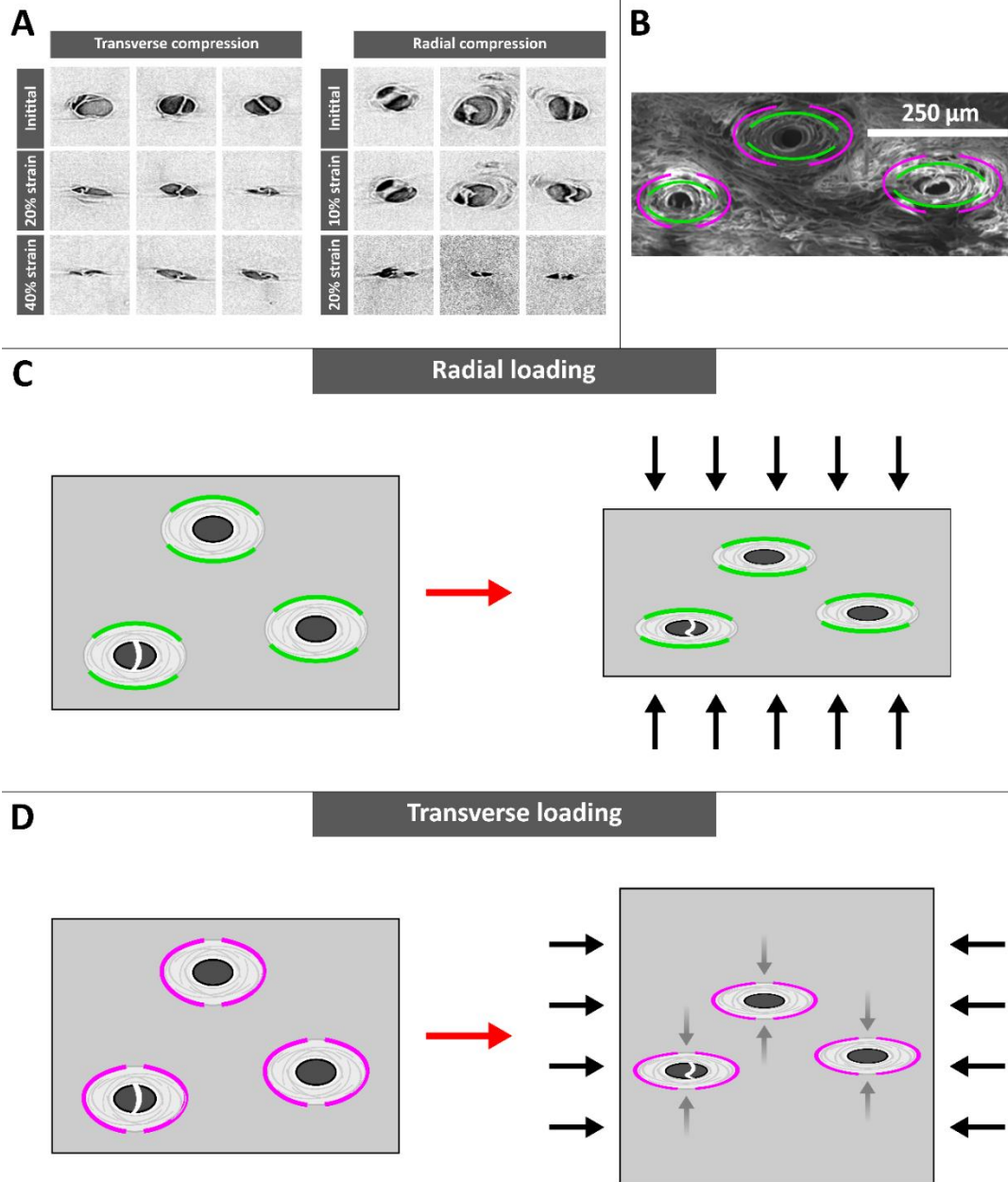
Figure 6.9 A.) Extracted images from microcomputed tomography (microCT) scans of individual tubule cavities being compressed in the transverse direction to 20% and 40% strain (scale: each of the microCT images shown in this panel is a square of 100 μm × 100 μm) B.) SEM image showing the fibers composing the tubule walls with fiber orientation perpendicular to radial loading emphasized in green and fiber orientation perpendicular to transverse loading emphasized with pink. C.) Samples compressed in the radial direction collapse easily along the minor axis of the tubules partially due to the weakness of the tubule wall's fiber orientation. D.) The arched fibers perpendicular to the tubules major axis resist transverse loading and instead tubules are compressed by the expansion of the matrix.

The tubule bridges are likely meant to compensate for this radial weakness. Most bridges are oriented along the radial axis, providing resistance to collapse and absorbing energy by buckling when tubule densification occurs. However, few, if any, bridges run perfectly perpendicular to the minor axis, and bridges rarely span the middle of the tubule, which is the most unsupported and most susceptible to buckling. If the bridges were truly meant to prevent the collapse of the tubule cavities, this would be the ideal placement and location. Instead, the bridges often cross the tubule's major axis at various angles, initiating and ending near the tubule's edges. The effect of this arrangement is that different parts of the tubules cross-section collapse at different stress levels. This distribution of support leads to a cascading failure mechanism that ensures that all the cavities do not compress simultaneously. Instead, areas with less support material fail first, followed by regions with bridges that are oriented closer to perpendicular to the loading and then progressively by areas with bridges oriented closer to parallel to the loading. This effect is further augmented by the irregular and varied thicknesses and geometries of the bridges.

Thomason et al. [12] found that the principal strains experienced within the hoof change during a horse's gait are often oriented at an angle to both the tubules and intertubular material and can vary between horses owing to differences in hoof geometry, stance, and size. As a result, complex loads can be experienced within the hoof. The distribution of bridge angles, thicknesses, and spacing has the added benefit of being well adapted to handling loads from any direction.

The role of the hoof tubules and their hollow medullary cavities have long been debated. It had been suggested that the hollow cavities are meant to transport moisture through the hoof or provide resistance to bending while reducing the overall weight of the hoof, only to be disproven [11]. Huang et al. [3], Lazarus et al. [8], and Kasapi and Gosline [4,6,7,11] showed that the tubule walls act as reinforcement, control crack propagation, and absorb energy via debonding from the

242

matrix. Yet, the role of the hollow center, and the recently described bridges, remained a mystery. Here, we propose the following explanation regarding the function of these features and their behavior. The cavities are meant to act as collapsible elements that can absorb strain energy during compression and, when the hoof is sufficiently hydrated, sustain plastic damage before the rest of the hoof wall. Due to the elliptical shape and fiber alignment of the reinforcement around the cavities, the tubules are weaker in the radial direction and prefer to collapse along this axis regardless of the compression direction. To improve the energy absorption of this failure mechanism, bridges span the tubule cavity, generally oriented along the radial axis, and buckle as the tubule collapses. These contorted bridges may also have the added benefit of helping the tubules recover their shape after collapsing. Predictably, the larger tubules at the interior of the hoof collapse at lower strains than the smaller ones near the exterior. Such failure mode may be preferable because the more hydrated tubules near the interior are more capable of recovering (as discussed in the next section), and, thus, it is ideal for them to collapse first. Since the hoof wall cannot remodel and repair itself, it would be detrimental to have all the cavities collapse at the same stress level, effectively making the fail-safe cavities a one-time use feature. To ensure that this does not happen, the thickness, orientation, and dimensions of the tubule bridges vary throughout the medullary cavity. The result is that different tubules and even different regions within a tubule collapse at different strains, beginning with the most recoverable tubules at the interior. On the macroscale, the result is a smooth stress plateau until 40% strain, during which only a few regions of the tubule cavities collapse at a time.

6.3.2 Relaxation Behavior
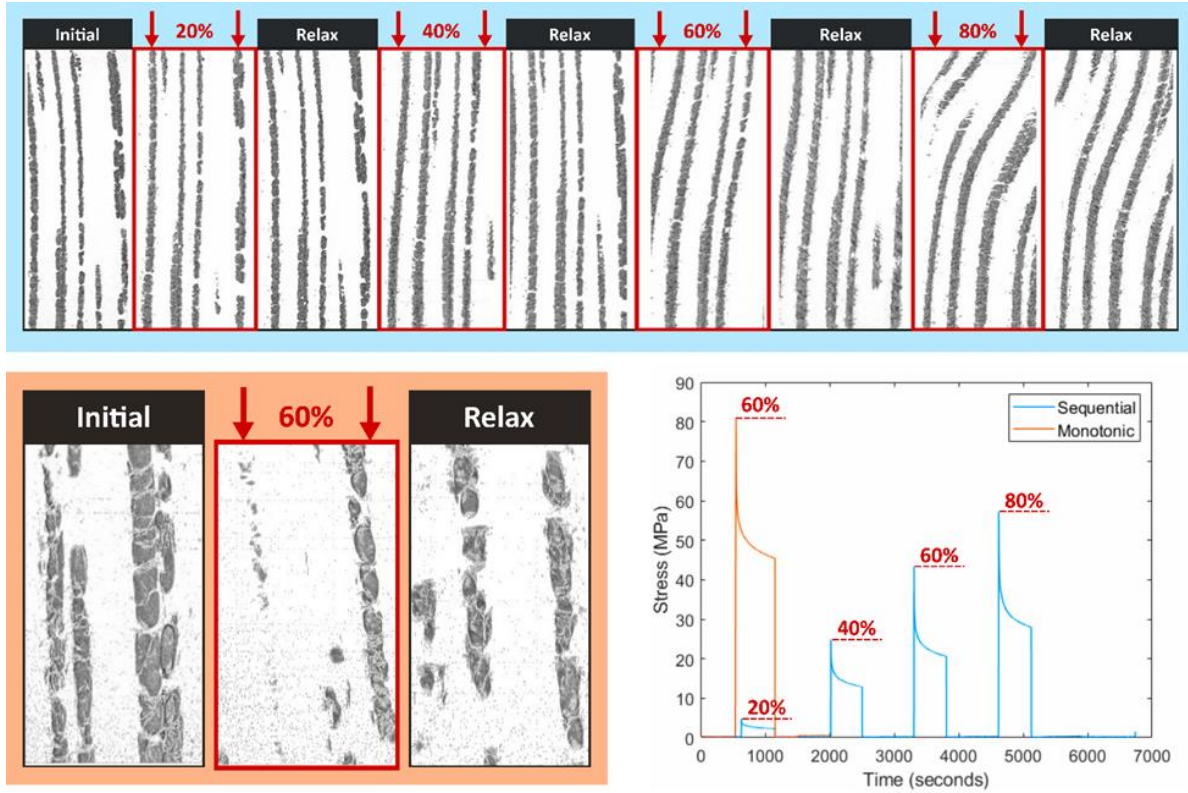
Figure 6.10 Comparison between the sequentially and monotonically loaded relaxation samples showing the progression from initial states through compression and relaxation periods. Plot of compressive stress (MPa) over time (seconds) for the two samples are depicted alongside. Orange: single loading to 60% of maximum stress and relaxation. Blue: sequential loading and relaxation to 80% of maximum stress.

The hoof wall displays significant viscoelastic behavior, as reported by Lazarus et al. [1]. Tomography imaging provides a unique glimpse into the appearance of what these hoof tubule cavities internally as they relax and recover from loading. Figure 6.10 shows two hydrated hoof samples, one sample compressed monotonically to 60% and released and another sample that experienced incremental compression and relaxation cycles up to 80% strain. Figure 6.10 displays a section of select tubules from each sample at each step. In the sequentially loaded sample, there appears to be little to no deformation change during 20% strain, 40% strain, and their respective relaxation periods. By 60%, the sample begins to bend, behaving similarly to the hydrated

compression tomography experiments. The relaxation period that follows the compression step to 60% shows the cavities bending back to their original shape, even within a few minutes. At 80% strain, the bending pattern seen at 60% strain is accentuated. Likewise, the relaxation period allows the cavities to recover and bend back. However, for the monotonically compressed sample sample, cavities collapse and no longer appear once compressed to 60%. This behavior is dissimilar to the sequentially loaded sample, where it seems that the sample's cavities did not collapse as easily. However, upon relaxation, a few of the cavity sections begin to reappear, implying that the tubules are stretching back out after being compressed rapidly. Not only does the sequentially loaded sample visually show an impressive recovery behavior, but it also shows a stark decrease in maximum stresses experienced. At 60% strain, the sequentially loaded sample experiences a maximum load of 43 MPa, which is significantly less than the monotonically compressed sample, 81 MPa, which is even greater than the maximum load achieved at 80% strain with the sequentially loaded sample. Additionally, during 60% compression, the monotonically compressed sample stress relaxes by 44.4% within 593 seconds, whereas the sequentially loaded and relaxed sample relaxes by 53.5% within 500 seconds. These findings correlate strongly with the results reported by Lazarus et al. [1] and provide supporting evidence that the hoof wall does have the ability to quickly dissipate compressive stresses through viscoelastic relaxation at the mesoscale. As previously suggested, such dissipation is particularly advantageous for the repeated loadings a galloping horse would experience, where preventing a build-up of strain could contribute to the hoof wall's durability.

6.3.2.1 Hydration Specific

Water content plays a significant role in the relaxation properties of the hoof wall [8]. The relaxation of the hoof wall was studied in the longitudinal direction, the predominant loading

direction in the hoof wall. Following the hydration control process, measurements were taken to quantify how moisture affects the volume of the hoof wall. It was found that as samples were hydrated from 0% to 15% water content, there was an increase in the volume of about 13%. With this increase in volume, the width and thickness experience the most change, 6% and 4%, respectively, whereas little change (just 2%) occurred along the height (longitudinal direction). This could be due to the IF orientation; when water molecules penetrate materials composed of alpha-helices with crystalline IFs, the nanoscale matrix that the IFs are embedded in absorbs water and expands while the IFs remain largely unchanged [19]. Thus, the material is expected to expand more perpendicular to the IF orientation.
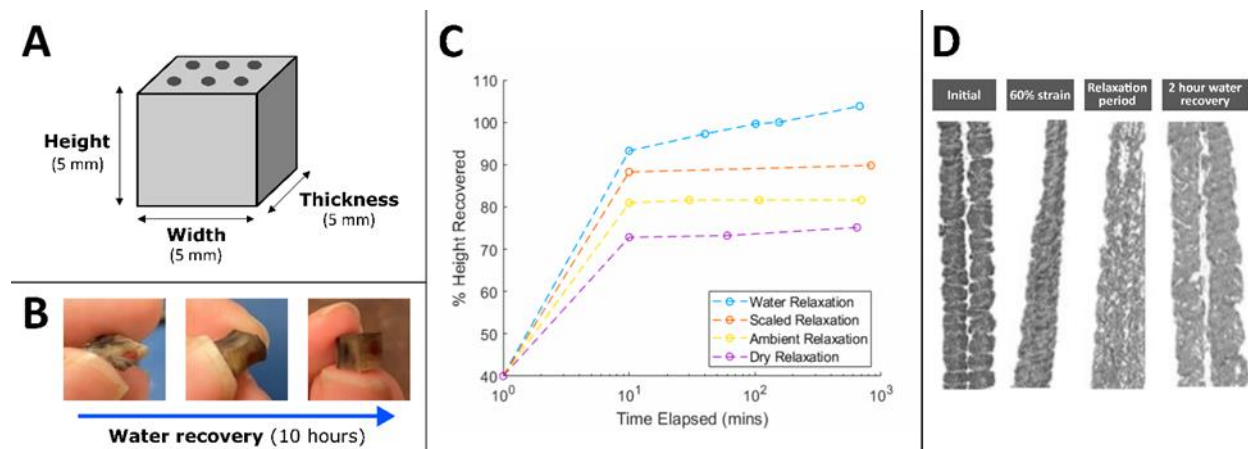
Figure 6.11 A) Schematic of hoof wall sample dimensions used for 4D microcomputed tomography (microCT) experiments. B) Compressed hoof wall sample's macroscopic recovery when submerged in water over a 10 hour period. C) Plot of % Height Recovered vs. Time Elapsed (minutes) on log scale of relaxation samples. D) MicroCT scans of the water relaxation sample at its initial state, 60% strain state, after 5 minutes of relaxation and after 2 hours of water submergement relaxation.

Figure 6.11 shows four hoof samples that were all compressed to 60% strain and allowed to relax in four different conditions. For water, sequentially loaded, and monotonically-loaded relaxation, samples were initially hydrated to 15% water content prior to testing. The sequentially loaded sample was compressed in increments of 20% strain with allowed relaxation periods

between loadings. After testing, the sequentially and monotonically loaded relaxation samples were left out in ambient conditions, whereas the water relaxation sample was placed in water. The dry relaxation sample had around 0% water content initially before testing. After testing, the dry relaxation was left out in ambient conditions. Out of all four samples, the water relaxation sample appears to have fully recovered, even regaining 103.8% of its original height after 10 hours of water recovery. Additionally, a glimpse of the water-relaxed sample cavity tomography is shown in Figure 6.11. Under 60% strain, the two depicted tubules bend significantly as bridges between cavity pockets begin to collapse. After the momentary relaxation period, the two tubules appear to straighten back upwards. After recovering in water for two hours, the two tubules appear to regain a semblance of their original shape and detail. The sequentially loaded relaxation sample performed better than the monotonically loaded relaxation sample achieving about 10% more of its own height recovery than the monotonically loaded sample by the end of the experiment. Within the first few minutes of hoof recovery from 60% compression strain, all samples at least recovered 70% of their initial shape.

6.3.3 Fracture Behavior

One of the most intriguing mechanical aspects of the hoof wall is the ability of its structure to control fracture behavior. Several design strategies are utilized to accomplish this, including varying the intermediate filament orientation and using the weak planes between them in the intertubular region to redirect cracks away from the living tissue inside the hoof wall [6]. The tubules, however, also play a key role, particularly in the innermost and outermost regions of the hoof, where cracks prefer to propagate along tubule interfaces with the matrix [7]. This observation was determined from post-fracture imaging on compact tension specimens. Post-impact fractography showed that tubules redirected cracks, causing tortuous crack paths and that the

tubules could even act as crack bridges and arresters [8]. The following section uses compact tension tests to detail fracture behavior in the hoof as cracks propagate.

6.3.3.1 Effect of structure

Several toughening mechanisms suggested by previous authors were confirmed with in-situ microCT. For example, the tortuous crack paths that arise from the tubule architecture can clearly be seen in Figure 6.12. To capture the tortuosity of the fracture, the centerline of the crack was traced (shown in blue) and measured and compared to the total lateral distance (shown in green) traveled by the crack. The ratio of these two values was calculated from measurements at 35 evenly spaced slices through the thickness of the sample, giving an average value of 1.24 and 1.32 at 500 μm and 1000 μm extension, respectively. This result suggests that the deflection caused by the tubules increases crack length by approximately 20%-30%. This is ~10% higher than that of the hoof-inspired 3D printed samples tested by Lazarus et al. [8].
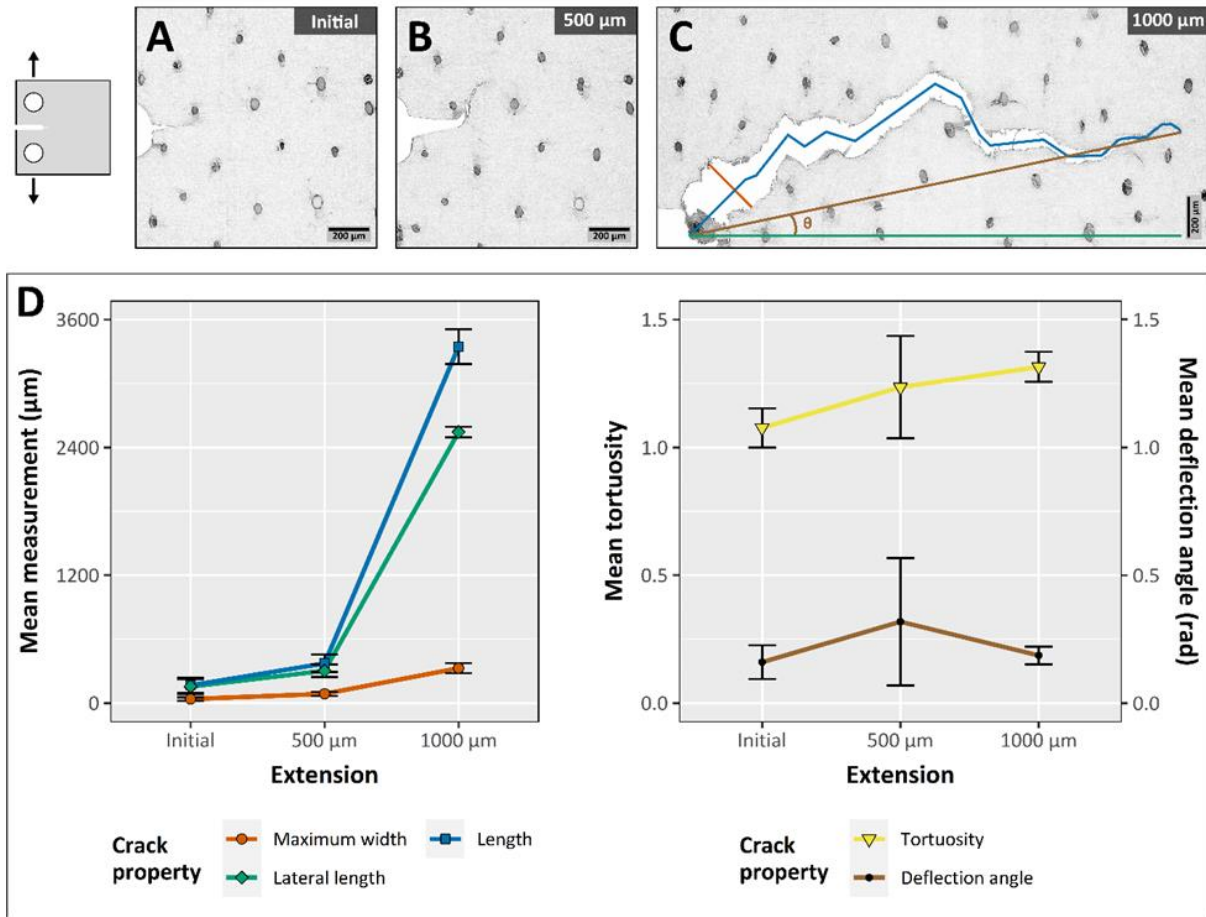
Figure 6.12 A-C) Images extracted from a series of microcomputed tomography (microCT) scans showing crack propagation within the hoof wall under ambient conditions. The number in the top right indicates the crosshead extension distance for the compact tension samples. C) Procedure for taking crack measurements; the blue line shows how the crack length was measured, while the green line measures the lateral distance that the crack has traveled through the sample. The ratio of these lines indicates how tortuous the crack path is. The brown line indicates the angle of deflection, Ɵ, from the start of the crack to the end and the orange line measures the maximum crack width. D) Plots of crack measurements at the different extension values (error bars represent standard deviation of the mean).

One reason for this could be the mechanism by which the tubules cause crack deflections. In the simplified 3D-printed samples, cracks would travel through the intertubular material until a tubule was encountered. Then, the crack would deflect around the tubule before continuing to travel straight. The hoof tubules, however, appear to capture approaching cracks, even ones that appear to be passing by harmlessly. Here, it seems that the crack is attracted to the tubule and is

"pulled" into the plane of weakness between the microscale tubular cortical layers rather than being redirected at the mesoscale interface between the tubules and intertubular material. A prime example of this behavior can be seen in the first two panels of Figure 6.13. The introduced precrack begins just below the tubule. In printed samples, this crack would likely deflect slightly down, away from the stiff tubular material, and then continue traveling to the right once it had passed the reinforced cortex (Figure 6.13, lower left panel). In the hoof sample, it gets pulled towards the tubule, curling behind it (Figure 6.13, top right panel). This is likely the result of the crack getting trapped in the planes of weakness between the cortical layers that surround the medullary cavity. These layers can be seen forming fiber bridges behind the crack tip, an extrinsic toughening mechanism well known to improve fracture toughness [20,21], as the fracture attempts to continue moving laterally through the sample. In the bottom right panel of Figure 6.13, multiscale crack bridging can be observed, with both whole tubules and smaller fibers spanning the crack wake. This crack deflection mechanism in the hoof samples leads to a lower angle of deflection (~10.5° after 1000 μm of extension) relative to bioinspired designs, which saw angles of deflection between 11°-18° after interacting with a similar number of tubules.
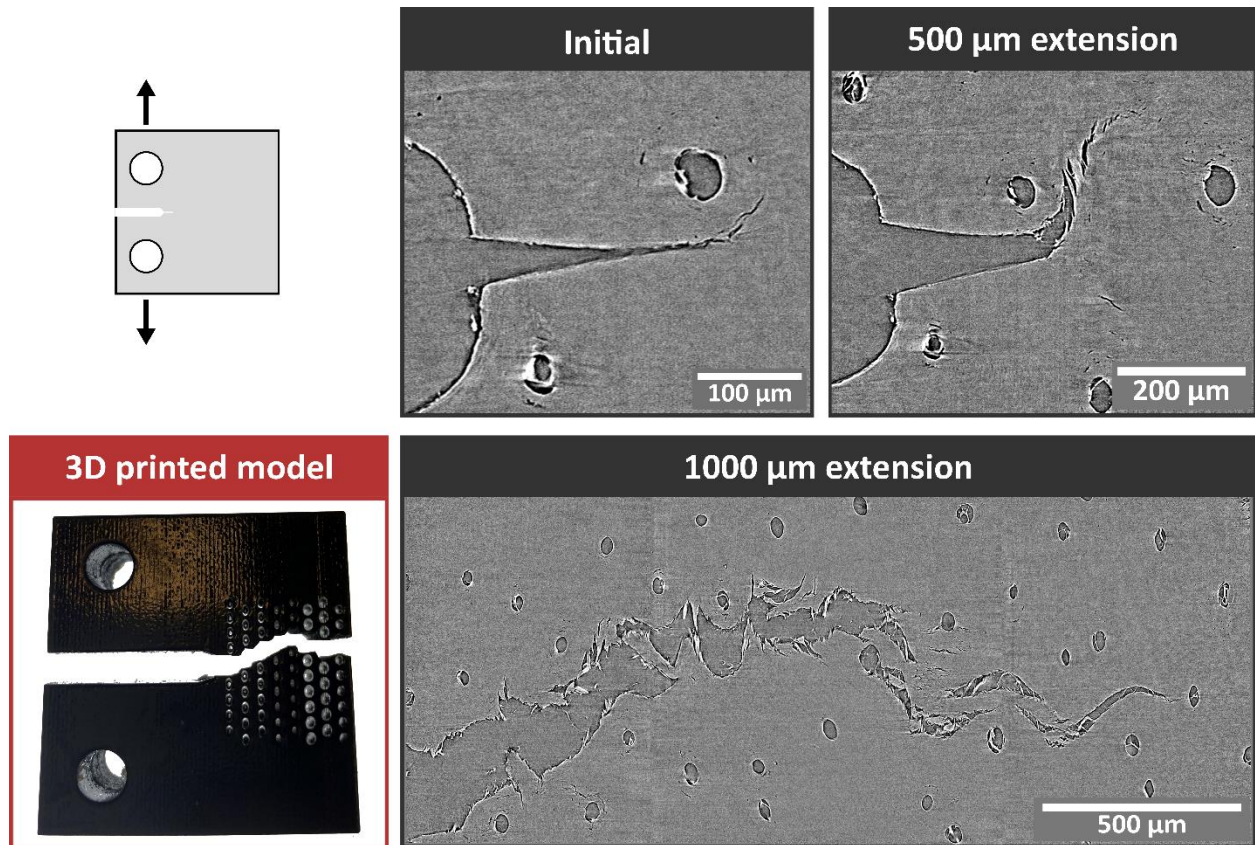
Figure 6.13 Microcomputed tomography (microCT) scans showing the crack deflection mechanism of the tubule region which "pulls" cracks in and trap them in the planes of weakness between the helical cortical layers of cells surrounding the medullary cavity.

6.3.3.2 Effect of hydration

Moisture has a large effect on the mechanical properties of keratin. When water molecules infiltrate keratinous materials, they disrupt the hydrogen bonds that stabilize the alpha helices and weakly cross-link adjacent polymer chains. The result is a dramatic decrease in stiffness and an increase in ductility. During the fracture events, this ductility causes a significant amount of crack blunting. Figure 6.14 shows the crack tip of a hydrated sample during compact tension testing.
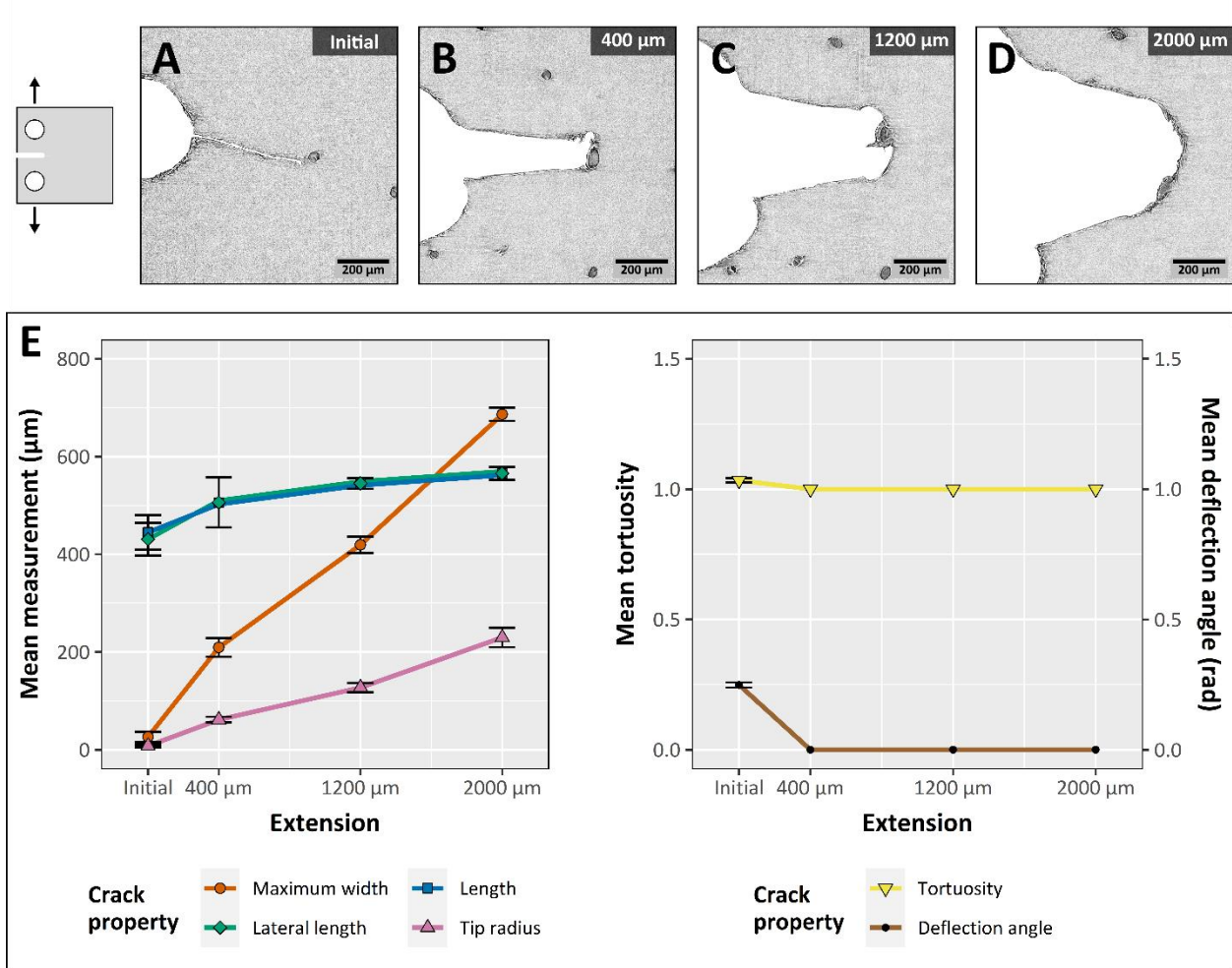
Figure 6.14 Hydrated hoof samples exhibit significant crack blunting. This can be seen by the increasing radius of curvature of the crack tip, while the crack length stays relatively the same. A-D) Images extracted from a series of microcomputed tomography (microCT) scans of hydrated samples at different extensions during compact tension test. E) Plots of the properties of the crack as it grows during testing (error bars represent standard deviation of the mean).

6.4 Conclusions

The horse hoof is a remarkable mechanical biological material with unique failure and recovery mechanisms. In this study, in-situ microcomputed tomography was used to explore the mechanisms, at both the meso and microscale, that are responsible for this outstanding performance. Novel experiments coupled with mechanical tests and characterization amplify the

findings of earlier studies [3,8,13,18] and provide new insights into the role of the hoof wall's structure.

Many tubules in the hoof wall tend to have a wavy structure that acts as a guide for how they buckle when compressed. No kinking/lateral cracking was observed in the tubule walls, likely due to the fibrous and more ductile (relative to engineered composite materials) nature of the hoof wall. This feature allows the reinforcing elements to continue resisting loading even after significant deformation, improving the material's toughness.

Previous authors observed tubule bridges and suggested that they played a role in stabilizing the tubule cavity. In this study, regions with less tubule bridging were observed to collapse prior to areas with more bridges. Finite element analysis revealed that the presence of bridges enhances the absorbed energy in a collapsing tubule.

Hydrated samples exhibited tubule buckling and collapse while dry samples cracked, often along an axis diagonal to the tubules. This might be due to the intertubular fiber orientation, as suggested by Kasapi and Gosline [6]. Dry samples also showed very little tubule or bridge distortion, while both were significantly deformed in the hydrated samples.

Interior tubules collapse more readily than those near the exterior. This is possibly the result of variations in tubule size and shape. This is particularly beneficial In-vivo since interior tubules are more hydrated than exterior tubules and, therefore, can recover more easily.

Tubules also prefer to collapse in the radial direction regardless of loading orientation. This is likely a result of the fiber concentration and alignment along the transverse axis. The tubule bridges are generally oriented along the radial direction but have a range of directions, positions, and sizes. Finite element analysis showed that when bridges are oriented parallel to the loading direction,

they can significantly improve the energy absorption of the tubule during the collapse. This finding agrees well with previous studies [3,18], which suggest that the hoof compresses more easily along the radial direction but also absorbs more energy. The variety of bridge geometries has the dual benefit of improving isotropy and creating a progressive collapse mechanism where different tubules and regions within the same tubule collapse at different stress levels.

To enhance our understanding of the role of the hoof wall's structure in its viscoelastic behavior, in-situ relaxation experiments were performed. The key findings are:

 Samples compressed at intervals of 20% strain until 60% (three cycles) and allowed to relax for five minutes between each loading cycle reached maximum stress that was about 46% lower than samples compressed to directly 60% strain. This highlights the dissipative viscoelastic response of the hoof wall, which can be beneficial in preventing the build-up of stress in the hoof during locomotion. Samples compressed in intervals also exhibited more tubule bending and less cavity collapse than samples compressed in one cycle.

Both the samples compressed in intervals and samples compressed directly to 60% strain displayed noticeable shape recovery, including collapsed cavities reopening. The samples compressed in intervals also showed tubules restraightening after relaxation.

In support of previous studies, samples hydrated more had significantly more shape recovery than drier samples. Full submersion in water provided maximum recovery. This is an important attribute of hooves: this is essentially a self-healing capability.

Finally, compact tension tests have previously been utilized [4,6,8] to probe the intriguing fracture behavior of the hoof wall. Here, several previous findings were verified, and new observations regarding how cracks propagate through the hoof were reported.

Previous authors have reported how tubules cause crack deflection [3,4,6–8] and can even bridge or arrest cracks [8]. Here, these mechanisms were observed during propagation for the first time. Using biomimetic compact tension samples, Lazarus et al. [8] proposed that cracks propagating towards tubules are pushed around the reinforced regions to continue traveling through the weaker intertubular regions. Instead, it seems that in the hoof wall, cracks traveling near tubules are pulled inward, becoming trapped within the helical, cortical planes that compose the tubular regions. This is akin to the mechanism discovered by Suksangpanya et al. [22] for the Bouligand structure of the mantis shrimp club. To continue traveling laterally through the hoof wall, cracks need to propagate through these fibrous lamellae. Thus, bridging cracks are formed. Similarly, intertubular fibers and even entire tubules were seen bridging crack wakes, introducing an extrinsic toughening mechanism on multiple hierarchical levels that resists further crack extension and enhances the toughness.

Measurements of the crack length showed that this tubular deflection mechanism causes significantly longer and more tortuous fracture paths. The "pulling" deflection mechanism of the hoof tubules also led to longer crack paths relative to the "pushing" bioinspired designs fabricated in a previous study [8].

Hydration has an important effect on crack propagation, causing significant crack tip blunting. Unlike dry samples, the hoof wall structure shows no discernable crack propagation upon impact.

6.5 Acknowledgements

Chapter 7. Impact Resistance in Jackfruit

7.1 Introduction

As discussed in Chapter 2, biological materials contain a wide variety of hierarchical design strategies that allow them to withstand the dynamic loading conditions imposed on them by their environment. To learn from these impressive systems, researchers have explored the mechanical properties of a vast array of materials generated by organisms within the animal kingdom ranging from airborne creatures like woodpeckers [126] and pelicans [474] to animals that thrive deep under the sea such as whales [243] and conches [11]. However, an oft overlooked area of the natural world is plant-based systems which have developed unique structural motifs, containing different constituent materials from their animal counterparts, to resist impact scenarios. The trunks of certain trees, for example, contain a remarkable number of mesoscale features such as porosity and lignified reinforcing elements whose arrangement dictates the material's response to impact [12].

More commonly, researchers have observed impact resistance in the nuts and fruits of certain plants, which need to withstand falling impacts and impacts from predation in nature. One of the most widely studied fruits is the pomelo which contains a thick porous mesocarp whose primary function is to protect the seeds on the fruit's interior. The mesocarp of the pomelo is an open cell

foam-like structure composed of fluid-filled struts. This structure imbues the fruit with numerous energy dissipative mechanisms during compression. The open cell-structure, which can reach a porosity of 80% [53], is highly collapsible and absorbs strain energy by compacting during impact. In fact, Seidel et al. [53] determined that the mesocarp only begins to densify at strains of ~55%, emphasizing the extreme collapsibility of this configuration. These results were verified by compressive in-situ CT experiments [475]. The pomelo utilizes numerous structural gradients in the mesocarp to enhance its collapsibility, including gradients in porosity, cell size, and stiffness gradients between adjoined features such as the stiffer, branching, lignified vascular bundles which act as fiber reinforcement and the foamy parenchymatic material that distributes load around the fruit. The pomelo peel also cleverly utilizes branch length of the vascular bundles; shorter branches are more resistance to buckling and bending so by varying the branch frequency in different regions of the peel, the fruit is able to tune the onset of densification by location [37]. Several groups have also observed, modeled, and replicated the viscoelastic and damping properties that arise from the strut structure leading to bioinspired materials with high energy dissipation under compression [36,38,39,175,476].

Other nut and fruit systems such as the macadamia nut [36,53,54], Brazil nut [477,478], coconut [55,153,479], and apple [52] have been explored as a means of obtaining inspiration from nature. Recently, Ha et al. [480] turned to the durian as a subject for bioinspiration to create impact resistant packaging to protect goods during transport. The durian's most striking feature is the thorns that cover its surface. Just beneath the thorns is a fleshy mesocarp layer which transitions into the endocarp and ultimately the nutritious flesh and seeds of the fruit above the core of the fruit. Ha et al. [480] performed uniaxial compressive tests on the thorny layer and the mesocarp layer beneath and found that the thorny layer had a specific energy absorption nearly twice that of

the mesocarp layer. They observed that when a small portion of the surface was impacted, thorns at the center of the impact would buckle and the reinforcing fibers within the thorns would delaminate, while thorns near the exterior of the sample would bend and compress fibers at their bases. The authors point out that these are unique failure and energy absorptive mechanisms compared to other biological materials and may provide a novel source of bioinspiration for impact resistant materials.

The jackfruit is similar to the durian but with several key differences. The average size of durian fruit is ~1.5kg and they grow approximately 12m up in trees corresponding to a falling energy of ~176 J. Jackfruit on the other hand are the largest fruit in the world reaching 35kg in weight, although record-holding jackfruit weighing upwards of 50kg have been reported. They grow along the branches and trunks of trees which can reach 25m in height [481,482]. Given these metrics, falling jackfruit can experience impact energies of >8.5kJ. To accommodate such massive impacts, the jackfruit has incorporated an extra layer of cushioning between the seeds and the endocarp. This region is composed of aligned tubules that run from the fruit's stiff core to the underside of the mesocarp where they densify before finally attaching to the base of an individual surface thorn, as can be seen in Figure 7.1. Ha et al. [480] note that the thorns of the durian have a high aspect ratio, making the thorns more susceptible to bending under impact. The jackfruit, on the other hand, has thorns that are shorter and wider, as shown in Figure 7.1.

The jackfruit has numerous structures and biomechanical functions that, to the authors' knowledge, have never before been explored from an engineering perspective. As such this biological system is a ripe candidate for bioinspiration. In this study, we explore the composition and structure of the different layers of the jackfruit and connect them to the properties and impact resistance that the fruit has evolved. To show that the designs observed in the jackfruit can be

transferred to engineered materials, jackfruit-inspired samples were 3D printed and subjected to impact tests.
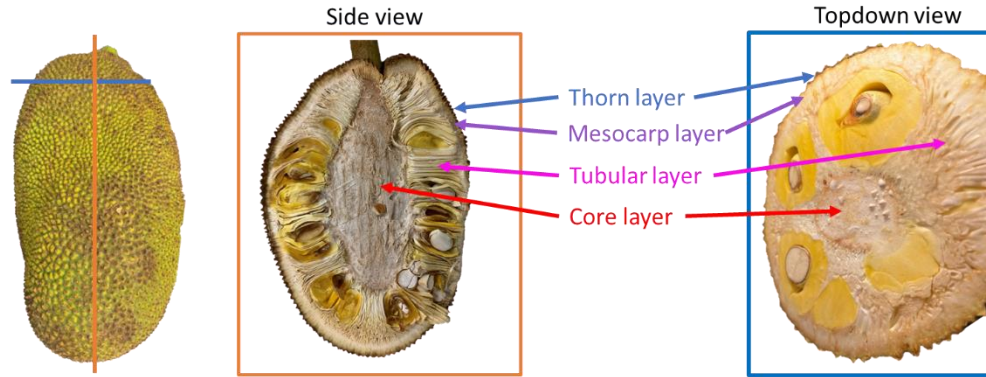
Figure 7.1 A visualization of the jackfruit's interior showing a vertical and horizontal cross-section of the fruit.

7.2 Methods and Materials

7.2.1 Sample acquisition

Whole jackfruits were acquired from 99 Ranch market in San Diego. Impact resistance in fruit may seem unintuitive since these energy rich capsules are often meant to act as vehicles for spreading an organism's offspring either through predation or by releasing seeds upon separation from the plant. Our hypothesis is that the impact resistance in jackfruit is meant to allow immature fruit to withstand falling damage and continue to ripen on the forest floor. Simple free fall tests, where jackfruit of different ages were dropped from a height of 25 feet onto a concrete slab, confirmed this; while older, ripe jackfruit ruptured, equally-sized unripe jackfruit withstood the impact, even surviving six subsequent drops. Concordantly, slightly underripe jackfruit, that were just beginning to transition from green to brown, were purchased for testing.

7.2.2 Microcomputed tomography

High resolution 3-D images were acquired by microcomputed tomography (Skyscan 1076, Bruker, Kontich, Belgium) at 35µm voxel resolution. The sample was wrapped in plastic wrap and enclosed in a sandwich-sized ziploc bag. The bag was wedged between styrofoam blocks, taped together, and then placed inside a plastic jar, and further secured using additional styrofoam blocks to minimize shifting during scanning. The sample was scanned as an oversized and wide (x2) scan in three fields encompassing the entire sample using imaging parameters of 60kVp, 167µA, Al 0.5 mm filter, 180 degrees, 0.5 degree step rotations, and 3 frame averaging. Scans were reconstructed (Smoothing = 1, Ring Artifact = 6, Beam Hardening = 40%, Gaussian kernel, Dynamic Range = -0.010 to 0.020, NRecon, Bruker, Kontich, Belgium) with auto x/y and z alignment and fusion to stitch the three sets of scans together. An image quality check was performed by positioning the cursor at the center of the sample (DataViewer, Bruker, Kontich, Belgium) in the skin, skin/fruit interface, and fruit, and three 2-D orthogonal views were checked for quality (presence and clarity of structural features) and absence of noise or imaging artifacts, and then recorded for presentation. The results were processed with Fiji/ImageJ (U. S. National Institutes of Health, Bethesda, Maryland, USA) [444] and 3D plugins [445,446].

7.2.3 Scanning electron microscopy

Samples were extracted from each layer of the jackfruit and imaged using an FEI Apreo FESEM (Thermo Fisher Scientific, Waltham, Massachusetts, USA) after being sputter coated (Emitech K575X, Quorum Technologies Ltd, East Sussex, United Kingdom) with iridium for eight seconds. Measurements were taken using Fiji/ImageJ (U. S. National Institutes of Health, Bethesda, Maryland, USA) [444]. To visualize its compressive behavior, sputter coated thorn samples were mounted between two screw driven compression plates using carbon tape. A small

section of the thorns' skin was cut and peeled back to reveal the cellular structure beneath. The screw was then turned to compress the sample to specific strains and images were taken of the structural changes that occurred both on the surface of the thorn as well as in the underlying region.

7.2.4 Optical microscopy

Thin slices of each layer were prepared by hand using a scalpel and stained with Toluidine Blue O (Sigma-Aldrich, St. Louis, USA) following the procedure laid out in [483]. Images of the stained samples were taken using an Olympus AX70 optical microscope (Olympus, Tokyo, Japan).

7.2.5 Thermogravimetric analysis (TGA)

Thermogravimetric analysis was performed on samples from each layer and were heated from 25 $^{\circ}$C to 700 $^{\circ}$C at a ramp rate of 10 $^{\circ}$C/min. Samples were dried in an oven at 105 $^{\circ}$C for 24 hours immediately before testing to remove as much moisture as possible.

7.2.6 Compression, stress relaxation, and compact tension

Quasi-static compressive tests were performed on samples taken from the different regions of the jackfruit at three different strain-rates ($10^0 s^{-1}$, $10^{-1} s^{-1}$, and $10^{-2} s^{-1}$). To maintain sample homogeneity 5x5x5mm^3 samples were prepared and were tested using an Instron 3342 universal testing system (Instron, High Wycombe, United Kingdom) equipped with a 500 N load cell. Owing to their small size, whole individual thorns were removed from the jackfruit exterior and tested. To perform stress-relaxation tests, samples were compressed to 90% of their original height at a strain rate of $10^{-1} s^{-1}$ and then allowed to relax for 900s. The resulting curves were fitted to a three-element Maxwell-Weichert model using a Prony series. This model involves a spring in parallel with three Maxwell elements (which consists of a spring and dashpot in series). Compact tension tests were also performed on two-layer samples which included the thorny exterior and mesocarp. These samples were fabricated to adhere to the Plastic ASTM D5045 – 14 standard (W=40 mm).

Tests were performed at three different cross-head speeds of 10mm/min, 60mm/min, and 120mm/min.

7.2.7 Digital image correlation

Samples were speckled using a Speckler Pattern Application Kit (Correlated Solution, Irmo, USA). A random speckle pattern with a dot size of 0.33 mm was imprinted on the surface of samples. Videos recorded during the tests and then still images were extracted. These stills were used to create strain maps during the tests using the open-source 2D-DIC Matlab software, Ncorr (Georgia Institute of Technology, Atlanta, USA).

7.2.8 Gas gun impact testing

Gas gun testing was performed using a modified paintball gun mounted to a frame 30 cm above the sample which was placed on a metal surface. Rubber balls 17.3mm in diameter with a mass of __ grams were used as projectiles. The paintball gun is connected to an Arduino microcontroller in order to fire the round. The microcontroller is used to activate a servo motor that in turn triggers the paintball gun. To trigger the high-speed camera, a laser trigger was set up in order to detect when the round is fired. This consists of a 5V laser (need to find out what laser) that is detected with a ThorLabs PDA10A2 Si Amplified Fixed Gain Detector. The output signal can be viewed through a Tektronix DPO 2014 oscilloscope. The oscilloscope is connected to a Tektronix AFG3022C function generator. Once the laser beam is broken, it is registered by the photodetector and displayed on the oscilloscope. This then causes the function generator to send a signal to trigger the i-Speed 716 high speed camera. Videos were recorded at frames per second (FPS) between 40,000 FPS and 75,000 FPS.

A total of 13 samples were prepared, each with two samples containing the following layers: mesocarp and tubules, mesocarp and thorns, mesocarp only, thin mesocarp and tubules.

Five samples were prepared consisting of thorns, mesocarp, and tubules, with all but one sample having speckles for digital image correlation (DIC). The samples were cut to have a cross-section of 3cm x 3cm, with the height dependent on which layers were being tested. Samples were tested within three hours of cutting.

7.2.9 Bioinspired samples

Bioinspired samples were designed based on cross-sectional images of the jackfruit. Traces of the thorn and tubule dimensions were extruded and then combined using Fusion 360 CAD software (Autodesk, San Rafael, USA). Four different types of jackfruit-inspired designs were printed; samples modeled after all three of the outer layers of the jackfruit (thorns, mesocarp, and tubules) as well as samples with just the thorn and mesocarp layers, mesocarp and tubular layers, and samples of just tubules. Two series of prints were fabricated for impact testing. The first utilized hard samples printed out of PETG using an Ender 3 Pro (Creality, Shenzen, China). Several different infills (of 10%, 15%, and 20%) were tested. The second series used softer materials and a multi-material 3D printer (Objet350 Connex3, Stratasys, Rehovot, Israel) was used to fabricate samples using proprietary resins of FLX9040-DM and TangoBlack+. These different materials were used to determine if the design principles uncovered in the jackfruit could be universally implemented or if they require optimum material properties to succeed. The jackfruit-inspired samples were compared against featureless rectangular samples of the same mass.

7.3 Results and Discussion

7.3.1 Structure and Composition

For this paper the jackfruit has been divided into four regions. From exterior to interior, these regions are the thorny surface exocarp, the mesocarp, the tubular region which contains the fruit's seeds, and the core of the fruit. The surface thorns were measured (N=16) to have an average

height of 4.4 ± 1.5 mm, with a base width of 4.6 ± 1.6 mm and an inclination angle of 57.1 ± 3.2°.

These measurements are indicated in Figure 7.2A, which shows a longitudinal slice of the top three

jackfruit layers. While there was significant variation in the height and base dimensions for

different thorns the inclination angle was relatively consistent. Measuring the thorns by hand

(N=30) revealed an average tip diameter of about 1.57 ± 0.19 mm and a polygonal base area of

33.21 ± 4.98 mm. 2D hexagons are one of the most efficient shapes for packing [484]. In the case

of the jackfruit, the irregular hexagonal bases are ideal for having a high density of thorn tips

covering the surface contours of the irregular 3D shape of the fruit. Using computed tomography

scans of the fruit's interior, the porosity of the tubular region was found to be approximately 57%.

Individual tubules (N=25) were observed to be elliptical in shape with an average aspect ratio of

2.26 ± 0.48 and average major and minor axis dimensions of 1312 μm ± 155 μm and 603 μm ±

139 μm, respectively. An example of these measurements can be seen in Figure 7.2B, which shows

a transverse slice of the jackfruit's tubule layer. Figure 7.2C-E show 3D renderings of the

jackfruit's different layers, excepting the core.
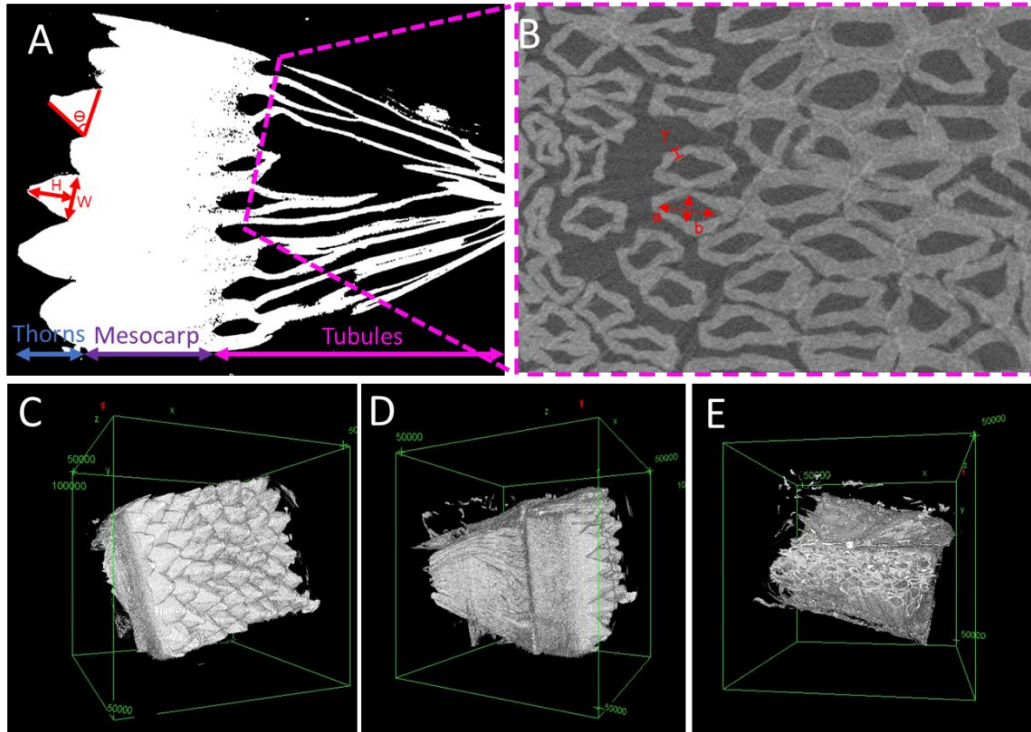
Figure 7.2 Microcomputed tomography scans showing A.) a through-thickness cross-section of the thorn, mesocarp and tubular layer, B.) a cross-section of the tubular region, and C-E.) 3D renderings of the jackfruit's outter three layers.

Toluidine Blue O is a polychromatic stain that can be used to differentiate plant tissues by preferentially binding with anionic groups in the cell wall. The result is a multicolored sample that gives insight into local composition. Figure 7.3A shows microscopy images from each layer of the jackfruit. In the thorns, the reinforcing fibers appear bright blue, suggesting that the fibers are composed of stiffened sclerenchyma with thicker, lignified cell walls. These sclerenchyma fibers are embedded in a matrix of irregularly shaped and sized cells that are generally larger than the sclerenchyma cells and appeared purplish when dyed. This suggests that these cells are likely the parenchyma "filler" cells, which make up much of the soft, unspecialized tissue found in the plants and whose walls are primarily cellulose [483,485]. These essentially act like a foam matrix for the lignified fibers to be embedded within. The cells in the thorn are small relative to other parenchyma cells such as those found in potatoes [486], but vary along the longitudinal axis of the thorn. Near

the base of the thorn, the major axis and minor axis of cells were measured to be 121.0 μm (s.d. = 25.9μm, N=25) and 44.4 μm (s.d. = 13.7μm, N=25), respectively, with cell walls approximately 2.0 μm (s.d. = 0.5μm). Meanwhile, closer to the peak of the thorns, cells were smaller and more circular with major and minor axes reduced to just 14.8μm (s.d. = 4.9μm) and 10.0μm (s.d. = 4.0μm, N=25) with thicker walls approximately 3.7 μm (s.d. = 1.0μm) across. Approximating the cells as ellipsoids, the volume percentage of the cell walls of the lower thorn was calculated to be just 2.1%, while in the upper thorn the thicker walls and smaller cells increased this value to 22.5%. For cellular solids, the effective elastic modulus of a material is approximately proportional to the density ratio of the cellular material relative to the bulk material; in the case of the jackfruit thorn one can assume that tip of the thorn is ~10 times stiffer than the base due to the change in material density that results from differences in cell size and cell wall thickness. In fact, this approximation may even be an underestimate, since the reinforcing fibers take up proportionally more volume as they near the tip of the thorn and the more elliptical-shaped cells near the base may collapse more easily.

The lignified fiber bundles continue into the mesocarp but become much thinner; whereas these bundles are 5-6 cells wide in the jackfruit's exocarp, they transition to only 2-3 cells wide in the mesocarp. Still, the significant amount of blue coloration suggests sporadic lignification throughout the mesocarp layer. The mesocarp layer also exhibits some pink coloration, which is associated with pectin. Recent research suggests that pectin interacts closely with the cellulose in cell walls, forming an interpenetrating network that enhances cross-linking between the cellulose microfibrils [487,488]. Pectin also plays an important role in enhancing cell-to-cell adhesion [488]. In the tubule layer, long pink fibers, one cell in width, run parallel to single-cell blue fibers. Both are embedded in a matrix of cells that are very lightly stained. Finally, the core is mostly pinkish-

purple, suggesting less lignification. Furthermore, the core has a sponge-like configuration with the cells acting as struts to form hexagonal pores.
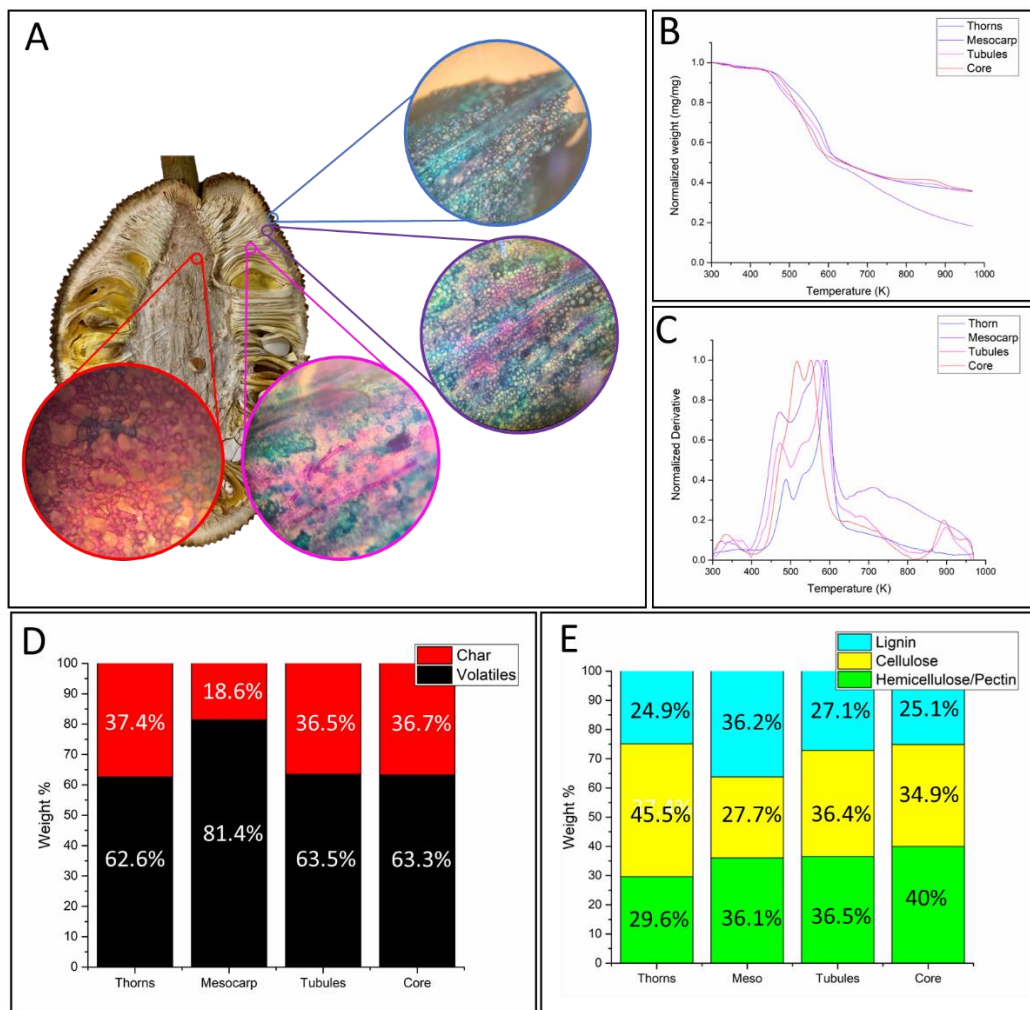
Figure 7.3 The composition of the jackfruit is different in each layer. A.) Optical micrographs showing the results of O Toluidine blue staining from each layer. B.) Normalized TGA curve and C.) normalized DTG curve of the different layers. D.) Bar chart showing the volatile and residual char percentages for each layer and E.) Estimates of the composition of each layer based on the DTG curves.

To further elucidate the composition of each layer, thermogravimetric analysis (TGA) was performed. Figure 7.3B shows the pyrolysis curve (normalized sample weight vs temperature) for

each of the four layers of the jackfruit while Figure 7.3C shows the normalized derivative thermogravimetric (DTG) curve. Figure 7.3D plots the amount of residual char vs volatiles in each of the samples. Each of the layers had nearly the same amount of residual char, about 37%, except for the mesocarp samples, which were about 19% char. This indicates that the mesocarp layer is composed of more volatiles such as hemicellulose, cellulose, and lignin than the other layers which contain more fixed carbon. The normalized DTG curve (Figure 7.3C) can be used to obtain further insights into the differences in the composition of the fruit's layers. Lopez-Velazquez et al. [489] performed TGA on orange peels and found DTG peaks at 485 K, 527 K, and 601 K which has fairly good agreement with the peaks observed in the jackfruit.

Recently, Diez et al. [490] used the TGA-PKM method to model the thermal pyrolysis of the individual components (hemicellulose, cellulose, and lignin) in wood. This method involves fitting multiple pseudo-component curves for each constituent since more than one peak can be attributed to each. Diez et al. [490] determined that there were two pseudo-components for hemicellulose, one for cellulose and three for lignin, corresponding to peak temperatures of ~488K and ~538K, ~ 596K, and ~616K, ~739K, and ~988K, respectively. The peaks and shoulders identified in the jackfruit DTG curves are listed in Table 7.1. The lower three peaks correlate well with the hemicellulose and cellulose pseudo-components identified by Diez et al. [490]. Thorn, mesocarp, and tubule samples all have a peak around 480 K and a shoulder around 535K, which can be attributed to hemicellulose, as well as a larger peak around 570K-590K that is likely the result of cellulose pyrolyzing. Interestingly, the ratio of the cellulose DTG peak to the first hemicellulose DTG peak was much larger for the thorn than for the mesocarp with the tubules falling in between the two. This could be the result of the cellulose curve shifting to a lower temperature and pulling up the hemicellulose curves up by overlapping with them more. This

suggests that there is a difference in cellulose crystallinity in the different layers, where the thorns and tubules are more crystalline, since amorphous cellulose will degrade at lower temperatures [491]. For core samples, the first peak, attributed to hemicellulose, appears as a slight shoulder while the second peak and third peak are nearly the same size. DTG curves of extracted pectin show a single sharp peak at temperatures between 495K - 515K [492,493]. Pectin generally composes only a small percentage of fruits and vegetables, however certain vegetal products like pumpkins and orange peels contain significantly elevated levels of pectin [494]. Begum et al. [495] examined the pectin contents of several food waste streams and found that jackfruit had one of the highest pectin contents, even greater than orange peel which is the primary source of industrial pectin [496], particularly in the core of the fruit. This agrees well with the observations of the core samples stained with Toluidine Blue O, which became much pinker than the other layers. The second peak in the core samples, therefore, could be a result of pectin degradation rather than that of hemicellulose.

Lignin is well known to slowly degrade over a wide range of temperatures, including higher temperatures of >600K, after which the cellulose and hemicellulose have pyrolyzed [489,490,497,498]. In tubule and core samples, a peak was observed between 890-900 K. Other researchers have observed this and attributed it to the last stage of lignin degradation [489,499,500]. In mesocarp samples, a slight peak can be seen around 708 K. The thorn on the other hand has relatively slight changes in degradation rate at higher temperatures, suggesting that lignin is less dominant in the thorns.

To get an approximation for the composition of each layer, the change in weight of the sample's volatiles over the temperature range for each DTG peak was calculated and is plotted in Figure 7.3E. As many plant systems contain relatively sparse amounts of pectin, researchers

utilizing TG often only include hemicellulose, cellulose, and lignin in their analysis. Since the temperature at which pectin degrades overlaps significantly with the range at which hemicellulose pyrolyzes, the two were combined here. The mesocarp sees a steep drop in mass starting at around 643 K. By this point nearly all of the hemicellulose, pectin, and cellulose should have degraded [489,490,499,500], suggesting that the mesocarp is more lignified than the other layers. In many plant systems, lignin acts as reinforcement for the softer tissue surrounding it, conferring rigidity and strength to the cells it fortifies [12,501–503]. Meanwhile, the core displayed elevated levels of pectin, which is often deposited at intercellular joints to enhance cell adhesion [504]. Given the sponge-like structure of the jackfruit's core, containing struts that are single cells wide, cellular adhesion is integral to the performance of this energy-dissipative layer, while the stiffness that would be imbued by lignin is not as important. Likewise, the thorns had the lowest lignin concentration and the largest cellulose concentration, suggesting that the protrusions are meant to function as soft impact dissipators.

From the compositional results obtained from staining and thermogravimetric analysis, one would expect the mesocarp to have the highest stiffness due to the observation of aligned lignified fibers and high lignin content. Meanwhile, both the staining and TGA results suggest that the core and thorns contain less lignin, and therefore might be expected to be less rigid and more ductile. The thorns contain lignified, sclerenchyma fibers embedded in a matrix of softer parenchyma cells, while the core exhibits a strut-like structure rich in pectin. The exact mechanical properties of pectin remain mysterious [505] but it has long been known to play a multifunctional role in plant growth and mechanics [506,507]. When modeling the mechanical behavior of plant fibers Keryvin et al. [508] assumed the properties of pectin to be the same as those of lignin with promising results, which suggests that the pectin-rich core and lignin-rich mesocarp may have similar

mechanical properties. Both the staining and TGA indicate that the tubules contain an intermediate amount of each constituent, however the highly porous mesostructured of this layer inherently decreases its effective modulus. This arrangement of a soft ductile material sandwiched between two denser and stiffer layers is a common design motif that is utilized by both nature and engineers to improve impact resistance [75].

Table 7.1 Peak temperature for each layer of the jackfruit. In parentheses is the height of the normalized DTG peak, i.e., the height of the peak relative to that layer's height peak.

	Thorn	Mesocarp	Tubule	Core
Peak 1	487 K (40.3%)	472 K (73.9%)	473 K (58.6%)	478 K (56.8%)[shoulder]
Peak 2	535 K (43.3%) [shoulder]	541 K (86.4%) [shoulder]	532 K (58.6%) [shoulder]	516 K (99.3%)
Peak 3	591 K (100%)	569 K (100%)	584 K (100%)	552 K (100%)
Peak 4	863 K (5.4%)	708 K (36.3%)	898 K (16.4%)	893 K (20%)

7.3.2 Quasi-static Mechanical Behavior

The jackfruit contains a series of progressive failure mechanisms that absorb strain energy and protect the jackfruit's precious seeds. The first layer to fail is the extremely porous, aligned tubular region on the fruit's interior. DIC quasi-static compression tests performed on three-layered samples (thorns, mesocarp, and tubular region) show this phenomenon and can be seen in Figure 7.4. Only once the tubules have almost entirely collapsed do the other two layers begin to deform and absorb strain energy. During an in-vivo impact the initial load would be distributed amongst the exterior thorny layer, however having an easily collapsible porous layer beneath this allows for easy transfer of impact energy to the deeper regions of the fruit.
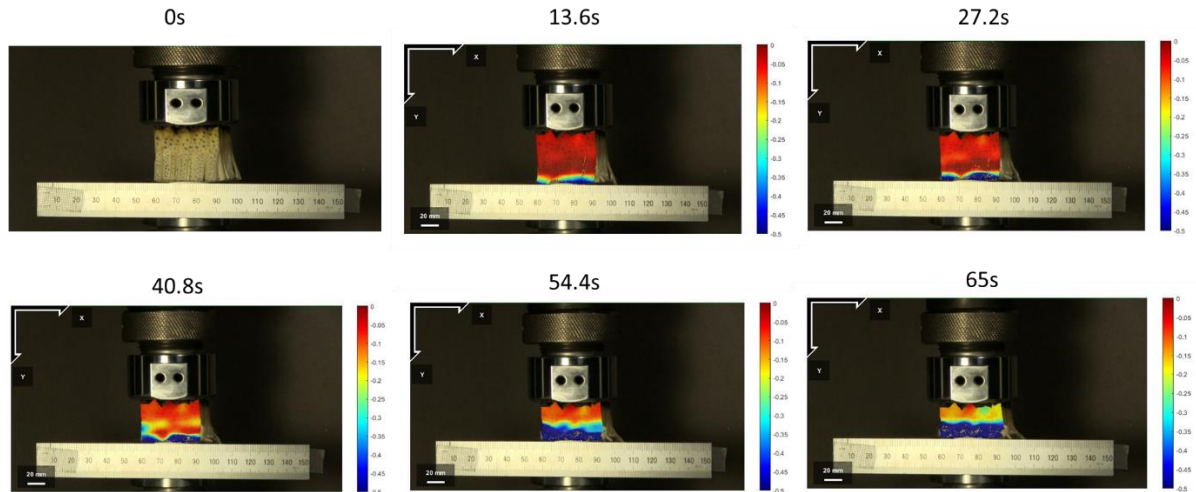
Figure 7.4 Digitial image correlation of three-layered jackfruit samples compressed at a strain-rate of $10^{-1}s^{-1}$. Nearly all of the strain is concentrated in the tubule layer until it has fully collapsed.

The next layer to deform during compression is the thorny exterior. When samples of just mesocarp and thorns were compressed, the thorny layer collapsed first as shown in Figure 7.5A. Upon being released, the thorns recovered nearly half of their initial height as can be seen in the last two frames. The underlying structure of the jackfruit thorn also plays a vital role in its compressive and viscoelastic behavior. The surface of the thorns is composed of skin with a highly

ordered, microscale wave-like configuration as shown in Figure 5B. Beneath this wrinkly exterior is a fiber-reinforced closed-cell foam-matrix composite, depicted in Figure 7.5C.
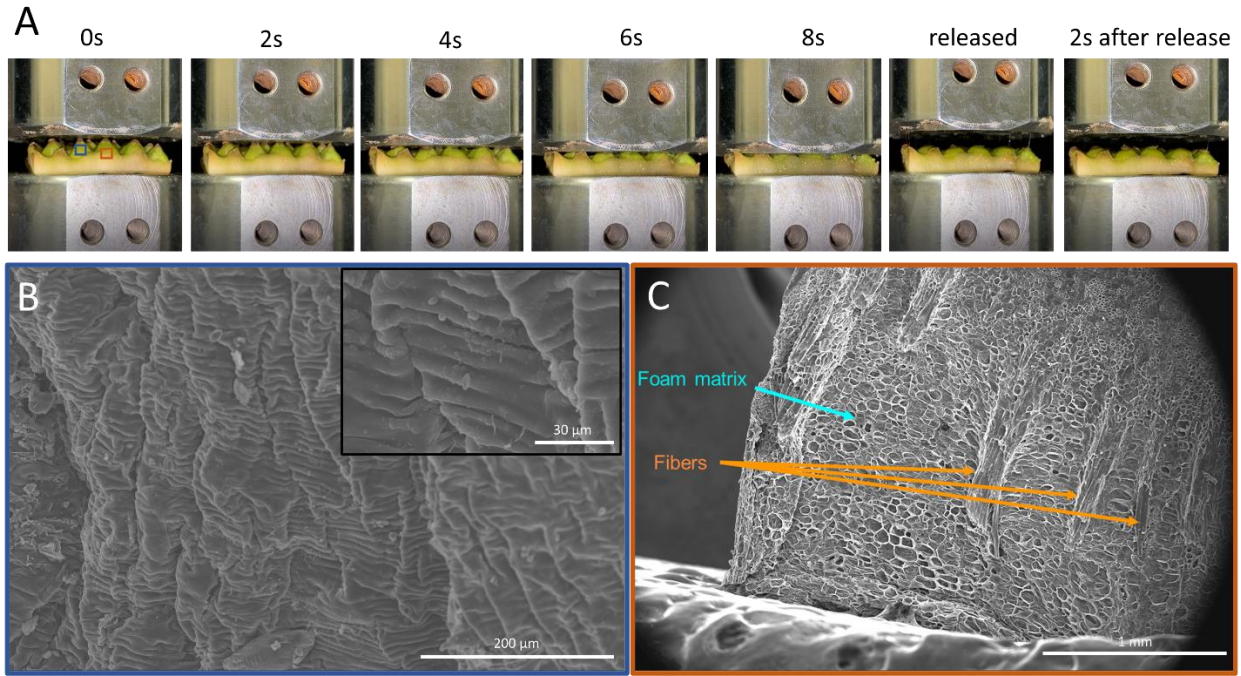
Figure 7.5 A.) Images of two-layer jackfruit samples composed of just the thorn and mesocarp layer being compressed and released . B.) SEM scans of the jackfruit thorn's ordered exterior and C.) the underlying structure of the jackfruit thorn where the fibers, cellular matrix, and gradient in cell size can be seen. The general location of images B and C are indicated by the boxes on the first panel of A.

Thorn samples were compressed and then imaged with SEM, revealing the collapsibility of the thorn's microstructure. Figure 7.6A and B show images of the underlying foam matrix before compression and at 72% strain, respectively. Buckling of the cell walls can be observed, but very little fracturing can be seen due to the extreme collapsibility of the sample. On the surface, the wrinkled skin behaves like an extended spring. As the thorn is compressed, the wrinkle spacing decreases, as shown in Figure 7.6C. Figure 7.6D shows how these wrinkles bunch together as the strain is increased. The highly ordered nature of the surface skin allows the jackfruit thorn to recruit substantial amounts of material to resist compression. Research into thin-walled, crashworthy

structures has shown that a progressive, stable collapse mode is often preferable for increased energy absorption during compression [509,510]. The wavy features of the thorn's exterior encourage this collapse mode by providing asymmetric planes of weakness along the length of the thorn that can fold and condense without failing. Furthermore, with minimal plastic deformation during compression, this structure is able to rebound after being compressed, even to high strains.
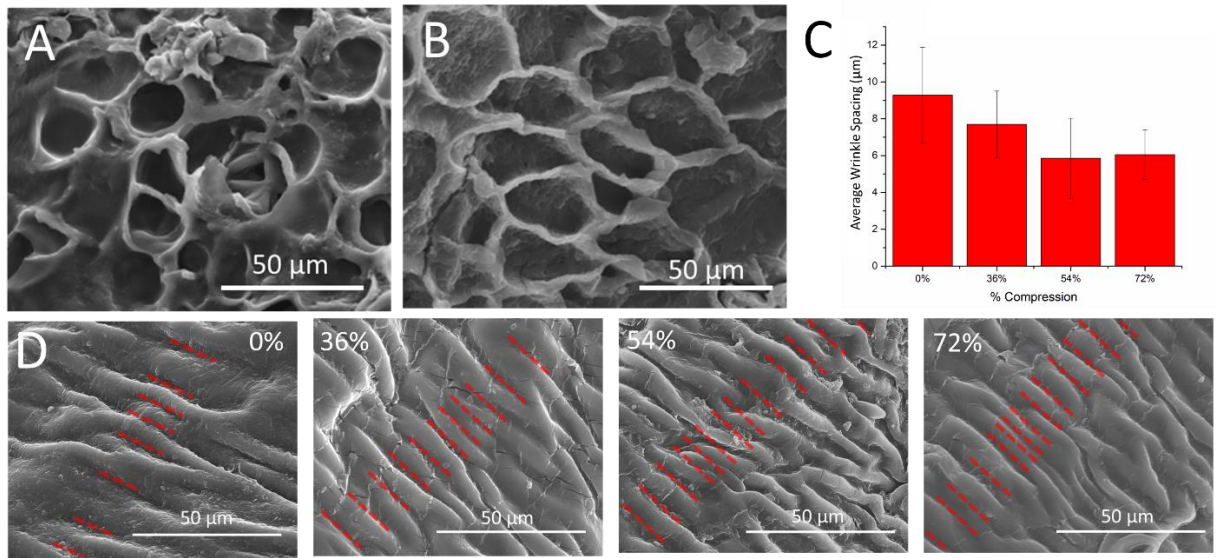
Figure 7.6 The thorn structure shows impressive ordered collapse and survivability during compression. A.) A pre-compression image taken of the underlying structure of the jackfruit thorn and B.) an image of the same structure after being compressed to 72%. C.) Measurements of the jackfruit thorn's wrinkle spacing at different compressive strains and D.) representative images visualizing how the wrinkles pack together during compression.
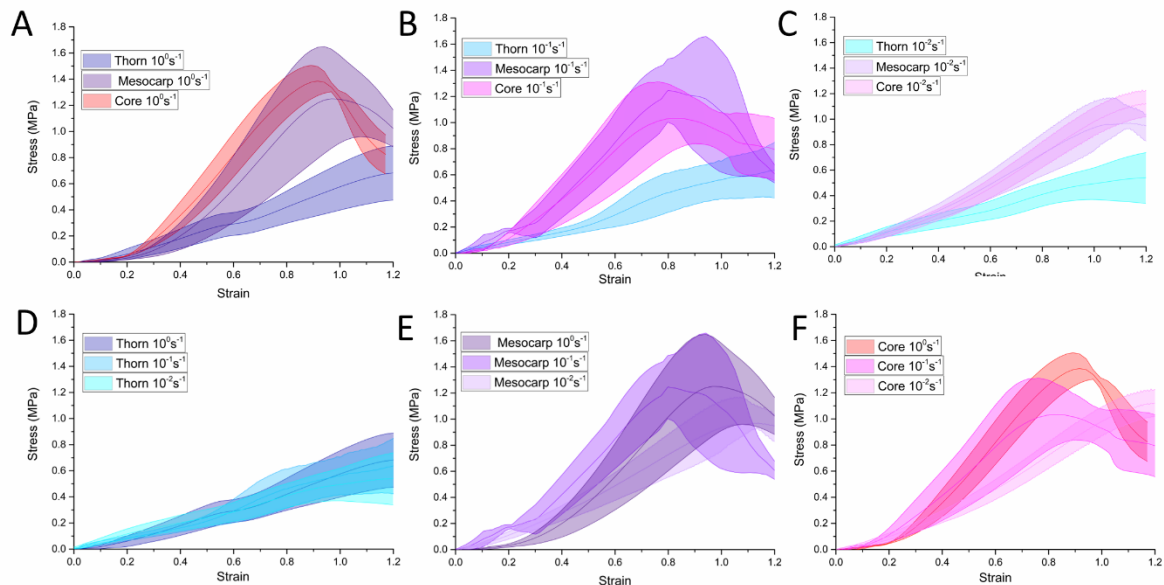
Figure 7.7 Each layer of the jackfruit (excepting the tubule layer) was compressed at three different strain-rates ($10^{0}s^{-1}$, $10^{-1}s^{-1}$, and $10^{-2}s^{-1}$). A-C.) Comparisons of the different layers at each strain-rate and D-F.) comparisons of the sample layer at different strain-rates.

Figure 7.7A-C shows a comparison of each layer's stress-strain curves at the compressive strain-rates of $10^{0}s^{-1}$, $10^{-1}s^{-1}$, and $10^{-2}s^{-1}$. Across all strain-rates, the behavior of core and mesocarp samples were the most similar, with the core samples exhibiting a comparable or slightly larger stiffness while mesocarp samples were able to reach a higher ultimate stress. Both layers see an increase in stress up until approximately 0.9 strain after which it begins to decrease. Thorn samples exhibited the lowest curves, collapsing much more easily at each strain-rate. This is due to the irregular shape of the thorn which leads to a top-down collapse mechanism. With the smallest cross-sectional area, the top of the thorn collapses easily with low loads, however as the cross-section increases larger and larger loads are required to continue collapse. The stress calculations for these curves were based on the base cross-sectional dimensions and the result is a steadily rising stress-strain curve. These values do not provide an accurate interpretation of the stress throughout the thorn (which is inconsistent due to the inconsistent cross-sectional area), however,

it does show the ingenuity of the thorn shape. The low cross-sectional area at the tip of the thorn allows it to collapse at low loads, absorbing strain energy before other parts of the fruit. The graceful collapse of the thorn discussed previously allows it to compress to very high strains without seeing a drop in load that would result from catastrophic failure (a phenomenon observed for the mesocarp and core samples). The high cellulose content and softer parenchyma cells likely also contribute to the lower stiffness of the thorns. Together, the macroscale shape, microscale features, and cellular composition allow the thorn to be one of the first parts of the fruit to absorb strain energy during compression while also being capable of doing so to high strains. Furthermore, the thorns exhibit very little variance between different strain-rates (Figure 7.7D), while the core and mesocarp samples become noticeably stiffer and stronger at higher strain-rates (Figure 7.7E and F). This ensures that the thorns remain collapsible cushions that protect the rest of the fruit during impact. The mesocarp and core layers however transition from a steady sloping curve at a strain-rate of $10^{-2}s^{-1}$ to a stiffer behavior that reaches a maximum stress at ~0.8 and ~0.95 strain when tested at strain-rates of $10^{-1}s^{-1}$ and $10^{-2}s^{-1}$, respectively. Interestingly, a trend was observed where samples were able to reach a higher ultimate strain and maximum stress at higher strain-rates. This suggests more energy can be absorbed by these layers during impact scenarios.
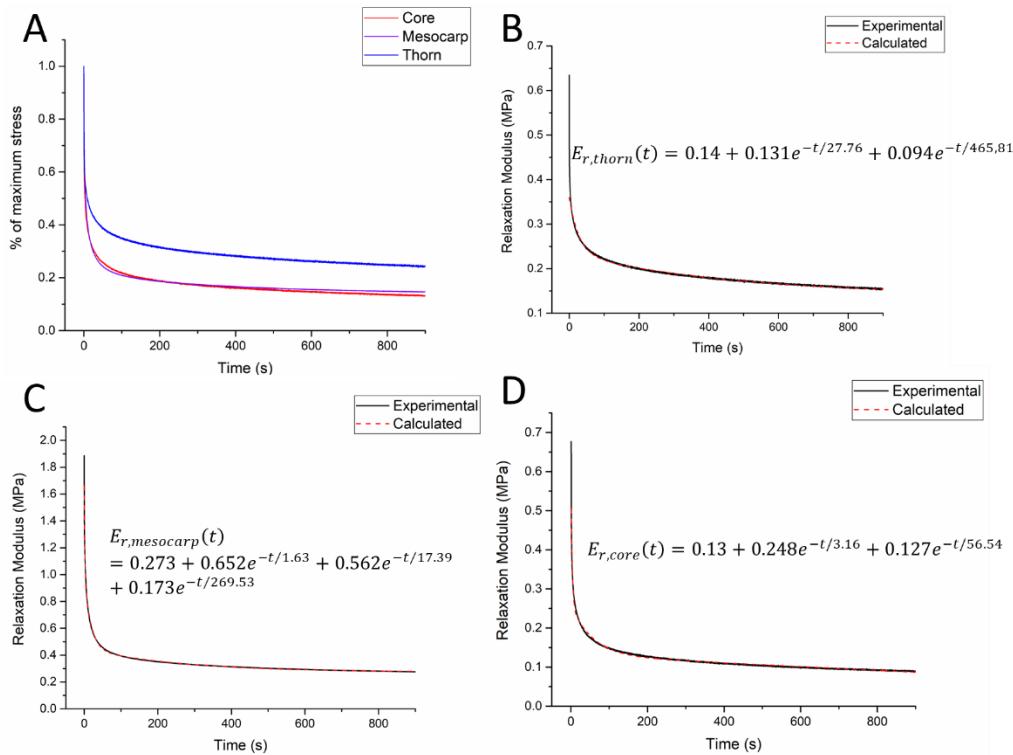
Figure 7.8 Stress-relaxation tests were performed to evaluate the viscoelastic behavior of each layer of the jackfruit. A.) Normalized stress decay curves comparing the core, mesocarp, and thorn layer. B-D.) The experimental relaxation modulus and fitted model for the thorn, mesocarp and core samples during the relaxation test.

Understanding the viscoelastic nature of the jackfruit's layers can provide some insight into their time-dependent behavior. Figure 7.8A shows the stress relaxation of the different layers in the jackfruit. Much like with the compressive results, the mesocarp and core have very similar behavior, relaxing to a plateau of about 20% of their initial stress. The thorns relax slightly less, however, this again might be skewed by the irregular shape of the thorn. Figure 7.8B-D shows the relaxation modulus of each layer and their respective fitted curves from the Prony series. The equations describing the resultant Maxwell-Weichert model are listed below:

$$E_{r,core}(t) = 0.13 + 0.248e^{-t/3.16} + 0.127e^{-t/56.54}$$

$$E_{r,mesocarp}(t) = 0.273 + 0.652e^{-t/1.63} + 0.562e^{-t/17.39} + 0.173e^{-t/269.53}$$

277

$$E_{r,thorn}(t) = 0.14 + 0.131e^{-t/27.76} + 0.094e^{-t/465,81}$$

Keryvin et al. [508] performed nanoindentation stress-relaxation tests on flax cell walls and identified four characteristic relaxation times of 0.3-0.54s, 1.4-2.3s, 7.6-10s, and 46-54s. These were attributed to hemicellulose, pectin, amorphous cellulose, and crystalline cellulose, respectively. For macroscale tensile relaxation tests performed on flax fibers these relaxation times smear together into two characteristic relaxation constants, one of 2.6±2.4s attributed to hemicellulose and pectin and one of 55±29s attributed to cellulose. This aligns well with our results, particularly for the core, which has calculated relaxation times of 3.2s and 56.5s. While a three-component model was fitted to each layer, the third component of the core and thorn made an insignificant contribution to the fit and were disregarded. The mesocarp, which contains less cellulose and more lignin as determined by TGA, has a third component with a longer relaxation time. This could be the result of the higher lignin concentration found in the mesocarp. The first and second relaxation times (Figure 7.8C) are also lower, which suggests there could be more hemicellulose and less crystalline cellulose in this layer of the jackfruit. The thorns, which contained the least hemicellulose and pectin, were not determined to have a relaxation constant on the scale of τ=0.1-10s (Figure 7.8B), instead only having an intermediate relaxation constant of 27.8s and a long-term relaxation constant of 465.81s. The former, is dominated by the cellulose relaxation that is pulled downward by the presence of relatively smaller quantities of more rapidly relaxing hemicellulose and pectin. The larger relaxation time, again, can likely be attributed to the bundles of lignin fibers identified in previous sections.

7.3.3 Dynamic Mechanical Behavior

While these quasi-static tests provide insight into the mechanical behavior of the jackfruit the response of the entire fruit during impact might be quite different. For example, during quasi-

static tests on a flat sample, the tubular layer is able to densify entirely, before the mesocarp and thorny layer begin to deform. However, when attached to the entire fruit this would likely not be possible without tearing the external two layers. Furthermore, under impact conditions the time dependency of stress-waves traveling through the outer two layers may reduce the percentage of strain energy absorbed by the tubular under-layer. To asses this, impact tests using a gas gun were conducted on different combinations of layers.
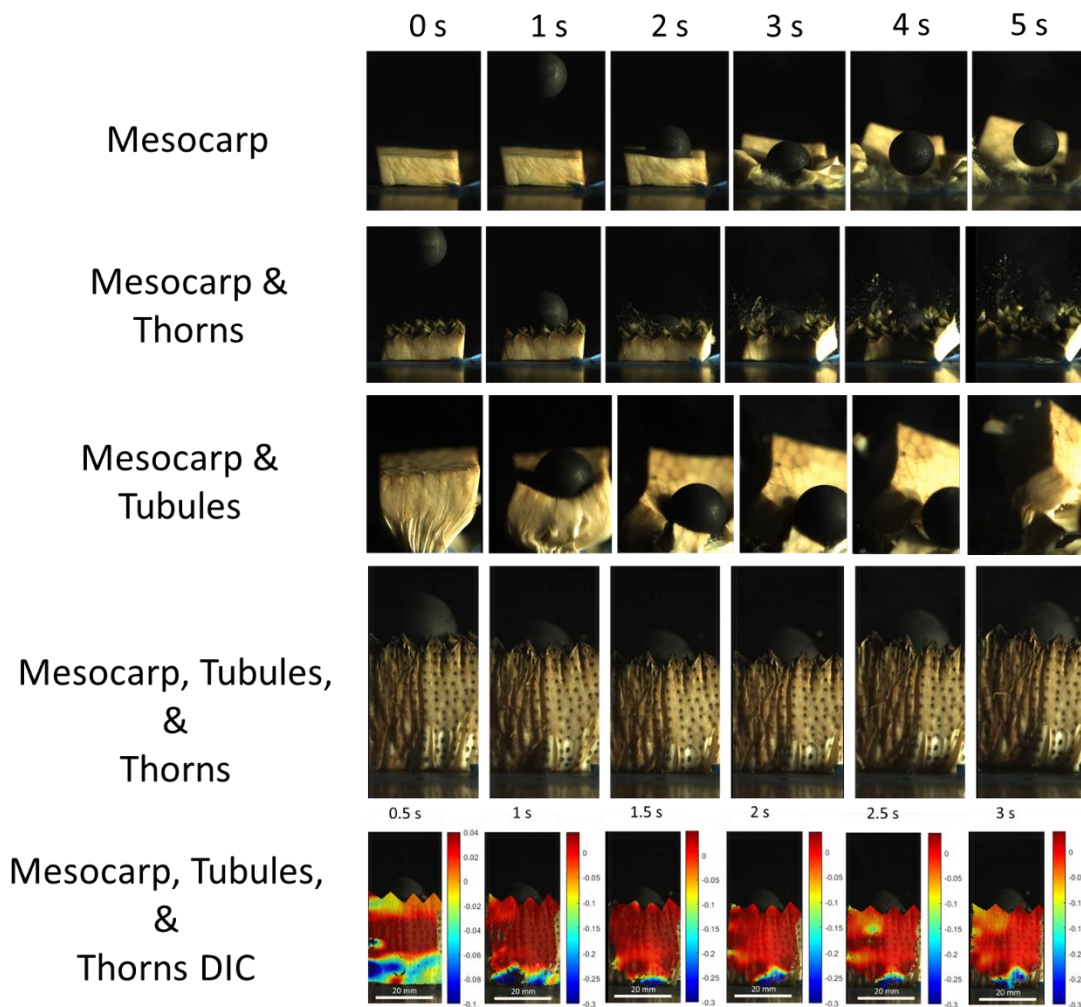
Figure 7.9 Still frames extracted from high speed video of gas gun impact tests on different combinations of jackfruit layers. The bottom panels show DIC on three-layer samples during impact.

Figure 7.9 shows still images extracted from high-speed footage of the impact event. Samples of mesocarp, mesocarp and thorns, and mesocarp and tubules failed completely. In these cases, the projectile penetrated entirely through the sample, hitting the metal backplate underneath. The mesocarp is composed of aligned fibers that easily peel apart under impact. This can be seen in the tests on the solitary mesocarp samples as well as the tests on the mesocarp and tubule layers, where the tubules begin to absorb the impact (row 3, frame 2) but then split apart and fail (row 3, frame 3) before the impactor can be rebounded. For the three-layer samples, nearly all the impact energy was absorbed by the tubule layer which collapsed to strains of ~ 0.3 before rebounding (the rebound could not be captured by DIC as the sample 'jumped' off the backplate in the process). This can be seen in DIC figures for the three-layer samples which show minimal strain values in the thorn or mesocarp layers throughout the impact, while the tubule layers collapse. Meanwhile, the thorny layer held the three-layer sample together preventing the splitting phenomenon observed in the samples of just mesocarp and tubules. When post-impacted samples were cut open, bruising was observed just beneath the thorns for three-layer samples, while samples without thorns were bruised through the whole thickness of the sample.

The thorny structure on the surface of the fruit both delocalizes damage while also containing it. When samples of just the thorny layer were impacted at a lower energy, that did not lead to ultimate failure, only the thorns that came into contact with the projectile exhibited damage. However, each of the impacted thorns experienced a similar level of deformation. Ha et al [480] observed a similar energy absorption mechanism resulting from the thorny structure of durian fruit. They noted that most of the energy absorbed by the fruit's exterior could be attributed to bending of the thorns, fracturing at the thorns' tips, and buckling, bending, and delamination of the thorn's reinforcing fibers. In the jackfruit, the thorns have a lower aspect ratio, are more densely packed,

and are less curved than the durian. Further, the jackfruit's surface is much more irregular and tends to have less curvature. As a result, the loading mode of the thorns is much more axial, leading to a failure mechanism that is dominated by crumpling and, later, splitting of the thorns. The gradient in thorn cell morphology, identified in section 3, encourages crumpling and buckling near the center of the thorn where the cross-section is still small but where fiber and matrix cell wall density are lower than at the thorn tip. The shape of the thorn provides an ingenious design for absorbing impact energy, by creating a weak initial contact surface that gradually becomes more resistant to loading as it is compressed. Simplifying the shape of a thorn to be a conical frustrum (Figure 7.10A) we can approximate the radius of the thorn at any given height to be

$$r(y) = r_o + (R - r(y))$$

$$r(y) = r_o + \frac{y}{\tan(\Theta)}$$

Where y is the compressive displacement and Θ is the inclination angle of the thorn. This can be used to calculate the increase in cross-sectional area as the sample is compressed:

$$A(y) = \pi * (r_o + \frac{y}{\tan(\Theta)})^2$$

During compression, the strain can be substituted in for the displacement, y, as such:

$$y = \varepsilon h$$

$$A(\varepsilon) = \pi * (r_o + \frac{\varepsilon h}{\tan(\Theta)})^2$$

During the elastic portion of thorn compression, the maximum stress will form at the smallest surface, which will be touching the compression plate. As such, during elastic compression, the maximum stress is

$$\sigma_{max} = \frac{F}{A(\varepsilon)} = \varepsilon E_{eff}$$

Using the approximation for the effective Elastic modulus of a cellular solid based on measurements of cell size and wall thickness (and assuming a linear gradient in cell size and wall thickness from the tip of the thorn to the base), the Elastic modulus of the thorn with respect to y can be estimated as:

$$E_{eff}(y) = 0.1 * E * y$$

or

$$E_{eff}(\varepsilon) = 0.1E(h\varepsilon)$$

Substituting this in we get

$$\sigma_{max} = \frac{F}{\pi * (r_o + \frac{\varepsilon h}{\tan(\Theta)})^2} = 0.1Eh\varepsilon^2$$

and

$$F = 0.1\pi h\varepsilon^2 E(r_o + \frac{\varepsilon h}{\tan(\Theta)})^2$$
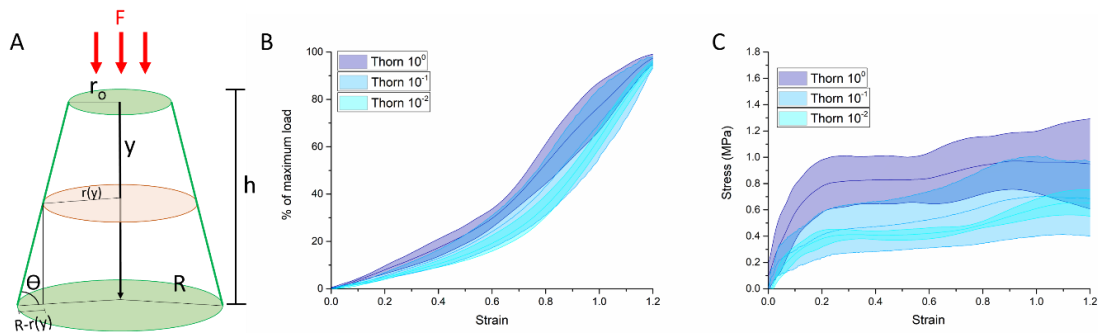
Figure 7.10 The shape of the thorn plays a vital role in its compressive behavior. A.) The thorns shape can be idealized as a conical frustrum with a circular cross-section whose radius varies with its height. B.) The load required to compress the thorn increases exponentially with increasing strain. C.) However, by accounting for the changing cross-section during compression, the stress in the thorn plateaus after reaching approximately 0.2 strain.

Figure 7.10B shows the % of the maximum load over the course of compressing the thorn quasi-statically. The results show a steadily increasing curve for all strain-rates, mirroring the results in Figure 7.7D which displays the stress at the base of the thorn. This phenomenon is typical during compression as the material densifies and barrels, however it is augmented by the thorn shape which has a naturally increasing cross-section, demanding a higher load be applied to continue compressing the material. Applying the equation for the change in cross-sectional area (Figure 7.10C) to account for this shows that at the compression surface of the thorn the stress plateaus at a strain of about 0.2. These results highlight the importance of the shape of the thorn in absorbing energy and cushioning impacts. Furthermore, the distribution in thorn heights leads to an even more gradual macroscopic collapse as certain thorns undergo compression during and axial impact before others. While more pronounced strain-rate sensitivity, particularly in plateau stress, can be seen in the quasi-static results depicted in Figure 7.10C the gradually increasing area of the thorns as a means to resist loading should hold true during higher strain-rate impact scenarios.

During impact, a preferential cracking mechanism was observed. In the thorn and mesocarp layers, cracks nearly always propagated between the irregular bases of the thorns. In this manner, fracture was controlled and prevented from spreading throughout the fruit's surface, while the irregular hexagonal base configuration leads to tortuous crack paths. The image on the left of Figure 7.11A shows the underside of the sample where both the damage control mechanism and the preferential cracking (highlighted by dashed red lines) can be more easily observed. A close look at the cracks also shows that the material has not entirely failed as intact fibers bridge the cracks faces. On the right of Figure 7.11A the exterior of the sample after impact can be seen, where splitting, crumpling, and discoloration of just the impacted thorns can be seen. Figure 7.11B shows still images just before the impact, during the impact, and after the impact of the projectile. Damage develops in the impacted thorns, while the adjacent thorns remain unaffected.
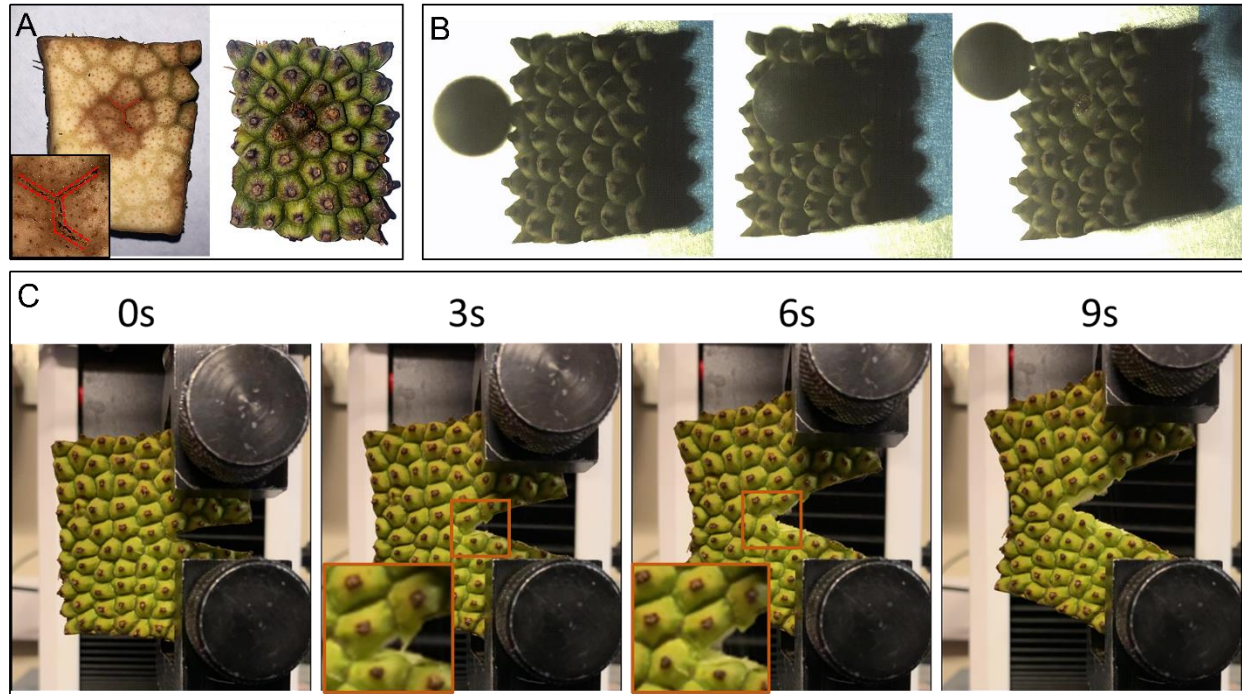
Figure 7.11 A.) During gas gun impact tests on the thorn jackfruit's thorn structure, cracks prefer to propogate between the thorns. Furthermore, by looking at the underside of thorn samples, bruising can be seen exclusively in the thorns that were in contact with the projectile. B.) Still images showing before, during, and after impact on the jackfruit's thorns. C.) Compact tension tests revealed that cracks prefer to propogate between the thorns even when a crack is being driven through the material under slower loading conditions.

To explore the preferential cracking mechanism in the jackfruit's thorny layer, compact tension specimens were prepared. A precrack was introduced and driven through the sample. Much like the cracks that developed during gas gun impact testing, there was a preferential crack path between the thorns, which is visualized by the still frames shown in Figure 7.11C. The extrinsic toughening mechanism of fiber bridging, where fibers span the crack interfaces behind the crack tip, was observed and can be seen in the insets of Figure 7.11C. The average load vs extension data for the compact tension tests performed at different crosshead speeds are plotted in Figure 7.12A. A clear strain-rate dependency can be seen in this plot, with the curves of faster crosshead speeds achieving higher loads. As a result, the energy absorbed (the area under the curve),

increases with increasing crosshead speed. This relationship between crosshead speed and energy absorbed is plotted and fitted with the following exponential function in Figure 7.12B:

$$E_{absorbed} = 0.096e^{(\frac{V_{crosshead}}{52.44})} + 0.313$$
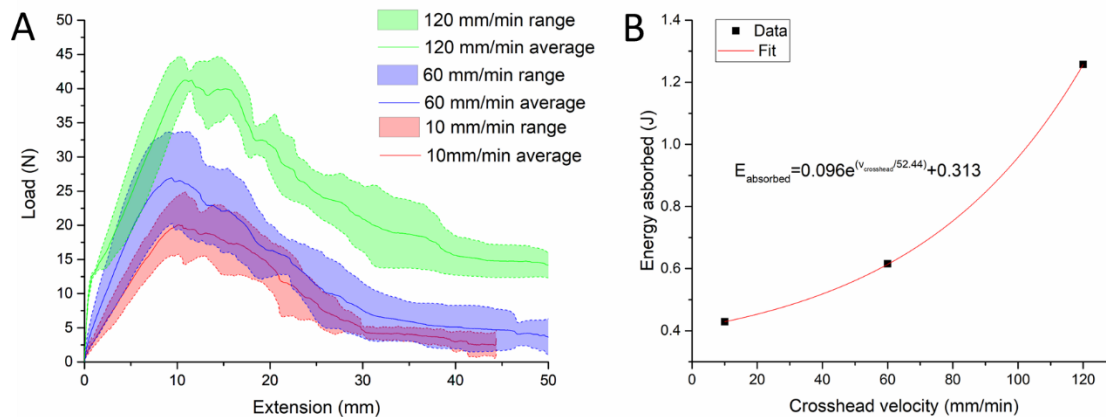
Figure 7.12 Compact tension tests were performed at multiple cross-head speeds. A.) A clear loading dependency can be seen in the load-extension curves of the jackfruit's outer later. B.) The energy absorbed during compact tension tests increased signficantly with an increase in crosshead velocity.

The sudden rises in load in the load-extension curve corresponds to when the crack encounters a thorn. When the crack bypasses the thorn and continues propagating through the valleys between them the load drops again.

7.3.4 Bioinspiration from the jackfruit

To show that the jackfruit structure can be translated to an engineered system. Impact tests were performed on 3D printed bioinspired designs, comprised of combinations of thorns, featureless mesocarp, and tubular layers. Figure 7.13A shows an exploded schematic of these layer designs. A variety of print materials were explored to understand which engineering scenarios are

best suited for the use of the jackfruit design. The first series of tests were printed out of relatively stiff, brittle PETG. Blocks of solid PETG were printed at decreasing increments of infill and tested until samples consistently failed during testing. Jackfruit inspired designs were then scaled to the same size of the control block and printed to be the same mass. For the first test a control block of PETG printed with 10% infill was used for comparison. Figure 7.13B shows the total failure of the control as the projectile travels through the entire length of the sample, causing fractures to initiate and propagate between the print layers in the process. The jackfruit inspired sample, shown in Figure 7.13C, sustained considerably less through-thickness damage. Owing to the fact that PETG is considerably stiffer than natural jackfruit, the impact stress was not effectively transmitted through the sample layers. The result is that the progressive collapse mechanism of tubule buckling, followed by thorn compression, before finally giving way to mesocarp densification was not observed. DIC analysis showed minimal strain (<0.01) in the tubular and mesocarp layer throughout the impact event. However, despite the mismatch in material properties, the thorn structure still efficiently absorbed impact energy and delocalized damage across the sample surface. This phenomenon can be observed in the post-impact still images of the samples, where the neat, control block has a hole approximately the same size as the impactor through its entirety, whereas the lower layers of the jackfruit-inspired sample are still intact while the outer thorn layer is completely obliterated. During impact, the thorns directly beneath the projectile collapse downward along their longitudinal axis, splitting vertically as they do, while adjacent thorns in contact with the impactor buckle and bend before snapping. Nearby thorns that are not in the impact zone provide lateral planes of weakness that encourage damage to spread horizontally through the sample rather than vertically. Samples printed with tubules but without the thorns did exhibit strain concentrations in the tubular layer before failing. Figure 7.13D shows strain maps of

these samples during impact. Due to the high stiffness of PETG minimal buckling, bending, or deformation was observed in the tubule layer with fractures initiating at strain values of about 0.067. However, much like biological jackfruit samples, nearly all the strain was concentrated in the tubular layer, as was the resultant damage.
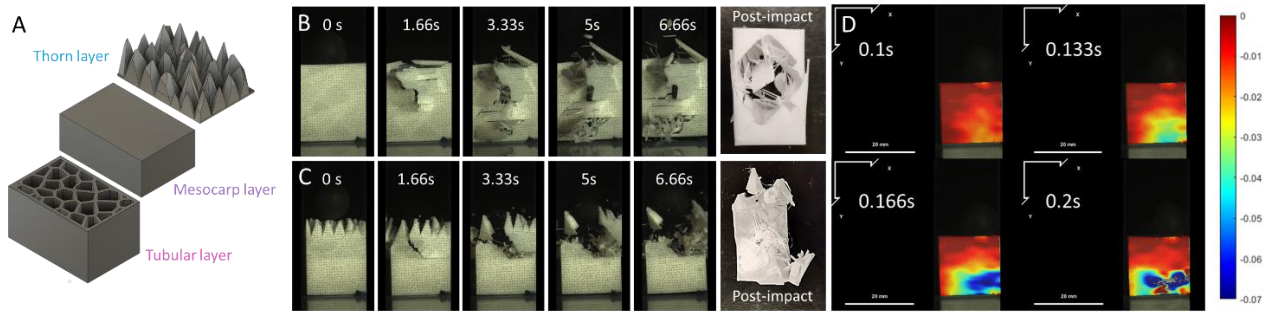
Figure 7.13 Bioinspired designs were fabricated to translate the impact resistant mechanism in the jackfruit to engineered materials. A.) An exploded CAD schematic showing the different layers of the bioinspired models. B.) Still images extracted from high-speed video of a featureless control block and C.) a three-layer jackfruit-inspire design during and after impact. D.) DIC analysis of two-layer jackfruit-inspired samples without thorns showing that strain is concentrated in the tubular layer before failure.

To further understand the interplay between the thorn layer and tubular layer, samples with higher infills of 15% and 20%, which would fail less easily, were printed. Figure 7.14 shows strain maps of impacted samples just prior (<0.033s) to the onset of fracture. Figure 7.14A and B show samples printed without thorns at infills of 20% and 15%, respectively. In these samples, the strain is concentrated in the tubular region, which reaches a maximum of 0.052 at 20% infill and 0.066 for the more flexible 15% infill before failing. Meanwhile, in samples that have thorns, the strain in the tubular region remains <0.01 for the duration of the impact, while most of the strain is spread amongst the thorns and the area just beneath them as shown in Figure 7.14C and D. The more flexible 15% infill sample allows the strain to spread deeper and more broadly into the mesocarp layer. These results highlight that the thorns act as an initial barrier to impact and disperse the strain energy near the surface much more than a flat exterior which allows the impact energy to be

transmitted deeper into the material. However, the progressive failure of the layers is inverted for the stiffer PETG samples which see failure of the thorns first and then the tubules, unlike the jackfruit samples. Regardless, both mechanisms continue to exist in stiffer samples.
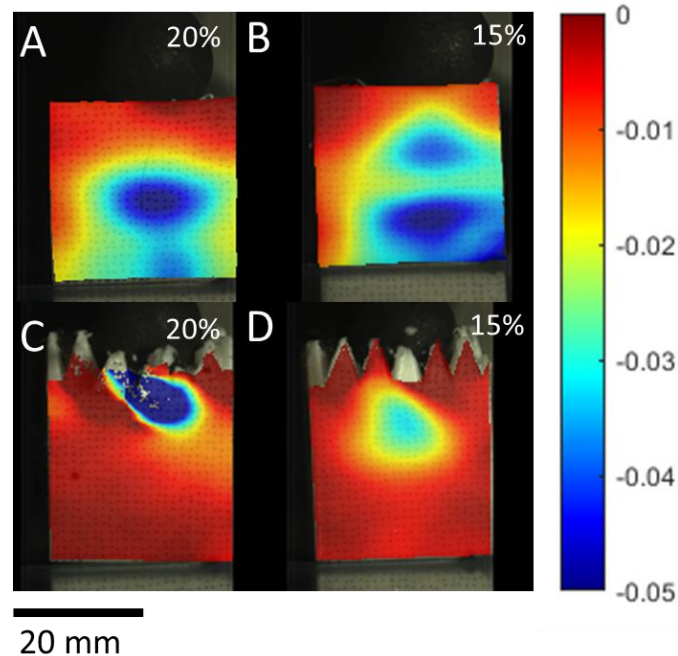
Figure 7.14 DIC anaysis of A.) tubule and mesocarp samples printed at 20% and B.) 15% infill and three-layer samples printed at C.) 20% and D.) 15% infill just before cracking initiates. In samples without thorns, strain is concentrated in the tubular layer while samples with thorns exhibit the most strain just below the thorns.

Naturally, this energy dispersion mechanism has an effect on how the samples fail during impact. Figure 7.15 shows the progression of damage for samples of mesocarp and tubules (A and B), all three layers (C and D), and tubules and thorns (E and F). In samples, without thorns (A and B) linear cracks form vertically through the sample, causing splitting between the tubules and sample failure. Generally, only a few large cracks were observed which split the sample in half or broke off large chunks of material. In samples with thorns, however, arcing cracks formed just below the thorn layer moving horizontally through the sample. Many smaller cracks were observed between and through thorns which propelled debris in every direction. While several cracks

reached the tubular layer, none were observed traveling all the way through the samples which were still intact after testing. To determine whether this was simply the result of more material in the three-layer samples, designs of just thorns and mesocarp were fabricated which have significantly less material. Still, no cracks traveled entirely through the sample, while crack arcing, multiple cracking, and large amounts of impact debris were still observed.
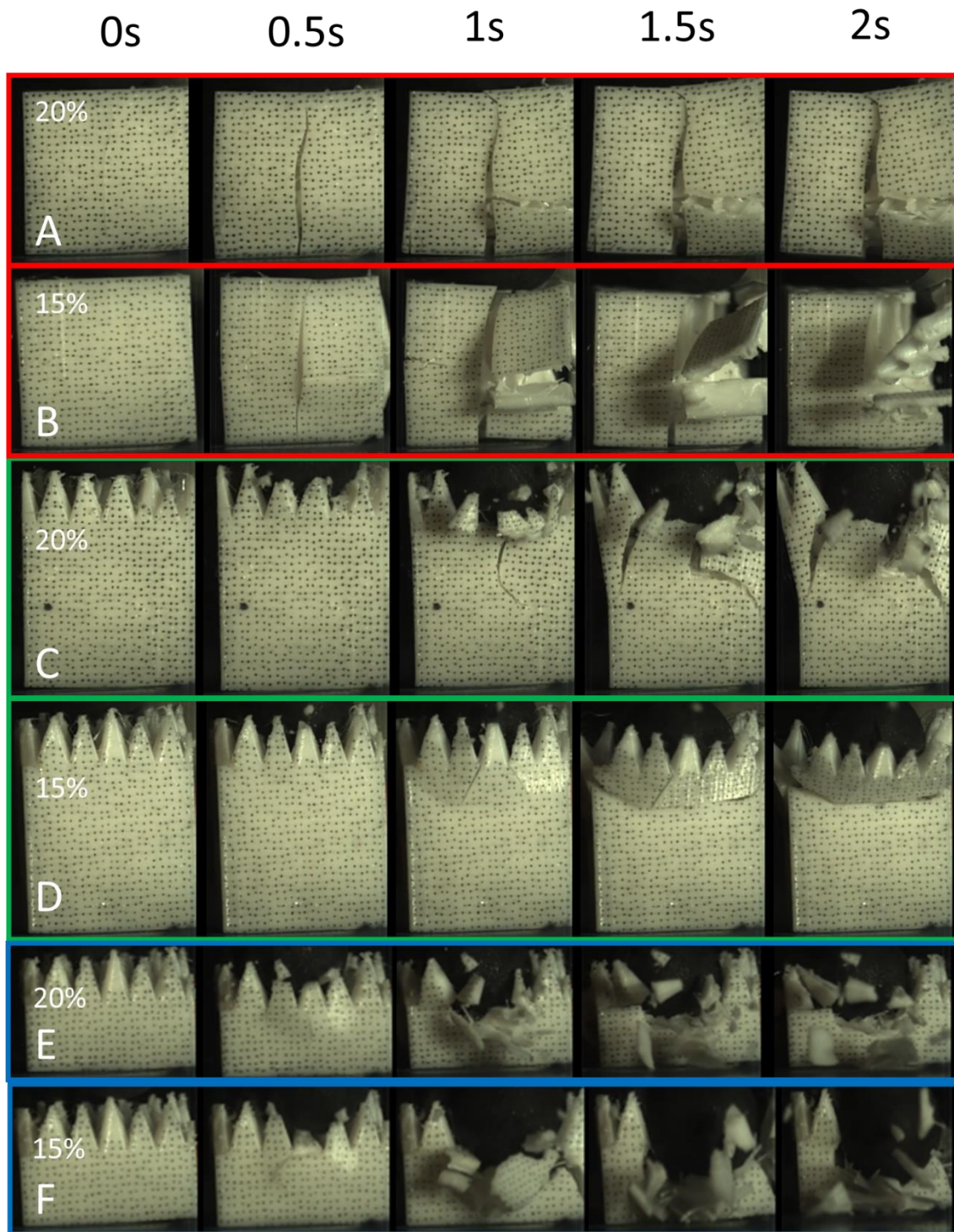
Figure 7.15 Extracted still images from high-speed video of gas gun impact tests on tubule and mesocarp samples printed at A.) 20% and B.) 15% infill, three-layer samples printed at C.) 20% and D.) 15% infill, and thorn and mesocarp samples printed at E.) 20% and F.) 15% infill.

These tests show that the jackfruit inspired designs can be successfully utilized to improve the impact resistance of engineered materials. While the exact behavior of the structure may vary from that of the jackfruit due to differences in material properties, the broad effects of the architectures are consistent. The thorns disperse impact energy and contain damage near the surface of the sample. While jackfruit thorns disperse energy via bending, compressing, buckling, and splitting, thorns in the stiffer 3D printed samples disperse energy by splintering and breaking off of the material while still requiring tortuous crack paths for fractures that propagate between them. There are many bioinspired designs that offer beneficial properties for engineers to choose from. The thorn structure is a particularly useful design motif for several reasons:

1. It can be transferred to materials with different properties (i.e. stiffness) while still providing benefits: Many bioinspired designs need to be replicated using materials that contain properties akin to those of the natural system. However, the thorn structure disperses impact damage along the surface of a material in both stiff and soft materials.

2. It can be easier to fabricate: Unlike other common bioinspired designs that resist impact like conch shells or horse hooves, the thorn structure is not inherently composite and can be fabricated out of a single material, making it easier to manufacture.

3. It can be combined with other designs: Many biological systems use composite interfaces as a means of fracture control [7] to improve impact resistance, but see these mechanisms breakdown, particularly near the surface, during impact scenarios [11]. Yet the thorn structure can yield preferential, tortuous cracking, even during impacts while using just a single material. This makes it a flexible design that can easily be combined with other toughening architectures to act as a first contact surface structure that reduces impact damage and channels initial cracking.

292

The tubules absorb strain energy by acting as a weak, porous layer that can easily collapse before the solid mesocarp layer. This phenomenon is diminished in stiffer samples yet was still observed in those without thorns. This suggests that the tubule layer would be the next to compress and fracture if impacted with more energy.

7.4 Conclusions

The jackfruit is the largest fruit in the world and is capable of withstanding tremendous falling impacts. The goal of this study was to understand how the jackfruit is able to survive such events. Here, we characterize the structure and composition of the jackfruit's layers for the first time.

1. MicroCT scans revealed a tubular layer that has a porosity of approximately 57% while SEM scans showed that the thorns on the exterior of the jackfruit have a fiber reinforced foam composite structure and are covered with an ordered, wavy skin.

2. Toluidine blue O staining suggested that these fibers are lignified while the surrounding matrix is primarily composed of cellulose-rich parenchyma cells that increase in size and decrease in cell wall thickness towards the base of the thorn. As a result, the tip has a much higher cell wall density than the base.

3. TGA suggested that the thorns had a significantly higher concentration of cellulose while the mesocarp contained relatively more lignin and the core contains excesses of pectin/hemicellulose. These results corroborated those of the staining experiments and agreed well with other studies.

These structural and compositional findings were then connected to the behavior of each of the jackfruit's layers with mechanical tests.

1. The lignin-rich mesocarp and pectin/hemicellulose rich core behaved relatively similarly, with the mesocarp samples generally reaching higher ultimate stresses. This suggests that these two layers form a sandwich structure around the tubular layer which collapses first when the outer three layers were compressed together.

2. The thorn on the other hand, even when adjusted for its variable cross-section, plateaued at a relatively low stress value but did not see a decrease even when compressed to 30% of its original height. This is optimal for continuously absorbing impact energy during falling, when the exterior of the fruit can experience very high strains. The conical structure of the jackfruit thorn is also ideal for absorbing impact energy. As the strain on the thorn increases, so does the cross-sectional area. This means that the tip of the thorn absorbs the brunt of the impact energy collapsing easily, while the increasing cross-sectional area leads to a gradual increase in resistance. Ultimately, this makes the thorn an ideal impact surface energy-absorber.

3. The irregular hexagonal base structure not only allows for optimal packing of the thorns, but it also led to increased crack tortuosity both during impact testing and during compact tension tests. Cracks prefer to initiate between the thorn and then to propagate around them rather than traveling through them. Furthermore, the thorn structure delocalized damage across the surface of the jackfruit.

4. Compact tension tests revealed that even when driven through the jackfruit skin, cracks prefer to travel between the thorns. The skin also absorbed more energy during compact tension tests at faster crosshead speeds.

The general structure of the jackfruit was then transferred to bioinspired designs to capture its mechanical capabilities.

1. During impact, the thorn structure effectively spread damage across the surface of the sample at all infills. Meanwhile, control samples of the same mass were punctured through their full thickness at low infills or experienced ultimate failure due to vertical cracking at high infills.

2. In three-layer samples, strain was concentrated in the thorn layer during impact, while in two-layer samples composed of just a bioinspired mesocarp and tubular layer, nearly all of the pre-failure strain developed in the deeper tubular layer.

3. These results suggest that jackfruit inspired designs can be transferred successfully to engineered materials. The jackfruit design in particular is quite useful since it can be printed out of a single material, can be successfully utilized in materials with different properties, and can be employed in tandem with other impact-resistant design elements.

7.5 Acknowledgements

Chapter 8. Conclusions

Biological materials exhibit a treasure trove of design strategies for engineers to learn from. Over millions of iterations, evolution has honed the structure of natural materials to withstand the demands placed on them by their environment. In materials that are subject to impact scenarios, organisms from across the natural world have converged on similar designs strategies to improve their impact resistance. This dissertation focuses on two of these systems: the horse hoof wall and the jackfruit.

While these two materials are composed of entirely different constituents, keratin for the hoof capsule and lignin, cellulose, hemicellulose, and pectin for the jackfruit, they each contain a structure that exhibits progressive failure of its features. In the jackfruit, this can be seen in the layer-by-layer collapse mechanism where the tubular layer buckles, before the thorns, and finally the mesocarp. In the hoof, the porous tubules have variations in shape, size, and bridge reinforcement which causes different medullary cavities to collapse at different stress levels. This allows the material to sacrifice just a portion at a time rather than experiencing complete failure at a specific stress level. It is also likely that the first regions to collapse are areas that will more readily recover and exhibit less plastic deformation than the rest of the material.

Both the jackfruit and hoof capsule also contain many of the design elements commonly observed in impact resistant biological materials including layered arrangements, sandwich structures, tubular features, and gradients. In the hooves, the layered structures work in tandem with the tubules to trap and redirect cracks. In the jackfruit, the tubules make up an entire layer themselves and absorb energy by collapsing and cushioning the fruit's seeds. The hoof utilizes a gradient in hydration to dissipate internal stresses between each footfall via viscoelastic relaxation

and contain a gradient in tubular configuration that can reduce impact damage. The jackfruit thorns contains a gradient in cell size and cell wall thickness that increases the amount of material in the initial impact zone at the thorn's tip.

Similarly, both systems contain hierarchical architectures in which fibers play a vital role. Figure 8.1 shows the remarkably similar fiber bridging mechanisms that occur behind the crack tip in both jackfruit and horse hooves. In each, the fibers are much smaller than other features that guide crack propagation, so the fibers are positioned to span the fracture interfaces as it moves through the material.
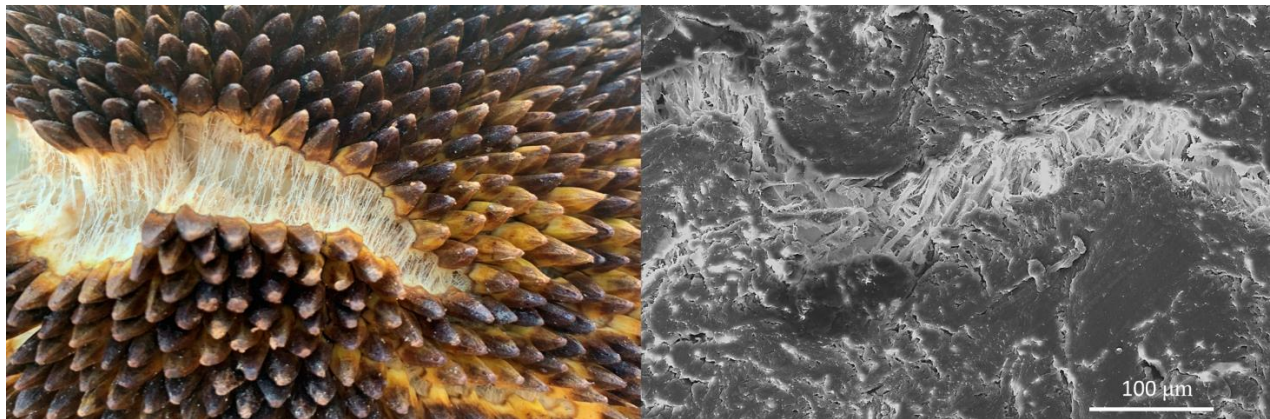
Figure 8.1 Fiber bridging occurs in both jackfruit and horse hoof walls as cracks travel through the material. This toughening mechanism resists further crack propagation, slowing fracture and making the process more energy demanding.

Several unique features were also observed in these systems. For example, in the horse hoof the physically intertwined nature of the tubular reinforcement toughens the interphase zone of the composite. This leads to several unique phenomena including tubule bridging, where whole tubules span the crack surfaces, crack trapping, where cracks become trapped in the planes of weakness between the tubule cortical layers, and fiber rupture during tubule pullout. The tubule bridges also bear a unique mechanical behavior, in which they resist collapse of the medullary cavity and absorb energy when it eventually does fail. Finally, viscoelastic modelling suggests that

the meso/macroscale features of the hoof wall play an important role in short-term relaxation to dissipate stress.

In the jackfruit, the exterior thorns provide an initial impact layer that steadily resists loading as it collapses. The conical shape of the thorn has a small surface area at the tip. This means when the thorn is first impacted the force can easily initiate collapse of the structure. However, as the thorn is compressed the surface increases, as does the thorn's resistance to collapse. The thorns have the added benefit of spreading the impact laterally to each of the thorns that comes in contact with the impactor while their irregular hexagonal bases trap cracks and cause meandering fracture paths.

This dissertation shows that the designs used by nature to improve the impact resistance of biological materials can successfully be transferred to engineered designs. Using additive manufacturing several of these impact resistant strategies were tested: hoof-inspired samples showed that gradients in reinforcement can reduce damage and control crack propagation while jackfruit-inspired specimens distributed load across the surface of the sample during impact rather than allowing projectiles to penetrate or induce through-thickness splitting. However, many impact resistant features observed in these biological materials could not be captured via 3D printing, particularly those reliant on hierarchical structure. As processing techniques continue to improve, so too does our ability to capture the ingenious designs found in nature. Hopefully, this work will lay the foundation for future researchers looking to enhance the properties of engineered materials by learning from nature.

References

[1]   Wegst UGK, Bai H, Saiz E, Tomsia AP, Ritchie RO. Bioinspired structural materials. Nat Mater 2015;14:23–36. https://doi.org/10.1038/nmat4089.

[2]   Wegst UGK, Ashby MF. The mechanical efficiency of natural materials. Philos Mag 2004;84:2167–86. https://doi.org/10.1080/14786430410001680935.

[3]   Gosline JM, DeMont ME, Denny MW. The structure and properties of spider silk. Endeavour 1986;10:37–43. https://doi.org/https://doi.org/10.1016/0160-9327(86)90049-9.

[4]   Agnarsson I, Kuntner M, Blackledge TA. Bioprospecting Finds the Toughest Biological Material: Extraordinary Silk from a Giant Riverine Orb Spider. PLoS One 2010;5:e11234.

[5]   Meyers MAA, McKittrick J, Chen P-Y. Structural Biological Materials: Critical Mechanics-Materials Connections. Science (80-) 2013;339:773–9. https://doi.org/10.1126/science.1220854.

[6]   Estrada S, Munera J, Hernandez J, Arroyave M, Arola D, Ossa A. Bioinspired hierarchical impact tolerant materials. Bioinspir Biomim 2020;15:046009.

[7]   Kuhn-Spearing LT, Kessler H, Chateau E, Ballarini R, Heuer AH, Spearing SM. Fracture mechanisms of the Strombus gigas conch shell: Implications for the design of brittle laminates. J Mater Sci 1996;31:6583–94. https://doi.org/10.1007/BF00356266.

[8]   Li H, Xu Z, Li X. Multiscale hierarchical assembly strategy and mechanical prowess in conch shells (Busycon carica). J Struct Biol 2013;184:409–16. https://doi.org/10.1016/j.jsb.2013.10.011.

[9]   Kamat S, Kessler H, Ballarini R, Nassirou M, Heuer AH. Fracture mechanisms of the Strombus gigas conch shell: II-micromechanics analyses of multiple cracking and large-scale crack bridging. Acta Mater 2004;52:2395–406. https://doi.org/10.1016/j.actamat.2004.01.030.

[10]   Marshall LSJ. Survival of juvenile queen conch, Strombus gigas, in natural habitats: Impact of prey, predator and habitat features. The College of William and Mary, 1992.

[11]   Li H, Shen J, Wei Q, Li X. Dynamic self-strengthening of a bio-nanostructured armor — conch shell. Mater Sci Eng C 2019;103:109820. https://doi.org/10.1016/j.msec.2019.109820.

[12]   Matsushita AK, Gonzalez D, Wang M, Doan J, Qiao Y, Mckittrick J. Beyond density: Mesostructural features of impact resistant wood. Mater Today Commun 2020;22:100697. https://doi.org/10.1016/j.mtcomm.2019.100697.

[13]   Jackson AP, Vincent JF V, Turner RM, Alexander RM. The mechanical design of nacre. Proc R Soc London Ser B Biol Sci 1988;234:415–40. https://doi.org/10.1098/rspb.1988.0056.

[14]   Sun J, Bhushan B. Hierarchical structure and mechanical properties of nacre: A review. RSC Adv 2012;2:7617–32. https://doi.org/10.1039/c2ra20218b.

[15]   Lin A, Meyers MA. Growth and structure in abalone shell. Mater Sci Eng A 2005;390:27–41. https://doi.org/https://doi.org/10.1016/j.msea.2004.06.072.

[16]   Lopez MI, Meza Martinez PE, Meyers MA. Organic interlamellar layers, mesolayers and mineral nanobridges: Contribution to strength in abalone (Haliotis rufescence) nacre. Acta Biomater 2014;10:2056–64. https://doi.org/https://doi.org/10.1016/j.actbio.2013.12.016.

[17]   Meyers MA, Lim CT, Li A, Hairul Nizam BR, Tan EPS, Seki Y, et al. The role of organic intertile layer in abalone nacre. Mater Sci Eng C 2009;29:2398–410.

https://doi.org/https://doi.org/10.1016/j.msec.2009.07.005.

[18]   Lin AY-M, Meyers MA. Interfacial shear strength in abalone nacre. J Mech Behav Biomed Mater 2009;2:607–12. https://doi.org/https://doi.org/10.1016/j.jmbbm.2009.04.003.

[19]   Lin AY-M, Chen P-Y, Meyers MA. The growth of nacre in the abalone shell. Acta Biomater 2008;4:131–8. https://doi.org/https://doi.org/10.1016/j.actbio.2007.05.005.

[20]   Song F, Bai YL. Effects of nanostructures on the fracture strength of the interfaces in nacre. J Mater Res 2003;18:1741–4. https://doi.org/DOI: 10.1557/JMR.2003.0239.

[21]   Song F, Zhang XH, Bai YL. Microstructure and Characteristics in the Organic Matrix Layers of Nacre. J Mater Res 2002;17:1567–70. https://doi.org/DOI: 10.1557/JMR.2002.0233.

[22]   Grossman M, Bouville F, Masania K, Studart AR. Quantifying the role of mineral bridges on the fracture resistance of nacre-like composites. Proc Natl Acad Sci 2018;115:12698 LP – 12703. https://doi.org/10.1073/pnas.1805094115.

[23]   Fan S, Yilong B. Mineral bridges of nacre and its effects. Acta Mech Sin 2001;17:251. https://doi.org/10.1007/BF02486881.

[24]   Checa AG, Cartwright JHE, Willinger M-G. Mineral bridges in nacre. J Struct Biol 2011;176:330–9. https://doi.org/https://doi.org/10.1016/j.jsb.2011.09.011.

[25]   Liu S, Xu S, Song J, Zhou J, Xu L, Li X, et al. Mechanical properties and failure deformation mechanisms of yak horn under quasi-static compression and dynamic impact. J Mech Behav Biomed Mater 2020:103753. https://doi.org/10.1016/j.jmbbm.2020.103753.

[26]   Li BW, Zhao HP, Feng XQ, Guo WW, Shan SC. Experimental study on the mechanical properties of the horn sheaths from cattle. J Exp Biol 2010;213:479–86. https://doi.org/10.1242/jeb.035428.

[27]   Magwene PM, Socha JJ. Biomechanics of Turtle Shells: How Whole Shells Fail in Compression. J Exp Zool Part A Ecol Genet Physiol 2013;319:86–98. https://doi.org/https://doi.org/10.1002/jez.1773.

[28]   Liu ZQ, Jiao D, Weng ZY, Zhang ZF. Structure and mechanical behaviors of protective armored pangolin scales and effects of hydration and orientation. J Mech Behav Biomed Mater 2016;56:165–74. https://doi.org/10.1016/j.jmbbm.2015.11.013.

[29]   Wang B, Yang W, Sherman VR, Meyers MA. Pangolin armor: Overlapping, structure, and mechanical properties of the keratinous scales. Acta Biomater 2016;41:60–74. https://doi.org/10.1016/j.actbio.2016.05.028.

[30]   Velasco-Hogan A, Xu J, Meyers MA. Additive Manufacturing as a Method to Design and Optimize Bioinspired Structures. Adv Mater 2018. https://doi.org/10.1002/adma.201800940.

[31]   Iyer AS, Paul K. Self-assembly: a review of scope and applications. IET Nanobiotechnology 2015;9:122–35. https://doi.org/10.1049/iet-nbt.2014.0020.

[32]   Levin A, Hakala TA, Schnaider L, Bernardes GJL, Gazit E, Knowles TPJ. Biomimetic peptide self-assembly for functional materials. Nat Rev Chem 2020;4:615–34. https://doi.org/10.1038/s41570-020-0215-y.

[33]   Li L, Sun R, Zheng R. Tunable morphology and functionality of multicomponent self-assembly: A review. Mater Des 2021;197:109209. https://doi.org/https://doi.org/10.1016/j.matdes.2020.109209.

[34] Xu Y. Hierarchical Materials. Mod Inorg Synth Chem Second Ed 2017:545–74. https://doi.org/10.1016/B978-0-444-63591-4.00019-7.

[35] Jia Z, Yu Y, Hou S, Wang L. Biomimetic architected materials with improved dynamic performance. J Mech Phys Solids 2018;125:178–97. https://doi.org/10.1016/j.jmps.2018.12.015.

[36] Bührig-Polaczek A, Fleck C, Speck T, Schüler P, Fischer SF, Caliaro M, et al. Biomimetic cellular metals-using hierarchical structuring for energy absorption. Bioinspir Biomim 2016;11:45002. https://doi.org/10.1088/1748-3190/11/4/045002.

[37] Thielen M, Schmitt CNZ, Eckert S, Speck T, Seidel R. Structure–function relationship of the foam-like pomelo peel (Citrus maxima)—an inspiration for the development of biomimetic damping materials with high energy dissipation. Bioinspir Biomim 2013;8:25001. https://doi.org/10.1088/1748-3182/8/2/025001.

[38] Zhang W, Yin S, Yu TX, Xu J. Crushing resistance and energy absorption of pomelo peel inspired hierarchical honeycomb. Int J Impact Eng 2019;125:163–72. https://doi.org/https://doi.org/10.1016/j.ijimpeng.2018.11.014.

[39] Li T-T, Wang H, Huang S-Y, Lou C-W, Lin J-H. Bioinspired foam composites resembling pomelo peel: Structural design and compressive, bursting and cushioning properties. Compos Part B Eng 2019;172:290–8. https://doi.org/https://doi.org/10.1016/j.compositesb.2019.04.046.

[40] Fischer SF, Thielen M, Loprang RR, Seidel R, Fleck C, Speck T, et al. Pummelos as Concept Generators for Biomimetically Inspired Low Weight Structures with Excellent Damping Properties. Adv Eng Mater 2010;12:B658–63. https://doi.org/https://doi.org/10.1002/adem.201080065.

[41] Zhang ZQ, Yang JL. Biomechanical dynamics of cranial sutures during simulated impulsive loading. Appl Bionics Biomech 2015. https://doi.org/10.1155/2015/596843.

[42] Alexander SL, Rafaels K, Gunnarsson CA, Weerasooriya T. Structural analysis of the frontal and parietal bones of the human skull. J Mech Behav Biomed Mater 2019;90:689–701. https://doi.org/10.1016/j.jmbbm.2018.10.035.

[43] Yoganandan N, Pintar FA, Sances A, Walsh PR, Ewing CL, Thomas DJ, et al. Biomechanics of skull fracture. J Neurotrauma 1995;12:659–68. https://doi.org/10.1089/neu.1995.12.659.

[44] Brown AD, Rafaels KA, Weerasooriya T. Microstructural and Rate-Dependent Shear Response of Human Skull Bones. 2020.

[45] Yang W, Chen IH, Gludovatz B, Zimmermann EA, Ritchie RO, Meyers MA. Natural Flexible Dermal Armor. Adv Mater 2013;25:31–48. https://doi.org/10.1002/adma.201202713.

[46] Rhee H, Horstemeyer MF, Hwang Y, Lim H, El Kadiri H, Trim W. A study on the structure and mechanical behavior of the Terrapene carolina carapace: A pathway to design bio-inspired synthetic composites. Mater Sci Eng C 2009;29:2333–9. https://doi.org/10.1016/j.msec.2009.06.002.

[47] Zhang W, Wu C, Zhang C, Chen Z. Microstructure and mechanical property of turtle shell. Theor Appl Mech Lett 2012;2:014009. https://doi.org/10.1063/2.1201409.

[48] Ampaw E, Owoseni TA, Du F, Pinilla N, Obayemi J, Hu J, et al. Compressive deformation and failure of trabecular structures in a turtle shell. Acta Biomater 2019;97:535–43. https://doi.org/https://doi.org/10.1016/j.actbio.2019.07.023.

[49] Achrai B, Wagner HD. Micro-structure and mechanical properties of the turtle carapace as a biological composite shield. Acta Biomater 2013;9:5890–902. https://doi.org/10.1016/j.actbio.2012.12.023.

[50] Hao P, Du J. Mechanical properties of bio-mimetic energy-absorbing materials under impact loading. J Mater Sci 2018;53:3189–97. https://doi.org/10.1007/s10853-017-1798-7.

[51] Rivera J, Hosseini MS, Restrepo D, Murata S, Vasile D. Toughening mechanisms of the elytra of the diabolical ironclad beetle. Nature 2020;586. https://doi.org/10.1038/s41586-020-2813-8.

[52] Ahmadi E, Barikloo H, Kashfi M. Viscoelastic finite element analysis of the dynamic behavior of apple under impact loading with regard to its different layers. Comput Electron Agric 2016. https://doi.org/10.1016/j.compag.2015.11.017.

[53] Seidel R, Thielen M, Schmitt C, Bührig-Polaczek A, Fleck C, Speck T. Fruit walls and nut shells as an inspiration for the design of bio-inspired impact-resistant hierarchically structured materials. Int J Des Nat Ecodynamics 2013;8:172–9. https://doi.org/10.2495/DNE-V8-N2-172-179.

[54] Schüler P, Speck T, Bührig-Polaczek A, Fleck C. Structure-Function Relationships in Macadamia integrifolia Seed Coats – Fundamentals of the Hierarchical Microstructure. PLoS One 2014;9:1–14. https://doi.org/10.1371/journal.pone.0102913.

[55] Gludovatz B, Walsh F, Zimmermann EA, Naleway SE, Ritchie RO, Kruzic JJ. Multiscale structure and damage tolerance of coconut shells. J Mech Behav Biomed Mater 2017;76:76–84. https://doi.org/10.1016/j.jmbbm.2017.05.024.

[56] Flores-Johnson EA, Carrillo JG, Zhai C, Gamboa RA, Gan Y, Shen L. Microstructure and mechanical properties of hard Acrocomia mexicana fruit shell. Sci Rep 2018;8:9668. https://doi.org/10.1038/s41598-018-27282-8.

[57] Van Der Wal C, Ahyong ST, Ho SYW, Lo N. The evolutionary history of Stomatopoda (Crustacea: Malacostraca) inferred from molecular data. PeerJ 2017;5:e3844. https://doi.org/10.7717/peerj.3844.

[58] Patek SN, Korff WL, Caldwell RL. Deadly strike mechanism of a mantis shrimp. Nature 2004;428:819–20. https://doi.org/10.1038/428819a.

[59] Huang W, Shishehbor M, Guarín-Zapata N, Kirchhofer ND, Li J, Cruz L, et al. A natural impact-resistant bicontinuous composite nanoparticle coating. Nat Mater 2020;19:1236–43. https://doi.org/10.1038/s41563-020-0768-7.

[60] Weaver JC, Milliron GW, Miserez A, Evans-Lutterodt K, Herrera S, Gallana I, et al. The stomatopod dactyl club: A formidable damage-tolerant biological hammer. Science (80-) 2012;336:1275–80. https://doi.org/10.1126/science.1218764.

[61] Grunenfelder LK, Suksangpanya N, Salinas C, Milliron G, Yaraghi N, Herrera S, et al. Bio-inspired impact-resistant composites. Acta Biomater 2014;10:3997–4008. https://doi.org/10.1016/j.actbio.2014.03.022.

[62] Suksangpanya N, Yaraghi NA, Kisailus D, Zavattieri P. Twisting cracks in Bouligand structures. J Mech Behav Biomed Mater 2017;76:38–57. https://doi.org/https://doi.org/10.1016/j.jmbbm.2017.06.010.

[63] Suksangpanya N, Yaraghi NA, Pipes RB, Kisailus D, Zavattieri P. Crack twisting and toughening strategies in Bouligand architectures. Int J Solids Struct 2018;150:83–106. https://doi.org/10.1016/j.ijsolstr.2018.06.004.

[64]   Ginzburg D, Pinto F, Iervolino O, Meo M. Damage tolerance of bio-inspired helicoidal composites under low velocity impact. Compos Struct 2017;161:187–203. https://doi.org/10.1016/j.compstruct.2016.10.097.

[65]   Amini S, Tadayon M, Loke JJ, Kumar A, Kanagavel D, Le Ferrand H, et al. A diecast mineralization process forms the tough mantis shrimp dactyl club. Proc Natl Acad Sci 2019;116:8685 LP – 8692. https://doi.org/10.1073/pnas.1816835116.

[66]   Grunenfelder LK, Milliron G, Herrera S, Gallana I, Yaraghi N, Hughes N, et al. Ecologically Driven Ultrastructural and Hydrodynamic Designs in Stomatopod Cuticles. Adv Mater 2018;30:1705295. https://doi.org/https://doi.org/10.1002/adma.201705295.

[67]   Yaraghi NA, Guarín-Zapata N, Grunenfelder LK, Hintsala E, Bhowmick S, Hiller JM, et al. A Sinusoidally Architected Helicoidal Biocomposite. Adv Mater 2016;28:6835–44. https://doi.org/https://doi.org/10.1002/adma.201600786.

[68]   Amini S, Tadayon M, Idapalapati S, Miserez A. The role of quasi-plasticity in the extreme contact damage tolerance of the stomatopod dactyl club. Nat Mater 2015;14:943–50. https://doi.org/10.1038/nmat4309.

[69]   Chon MJ, Daly M, Wang B, Xiao X, Zaheri A, Meyers MA, et al. Journal of the Mechanical Behavior of Biomedical Materials Lamellae spatial distribution modulates fracture behavior and toughness of african pangolin scales. J Mech Behav Biomed Mater 2017;76:30–7. https://doi.org/10.1016/j.jmbbm.2017.06.009.

[70]   Sherman VR, Quan H, Yang W, Ritchie RO, Meyers MA. A comparative study of piscine defense: The scales of Arapaima gigas, Latimeria chalumnae and Atractosteus spatula. J Mech Behav Biomed Mater 2017;73:1–16. https://doi.org/10.1016/j.jmbbm.2016.10.001.

[71]   Sun BH, Zhao J, Yang Z, Ren LQ, Zhu B. Design and Analysis of the Bio-Inspired Rear Under-Run Protection Devices for Heavy Truck. Appl Mech Mater 2014;461:499–505. https://doi.org/10.4028/www.scientific.net/AMM.461.499.

[72]   Meyers MA, Lin YS, Olevsky EA, Chen P-Y. Battle in the Amazon: Arapaima versus Piranha. Adv Eng Mater 2012;14:B279–88. https://doi.org/https://doi.org/10.1002/adem.201180027.

[73]   Liu Z, Zhang Z, Ritchie RO. Interfacial toughening effect of suture structures. Acta Biomater 2020;102:75–82. https://doi.org/https://doi.org/10.1016/j.actbio.2019.11.034.

[74]   Chen IH, Yang W, Meyers MA. Leatherback sea turtle shell: A tough and flexible biological design. Acta Biomater 2015;28:2–12. https://doi.org/10.1016/j.actbio.2015.09.023.

[75]   Lazarus BS, Velasco-Hogan A, Gómez-del Río T, Meyers MA, Jasiuk I. A review of impact resistant biological and bioinspired materials and structures. J Mater Res Technol 2020;9:15705–38. https://doi.org/https://doi.org/10.1016/j.jmrt.2020.10.062.

[76]   Huang W, Zaheri A, Jung J, Espinosa HD, Mckittrick J. Hierarchical structure and compressive deformation mechanisms of bighorn sheep (Ovis canadensis) horn. Acta Biomater 2017;64:1–14. https://doi.org/10.1016/j.actbio.2017.09.043.

[77]   McElhaney JH. Dynamic response of bone and muscle tissue. J Appl Physiol 1966. https://doi.org/10.1152/jappl.1966.21.4.1231.

[78]   Huang W, Yaraghi NA, Yang W, Velazquez-Olivera A, Li Z, Ritchie RO, et al. A natural energy absorbent polymer composite: The equine hoof wall. Acta Biomater 2019;90:267–77. https://doi.org/10.1016/j.actbio.2019.04.003.

[79]   Kasapi MA, Gosline JM. Strain-rate-dependent mechanical properties of the equine hoof wall. J Exp Biol 1996;199:1133–46.

[80]   Bertram JE, Gosline JM. Fracture toughness design in horse hoof keratin. J Exp Biol 1986;125:29–47.

[81]   Kasapi MA, Gosline JM. Design complexity and fracture control in the equine hoof wall. J Exp Biol 1997;200:1639–59.

[82]   Kasapi MA, Gosline JM. Micromechanics of the equine hoof wall: Optimizing crack control and material stiffness through modulation of the properties of keratin. J Exp Biol 1999;202:337–91.

[83]   Lee S, Novitskaya EE, Reynante B, Vasquez J, Urbaniak R, Takahashi T, et al. Impact testing of structural biological materials. Mater Sci Eng C 2011;31:730–9. https://doi.org/10.1016/j.msec.2010.10.017.

[84]   Fessel G, Snedeker JG. Evidence against proteoglycan mediated collagen fibril load transmission and dynamic viscoelasticity in tendon. Matrix Biol 2009;28:503–10. https://doi.org/10.1016/j.matbio.2009.08.002.

[85]   Handl M, Držík M, Cerulli G, Povýšil C, Chlpík J, Varga F, et al. Reconstruction of the anterior cruciate ligament: Dynamic strain evaluation of the graft. Knee Surgery, Sport Traumatol Arthrosc 2007;15:233–41. https://doi.org/10.1007/s00167-006-0175-x.

[86]   Paulos LE, Patrick W. Impact biomechanics of lateral knee bracing The anterior cruciate ligament n.d.

[87]   Burgin L V., Aspden RM. Impact testing to determine the mechanical properties of articular cartilage in isolation and on bone. J Mater Sci Mater Med 2008;19:703–11. https://doi.org/10.1007/s10856-007-3187-2.

[88]   Kaleem B, Maier F, Drissi H, Pierce DM. Low-energy impact of human cartilage: predictors for microcracking the network of collagen. Osteoarthr Cartil 2017;25:544–53. https://doi.org/10.1016/j.joca.2016.11.009.

[89]   Zhai X, Gao J, Nie Y, Guo Z, Kedir N, Claus B, et al. Real-time visualization of dynamic fractures in porcine bones and the loading-rate effect on their fracture toughness. J Mech Phys Solids 2019;131:358–71. https://doi.org/10.1016/j.jmps.2019.07.010.

[90]   Launey ME, Chen P, Mckittrick J, Ritchie RO. Mechanistic aspects of the fracture toughness of elk antler bone. Acta Biomater 2010;6:1505–14. https://doi.org/10.1016/j.actbio.2009.11.026.

[91]   Harrigan JJ, Ahonsi B, Palamidi E, Reid SR. Experimental and numerical investigations on the use of polymer Hopkinson pressure bars Author for correspondence : 2014.

[92]   Chen W, Zhang B, Forrestal MJ. A Split Hopkinson Bar Technique for Low-impedance Materials n.d.:81–5.

[93]   Siviour CR, Jordan JL. High Strain Rate Mechanics of Polymers: A Review. J Dyn Behav Mater 2016;2:15–32. https://doi.org/10.1007/s40870-016-0052-8.

[94]   Wang L, Cui Y, Qin Q, Wang H, Wang J. Helical fiber pull-out in biological materials. Acta Mech Solida Sin 2016;29:245–56. https://doi.org/10.1016/S0894-9166(16)30159-8.

[95]   Huang NC, Liu XY. Debonding and fiber pull-out in reinforced composites. Theor Appl Fract Mech 1994;21:157–76. https://doi.org/10.1016/0167-8442(94)90031-0.

[96]   Parsons KJ, Spence AJ, Morgan R, Thompson JA, Wilson AM. High speed field kinematics of foot contact in elite galloping horses in training. Equine Vet J 2011;43:216–22. https://doi.org/10.1111/j.2042-3306.2010.00149.x.

[97]   Bertram JE, Gosline JM. Functional design of horse hoof keratin: the modulation of mechanical properties through hydration effects. J Exp Biol 1987;130:121–36.

[98]   Douglas JE, Mittal C, Thomason JJ, Jofriet JC. The modulus of elasticity of equine hoof wall: Implications for the mechanical function of the hoof. J Exp Biol 1996;199:1829–36.

[99]   Reilly JD, Cottrell DF, Martin RJ, Cuddeford D. Tubule density in equine hoof horn. Biomimetics 1996;4:23–35.

[100]   Huang W. Impact resistant and energy absorbent natural keratin materials: horns and hooves (PhD Thesis). University of California San Diego, 2018.

[101]   Seki Y, Kad B, Benson D, Meyers MA. The toucan beak: Structure and mechanical response. Mater Sci Eng C 2006;26:1412–20. https://doi.org/https://doi.org/10.1016/j.msec.2005.08.025.

[102]   Drake A, Haut TL, Stansloski M, Fox K, Wheatley BB, Donahue SW. Horn and horn core trabecular bone of bighorn sheep rams absorbs impact energy and reduces brain cavity accelerations during high impact ramming of the skull. Acta Biomater 2016;44:41–50. https://doi.org/10.1016/j.actbio.2016.08.019.

[103]   Tombolato L, Novitskaya EE, Chen P, Sheppard FA, McKittrick J. Microstructure , elastic properties and deformation mechanisms of horn keratin. Acta Biomater 2010;6:319–30. https://doi.org/10.1016/j.actbio.2009.06.033.

[104]   Trim MW, Horstemeyer MF, Rhee H, El H, Williams LN, Liao J, et al. The effects of water and microstructure on the mechanical properties of bighorn sheep (Ovis canadensis) horn keratin. Acta Biomater 2011;7:1228–40. https://doi.org/10.1016/j.actbio.2010.11.024.

[105]   Fratzl P, editor. Collagen: Structure and Mechanics. Springer; 2008.

[106]   Cowin S, Doty S. Tissue Mechanics. Springer; 2007.

[107]   Shen ZL, Dodge MR, Kahn H, Ballarini R, Eppell SJ. Stress-strain experiments on individual collagen fibrils. Biophys J 2008;95:3956–63. https://doi.org/10.1529/biophysj.107.124602.

[108]   Shen ZL, Kahn H, Ballarini R, Eppell SJ. Viscoelastic properties of isolated collagen fibrils. Biophys J 2011;100:3008–15. https://doi.org/10.1016/j.bpj.2011.04.052.

[109]   Silver FH, Freeman JW, Seehra GP. Collagen self-assembly and the development of tendon mechanical properties. J Biomech 2003;36:1529–53. https://doi.org/10.1016/S0021-9290(03)00135-0.

[110]   Deymier AC, An Y, Boyle JJ, Schwartz AG, Birman V, Genin GM, et al. Micro-mechanical properties of the tendon-to-bone attachment. Acta Biomater 2017;56:25–35. https://doi.org/10.1016/j.actbio.2017.01.037.

[111]   Mow V, Gu W, Chen F. Structure and function of articular cartilage and meniscus. In: Mow V, Huiskes R, editors. Basic Orthop. Biomech. mechano-biology. 3rd ed., Philadelphia: Lippincott Williams & Wilkins; 2005, p. 181–258.

[112]   Mow V, Proctor C, Kelly M. Biomechanics of articular cartilage. In: Nordin M, Frankel V, editors. Basic Biomech. Musculoskelet. Syst. 2nd ed., Philadelphia: Lea & Febiger; 1989, p. 31–57.

[113] Mohammadi H, Mequanint K, Herzog W. Computational aspects in mechanical modeling of the articular cartilage tissue. Proc Inst Mech Eng Part H J Eng Med 2013;227:402–20. https://doi.org/10.1177/0954411912470239.

[114] Olszta MJ, Cheng X, Jee SS, Kumar R, Kim YY, Kaufman MJ, et al. Bone structure and formation: A new perspective. Mater Sci Eng R Reports 2007;58:77–116. https://doi.org/10.1016/j.mser.2007.05.001.

[115] Nordin M, Frankel V. Basic Biomechanics of the Muscoskeletal System. 3rd ed. Lippincott Williams & Wilkins; 2001.

[116] Cowin S, editor. Bone Mechanics Handbook. 2nd ed. CRC Press; 2001.

[117] Novitskaya E, Chen P-Y, Hamed E, Jun L, Lubarda V, Jasiuk I, et al. Recent advances on the measurement and calculation of the elastic moduli of cortical and trabecular bone: A review. Theor Appl Mech 2011;38:209–97. https://doi.org/10.2298/tam1103209n.

[118] O'Connor DT, Elkhodary KI, Fouad Y, Greene MS, Sabet FA, Qian J, et al. Modeling orthotropic elasticity, localized plasticity and fracture in trabecular bone. Comput Mech 2016;58:423–39. https://doi.org/10.1007/s00466-016-1301-3.

[119] Johnson TPM, Socrate S, Boyce MC. A viscoelastic, viscoplastic model of cortical bone valid at low and high strain rates. Acta Biomater 2010;6:4073–80. https://doi.org/10.1016/j.actbio.2010.04.017.

[120] Solomon SE, Hendrickson JR, Hendrickson LP. The structure of the carapace and plastron of juvenile turtles, Chelonia mydas (the green turtle) and Caretta caretta (the loggerhead turtle). J Anat 1986;145:123–31.

[121] Wu Q, Yang C, Ohrndorf A, Christ HJ, Han J, Xiong J. Impact behaviors of human skull sandwich cellular bones: Theoretical models and simulation. J Mech Behav Biomed Mater 2020;104:103669. https://doi.org/10.1016/j.jmbbm.2020.103669.

[122] Wang LZ, Lu S, Liu XY, Niu XF, Wang C, Ni YK, et al. Biomechanism of impact resistance in the woodpecker's head and its application. Sci China Life Sci 2013;56:715–9. https://doi.org/10.1007/s11427-013-4523-z.

[123] Yoon SH, Park S. A mechanical analysis of woodpecker drumming and its application to shock-absorbing systems. Bioinspiration and Biomimetics 2011;6:016003. https://doi.org/10.1088/1748-3182/6/1/016003.

[124] Wang LZ, Zhang HQ, Fan YB. Comparative study of the mechanical properties, micro-structure, and composition of the cranial and beak bones of the great spotted woodpecker and the lark bird. Sci China Life Sci 2011;54:1036–41. https://doi.org/10.1007/s11427-011-4242-2.

[125] Wang L, Niu X, Ni Y, Xu P, Liu X, Lu S, et al. Effect of microstructure of spongy bone in different parts of woodpecker's skull on resistance to impact injury. J Nanomater 2013. https://doi.org/10.1155/2013/924564.

[126] Wu CW, Zhu ZD, Zhang W. How woodpecker avoids brain injury? J. Phys. Conf. Ser., 2015, p. 628 012007. https://doi.org/10.1088/1742-6596/628/1/012007.

[127] Lee N, Horstemeyer MF, Prabhu R, Liao J, Rhee H, Hammi Y, et al. The geometric effects of a woodpecker's hyoid apparatus for stress wave mitigation. Bioinspiration and Biomimetics 2016;11:066004. https://doi.org/10.1088/1748-3190/11/6/066004.

[128] Zhou P, Kong XQ, Wu CW, Chen Z. The novel mechanical property of tongue of a woodpecker. J Bionic Eng 2009;6:214–8. https://doi.org/10.1016/S1672-6529(08)60126-2.

[129] Bouligand Y. Twisted fibrous arrangements in biological materials and cholesteric mesophases. Tissue Cell 1971;4:189–217.

[130] Chai GB, Zhu S. A review of low-velocity impact on sandwich structures. Proc Inst Mech Eng Part L J Mater Des Appl 2011;225:207–30. https://doi.org/10.1177/1464420711409985.

[131] Abrate S. Localized impact on sandwich structures with laminated facings. Appl Mech Rev 1997;50:69–82. https://doi.org/10.1115/1.3101689.

[132] Dear JP, Lee H, Brown SA. Impact damage processes in composite sheet and sandwich honeycomb materials. Int J Impact Eng 2005;32:130–54. https://doi.org/10.1016/j.ijimpeng.2005.02.005.

[133] Schubel PM, Luo JJ, Daniel IM. Impact and post impact behavior of composite sandwich panels. Compos Part A Appl Sci Manuf 2007;38:1051–7. https://doi.org/10.1016/j.compositesa.2006.06.022.

[134] Raju KS, Smith BL, Tomblin JS, Liew KH, Guarddon JC. Impact damage resistance and tolerance of honeycomb core sandwich panels. J Compos Mater 2008;42:385–412. https://doi.org/10.1177/0021998307088596.

[135] Ha NS, Lu G, Xiang X. Energy absorption of a bio-inspired honeycomb sandwich panel. J Mater Sci 2019;54:6286–300. https://doi.org/10.1007/s10853-018-3163-x.

[136] Tsang HH, Raza S. Impact energy absorption of bio-inspired tubular sections with structural hierarchy. Compos Struct 2018;195:199–210. https://doi.org/10.1016/j.compstruct.2018.04.057.

[137] Clark J, Jenson S, Schultz J, Hoffman J, Takak S, Ali M, et al. Study of impact properties of a fluid-filled honeycomb structure. ASME Int Mech Eng Congr Expo Proc 2013;9:2–7. https://doi.org/10.1115/IMECE2013-62113.

[138] Caglayan C, Osken I, Ataalp A, Turkmen HS, Cebeci H. Impact response of shear thickening fluid filled polyurethane foam core sandwich composites. Compos Struct 2020;243:112171. https://doi.org/10.1016/j.compstruct.2020.112171.

[139] Fu K, Wang H, Chang L, Foley M, Friedrich K, Ye L. Low-velocity impact behaviour of a shear thickening fluid (STF) and STF-filled sandwich composite panels. Compos Sci Technol 2018;165:74–83. https://doi.org/10.1016/j.compscitech.2018.06.013.

[140] Warren J, Kota KR, Westberg SM, Lacy T, Kundu S, Toghiani H, et al. Hypervelocity impacts of shear thickening fluid imbibed metallic foam core sandwich panels. Am. Soc. Compos. - 30th Tech. Conf. ACS 2015., 2015.

[141] McKittrick J, Chen PY, Tombolato L, Novitskaya EE, Trim MW, Hirata GA, et al. Energy absorbent natural materials and bioinspired design strategies: A review. Mater Sci Eng C 2010;30:331–42. https://doi.org/10.1016/j.msec.2010.01.011.

[142] Gu GX, Takaffoli M, Buehler MJ. Hierarchically enhanced impact resistance of bioinspired composites. Adv Mater 2017;29:1–7. https://doi.org/10.1002/adma.201700060.

[143] Jia Z, Yu Y, Wang L. Learning from nature : Use material architecture to break the performance tradeoffs. Mater Des 2019;168:107650. https://doi.org/10.1016/j.matdes.2019.107650.

[144] Ghazlan A, Ngo TD, Tran P. Three-dimensional Voronoi model of a nacre-mimetic composite

structure under impulsive loading. Compos Struct 2016;153:278–96. https://doi.org/10.1016/j.compstruct.2016.06.020.

[145] Flores-Johnson EA, Shen L, Guiamatsia I, Nguyen GD. Numerical investigation of the impact behaviour of bioinspired nacre-like aluminium composite plates. Compos Sci Technol 2014;96:13–22. https://doi.org/10.1016/j.compscitech.2014.03.001.

[146] Tran P, Ngo TD, Mendis P. Bio-inspired composite structures subjected to underwater impulsive loading. Comput Mater Sci 2014;82:134–9. https://doi.org/10.1016/j.commatsci.2013.09.033.

[147] Ghazlan A, Ngo TD, Tran P. Influence of interfacial geometry on the energy absorption capacity and load sharing mechanisms of nacreous composite shells. Compos Struct 2015;132:299–309. https://doi.org/10.1016/j.compstruct.2015.05.045.

[148] Miranda P, Pajares A, Meyers MA. Bioinspired composite segmented armour : Numerical simulations. Integr Med Res 2018;8:1274–87. https://doi.org/10.1016/j.jmrt.2018.09.007.

[149] Apichattrabrut T, Ravi-Chandar K. Helicoidal composites. Mech Adv Mater Struct 2006;13:61–76. https://doi.org/10.1080/15376490500343808.

[150] Chen R, Liu J, Yang C, Weitz DA, He H, Li D, et al. Transparent impact-resistant composite films with bioinspired hierarchical structure. ACS Appl Mater Interfaces 2019;11:23616–22. https://doi.org/10.1021/acsami.9b06500.

[151] Liu Z, Meyers MA, Zhang Z, Ritchie RO. Progress in Materials Science Functional gradients and heterogeneities in biological materials : Design principles , functions , and bioinspired applications. Prog Mater Sci 2017;88:467–98. https://doi.org/10.1016/j.pmatsci.2017.04.013.

[152] Huang CY, Chen YL. Design and impact resistant analysis of functionally graded Al2O3-ZrO2 ceramic composite. Mater Des 2016;91:294–305. https://doi.org/10.1016/j.matdes.2015.11.091.

[153] Graupner N, Labonte D, Humburg H, Buzkan T, Dörgens A, Kelterer W, et al. Functional gradients in the pericarp of the green coconut inspire asymmetric fibre-composites with improved impact strength, and preserved flexural and tensile properties. Bioinspiration and Biomimetics 2017;12:026009. https://doi.org/10.1088/1748-3190/aa5262.

[154] Mirzaali MJ, Herranz A, Nava D, Gunashekar D. Fracture behavior of bio-inspired functionally graded soft – hard composites made by multi-material 3D printing : The case of colinear cracks. Materials (Basel) 2019;12.

[155] Ha NS, Lu G. A review of recent research on bio-inspired structures and materials for energy absorption applications. Compos Part B Eng 2020;181:107496. https://doi.org/10.1016/j.compositesb.2019.107496.

[156] Zou M, Xu S, Wei C, Wang H, Liu Z. A bionic method for the crashworthiness design of thin-walled structures inspired by bamboo. Thin-Walled Struct 2016;101:222–30. https://doi.org/10.1016/j.tws.2015.12.023.

[157] Chen BC, Zou M, Liu GM, Song JF, Wang HX. Experimental study on energy absorption of bionic tubes inspired by bamboo structures under axial crushing. Int J Impact Eng 2018;115:48–57. https://doi.org/10.1016/j.ijimpeng.2018.01.005.

[158] Song JF, Xu SC, Wang HX, Wu XQ, Zou M. Bionic design and multi-objective optimization for variable wall thickness tube inspired bamboo structures. Thin-Walled Struct 2018;125:76–88. https://doi.org/10.1016/j.tws.2018.01.010.

[159] Hu D, Wang Y, Song B, Dang L, Zhang Z. Energy-absorption characteristics of a bionic honeycomb tubular nested structure inspired by bamboo under axial crushing. Compos Part B Eng 2019;162:21–32. https://doi.org/10.1016/j.compositesb.2018.10.095.

[160] Fu J, Liu Q, Liufu K, Deng Y, Fang J, Li Q. Design of bionic-bamboo thin-walled structures for energy absorption. Thin-Walled Struct 2019;135:400–13. https://doi.org/10.1016/j.tws.2018.10.003.

[161] Sun Z, Lee E, Herring SW. Cranial sutures and bones: Growth and fusion in relation to masticatory strain. Anat Rec 2004;276A:150–61. https://doi.org/10.1002/ar.a.20002.

[162] Jaslow CR. Mechanical properties of cranial sutures. J Biomech 1990. https://doi.org/10.1016/0021-9290(90)90059-C.

[163] Lee N, Horstemeyer MF, Rhee H, Nabors B, Liao J, Williams LN. Hierarchical multiscale structure–property relationships of the red-bellied woodpecker Beak. J R Soc Interface 2014;11:20140274.

[164] Achrai B, Daniel Wagner H. The red-eared slider turtle carapace under fatigue loading: The effect of rib-suture arrangement. Mater Sci Eng C 2015;53:128–33. https://doi.org/10.1016/j.msec.2015.04.040.

[165] Yang W, Naleway SE, Porter MM, Meyers MA, McKittrick J. The armored carapace of the boxfish. Acta Biomater 2015;23:1–10. https://doi.org/10.1016/j.actbio.2015.05.024.

[166] Lee N, Williams LN, Mun S, Rhee H, Prabhu R, Bhattarai KR, et al. Stress wave mitigation at suture interfaces. Biomed Phys Eng Express 2017. https://doi.org/10.1088/2057-1976/aa777e.

[167] Maloul A, Fialkov J, Wagner D, Whyne CM. Characterization of craniofacial sutures using the finite element method. J Biomech 2014. https://doi.org/10.1016/j.jbiomech.2013.09.009.

[168] Wang B, Yang W, McKittrick J, Meyers MA. Keratin: Structure, mechanical properties, occurrence in biological organisms, and efforts at bioinspiration. Prog Mater Sci 2016;76:229–318.

[169] Song B, Lu WY, Syn CJ, Chen W. The effects of strain rate, density, and temperature on the mechanical properties of polymethylene diisocyanate (PMDI)-based rigid polyurethane foams during compression. J Mater Sci 2009;44:351–7. https://doi.org/10.1007/s10853-008-3105-0.

[170] Kulin RM, Chen PY, Jiang F, Vecchio KS. A study of the dynamic compressive behavior of Elk antler. Mater Sci Eng C 2011;31:1030–41. https://doi.org/10.1016/j.msec.2011.03.002.

[171] Neumann M, Herter J, Droste BO, Hartwig S. Compressive behaviour of axially loaded spruce wood under large deformations at different strain rates. Eur J Wood Wood Prod 2011;69:345–57. https://doi.org/10.1007/s00107-010-0442-x.

[172] Brodt M, Lakes RS. Composite materials which exhibit high stiffness and high viscoelastic damping. J Compos Mater 1995. https://doi.org/10.1177/002199839502901402.

[173] Zhu ZD, Ma GJ, Wu CW, Chen Z. Numerical study of the impact response of woodpecker's head. AIP Adv 2012. https://doi.org/10.1063/1.4770305.

[174] Edelsten L, Jeffrey JE, Burgin L V., Aspden RM. Viscoelastic deformation of articular cartilage during impact loading. Soft Matter 2010. https://doi.org/10.1039/c0sm00097c.

[175] Thielen M, Speck T, Seidel R. Viscoelasticity and compaction behaviour of the foam-like pomelo (Citrus maxima) peel. J Mater Sci 2013. https://doi.org/10.1007/s10853-013-7137-8.

[176] Ranganathan N, Oksman K, Nayak S, Sain M. Impact toughness, viscoelastic behavior, and morphology of polypropylene-jute-viscose hybrid composites. J Appl Polym Sci 2015;133:n/a-n/a. https://doi.org/10.1002/app.42981.

[177] Mahmud A. The impact of armor on the design, utilization and survivability of ground vehicles: The history of armor development and use. Naval Postgraduate School, 2003.

[178] David N V., Gao XL, Zheng JQ. Ballistic resistant body armor: Contemporary and prospective materials and related protection mechanisms. Appl Mech Rev 2009;62:1–20. https://doi.org/10.1115/1.3124644.

[179] Abtew MA, Boussu F, Bruniaux P, Loghin C, Cristian I. Ballistic impact mechanisms – A review on textiles and fibre-reinforced composites impact responses. Compos Struct 2019;223:110966. https://doi.org/10.1016/j.compstruct.2019.110966.

[180] Qin J, Guo B, Zhang L, Wang T, Zhang G, Shi X. Soft armor materials constructed with Kevlar fabric and a novel shear thickening fluid. Compos Part B Eng 2020;183:107686. https://doi.org/10.1016/j.compositesb.2019.107686.

[181] Laha A, Majumdar A. Interactive effects of p-aramid fabric structure and shear thickening fluid on impact resistance performance of soft armor materials. Mater Des 2016;89:286–93. https://doi.org/10.1016/j.matdes.2015.09.077.

[182] Ding J, Tracey P, Li W, Peng G, Whitten PG, Wallace GG. Review on shear thickening fluids and applications. Text Light Ind Sci Technol 2013;2:161–73.

[183] Grogan J, Tekalur SA, Shukla A, Bogdanovich A, Coffelt RA. Ballistic resistance of 2D and 3D woven sandwich composites. J Sandw Struct Mater 2007;9:283–302. https://doi.org/10.1177/1099636207067133.

[184] Ghassemieh E. Materials in automotive application, state of the art and prospects. New Trends Dev Automot Ind 2011. https://doi.org/10.5772/13286.

[185] Hyer MW. Stress analysis of fiber-reinforced composite materials. WCB/McGraw-Hill; 1998.

[186] Sun L, Gibson RF, Gordaninejad F, Suhr J. Energy absorption capability of nanocomposites: A review. Compos Sci Technol 2009;69:2392–409. https://doi.org/10.1016/j.compscitech.2009.06.020.

[187] Fu S, Sun Z, Huang P, Li Y, Hu N. Some basic aspects of polymer nanocomposites: A critical review. Nano Mater Sci 2019;1:2–30. https://doi.org/10.1016/j.nanoms.2019.02.006.

[188] Dasari A, Yu ZZ, Yang M, Zhang QX, Xie XL, Mai YW. Micro- and nano-scale deformation behavior of nylon 66-based binary and ternary nanocomposites. Compos Sci Technol 2006;66:3097–114. https://doi.org/10.1016/j.compscitech.2005.03.020.

[189] Mourad AHI, Zaaroura N. Impact of nanofillers incorporation on laminated nanocomposites performance. J Mater Eng Perform 2018;27:4453–61. https://doi.org/10.1007/s11665-018-3523-3.

[190] Mourad AHI, Idrisi AH, Zaaroura N, Sherif MM, Fouad H. Damage assessment of nanofiller-reinforced woven kevlar KM2plus/Epoxy resin laminated composites. Polym Test 2020;86:106501. https://doi.org/10.1016/j.polymertesting.2020.106501.

[191] Bisht A, Dasgupta K, Lahiri D. Investigating the role of 3D network of carbon nanofillers in improving the mechanical properties of carbon fiber epoxy laminated composite. Compos Part A Appl Sci Manuf 2019;126:105601. https://doi.org/10.1016/j.compositesa.2019.105601.

[192] Gagg CR. Cement and concrete as an engineering material: An historic appraisal and case study analysis. Eng Fail Anal 2014;40:114–40. https://doi.org/10.1016/j.engfailanal.2014.02.004.

[193] Hao H, Hao Y, Li J, Chen W. Review of the current practices in blast-resistant analysis and design of concrete structures. Adv Struct Eng 2016;19:1193–223. https://doi.org/10.1177/1369433216656430.

[194] Li LJ, Tu GR, Lan C, Liu F. Mechanical characterization of waste-rubber-modified recycled-aggregate concrete. J Clean Prod 2016;124:325–38. https://doi.org/10.1016/j.jclepro.2016.03.003.

[195] Stevenson P, editor. Foam engineering: Fundamentals and applications. Wiley Online Books; 2012. https://doi.org/doi:10.1002/9781119954620.fmatter.

[196] Exerowa D, Kruglyakov PMBT-S in IS, editors. Foam and foam films: Theory, experiment, application. vol. 5. Elsevier; 1998. https://doi.org/https://doi.org/10.1016/S1383-7303(13)60003-4.

[197] Xu F, Zhang X, Zhang H. A review on functionally graded structures and materials for energy absorption. Eng Struct 2018;171:309–25. https://doi.org/10.1016/j.engstruct.2018.05.094.

[198] Toudehdehghan A, Lim JW, Foo KE, Ma'Arof MIN, Mathews J. A brief review of functionally graded materials. MATEC Web Conf 2017;131:1–6. https://doi.org/10.1051/matecconf/201713103010.

[199] Sarathchandra DT, Kanmani Subbu S, Venkaiah N. Functionally graded materials and processing techniques: An art of review. Mater Today Proc 2018;5:21328–34. https://doi.org/10.1016/j.matpr.2018.06.536.

[200] Bohidar SK, Sharma R, Mishra PR. Functionally graded materials: A critical review. Int J Res 2014;1:289–301.

[201] Singh R, Bhavar V, Kattire P, Thakare S, Patil S, Singh RKP. A review on functionally gradient materials (FGMs) and their applications. IOP Conf Ser Mater Sci Eng 2017;229. https://doi.org/10.1088/1757-899X/229/1/012021.

[202] Zhang C, Chen F, Huang Z, Jia M, Chen G, Ye Y, et al. Additive manufacturing of functionally graded materials: A review. Mater Sci Eng A 2019;764:138209. https://doi.org/10.1016/j.msea.2019.138209.

[203] Choy SY, Sun CN, Leong KF, Wei J. Compressive properties of functionally graded lattice structures manufactured by selective laser melting. Mater Des 2017;131:112–20. https://doi.org/10.1016/j.matdes.2017.06.006.

[204] Wang RZ, Wen HB, Cui FZ, Zhang HB, Li HD. Observations of damage morphologies in nacre during deformation and fracture. J Mater Sci 1995;30:2299–304. https://doi.org/10.1007/BF01184577.

[205] Meyers MA, Chen PY, Lin AYM, Seki Y. Biological materials: Structure and mechanical properties. Prog Mater Sci 2008;53:1–206. https://doi.org/10.1016/j.pmatsci.2007.05.002.

[206] Ward C. Materials genome initiative for global competitiveness. Washington, D.C.: 2011.

[207] Bragulla HH, Homberger DG. Structure and functions of keratin proteins in simple, stratified, keratinized and cornified epithelia. J Anat 2009;214:516–59. https://doi.org/https://doi.org/10.1111/j.1469-7580.2009.01066.x.

[208] Fraser RDB, MacRae TP, Suzuki E. Structure of the α-keratin microfibril. J Mol Biol 1976. https://doi.org/10.1016/S0022-2836(76)80129-5.

[209] Pace CN, Scholtz JM. A helix propensity scale based on experimental studies of peptides and proteins. Biophys J 1998;75:422–7. https://doi.org/10.1016/s0006-3495(98)77529-0.

[210] Rojas-Martínez LE, Flores-Hernandez CG, López-Marín LM, Martinez-Hernandez AL, Thorat SB, Reyes Vasquez CD, et al. 3D printing of PLA composites scaffolds reinforced with keratin and chitosan: Effect of geometry and structure. Eur Polym J 2020;141:110088. https://doi.org/https://doi.org/10.1016/j.eurpolymj.2020.110088.

[211] Singamneni S, Velu R, Behera MP, Scott S, Brorens P, Harland D, et al. Selective laser sintering responses of keratin-based bio-polymer composites. Mater Des 2019;183:108087. https://doi.org/https://doi.org/10.1016/j.matdes.2019.108087.

[212] Burkhard P, Stetefeld J, Strelkov S V. Coiled coils: a highly versatile protein folding motif. Trends Cell Biol 2001;11:82–8. https://doi.org/10.1016/s0962-8924(00)01898-5.

[213] Crick FHC. Is α-keratin a coiled coil? Nature 1952;170:882–3. https://doi.org/10.1038/170882b0.

[214] Chou CC, Buehler MJ. Structure and mechanical properties of human trichocyte keratin intermediate filament protein. Biomacromolecules 2012;13:3522–32. https://doi.org/10.1021/bm301254u.

[215] Bray DJ, Walsh TR, Noro MG, Notman R. Complete structure of an epithelial keratin dimer: Implications for intermediate filament assembly. PLoS One 2015;10:1–22. https://doi.org/10.1371/journal.pone.0132706.

[216] McKittrick J, Chen PY, Bodde SG, Yang W, Novitskaya EE, Meyers MA. The structure, functions, and mechanical properties of keratin. Jom 2012;64:449–68. https://doi.org/10.1007/s11837-012-0302-8.

[217] Toni M, Dalla Valle L, Alibardi L. Hard (beta-)keratins in the epidermis of reptiles: Composition, sequence, and molecular organization. J Proteome Res 2007;6:3377–92. https://doi.org/10.1021/pr0702619.

[218] Fraser RDB, Parry DAD. The structural basis of the filament-matrix texture in the avian/reptilian group of hard β-keratins. J Struct Biol 2011;173:391–405. https://doi.org/10.1016/j.jsb.2010.09.020.

[219] Li Y, Ortiz C, Boyce MC. Stiffness and strength of suture joints in nature. Phys Rev E Stat Nonlin Soft Matter Phys 2011;84:62904. https://doi.org/10.1103/PhysRevE.84.062904.

[220] Lin E, Li Y, Ortiz C, Boyce MC. 3D printed, bio-inspired prototypes and analytical models for structured suture interfaces with geometrically-tuned deformation and failure behavior. J Mech Phys Solids 2014;73:166–82. https://doi.org/https://doi.org/10.1016/j.jmps.2014.08.011.

[221] Lin E, Li Y, Weaver JC, Ortiz C, Boyce MC. Tunability and enhancement of mechanical behavior with additively manufactured bio-inspired hierarchical suture interfaces. J Mater Res 2014;29:1867–75. https://doi.org/DOI: 10.1557/jmr.2014.175.

[222] Li Y, Ortiz C, Boyce MC. Bioinspired, mechanical, deterministic fractal model for hierarchical suture joints. Phys Rev E Stat Nonlin Soft Matter Phys 2012;85:31901. https://doi.org/10.1103/PhysRevE.85.031901.

[223] Li Y, Ortiz C, Boyce MC. A generalized mechanical model for suture interfaces of arbitrary geometry. J Mech Phys Solids 2013;61:1144–67. https://doi.org/https://doi.org/10.1016/j.jmps.2012.10.004.

[224] Yu Y, Yang W, André Meyers M. Viscoelastic properties of α-keratin fibers in hair. Acta Biomater 2017;64:15–28. https://doi.org/10.1016/j.actbio.2017.09.012.

[225] Qin Z, Kreplak L, Buehler MJ. Hierarchical Structure Controls Nanomechanical Properties of Vimentin Intermediate Filaments. PLoS One 2009;4:e7294.

[226] Qin Z, Buehler MJ. Structure and dynamics of human vimentin intermediate filament dimer and tetramer in explicit and implicit solvent models. J Mol Model 2011;17:37–48. https://doi.org/10.1007/s00894-010-0696-6.

[227] Qin Z, Chou C-C, Kreplak L, Buehler MJ. Structural, Mechanical and Functional Properties of Intermediate Filaments from the Atomistic to the Cellular Scales BT - Advances in Cell Mechanics. In: Li S, Sun B, editors., Berlin, Heidelberg: Springer Berlin Heidelberg; 2011, p. 117–66. https://doi.org/10.1007/978-3-642-17590-9_4.

[228] Chou C-C, Lepore E, Antonaci P, Pugno N, Buehler MJ. Mechanics of trichocyte alpha-keratin fibers: Experiment, theory, and simulation. J Mater Res 2015;30:26–35. https://doi.org/DOI: 10.1557/jmr.2014.267.

[229] Fraser RDB, Parry DAD. Amino acid sequence homologies in the hard keratins of birds and reptiles, and their implications for molecular structure and physical properties. J Struct Biol 2014;188:213–24. https://doi.org/10.1016/j.jsb.2014.10.012.

[230] Greenberg DA, Fudge DS. Regulation of hard α-keratin mechanics via control of intermediate filament hydration: Matrix squeeze revisited. Proc R Soc B Biol Sci 2013;280:20122158. https://doi.org/10.1098/rspb.2012.2158.

[231] Smack D, Korge BP, James WD. Keratin and keratinization. J Am Acad Dermatol 1994;30:85–102. https://doi.org/10.1016/S0190-9622(94)70012-5.

[232] Parbhu AN, Bryson WG, Lal R. Disulfide bonds in the outer layer of keratin fibers confer higher mechanical rigidity: Correlative nano-indentation and elasticity measurement with an AFM. Biochemistry 1999;38:11755–61. https://doi.org/10.1021/bi990746d.

[233] Chapman B. A Mechanical Model for Wool and other Keratin Fibers. Text Res J 1969;39:1102–9. https://doi.org/10.1177/004051756903901204.

[234] Cao J. Is the α-β transition of keratin a transition of α-helices to β-pleated sheets. II. Synchrotron investigation for stretched single specimens. J Mol Struct 2002;607:69–75. https://doi.org/10.1016/S0022-2860(01)00901-2.

[235] Paquin R, Colomban P. Nanomechanics of single keratin fibres: A Raman study of the α-helix → β-sheet transition and the effect of water. J Raman Spectrosc 2007;38:504–14. https://doi.org/10.1002/jrs.1672.

[236] Kreplak L, Doucet J, Dumas P, Briki F. New aspects of the α-helix to β-sheet transition in stretched hard α-keratin fibers. Biophys J 2004;87:640–7. https://doi.org/10.1529/biophysj.103.036749.

[237] Bendit EG. The α–β Transformation in Keratin. Nature 1957;179:535. https://doi.org/10.1038/179535a0.

[238] Ciferri A. The αβ transformation in keratin. Trans Faraday Soc 1963;59:562–9. https://doi.org/10.1039/TF9635900562.

[239] Feughelman M. A Two-Phase Structure for Keratin Fibers. Text Res J 1959;29:223–8.

https://doi.org/10.1177/004051755902900305.

[240] Hearle JWS. The structural mechanics of fibers. J Polym Sci Part C Polym Symp 1967;20:215–51. https://doi.org/https://doi.org/10.1002/polc.5070200118.

[241] Feughelman M. Natural protein fibers. J Appl Polym Sci 2002;83:489–507. https://doi.org/https://doi.org/10.1002/app.2255.

[242] Taylor AM, Bonser RHC, Farrent JW. The influence of hydration on the tensile and compressive properties of avian keratinous tissues. J Mater Sci 2004;39:939–42. https://doi.org/10.1023/B:JMSC.0000012925.92504.08.

[243] Wang B, Sullivan TN, Pissarenko A, Zaheri A, Espinosa HD, Meyers MA. Lessons from the Ocean: Whale Baleen Fracture Resistance. Adv Mater 2019;31:1804574. https://doi.org/https://doi.org/10.1002/adma.201804574.

[244] Fudge DS, Gardner KH, Forsyth VT, Riekel C, Gosline JM. The mechanical properties of hydrated intermediate filaments: insights from hagfish slime threads. Biophys J 2003;85:2015–27. https://doi.org/10.1016/S0006-3495(03)74629-3.

[245] Collins SN, Cope BC, Hopegood L, Latham RJ, Linford RG, Reilly JD. Stiffness as a function of moisture content in natural materials: Characterisation of hoof horn samples. J Mater Sci 1998;33:5185–91. https://doi.org/10.1023/A:1004479803611.

[246] Johnson KL, Trim MW, Francis DK, Whittington WR, Miller JA, Bennett CE, et al. Moisture, anisotropy, stress state, and strain rate effects on bighorn sheep horn keratin mechanical properties. Acta Biomater 2017;48:300–8. https://doi.org/10.1016/j.actbio.2016.10.033.

[247] Winegard TM, Fudge DS. Deployment of hagfish slime thread skeins requires the transmission of mixing forces via mucin strands. J Exp Biol 2010;213:1235–340. https://doi.org/10.1242/jeb.038075.

[248] Wu KS, van Osdol WW, Dauskardt RH. Mechanical properties of human stratum corneum: Effects of temperature, hydration, and chemical treatment. Biomaterials 2006;27:785–95. https://doi.org/https://doi.org/10.1016/j.biomaterials.2005.06.019.

[249] Fraser RD, Macrae TP. Molecular structure and mechanical properties of keratins. Symp Soc Exp Biol 1980;34:211–46.

[250] Morton WE, Hearle JWS. Chapter 13 - Tensile properties. In: Morton WE, Hearle JWSBT-PP of TF (Fourth E, editors. Woodhead Publ. Ser. Text., Woodhead Publishing; 2008, p. 274–321. https://doi.org/https://doi.org/10.1533/9781845694425.274.

[251] Yang W, Chao C, McKittrick J. Axial compression of a hollow cylinder filled with foam: A study of porcupine quills. Acta Biomater 2013;9:5297–304. https://doi.org/10.1016/j.actbio.2012.09.004.

[252] Szewciw LJ, de Kerckhove DG, Grime GW, Fudge DS. Calcification provides mechanical reinforcement to whale baleen α-keratin. Proc R Soc B Biol Sci 2010;277:2597–605. https://doi.org/10.1098/rspb.2010.0399.

[253] Seki Y, Schneider MS, Meyers MA. Structure and mechanical behavior of a toucan beak. Acta Mater 2005;53:5281–96. https://doi.org/https://doi.org/10.1016/j.actamat.2005.04.048.

[254] Klein M-C, Deuschle J, Gorb S. Material properties of the skin of the Kenyan sand boa Gongylophis colubrinus (Squamata, Boidae) A Neuroethology, sensory, neural, and behavioral physiology. J Comp Physiol 2010;196:659–68. https://doi.org/10.1007/s00359-010-0556-y.

[255] Farran L, Ennos AR, Starkie M, Eichhorn SJ. Tensile and shear properties of fingernails as a function of a changing humidity environment. J Biomech 2009;42:1230–5. https://doi.org/https://doi.org/10.1016/j.jbiomech.2009.03.020.

[256] Yu Y, Yang W, Wang B, Meyers MA. Structure and mechanical behavior of human hair. Mater Sci Eng C 2017;73:152–63. https://doi.org/https://doi.org/10.1016/j.msec.2016.12.008.

[257] Prowse MS, Wilkinson M, Puthoff JB, Mayer G, Autumn K. Effects of humidity on the mechanical properties of gecko setae. Acta Biomater 2011;7:733–8. https://doi.org/https://doi.org/10.1016/j.actbio.2010.09.036.

[258] Wang B, Yang W, McKittrick J, Meyers MAAA. Keratin: Structure, mechanical properties, occurrence in biological organisms, and efforts at bioinspiration. Prog Mater Sci 2016;76:229–318. https://doi.org/10.1016/j.pmatsci.2015.06.001.

[259] Huang W, Zaheri A, Yang W, Kisailus D, Ritchie RO, Espinosa H, et al. How Water Can Affect Keratin: Hydration-Driven Recovery of Bighorn Sheep (Ovis Canadensis) Horns. Adv Funct Mater 2019;29:1901077. https://doi.org/10.1002/adfm.201901077.

[260] Liu ZQ, Jiao D, Zhang ZF. Remarkable shape memory effect of a natural biopolymer in aqueous environment. Biomaterials 2015;65:13–21. https://doi.org/https://doi.org/10.1016/j.biomaterials.2015.06.032.

[261] Sullivan TN, Zhang Y, Zavattieri PD, Meyers MA. Hydration-Induced Shape and Strength Recovery of the Feather. Adv Funct Mater 2018;28:1801250. https://doi.org/10.1002/adfm.201801250.

[262] Liu ZQ, Jiao D, Weng ZY, Zhang ZF. Water-assisted self-healing and property recovery in a natural dermal armor of pangolin scales. J Mech Behav Biomed Mater 2016;56:14–22. https://doi.org/10.1016/j.jmbbm.2015.10.031.

[263] Quan H, Kisailus D, Meyers MA. Hydration-induced reversible deformation of biological materials. Nat Rev Mater 2021;6:264–83. https://doi.org/10.1038/s41578-020-00251-2.

[264] Mao N, Russell SJ. The Thermal Insulation Properties of Spacer Fabrics with a Mechanically Integrated Wool Fiber Surface. Text Res J 2007;77:914–22. https://doi.org/10.1177/0040517507083524.

[265] Sullivan TN, Wang B, Espinosa HD, Meyers MA. Extreme lightweight structures: avian feathers and bones. Mater Today 2017;20:377–91. https://doi.org/10.1016/j.mattod.2017.02.004.

[266] Seki Y, Bodde SG, Meyers MA. Toucan and hornbill beaks: A comparative study. Acta Biomater 2010;6:331–43. https://doi.org/https://doi.org/10.1016/j.actbio.2009.08.026.

[267] Gao J, Yu W, Pan N. Structures and Properties of the Goose Down as a Material for Thermal Insulation. Text Res J 2007;77:617–26. https://doi.org/10.1177/0040517507079408.

[268] Cui Y, Gong H, Wang Y, Li D, Bai H. A Thermally Insulating Textile Inspired by Polar Bear Hair. Adv Mater 2018;30:1706807. https://doi.org/https://doi.org/10.1002/adma.201706807.

[269] Autumn K, Sitti M, Liang YA, Peattie AM, Hansen WR, Sponberg S, et al. Evidence for van der Waals adhesion in gecko setae. Proc Natl Acad Sci 2002;99:12252–6. https://doi.org/10.1073/pnas.192252799.

[270] Watson GS, Schwarzkopf L, Cribb BW, Myhra S, Gellender M, Watson JA. Removal mechanisms of dew via self-propulsion off the gecko skin. J R Soc Interface 2015;12:20141396.

https://doi.org/10.1098/rsif.2014.1396.

[271] Liu Y, Chen X, Xin JH. Hydrophobic duck feathers and their simulation on textile substrates for water repellent treatment. Bioinspir Biomim 2008;3:46007. https://doi.org/10.1088/1748-3182/3/4/046007.

[272] Zhang D, Arola DD, Reprogel RK, Zheng W, Tasch U, Dyer RM. A method for characterizing the mechanical behaviour of hoof horn. J Mater Sci 2007;42:1108–15. https://doi.org/10.1007/s10853-006-0614-6.

[273] Lanovaz JL, Clayton HM, Watson LG. In vitro attenuation of impact shock in equine digits. Equine Vet J Suppl 1998:96–102. https://doi.org/10.1111/j.2042-3306.1998.tb05127.x.

[274] Setterbo JJ, Garcia TC, Campbell IP, Reese JL, Morgan JM, Kim SY, et al. Hoof accelerations and ground reaction forces of Thoroughbred racehorses measured on dirt, synthetic, and turf track surfaces. Am J Vet Res 2009;70:1220–9. https://doi.org/10.2460/ajvr.70.10.1220.

[275] Rice C, Tan KT. Horse hoof inspired biomimetic structure for improved damage tolerance and crack diversion. Compos Struct 2019;220:362–70. https://doi.org/10.1016/j.compstruct.2019.04.009.

[276] Wang B, Zhou B, Zhang X. A high toughness and light weight armor structure bioinspired design based on a bovine hoof wall. Mater Lett 2020;264:127296. https://doi.org/10.1016/j.matlet.2020.127296.

[277] Ma W, Xie S, Li Z. Mechanical performance of bio-inspired corrugated tubes with varying vertex configurations. Int J Mech Sci 2020;172:105399. https://doi.org/https://doi.org/10.1016/j.ijmecsci.2019.105399.

[278] Kassar S, Siblini S, Wehbi B, Abro O, Shehadeh MA. Towards a Safer Design of Helmets: Finite Element and Experimental Assessment. Emerg. Technol. Mater. Genet. to Struct. Saf. Eng. Risk Anal., Phoenix, Arizona, USA: ASME 2016 International Mechanincal Engineering Congress and Exposition; 2016.

[279] Zhang Y, Zuo C, Wang Y, Sun S, Ren L. Study of a Bionic Paddy Impeller Inspired by Buffalo Hoof. J Bionic Eng 2008;5:79–86. https://doi.org/https://doi.org/10.1016/S1672-6529(08)60076-1.

[280] Metwally S, Martínez Comesaña S, Zarzyka M, Szewczyk PK, Karbowniczek JE, Stachewicz U. Thermal insulation design bioinspired by microstructure study of penguin feather and polar bear hair. Acta Biomater 2019;91:270–83. https://doi.org/https://doi.org/10.1016/j.actbio.2019.04.031.

[281] Jia H, Guo J, Zhu J. Comparison of the Photo-thermal Energy Conversion Behavior of Polar Bear Hair and Wool of Sheep. J Bionic Eng 2017;14:616–21. https://doi.org/https://doi.org/10.1016/S1672-6529(16)60427-4.

[282] Kasturiya N, Subbulakshmi M, Gupta S, Raj H. System Design of Cold Weather Protective Clothing. Def Sci J 1999;49:457–64.

[283] Havenith G. Benchmarking Functionality of Historical Cold Weather Clothing: Robert F. Scott, Roald Amundsen, George Mallory. J Fiber Bioeng Informatics 2010;3:121–9. https://doi.org/10.3993/jfbi12201001.

[284] Gao J, Pan N, Yu W. Compression behavior evaluation of single down fiber and down fiber assemblies. J Text Inst 2010;101:253–60. https://doi.org/10.1080/00405000802377342.

[285] Martin PJ. Heat transfer through low density fibrous assemblies. University of Leeds, PhD thesis.

The University of Leeds, 1987.

[286] Fuller ME. The structure and properties of down feathers and their use in the outdoor industry. University of Leeds, PhD thesis. University of Leeds, 2015.

[287] Gorb SN. Biological attachment devices: exploring nature's diversity for biomimetics. Philos Trans R Soc A Math Phys Eng Sci 2008;366:1557–74. https://doi.org/10.1098/rsta.2007.2172.

[288] Arzt E, Gorb S, Spolenak R. From micro to nano contacts in biological attachment devices. Proc Natl Acad Sci U S A 2003;100:10603–6. https://doi.org/10.1073/pnas.1534701100.

[289] Alibardi L. Cell organization of barb ridges in regenerating feathers of the quail: Implications of the elongation of barb ridges for the evolution and diversification of feathers. Acta Zool 2007;88:101–17. https://doi.org/10.1111/j.1463-6395.2007.00257.x.

[290] Sullivan TN, Chon M, Ramachandramoorthy R, Roenbeck MR, Hung T-T, Espinosa HD, et al. Reversible Attachment with Tailored Permeability: The Feather Vane and Bioinspired Designs. Adv Funct Mater 2017;27:1702954.

[291] Sullivan TN, Hung TT, Velasco-Hogan A, Meyers MA. Bioinspired avian feather designs. Mater Sci Eng C 2019;105:110066. https://doi.org/10.1016/j.msec.2019.110066.

[292] Niewiarowski PH, Stark AY, Dhinojwala A. Sticking to the story: Outstanding challenges in gecko-inspired adhesives. J Exp Biol 2016;219:912–9. https://doi.org/10.1242/jeb.080085.

[293] Wang L, Hui Y, Fu C, Wang Z, Zhang M, Zhang T. Recent advances in Gecko-inspired adhesive materials and application. J Adhes Sci Technol 2020;34:2275–91. https://doi.org/10.1080/01694243.2020.1760478.

[294] Zhou M, Pesika N, Zeng H, Tian Y, Israelachvili J. Recent advances in gecko adhesion and friction mechanisms and development of gecko-inspired dry adhesive surfaces. Friction 2013;1:114–29. https://doi.org/10.1007/s40544-013-0011-5.

[295] Jeong HE, Suh KY. Nanohairs and nanotubes: Efficient structural elements for gecko-inspired artificial dry adhesives. Nano Today 2009;4:335–46. https://doi.org/10.1016/j.nantod.2009.06.004.

[296] Boesel LF, Cremer C, Arzt E, Campo A Del. Gecko-inspired surfaces: A path to strong and reversible dry adhesives. Adv Mater 2010;22:2125–37. https://doi.org/10.1002/adma.200903200.

[297] Stark AY, Mitchell CT. Stick or Slip: Adhesive Performance of Geckos and Gecko-Inspired Synthetics in Wet Environments. Integr Comp Biol 2019;59:214–26. https://doi.org/10.1093/icb/icz008.

[298] Li X, Tao D, Lu H, Bai P, Liu Z, Ma L, et al. Recent developments in gecko-inspired dry adhesive surfaces from fabrication to application. Surf Topogr Metrol Prop 2019;7:023001. https://doi.org/10.1088/2051-672X/ab1447.

[299] Russell AP, Stark AY, Higham TE. The Integrative Biology of Gecko Adhesion: Historical Review, Current Understanding, and Grand Challenges. Integr Comp Biol 2019;59:101–16. https://doi.org/10.1093/icb/icz032.

[300] Kroner E, Davis CS. A Study of the Adhesive Foot of the Gecko: Translation of a Publication by Franz Weitlaner. J Adhes 2015;91:481–7. https://doi.org/10.1080/00218464.2014.922418.

[301] Rong Z, Zhou Y, Chen B, Robertson J, Federle W, Hofmann S, et al. Bio-Inspired Hierarchical Polymer Fiber–Carbon Nanotube Adhesives. Adv Mater 2014;26:1456–61. https://doi.org/https://doi.org/10.1002/adma.201304601.

[302] Murphy MP, Aksak B, Sitti M. Gecko-Inspired Directional and Controllable Adhesion. Small 2009;5:170–5. https://doi.org/https://doi.org/10.1002/smll.200801161.

[303] Murphy MP, Kim S, Sitti M. Enhanced Adhesion by Gecko-Inspired Hierarchical Fibrillar Adhesives. ACS Appl Mater Interfaces 2009;1:849–55. https://doi.org/10.1021/am8002439.

[304] Tian Y, Pesika N, Zeng H, Rosenberg K, Zhao B, McGuiggan P, et al. Adhesion and friction in gecko toe attachment and detachment. Proc Natl Acad Sci 2006;103:19320 LP – 19325. https://doi.org/10.1073/pnas.0608841103.

[305] Hansen WR, Autumn K. Evidence for self-cleaning in gecko setae. Proc Natl Acad Sci U S A 2005;102:385 LP – 389. https://doi.org/10.1073/pnas.0408304102.

[306] Hu S, Lopez S, Niewiarowski PH, Xia Z. Dynamic self-cleaning in gecko setae via digital hyperextension. J R Soc Interface 2012;9:2781–90. https://doi.org/10.1098/rsif.2012.0108.

[307] Mengüç Y, Röhrig M, Abusomwan U, Hölscher H, Sitti M. Staying sticky: contact self-cleaning of gecko-inspired adhesives. J R Soc Interface 2014;11:20131205. https://doi.org/10.1098/rsif.2013.1205.

[308] Xu Q, Wan Y, Hu TS, Liu TX, Tao D, Niewiarowski PH, et al. Robust self-cleaning and micromanipulation capabilities of gecko spatulae and their bio-mimics. Nat Commun 2015;6:8949. https://doi.org/10.1038/ncomms9949.

[309] Arzt E, Quan H, McMeeking RM, Hensel R. Functional surface microstructures inspired by nature – From adhesion and wetting principles to sustainable new devices. Prog Mater Sci 2021;119:100778. https://doi.org/https://doi.org/10.1016/j.pmatsci.2021.100778.

[310] Lamblet M, Verneuil E, Vilmin T, Buguin A, Silberzan P, Léger L. Adhesion Enhancement through Micropatterning at Polydimethylsiloxane−Acrylic Adhesive Interfaces. Langmuir 2007;23:6966–74. https://doi.org/10.1021/la063104h.

[311] Peressadko A, Gorb SN. When less is more: experimental evidence for tenacity enhancement by division of contact area. J Adhes 2004;80:247–61. https://doi.org/10.1080/00218460490430199.

[312] Crosby AJ, Hageman M, Duncan A. Controlling polymer adhesion with "pancakes". Langmuir 2005;21:11738–43. https://doi.org/10.1021/la051721k.

[313] Varenberg M, Gorb S. Shearing of fibrillar adhesive microstructure: friction and shear-related changes in pull-off force. J R Soc Interface 2007;4:721–5. https://doi.org/10.1098/rsif.2007.0222.

[314] Gorb SN, Sinha M, Peressadko A, Daltorio KA, Quinn RD. Insects did it first: a micropatterned adhesive tape for robotic applications. Bioinspir Biomim 2007;2:S117–25. https://doi.org/10.1088/1748-3182/2/4/s01.

[315] Gorb SN, Varenberg M. Mushroom-shaped geometry of contact elements in biological adhesive systems. J Adhes Sci Technol 2007;21:1175–83. https://doi.org/10.1163/156856107782328317.

[316] Gorb S, Varenberg M, Peressadko A, Tuma J. Biomimetic mushroom-shaped fibrillar adhesive microstructure. J R Soc Interface 2007;4:271–5. https://doi.org/10.1098/rsif.2006.0164.

[317] Hu H, Tian H, Li X, Shao J, Ding Y, Liu H, et al. Biomimetic Mushroom-Shaped Microfibers for Dry Adhesives by Electrically Induced Polymer Deformation. ACS Appl Mater Interfaces 2014;6:14167–73. https://doi.org/10.1021/am503493u.

[318] Northen MT, Turner KL. Meso-scale adhesion testing of integrated micro- and nano-scale structures. Sensors Actuators A Phys 2006;130–131:583–7.

https://doi.org/https://doi.org/10.1016/j.sna.2005.10.032.

[319] Northen MT, Turner KL. A batch fabricated biomimetic dry adhesive. Nanotechnology 2005;16:1159–66. https://doi.org/10.1088/0957-4484/16/8/030.

[320] Aksak B, Murphy MP, Sitti M. Adhesion of Biologically Inspired Vertical and Angled Polymer Microfiber Arrays. Langmuir 2007;23:3322–32. https://doi.org/10.1021/la062697t.

[321] Campo A del, Greiner C. SU-8: a photoresist for high-aspect-ratio and 3D submicron lithography. J Micromechanics Microengineering 2007;17:R81–95. https://doi.org/10.1088/0960-1317/17/6/r01.

[322] Davies J, Haq S, Hawke T, Sargent JP. A practical approach to the development of a synthetic Gecko tape. Int J Adhes Adhes 2009;29:380–90. https://doi.org/https://doi.org/10.1016/j.ijadhadh.2008.07.009.

[323] Jeong HE, Lee J-K, Kim HN, Moon SH, Suh KY. A nontransferring dry adhesive with hierarchical polymer nanohairs. Proc Natl Acad Sci U S A 2009;106:5639–44. https://doi.org/10.1073/pnas.0900323106.

[324] Geim AK, Dubonos S V, Grigorieva I V, Novoselov KS, Zhukov AA, Shapoval SY. Microfabricated adhesive mimicking gecko foot-hair. Nat Mater 2003;2:461–3. https://doi.org/10.1038/nmat917.

[325] Hu S, Xia Z, Dai L. Advanced gecko-foot-mimetic dry adhesives based on carbon nanotubes. Nanoscale 2013;5 2:475–86.

[326] Yurdumakan B, Raravikar NR, Ajayan PM, Dhinojwala A. Synthetic gecko foot-hairs from multiwalled carbon nanotubes. Chem Commun (Camb) 2005;30:3799–801. https://doi.org/10.1039/b506047h.

[327] Qu L, Dai L, Stone M, Xia Z, Wang ZL. Carbon Nanotube Arrays with Strong Shear Binding-On and Easy Normal Lifting-Off. Science (80-) 2008;322:238 LP – 242. https://doi.org/10.1126/science.1159503.

[328] Jeong HE, Lee SH, Kim P, Suh KY. Stretched Polymer Nanohairs by Nanodrawing. Nano Lett 2006;6:1508–13. https://doi.org/10.1021/nl061045m.

[329] Sitti M, Fearing RS. Synthetic gecko foot-hair micro/nano-structures as dry adhesives. J Adhes Sci Technol 2003;17:1055–73. https://doi.org/10.1163/156856103322113788.

[330] Glassmaker NJ, Jagota A, Hui C-Y, Kim J. Design of biomimetic fibrillar interfaces: 1. Making contact. J R Soc Interface 2004;1:23–33. https://doi.org/10.1098/rsif.2004.0004.

[331] Greiner C, del Campo A, Arzt E. Adhesion of Bioinspired Micropatterned Surfaces: Effects of Pillar Radius, Aspect Ratio, and Preload. Langmuir 2007;23:3495–502. https://doi.org/10.1021/la0633987.

[332] Mahdavi A, Ferreira L, Sundback C, Nichol JW, Chan EP, Carter DJD, et al. A biodegradable and biocompatible gecko-inspired tissue adhesive. Proc Natl Acad Sci U S A 2008;105:2307–12. https://doi.org/10.1073/pnas.0712117105.

[333] Hensel R, Moh K, Arzt E. Engineering Micropatterned Dry Adhesives: From Contact Theory to Handling Applications. Adv Funct Mater 2018;28:1800865. https://doi.org/https://doi.org/10.1002/adfm.201800865.

[334] Raut HK, Baji A, Hariri HH, Parveen H, Soh GS, Low HY, et al. Gecko-Inspired Dry Adhesive

Based on Micro–Nanoscale Hierarchical Arrays for Application in Climbing Devices. ACS Appl Mater Interfaces 2018;10:1288–96. https://doi.org/10.1021/acsami.7b09526.

[335] del Campo A, Greiner C, Arzt E. Contact Shape Controls Adhesion of Bioinspired Fibrillar Surfaces. Langmuir 2007;23:10235–43. https://doi.org/10.1021/la7010502.

[336] Spuskanyuk A V, McMeeking RM, Deshpande VS, Arzt E. The effect of shape on the adhesion of fibrillar surfaces. Acta Biomater 2008;4:1669–76. https://doi.org/https://doi.org/10.1016/j.actbio.2008.05.026.

[337] Aksak B, Sahin K, Sitti M. The optimal shape of elastomer mushroom-like fibers for high and robust adhesion. Beilstein J Nanotechnol 2014;5:630–8.

[338] Balijepalli RG, Begley MR, Fleck NA, McMeeking RM, Arzt E. Numerical simulation of the edge stress singularity and the adhesion strength for compliant mushroom fibrils adhered to rigid substrates. Int J Solids Struct 2016;85–86:160–71. https://doi.org/https://doi.org/10.1016/j.ijsolstr.2016.02.018.

[339] Fleck NA, Khaderi SN, McMeeking RM, Arzt E. Cohesive detachment of an elastic pillar from a dissimilar substrate. J Mech Phys Solids 2017;101:30–43. https://doi.org/https://doi.org/10.1016/j.jmps.2017.01.001.

[340] Balijepalli RG, Fischer SCL, Hensel R, McMeeking RM, Arzt E. Numerical study of adhesion enhancement by composite fibrils with soft tip layers. J Mech Phys Solids 2017;99:357–78. https://doi.org/https://doi.org/10.1016/j.jmps.2016.11.017.

[341] Li Y, Krahn J, Menon C. Bioinspired dry adhesive materials and their application in robotics: A review. J Bionic Eng 2016;13:181–99. https://doi.org/10.1016/S1672-6529(16)60293-7.

[342] Asbeck A, Dastoor S, Parness A, Fullerton L, Esparza N, Soto D, et al. Climbing rough vertical surfaces with hierarchical directional adhesion. 2009 IEEE Int. Conf. Robot. Autom., 2009, p. 2675–80. https://doi.org/10.1109/ROBOT.2009.5152864.

[343] Jiang H, Hawkes EW, Fuller C, Estrada MA, Suresh SA, Abcouwer N, et al. A robotic device using gecko-inspired adhesives can grasp and manipulate large objects in microgravity. Sci Robot 2017;2:eaan4545. https://doi.org/10.1126/scirobotics.aan4545.

[344] Jiang H, Hawkes EW, Arutyunov V, Tims J, Fuller C, King JP, et al. Scaling controllable adhesives to grapple floating objects in space. 2015 IEEE Int. Conf. Robot. Autom., 2015, p. 2828–35. https://doi.org/10.1109/ICRA.2015.7139584.

[345] Kalouche S, Wiltsie N, Su H, Parness A. Inchworm style gecko adhesive climbing robot. 2014 IEEE/RSJ Int. Conf. Intell. Robot. Syst., 2014, p. 2319–24. https://doi.org/10.1109/IROS.2014.6942876.

[346] Hawkes EW, Christensen DL, Han AK, Jiang H, Cutkosky MR. Grasping without squeezing: Shear adhesion gripper with fibrillar thin film. 2015 IEEE Int. Conf. Robot. Autom., 2015, p. 2305–12. https://doi.org/10.1109/ICRA.2015.7139505.

[347] Hawkes EW, Christensen DL, Cutkosky MR. Vertical dry adhesive climbing with a 100× bodyweight payload. 2015 IEEE Int. Conf. Robot. Autom., 2015, p. 3762–9. https://doi.org/10.1109/ICRA.2015.7139722.

[348] Seo T, Sitti M. Tank-Like Module-Based Climbing Robot Using Passive Compliant Joints. IEEE/ASME Trans Mechatronics 2013;18:397–408. https://doi.org/10.1109/TMECH.2011.2182617.

[349] Henrey M, Ahmed A, Boscariol P, Shannon L, Menon C. Abigaille-III: A Versatile, Bioinspired Hexapod for Scaling Smooth Vertical Surfaces. J Bionic Eng 2014;11:1–17. https://doi.org/https://doi.org/10.1016/S1672-6529(14)60015-9.

[350] Ko H, Yi H, Jeong HE. Wall and ceiling climbing quadruped robot with superior water repellency manufactured using 3D printing (UNIclimb). Int J Precis Eng Manuf Technol 2017;4:273–80. https://doi.org/10.1007/s40684-017-0033-y.

[351] Estrada MA, Hockman B, Bylard A, Hawkes EW, Cutkosky MR, Pavone M. Free-flyer acquisition of spinning objects with gecko-inspired adhesives. 2016 IEEE Int. Conf. Robot. Autom., 2016, p. 4907–13. https://doi.org/10.1109/ICRA.2016.7487696.

[352] Dadkhah M, Zhao Z, Wettels N, Spenko M. A self-aligning gripper using an electrostatic/gecko-like adhesive. 2016 IEEE/RSJ Int. Conf. Intell. Robot. Syst., 2016, p. 1006–11. https://doi.org/10.1109/IROS.2016.7759172.

[353] Zhou M, Tian Y, Sameoto D, Zhang X, Meng Y, Wen S. Controllable Interfacial Adhesion Applied to Transfer Light and Fragile Objects by Using Gecko Inspired Mushroom-Shaped Pillar Surface. ACS Appl Mater Interfaces 2013;5:10137–44. https://doi.org/10.1021/am402815x.

[354] Purtov J, Frensemeier M, Kroner E. Switchable Adhesion in Vacuum Using Bio-Inspired Dry Adhesives. ACS Appl Mater Interfaces 2015;7:24127–35. https://doi.org/10.1021/acsami.5b07287.

[355] Song S, Sitti M. Soft Grippers Using Micro-fibrillar Adhesives for Transfer Printing. Adv Mater 2014;26:4901–6. https://doi.org/https://doi.org/10.1002/adma.201400630.

[356] Liu ZQ, Jiao D, Meyers MA, Zhang ZF. Structure and mechanical properties of naturally occurring lightweight foam-filled cylinder – The peacock's tail coverts shaft and its components. Acta Biomater 2015;17:137–51. https://doi.org/https://doi.org/10.1016/j.actbio.2015.01.035.

[357] Tee YL, Leary M, Tran P. Porcupine Quill: Buckling Resistance Analysis and Design for 3D Printing. In: Wang C, Dao V, Kitipornchai S, editors. Lect. Notes Civ. Eng. vol 101, Singapore: Springer; 2021, p. 1311–9. https://doi.org/10.1007/978-981-15-8079-6_123.

[358] Vincent JFV, Owers P. Mechanical design of hedgehog spines and porcupine quills. J Zool 1986;210:55–7. https://doi.org/10.1111/j.1469-7998.1986.tb03620.x.

[359] Vincent JFV. Survival of the cheapest. Mater Today 2002;5:28–41. https://doi.org/10.1016/s1369-7021(02)01237-3.

[360] Drol CJ, Kennedy EB, Hsiung BK, Swift NB, Tan KT. Bioinspirational understanding of flexural performance in hedgehog spines. Acta Biomater 2019;94:553–64. https://doi.org/10.1016/j.actbio.2019.04.036.

[361] Gruson H, Elias M, Andraud C, Djediat C, Berthier S, Doutrelant C, et al. Hummingbird iridescence: An unsuspected structural diversity influences colouration at multiple scales. BioRxiv 2019. https://doi.org/10.1101/699744.

[362] Freyer P, Stavenga DG. Biophotonics of diversely coloured peacock tail feathers. Faraday Discuss 2020;223. https://doi.org/10.1039/d0fd00033g.

[363] Weiss IM, Kirchner HOK. The peacock's train (Pavo cristatus and Pavo cristatus mut. alba) I. structure, mechanics, and chemistry of the tail feather coverts. J Exp Zool Part A Ecol Genet Physiol 2010;313A:690–703. https://doi.org/10.1002/jez.641.

[364] Zi J, Yu X, Li Y, Hu X, Xu C, Wang X, et al. Coloration strategies in peacock feathers. Proc Natl Acad Sci 2003;100:12576–8. https://doi.org/10.1073/pnas.2133313100.

[365] Stavenga DG, Van Der Kooi CJ, Wilts BD. Structural coloured feathers of mallards act by simple multilayer photonics. J R Soc Interface 2017;14:18317. https://doi.org/10.1098/rsif.2017.0407.

[366] Parnell AJ, Washington AL, Mykhaylyk OO, Hill CJ, Bianco A, Burg SL, et al. Spatially modulated structural colour in bird feathers. Sci Rep 2015;5. https://doi.org/10.1038/srep18317.

[367] Burg SL, Parnell AJ. Self-assembling structural colour in nature. J Phys Condens Matter 2018;30:413001. https://doi.org/10.1088/1361-648X/aadc95.

[368] Noh H, Liew SF, Saranathan V, Mochrie SGJ, Prum RO, Dufresne ER, et al. How noniridescent colors are generated by quasi-ordered structures of bird feathers. Adv Mater 2010;22:2871–80. https://doi.org/10.1002/adma.200903699.

[369] Xiao M, Li Y, Allen MC, Deheyn DD, Yue X, Zhao J, et al. Bio-inspired structural colors produced via self-assembly of synthetic melanin nanoparticles. ACS Nano 2015;9:5454–60. https://doi.org/10.1021/acsnano.5b01298.

[370] Fu Y, Tippets CA, Donev EU, Lopez R. Structural colors: from natural to artificial systems. Wiley Interdiscip Rev Nanomedicine Nanobiotechnology 2016;8:758–75. https://doi.org/10.1002/wnan.1396.

[371] Steindorfer MA, Schmidt V, Belegratis M, Stadlober B, Krenn JR. Detailed simulation of structural color generation inspired by the Morpho butterfly. Opt Express 2012;20:21485–94. https://doi.org/10.1364/oe.20.021485.

[372] Zhang S, Chen Y. Nanofabrication and coloration study of artificial Morpho butterfly wings with aligned lamellae layers. Sci Rep 2015;5:16637. https://doi.org/10.1038/srep16637.

[373] Chung K, Yu S, Heo CJ, Shim JW, Yang SM, Han MG, et al. Flexible, angle-independent, structural color reflectors inspired by morpho butterfly wings. Adv Mater 2012;24:2375–9. https://doi.org/10.1002/adma.201200521.

[374] Wang S, Yang Z, Gong G, Wang J, Wu J, Yang S, et al. Icephobicity of Penguins Spheniscus Humboldti and an Artificial Replica of Penguin Feather with Air-Infused Hierarchical Rough Structures. J Phys Chem C 2016;120:15923–9. https://doi.org/10.1021/acs.jpcc.5b12298.

[375] Nishino T, Meguro M, Nakamae K, Matsushita M, Ueda Y. The Lowest Surface Free Energy Based on −CF3 Alignment. Langmuir 1999;15:4321–3. https://doi.org/10.1021/la981727s.

[376] Green DW, Lee KK-H, Watson JA, Kim H-Y, Yoon K-S, Kim E-J, et al. High Quality Bioreplication of Intricate Nanostructures from a Fragile Gecko Skin Surface with Bactericidal Properties. Sci Rep 2017;7:41023. https://doi.org/10.1038/srep41023.

[377] Vucko MJ, Schwarzkopf L, Scardino AJ. A New Method to Examine the Oberhautchen of Lizard Skin. Copeia 2008;2008:868–71. https://doi.org/10.1643/CH-07-152.

[378] Shavandi A, Silva TH, Bekhit AA, Bekhit AE-DA. Keratin: dissolution, extraction and biomedical application. Biomater Sci 2017;5:1699–735. https://doi.org/10.1039/C7BM00411G.

[379] Feroz S, Muhammad N, Ranayake J, Dias G. Keratin - Based materials for biomedical applications. Bioact Mater 2020;5:496–509. https://doi.org/10.1016/j.bioactmat.2020.04.007.

[380] Beyer C. German patent: DE22643, 1907.

[381] Goldsmith B. American Patent US922692A: Thermoplastic composition containing keratin. 922,692, 1909.

[382] Dale H. Keratin and other coatings for pills. Pharm J 1932;129:494–5.

[383] Rouse JG, Van Dyke ME. A Review of Keratin-Based Biomaterials for Biomedical Applications. Materials (Basel) 2010;3:999–1014. https://doi.org/10.3390/ma3020999.

[384] Roy DC, Tomblyn S, Burmeister DM, Wrice NL, Becerra SC, Burnett LR, et al. Ciprofloxacin-Loaded Keratin Hydrogels Prevent Pseudomonas aeruginosa Infection and Support Healing in a Porcine Full-Thickness Excisional Wound. Adv Wound Care 2015;4:457–68. https://doi.org/10.1089/wound.2014.0576.

[385] Dickerson MB, Sierra AA, Bedford NM, Lyon WJ, Gruner WE, Mirau PA, et al. Keratin-based antimicrobial textiles, films, and nanofibers. J Mater Chem B 2013;1:5505–14. https://doi.org/10.1039/C3TB20896F.

[386] Zhen L. Ben Cao Gang Mu. Changchun, Jilin, China: The Time Literature & Art Press; 2005.

[387] Noishiki Y, Ito H, Miyamoto T, Inagaki H. Application of denatured wool keratin derivatives to an antithrombogenic biomaterial-vascular graft coated with a heparinized keratin derivative. Kobunshi Ronbunshu 1982;39:221–7.

[388] Ito H, Miyamoto T, Inagaki H, Noishiki Y. Biocompatibility of denatured keratins from wool. Kobunshi Ronbunshu 1982;39:249–56.

[389] Jarman T, Light J. Prospects for novel biomaterials development. World Biotech Rep 1985:502–12.

[390] Various Authors. Biomaterial forefront: Keratin which can be extracted by simple chemical technique. Kogyo Zair 1993:106–9.

[391] Tanabe T, Okitsu N, Tachibana A, Yamauchi K. Preparation and characterization of keratin-chitosan composite film. Biomaterials 2002;23:817–25. https://doi.org/10.1016/s0142-9612(01)00187-9.

[392] Lin C-W, Chen Y-K, Lu M, Lou K-L, Yu J. Photo-Crosslinked Keratin/Chitosan Membranes as Potential Wound Dressing Materials. Polymers (Basel) 2018;10:987. https://doi.org/10.3390/polym10090987.

[393] Lin Y-H, Huang K-W, Chen S-Y, Cheng N-C, Yu J. Keratin/chitosan UV-crosslinked composites promote the osteogenic differentiation of human adipose derived stem cells. J Mater Chem B 2017;5:4614–22. https://doi.org/10.1039/C7TB00188F.

[394] Lee KY, Ha WS. DSC studies on bound water in silk fibroin/S-carboxymethyl kerateine blend films. Polymer (Guildf) 1999;40:4131–4. https://doi.org/https://doi.org/10.1016/S0032-3861(98)00611-9.

[395] Vu T, Xue Y, Vuong T, Erbe M, Bennet C, Palazzo B, et al. Comparative Study of Ultrasonication-Induced and Naturally Self-Assembled Silk Fibroin-Wool Keratin Hydrogel Biomaterials. Int J Mol Sci 2016;17:1497. https://doi.org/10.3390/ijms17091497.

[396] Lee KY, Kong SJ, Park WH, Ha WS, Kwon IC. Effect of surface properties on the antithrombogenicity of silk fibroin/S-carboxymethyl kerateine blend films. J Biomater Sci Polym Ed 1998;9:905–14. https://doi.org/10.1163/156856298x00235.

[397] Lee KY. Characterization of silk fibroin/S-carboxymethyl kerateine surfaces: Evaluation of

biocompatibility by contact angle measurements. Fibers Polym 2001;2:71–4.
https://doi.org/10.1007/BF02875261.

[398]   Vasconcelos A, Freddi G, Cavaco-Paulo A. Biodegradable materials based on silk fibroin and
keratin. Biomacromolecules 2008;9:1299–305. https://doi.org/10.1021/bm7012789.

[399]   Wang Y, Li P, Xiang P, Lu J, Yuan J, Shen J. Electrospun polyurethane/keratin/AgNP
biocomposite mats for biocompatible and antibacterial wound dressings. J Mater Chem B
2016;4:635–48. https://doi.org/10.1039/C5TB02358K.

[400]   Yue K, Liu Y, Byambaa B, Singh V, Liu W, Li X, et al. Visible light crosslinkable human hair
keratin hydrogels. Bioeng Transl Med 2018;3:37–48.
https://doi.org/https://doi.org/10.1002/btm2.10077.

[401]   Katoh K, Tanabe T, Yamauchi K. Novel approach to fabricate keratin sponge scaffolds with
controlled pore size and porosity. Biomaterials 2004;25:4255–62.
https://doi.org/10.1016/j.biomaterials.2003.11.018.

[402]   Tachibana A, Furuta Y, Takeshima H, Tanabe T, Yamauchi K. Fabrication of wool keratin sponge
scaffolds for long-term cell cultivation. J Biotechnol 2002;93:165–70.
https://doi.org/10.1016/s0168-1656(01)00395-9.

[403]   Lin C-W, Chen Y-K, Tang K-C, Yang K-C, Cheng N-C, Yu J. Keratin scaffolds with human
adipose stem cells: Physical and biological effects toward wound healing. J Tissue Eng Regen
Med 2019;13:1044–58. https://doi.org/https://doi.org/10.1002/term.2855.

[404]   Kurimoto A, Tanabe T, Tachibana A, Yamauchi K. Keratin sponge: immobilization of lysozyme.
J Biosci Bioeng 2003;96:307–9. https://doi.org/10.1016/s1389-1723(03)80199-8.

[405]   Tachibana A, Kaneko S, Tanabe T, Yamauchi K. Rapid fabrication of keratin-hydroxyapatite
hybrid sponges toward osteoblast cultivation and differentiation. Biomaterials 2005;26:297–302.
https://doi.org/10.1016/j.biomaterials.2004.02.032.

[406]   Peplow P V, Dias GJ. A study of the relationship between mass and physical strength of keratin
bars in vivo. J Mater Sci Mater Med 2004;15:1217–20. https://doi.org/10.1007/s10856-004-5803-
8.

[407]   Srinivasan B, Kumar R, Shanmugam K, Sivagnam UT, Reddy NP, Sehgal PK. Porous keratin
scaffold-promising biomaterial for tissue engineering and drug delivery. J Biomed Mater Res B
Appl Biomater 2010;92:5–12. https://doi.org/10.1002/jbm.b.31483.

[408]   Verma V, Verma P, Ray P, Ray AR. Preparation of scaffolds from human hair proteins for tissue-
engineering applications. Biomed Mater 2008;3:25007. https://doi.org/10.1088/1748-
6041/3/2/025007.

[409]   Than MP, Smith RA, Hammond C, Kelly R, Marsh C, Maderal AD, et al. Keratin-based Wound
Care Products for Treatment of Resistant Vascular Wounds. J Clin Aesthet Dermatol 2012;5:31–5.

[410]   Konop M, Sulejczak D, Czuwara J, Kosson P, Misicka A, Lipkowski AW, et al. The role of
allogenic keratin-derived dressing in wound healing in a mouse model. Wound Repair Regen Off
Publ Wound Heal Soc [and] Eur Tissue Repair Soc 2017;25:62–74.
https://doi.org/10.1111/wrr.12500.

[411]   Poranki D, Whitener W, Howse S, Mesen T, Howse E, Burnell J, et al. Evaluation of skin
regeneration after burns in vivo and rescue of cells after thermal stress in vitro following
treatment with a keratin biomaterial. J Biomater Appl 2014;29:26–35.

https://doi.org/10.1177/0885328213513310.

[412] Sionkowska A, Skopinska-Wisniewska J, Planecka A, Kozlowska J. The influence of UV irradiation on the properties of chitosan films containing keratin. Polym Degrad Stab 2010;95:2486–91. https://doi.org/https://doi.org/10.1016/j.polymdegradstab.2010.08.002.

[413] Katoh K, Shibayama M, Tanabe T, Yamauchi K. Preparation and physicochemical properties of compression-molded keratin films. Biomaterials 2004;25:2265–72. https://doi.org/https://doi.org/10.1016/j.biomaterials.2003.09.021.

[414] Ducheyne P, Healy K, Hutmacher D, Grainger D, Kirkpatrick C. Comprehensive biomaterials ii. 2017.

[415] Zoccola M, Montarsolo A, Aluigi A, Varesano A, Vineis C, Tonin C. Electrospinning of polyamide 6/modified-keratin blends. E-Polymers 2007;7.

[416] Shrivastava A, Dondapati S. Biodegradable composites based on biopolymers and natural bast fibres: A review. Mater Today Proc 2021;(In press). https://doi.org/https://doi.org/10.1016/j.matpr.2021.02.652.

[417] García M, Garmendia I, García J. Influence of natural fiber type in eco-composites. J Appl Polym Sci 2008;107:2994–3004. https://doi.org/https://doi.org/10.1002/app.27519.

[418] Zia KM, Barikani M, Bhatti IA, Zuber M, Bhatti HN. Synthesis and characterization of novel, biodegradable, thermally stable chitin-based polyurethane elastomers. J Appl Polym Sci 2008;110:769–76. https://doi.org/https://doi.org/10.1002/app.28533.

[419] Quirino RL, Garrison TF, Kessler MR. Matrices from vegetable oils, cashew nut shell liquid, and other relevant systems for biocomposite applications. Green Chem 2014;16:1700–15. https://doi.org/10.1039/C3GC41811A.

[420] Väisänen T, Haapala A, Lappalainen R, Tomppo L. Utilization of agricultural and forest industry waste and residues in natural fiber-polymer composites: A review. Waste Manag 2016;54:62–73. https://doi.org/https://doi.org/10.1016/j.wasman.2016.04.037.

[421] Zoccola M, Aluigi A, Tonin C. Characterisation of keratin biomass from butchery and wool industry wastes. J Mol Struct 2009;938:35–40. https://doi.org/https://doi.org/10.1016/j.molstruc.2009.08.036.

[422] Conzatti L, Giunco F, Stagnaro P, Patrucco A, Marano C, Rink M, et al. Composites based on polypropylene and short wool fibres. Compos Part A Appl Sci Manuf 2013;47:165–71. https://doi.org/https://doi.org/10.1016/j.compositesa.2013.01.002.

[423] Donato RK, Mija A. Keratin Associations with Synthetic, Biosynthetic and Natural Polymers: An Extensive Review. Polymers (Basel) 2019;12:32. https://doi.org/10.3390/polym12010032.

[424] Song K, Xu H, Xie K, Yang Y. Keratin-Based Biocomposites Reinforced and Cross-Linked with Dual-Functional Cellulose Nanocrystals. ACS Sustain Chem Eng 2017;5:5669–78. https://doi.org/10.1021/acssuschemeng.7b00085.

[425] Shavandi A, Ali MA. Keratin based thermoplastic biocomposites: a review. Rev Environ Sci Bio/Technology 2019;18:299–316. https://doi.org/10.1007/s11157-019-09497-x.

[426] Fudge DS, Hillis S, Levy N, Gosline JM. Hagfish slime threads as a biomimetic model for high performance protein fibres. Bioinspir Biomim 2010;5:35002. https://doi.org/10.1088/1748-3182/5/3/035002.

[427] Koch EA, Spitzer RH, Pithawalla RB, Parry DA. An unusual intermediate filament subunit from the cytoskeletal biopolymer released extracellularly into seawater by the primitive hagfish (Eptatretus stouti). J Cell Sci 1994;107:3133–44.

[428] Koch EA, Spitzer RH, Pithawalla RB, Castillos FA 3rd, Parry DA. Hagfish biopolymer: a type I/type II homologue of epidermal keratin intermediate filaments. Int J Biol Macromol 1995;17:283–92. https://doi.org/10.1016/0141-8130(95)98156-s.

[429] Keten S, Xu Z, Ihle B, Buehler MJ. Nanoconfinement controls stiffness, strength and mechanical toughness of β-sheet crystals in silk. Nat Mater 2010;9:359–67. https://doi.org/10.1038/nmat2704.

[430] Mostaert AS, Jarvis SP. Beneficial characteristics of mechanically functional amyloid fibrils evolutionarily preserved in natural adhesives. Nanotechnology 2007;18:44010.

[431] Pourjavaheri F, Jones OAH, Czajka M, Martinez-Pardo I, Blanch EW, Shanks RA. Design and characterization of sustainable bio-composites from waste chicken feather keratin and thermoplastic polyurethane. Polym Compos 2018;39:E620–32. https://doi.org/https://doi.org/10.1002/pc.24794.

[432] Tran CD, Mututuvari TM. Cellulose, Chitosan and Keratin Composite Materials: Facile and Recyclable Synthesis, Conformation and Properties. ACS Sustain Chem Eng 2016;4:1850–61. https://doi.org/10.1021/acssuschemeng.6b00084.

[433] Hearle JWS. A critical review of the structural mechanics of wool and hair fibres. Int J Biol Macromol 2000;27:123–38. https://doi.org/https://doi.org/10.1016/S0141-8130(00)00116-1.

[434] Haly AR, Snaith JW. The Heat of the Phase Transformation in Wool Keratin Under Various Conditions. Text Res J 1970;40:142–6. https://doi.org/10.1177/004051757004000207.

[435] Mason P. Thermal Transitions in Keratin: Part III: Stress and Temperature Effects in Relation to the Alpha Beta Transition. Text Res J 1965;35:483–90. https://doi.org/10.1177/004051756503500601.

[436] Miserez A, Wasko SS, Carpenter CF, Waite JH. Non-entropic and reversible long-range deformation of an encapsulating bioelastomer. Nat Mater 2009;8:910–6. https://doi.org/10.1038/nmat2547.

[437] Chapman B. A review of the mechanical properties of keratin fibres. J Text Inst 1969;60:181–207. https://doi.org/10.1080/00405006908629920.

[438] Cera L, Gonzalez GM, Liu Q, Choi S, Chantre CO, Lee J, et al. A bioinspired and hierarchically structured shape-memory material. Nat Mater 2021;20:242–9. https://doi.org/10.1038/s41563-020-0789-2.

[439] Harrington MJ, Speck O, Speck T, Wagner S, Weinkamer R. Biological Archetypes for Self-Healing Materials BT - Self-healing Materials. In: Hager MD, van der Zwaag S, Schubert US, editors., Cham: Springer International Publishing; 2016, p. 307–44. https://doi.org/10.1007/12_2015_334.

[440] Leach DH. The Structure and Function of the Equine Hoof Wall (PhD Thesis). University of Saskatchewan, 1980.

[441] Lazarus B, Chadha C, Velasco-Hogan A, Barbosa JD V, Jasiuk I, Meyers MA. Engineering with Keratin: A Functional Material and a Source of Bioinspiration. IScience 2021:102798. https://doi.org/https://doi.org/10.1016/j.isci.2021.102798.

[442] Fortier P, Suei S, Kreplak L. Nanoscale Strain-Hardening of Keratin Fibres. PLoS One 2012;7:e41814.

[443] Kreplak L, Doucet J, Briki F. Unraveling double stranded α-helical coiled coils: An x-ray diffraction study on hard α-keratin fibers. Biopolymers 2001;58:526–33. https://doi.org/https://doi.org/10.1002/1097-0282(20010415)58:5<526::AID-BIP1028>3.0.CO;2-L.

[444] Schindelin J, Arganda-Carreras I, Frise E, Kaynig V, Longair M, Pietzsch T, et al. Fiji: an open-source platform for biological-image analysis. Nat Methods 2012;9:676–82. https://doi.org/10.1038/nmeth.2019.

[445] Legland D, Arganda-Carreras I, Andrey P. MorphoLibJ: integrated library and plugins for mathematical morphology with ImageJ. Bioinformatics 2016;32:3532–4. https://doi.org/10.1093/bioinformatics/btw413.

[446] Ollion J, Cochennec J, Loll F, Escudé C, Boudier T. TANGO: a generic tool for high-throughput 3D image analysis for studying nuclear organization. Bioinformatics 2013;29:1840–1. https://doi.org/10.1093/bioinformatics/btt276.

[447] Breakspear S, Noecker B, Popescu C. Relevance and evaluation of hydrogen and disulfide bond contribution to the mechanics of hard α-keratin fibers. J Phys Chem B 2019;123:4505–11. https://doi.org/10.1021/acs.jpcb.9b01690.

[448] Fudge DS, Gosline JM. Molecular design of the α-keratin composite: Insights from a matrix-free model, hagfish slime threads. Proc R Soc B Biol Sci 2003;271:291–9. https://doi.org/10.1098/rspb.2003.2591.

[449] Clayton HM, Hobbs SJ. A review of biomechanical gait classification with reference to collected trot, passage and piaffe in dressage horses. Anim an Open Access J from MDPI 2019;9:763. https://doi.org/10.3390/ani9100763.

[450] Thomason J, Biewener A, Bertram J. Surface strain on the equine hoof wall in vivo: implications for the material design and functional morphology of the wall. J Exp Biol 1992;166:145–68.

[451] Mirkhalaf M, Dastjerdi AK, Barthelat F. Overcoming the brittleness of glass through bio-inspiration and micro-architecture. Nat Commun 2014;5:3166. https://doi.org/10.1038/ncomms4166.

[452] Ritchie RO. The conflicts between strength and toughness. Nat Mater 2011;10:817–22. https://doi.org/10.1038/nmat3115.

[453] Rizvi R, Anwer A, Fernie G, Dutta T, Naguib H. Multifunctional textured surfaces with enhanced friction and hydrophobic behaviors produced by fiber debonding and pullout. ACS Appl Mater Interfaces 2016;8:29818–26. https://doi.org/10.1021/acsami.6b11497.

[454] Naaman A, Namur G, Alwan J, Najm H. Fiber pullout and bond slip. II: experimental validation. J Struct Eng 1991;117:2791–800. https://doi.org/10.1061/(ASCE)0733-9445(1991)117:9(2791).

[455] Naaman A, Namur G, Alwan J, Najm H. Fiber pullout and bond slip. I: analytical study. J Struct Eng 1991;117:2769–90. https://doi.org/10.1061/(ASCE)0733-9445(1991)117:9(2769).

[456] Cantwell WJ, Morton J. The impact resistance of composite materials - a review. Composites 1991;22:347–62. https://doi.org/10.1016/0010-4361(91)90549-V.

[457] Beaumont PWR. Fracture Mechanisms in Fibrous Composites. In: SMITH RABT-FM, editor.,

Pergamon; 1979, p. 211–33. https://doi.org/https://doi.org/10.1016/B978-0-08-024766-3.50012-4.

[458] Wu Q, Wan Q, Liu Q, He J, Zhao R, Yang X, et al. Synergistic strengthening and toughening the interphase of composites by constructing alternating "rigid-and-soft" structure on carbon fiber surface. Adv Mater Interfaces 2019;6:1900970. https://doi.org/https://doi.org/10.1002/admi.201900970.

[459] Isitman NA, Aykol M, Kaynak C. Nanoclay assisted strengthening of the fiber/matrix interface in functionally filled polyamide 6 composites. Compos Struct 2010;92:2181–6. https://doi.org/10.1016/j.compstruct.2009.09.007.

[460] Zabihi O, Ahmadi M, Li Q, Shafei S, Huson MG, Naebe M. Carbon fibre surface modification using functionalized nanoclay: A hierarchical interphase for fibre-reinforced polymer composites. Compos Sci Technol 2017;148:49–58. https://doi.org/10.1016/j.compscitech.2017.05.013.

[461] Li R, Lachman N, Florin P, Wagner HD, Wardle BL. Hierarchical carbon nanotube carbon fiber unidirectional composites with preserved tensile and interfacial properties. Compos Sci Technol 2015;117:139–45. https://doi.org/https://doi.org/10.1016/j.compscitech.2015.04.014.

[462] Hong S, Minary-Jolandan M, Naraghi M. Controlling the wettability and adhesion of carbon fibers with polymer interfaces via grafted nanofibers. Compos Sci Technol 2015;117:130–8. https://doi.org/https://doi.org/10.1016/j.compscitech.2015.06.008.

[463] Jiang S, Li Q, Zhao Y, Wang J, Kang M. Effect of surface silanization of carbon fiber on mechanical properties of carbon fiber reinforced polyurethane composites. Compos Sci Technol 2015;110:87–94. https://doi.org/https://doi.org/10.1016/j.compscitech.2015.01.022.

[464] Gargano A, Pingkarawat K, Pickerd VL, Ibrahim ME, Mouritz AP. Effect of fibre-matrix interfacial strength on the explosive blast resistance of carbon fibre laminates. Compos Sci Technol 2017;138:68–79. https://doi.org/https://doi.org/10.1016/j.compscitech.2016.11.009.

[465] Gnädinger F, Middendorf P, Fox B. Interfacial shear strength studies of experimental carbon fibres, novel thermosetting polyurethane and epoxy matrices and bespoke sizing agents. Compos Sci Technol 2016;133:104–10. https://doi.org/https://doi.org/10.1016/j.compscitech.2016.07.029.

[466] Wei Z, Xu X. Gradient design of bio-inspired nacre-like composites for improved impact resistance. Compos Part B Eng 2021;215:108830. https://doi.org/https://doi.org/10.1016/j.compositesb.2021.108830.

[467] Kasapi MA, Gosline JM. Exploring the possible functions of equine hoof wall tubules. Equine Vet J 1998;30:10–4. https://doi.org/https://doi.org/10.1111/j.2042-3306.1998.tb05116.x.

[468] O'Grady SE. How to manage a quarter crack. Annu. Conv. AAEP, 2010, p. 141–7.

[469] Lazarus BS, Luu RK, Ruiz-Pérez S, Bezerra WBA, Becerra-Santamaria K, Leung V, et al. Equine hoof wall: Structure, properties, and bioinspired designs. Acta Biomater 2022:8205. https://doi.org/10.1016/j.actbio.2022.08.028.

[470] Pollitt CC. The anatomy and physiology of the hoof wall. Equine Vet Educ 1998;10:318–25. https://doi.org/10.1111/j.2042-3292.1998.tb00902.x.

[471] Budiansky B, Fleck NA. Compressive failure of fibre composites. J Mech Phys Solids 1993;41:183–211. https://doi.org/https://doi.org/10.1016/0022-5096(93)90068-Q.

[472] Lankford J. Compressive failure of fibre-reinforced composites: buckling, kinking, and the role of the interphase. J Mater Sci 1995;30:4343–8. https://doi.org/10.1007/BF00361515.

[473] Chung I, Weitsman Y. On the buckling/kinking compressive failure of fibrous composites. Int J Solids Struct 1995;32:2329–44. https://doi.org/https://doi.org/10.1016/0020-7683(94)00252-R.

[474] Dike S, Yang W, Pissarenko A, Quan H, Garcia Filho FC, Ritchie RO, et al. On the gular sac tissue of the brown pelican: Structural characterization and mechanical properties. Acta Biomater 2020;118:161–81. https://doi.org/https://doi.org/10.1016/j.actbio.2020.10.008.

[475] Wang B, Pan B, Lubineau G. Morphological evolution and internal strain mapping of pomelo peel using X-ray computed tomography and digital volume correlation. Mater Des 2018;137:305–15. https://doi.org/https://doi.org/10.1016/j.matdes.2017.10.038.

[476] Schäfer I, Mlikota M, Schmauder S, Weber U. Modelling the damping response of biomimetic foams based on pomelo fruit. Comput Mater Sci 2020;183:109801. https://doi.org/https://doi.org/10.1016/j.commatsci.2020.109801.

[477] Sonego M, Fleck C, Pessan LA. Mesocarp of Brazil nut (Bertholletia excelsa) as inspiration for new impact resistant materials. Bioinspiration and Biomimetics 2019;14. https://doi.org/10.1088/1748-3190/ab2298.

[478] Scussel VM, Manfio D, Savi GD, Moecke EHS. Stereoscopy and Scanning Electron Microscopy of Brazil Nut (Bertholletia excelsa H.B.K.) Shell, Brown Skin, and Edible Part: Part One-Healthy Nut. J Food Sci 2014;79:1443–53. https://doi.org/10.1111/1750-3841.12502.

[479] Nguyen XT, Hou S, Liu T, Han X. A potential natural energy absorption material – Coconut mesocarp: Part A: Experimental investigations on mechanical properties. Int J Mech Sci 2016;115–116:564–73. https://doi.org/https://doi.org/10.1016/j.ijmecsci.2016.07.017.

[480] Ha NS, Lu G, Shu D, Yu TX. Mechanical properties and energy absorption characteristics of tropical fruit durian (Durio zibethinus). J Mech Behav Biomed Mater 2020;104:103603. https://doi.org/https://doi.org/10.1016/j.jmbbm.2019.103603.

[481] Prakash O, Kumar R, Mishra A, Gupta R. Artocarpus heterophyllus (Jackfruit): an overview. Pharmacogn Rev 2009;3:353.

[482] Elevitch CR, Manner HI. Artocarpus heterophyllus (jackfruit). Species Profiles Pacific Isl Agrofor 2006;10:1–25.

[483] Pradhan Mitra P, Loqué D. Histochemical staining of Arabidopsis thaliana secondary cell wall elements. J Vis Exp 2014:51381. https://doi.org/10.3791/51381.

[484] Fukshansky L. Revisiting the hexagonal lattice: on optimal lattice circle packing. Elem Der Math 2011;66:1–9.

[485] O'Brien TP, Feder N, Mccully ME. Polychromatic staining of plant cell walls by toluidine blue O. Protoplasma 1964;59:368–73.

[486] Hepworth DG, Bruce DM. A method of calculating the mechanical properties of nanoscopic plant cell wall components from tissue properties. J Mater Sci 2000;35:5861–5. https://doi.org/10.1023/A:1026716710498.

[487] Anderson CT. Pectic Polysaccharides in Plants: Structure, Biosynthesis, Functions, and Applications BT - Extracellular Sugar-Based Biopolymers Matrices. In: Cohen E, Merzendorfer H, editors., Cham: Springer International Publishing; 2019, p. 487–514. https://doi.org/10.1007/978-3-030-12919-4_12.

[488] Wang D, Yeats TH, Uluisik S, Rose JKC, Seymour GB. Fruit Softening: Revisiting the Role of

Pectin. Trends Plant Sci 2018;23:302–10.
https://doi.org/https://doi.org/10.1016/j.tplants.2018.01.006.

[489] Lopez-Velazquez MA, Santes V, Balmaseda J, Torres-Garcia E. Pyrolysis of orange waste: A thermo-kinetic study. J Anal Appl Pyrolysis 2013;99:170–7.
https://doi.org/https://doi.org/10.1016/j.jaap.2012.09.016.

[490] Díez D, Urueña A, Piñero R, Barrio A, Tamminen T. Determination of Hemicellulose, Cellulose, and Lignin Content in Different Types of Biomasses by Thermogravimetric Analysis and Pseudocomponent Kinetic Model (TGA-PKM Method). Process 2020;8.
https://doi.org/10.3390/pr8091048.

[491] Wang Z, McDonald AG, Westerhof RJM, Kersten SRA, Cuba-Torres CM, Ha S, et al. Effect of cellulose crystallinity on the formation of a liquid intermediate and on product distribution during pyrolysis. J Anal Appl Pyrolysis 2013;100:56–66.
https://doi.org/https://doi.org/10.1016/j.jaap.2012.11.017.

[492] Aburto J, Moran M, Galano A, Torres-García E. Non-isothermal pyrolysis of pectin: A thermochemical and kinetic approach. J Anal Appl Pyrolysis 2015;112:94–104.
https://doi.org/https://doi.org/10.1016/j.jaap.2015.02.012.

[493] Ge S, Xu Y, Tian Z, She S, Huang L, Zhang Z, et al. Pyrolysis study of pectin by tunable synchrotron vacuum ultraviolet photoionization mass spectrometry. J Therm Anal Calorim 2015;120:1399–405. https://doi.org/10.1007/s10973-015-4440-4.

[494] Müller-Maatsch J, Bencivenni M, Caligiani A, Tedeschi T, Bruggeman G, Bosch M, et al. Pectin content and composition from different food waste streams. Food Chem 2016;201:37–45.
https://doi.org/https://doi.org/10.1016/j.foodchem.2016.01.012.

[495] Begum R, Yusof YA, Aziz MG, Uddin MB. Screening of Fruit Wastes as Pectin Source. J Environ Sci Nat Resour 2017;10:65–70. https://doi.org/10.3329/jesnr.v10i1.34696.

[496] May CD. Industrial pectins: Sources, production and applications. Carbohydr Polym 1990;12:79–99. https://doi.org/https://doi.org/10.1016/0144-8617(90)90105-2.

[497] Grønli MG, Várhegyi G, Di Blasi C. Thermogravimetric Analysis and Devolatilization Kinetics of Wood. Ind Eng Chem Res 2002;41:4201–8. https://doi.org/10.1021/ie0201157.

[498] Burhenne L, Messmer J, Aicher T, Laborie M-P. The effect of the biomass components lignin, cellulose and hemicellulose on TGA and fixed bed pyrolysis. J Anal Appl Pyrolysis 2013;101:177–84. https://doi.org/https://doi.org/10.1016/j.jaap.2013.01.012.

[499] Amutio M, Lopez G, Aguado R, Artetxe M, Bilbao J, Olazar M. Kinetic study of lignocellulosic biomass oxidative pyrolysis. Fuel 2012;95:305–11.
https://doi.org/https://doi.org/10.1016/j.fuel.2011.10.008.

[500] Orfão JJM, Antunes FJA, Figueiredo JL. Pyrolysis kinetics of lignocellulosic materials—three independent reactions model. Fuel 1999;78:349–58. https://doi.org/https://doi.org/10.1016/S0016-2361(98)00156-2.

[501] Rüggeberg M, Speck T, Paris O, Lapierre C, Pollet B, Koch G, et al. Stiffness gradients in vascular bundles of the palm Washingtonia robusta. Proc R Soc B Biol Sci 2008;275:2221–9.
https://doi.org/10.1098/rspb.2008.0531.

[502] dos Santos Abreu H, do Nascimento AM, Maria MA. Lignin structure and wood properties. Wood Fiber Sci 1999;31:426–33.

[503] Liu Q, Luo L, Zheng L. Lignins: Biosynthesis and Biological Functions in Plants. Int J Mol Sci 2018;19. https://doi.org/10.3390/ijms19020335.

[504] Jarvis MC, Briggs SPH, Knox JP. Intercellular adhesion and cell separation in plants. Plant Cell Environ 2003;26:977–89. https://doi.org/https://doi.org/10.1046/j.1365-3040.2003.01034.x.

[505] Gibson LJ. The hierarchical structure and mechanics of plant materials. J R Soc Interface 2012;9:2749–66.

[506] Willats WGT, McCartney L, Mackie W, Knox JP. Pectin: cell biology and prospects for functional analysis. Plant Mol Biol 2001;47:9–27. https://doi.org/10.1023/A:1010662911148.

[507] Baez LA, Tichá T, Hamann T. Cell wall integrity regulation across plant species. Plant Mol Biol 2022;109:483–504. https://doi.org/10.1007/s11103-022-01284-7.

[508] Keryvin V, Lan M, Bourmaud A, Parenteau T, Charleux L, Baley C. Analysis of flax fibres viscoelastic behaviour at micro and nano scales. Compos Part A Appl Sci Manuf 2015;68:219–25. https://doi.org/https://doi.org/10.1016/j.compositesa.2014.10.006.

[509] Carruthers JJ, Kettle AP, Robinson AM. Energy Absorption Capability and Crashworthiness of Composite Material Structures: A Review. Appl Mech Rev 1998;51:635–49. https://doi.org/10.1115/1.3100758.

[510] Zhang L, Bai Z, Bai F. Crashworthiness design for bio-inspired multi-cell tubes with quadrilateral , hexagonal and octagonal sections. Thin Walled Struct 2018;122:42–51. https://doi.org/10.1016/j.tws.2017.10.010.